



ΠΑΝΕΠΙΣΤΗΜΙΟ ΙΩΑΝΝΙΝΩΝ

ΣΧΟΛΗ ΘΕΤΙΚΩΝ ΕΠΙΣΤΗΜΩΝ

ΤΜΗΜΑ ΧΗΜΕΙΑΣ

Δυναμικές ιδιότητες της ολμεσαρτάνης στο διάλυμα και στο ενεργό κέντρο του υποδοχέα τύπου 1 της αγγειοτασίνης II. Βελτιστοποίηση φαρμακευτικού προφίλ βιοδραστικών ενώσεων μέσω συμπλόκων εγκλεισμού.

Ταχσίν Κελίτσης

Χημικός, MSc

ΔΙΔΑΚΤΟΡΙΚΗ ΔΙΑΤΡΙΒΗ

2017

«Η έγκριση της διδακτορικής διατριβής από το Τμήμα Χημείας της Σχολής Θετικών Επιστημών, του Πανεπιστημίου Ιωαννίνων δεν υποδηλώνει αποδοχή των γνώμων του συγγραφέα Ν. 5343/32, άρθρο 202, παράγραφος 2»

Ορισμός Τριμελούς Συμβουλευτικής Επιτροπής από τη Γ.Σ.Ε.Σ.: 875^Α/24-1-2014

Μέλη Τριμελούς Συμβουλευτικής Επιτροπής:

Επιβλέπων:

Ανδρέας Γ. Τζάκος, Επίκουρος Καθηγητής, Τμήμα Χημείας, Πανεπιστήμιο Ιωαννίνων

Μέλη:

Ιωάννης Γεροθανάσης, Καθηγητής, Τμήμα Χημείας, Πανεπιστήμιο Ιωαννίνων

Θωμάς Μαυρομούστακος, Καθηγητής, Τμήμα Χημείας, Εθνικό και Καποδιστριακό Πανεπιστήμιο Αθηνών

Ημερομηνία ορισμού θέματος: 933/23-9-2016

Θέμα: «Δυναμικές ιδιότητες της ολμεσαρτάνης στο διάλυμα και στο ενεργό κέντρο του υποδοχέα τύπου I της αγγειοτασίνης II. Βελτιστοποίηση φαρμακευτικού προφίλ βιοδραστικών ενώσεων μέσω συμπλόκων εγκλεισμού.»

ΟΡΙΣΜΟΣ ΕΠΤΑΜΕΛΟΥΣ ΕΞΕΤΑΣΤΙΚΗΣ ΕΠΙΤΡΟΠΗΣ από τη Γ.Σ.Ε.Σ.: 941^Α/23-12-2016

1. **Ανδρέας Τζάκος**, Επίκουρος Καθηγητής, Τμήμα Χημείας, Πανεπιστήμιο Ιωαννίνων
2. **Ιωάννης Γεροθανάσης**, Καθηγητής, Τμήμα Χημείας, Πανεπιστήμιο Ιωαννίνων
3. **Θωμάς Μαυρομούστακος**, Καθηγητής, Τμήμα Χημείας, Εθνικό και Καποδιστριακό Πανεπιστήμιο Αθηνών
4. **Σωτήριος Χατζηκακού**, Καθηγητής, Τμήμα Χημείας, Πανεπιστήμιο Ιωαννίνων
5. **Γεωργία Βαλσαμή**, Αναπληρώτρια Καθηγήτρια, Τμήμα Φαρμακευτικής, Εθνικό και Καποδιστριακό Πανεπιστήμιο Αθηνών
6. **Θεόδωρος Τσέλιος**, Αναπληρωτής Καθηγητής, Τμήμα Χημείας, Πανεπιστήμιο Πατρών
7. **Νικόλαος Κουρκουμέλης**, Επίκουρος Καθηγητής, Τμήμα Ιατρικής, Πανεπιστήμιο Ιωαννίνων

Έγκριση Διδακτορικής Διατριβής με βαθμό «ΑΡΙΣΤΑ» στις 14-2-2017

Η Πρόεδρος του Τμήματος Χημείας
Λέκκα Μαρία - Ελένη, Καθηγήτρια

Η Γραμματέας του Τμήματος
Ζωή-Βαλεντίνα Βαμβέτσου

ABSTRACT

In this thesis, we utilized an array of biophysical techniques to characterize in atomic level the interactions formed in small molecules and their receptors along with inclusion complexes. A special emphasis was given to complement the specific studies with *in silico* studies. The conformational properties of olmesartan and its methylated analogue were charted using a combination of NMR spectroscopy and molecular modeling. For the molecular docking calculations three different types of angiotensin II type 1 receptor (AT₁R) have been used: (a) the crystal structure; (b) a homology model based on the structure of CXCR4 and (c) a homology model based on the structure of rhodopsin. The aim of this study was to possibly explain the differences between the experimental findings derived from mutagenesis studies on this receptor and the crystal structure of the AT₁R-olmesartan complex. Molecular Dynamics (MD) experiments were performed to show the stability of the AT₁R-inverse agonist complex and the most prominent interactions during the simulated trajectory. The obtained results showed that olmesartan and its methyl ether exert similar interactions with critical residues justifying their almost identical *in vitro* activity. However, the docking and MD experiments failed to justify the mutation findings in a satisfactory matter, indicating that the real system is more complex and crystal structure or homology models of AT₁R receptors cannot simulate it sufficiently. Various conformations of olmesartan and olmesartan methyl ether were simulated to provide chemical shifts. These were compared with the experimental NMR results. Useful information regarding the putative bioactive conformations of olmesartan and its methylated analogue has been obtained. Finally, comparative data regarding the binding poses and energies of olmesartan, olmesartan methyl ether and three derivative compounds of olmesartan (R239470, R781253, R794847) were acquired using Prime/MM-GBSA calculations.

In silico studies, have been also utilized in an effort to determine the architecture of inclusion complexes of natural products and hosts. As host we used both different cyclodextrin derivatives as also calixarens. Specifically, the interaction between the hepatoprotectant drug silibinin and the host 2-hydroxypropyl- β -cyclodextrin (HP- β -CD) has been elucidated at the molecular level. The complexation product of silibinin with HP- β -CD has been characterized by Differential Scanning Calorimetry, solid and liquid high resolution NMR spectroscopy. The chemical shift changes using ¹³C CP/MAS on the

complexation of the guest with the host provided significant information on the molecular interactions and they were in agreement with the 2D NOESY results. These results point out that both in solid and liquid forms, the drug is engulfed and interacts with HP- β -CD in identical manner. Molecular dynamics calculations have been conducted to explore the thermodynamic characteristics associated with the silibinin–HP- β -CD interactions and to study the stability of the complex. To approximate the physiological conditions, the aqueous solubility and dissolution characteristics of the complex at pH states simulating those of the upper gastrointestinal tract have been applied. To evaluate and compare the antiproliferative activity of silibinin–HP- β -CD complex with respect to the parent silibinin, MTT assays have been conducted in MCF-7 human cancer cells.

Furthermore, *p*-sulphonatocalix[4]arene has been used as complexing agent for the poorly water soluble quercetin to enhance its solubility and bioavailability. The 1:1 complex formed between *p*-sulphonatocalix[4]arene and quercetin was confirmed by Job's plot, solid state NMR and molecular modeling. A gold nanoparticle was then established on the basis of this architectural scaffold which presented enhanced potency against cancer cell lines.

Parts of the present thesis were published in the following journals: *Molecules* [20(3):3868-3897, 2015], *Molecular Pharmaceutics* [12(3), 954-965, 2015], *Expert Opinion in Therapeutic Patents* [25(11), 1305-1317, 2015], *Current Medicinal Chemistry*, [23(1), 36-59, 2016] and *Arabian Journal of Chemistry* [doi: <http://dx.doi.org/10.1016/j.arabjc.2016.11.014>]. In addition, I have participated in other scientific projects that have been published in the following journals: *BBA–Biomembranes*, *Comb. Chem. High Throughput Screen.*, *Carbohydrate Res.*, *BBA-General Subjects*, *Chemico-Biological Interactions*, *MedChemComm*, *Int. J. Pharm.*, *J. Agr. Food Chem.*, *J. Biomol. Struct. Dyn.*, *Bioinformatics*, *J. Mol. Str.*, *Arzneimittelforschung-Drug Research*, *Platelets*.

ΠΕΡΙΛΗΨΗ

Στην παρούσα διατριβή, οι διαμορφωτικές ιδιότητες της ολμεσαρτάνης και του μεθυλιωμένου παραγώγου της έχουν μελετηθεί χρησιμοποιώντας ένα συνδυασμό φασματοσκοπίας NMR και μοριακής μοντελοποίησης. Για τα πειράματα μοριακής πρόσδεσης χρησιμοποιήθηκαν τρεις διαφορετικές τρισδιάστατες δομές του υποδοχέα τύπου 1 της αγγειοτασίνης II (AT₁R): α) κρυσταλλική δομή, β) ομόλογο μοντέλο με βάση τη τρισδιάστατη δομή του υποδοχέα CXCR4 και γ) ομόλογο μοντέλο με βάση τη ροδοψίνη. Σκοπός της συγκεκριμένης διατριβής ήταν η πιθανή εξήγηση των διαφορών μεταξύ των πειραματικών αποτελεσμάτων των μελετών μεταλλαξιγένεσης στον συγκεκριμένο υποδοχέα και της κρυσταλλικής δομής του συμπλόκου AT₁R-ολμεσαρτάνη. Διεξήχθησαν πειράματα μοριακής δυναμικής για να μελετηθεί η σταθερότητα του συμπλόκου AT₁R-αντίστροφου αγωνιστή και τις κύριες αλληλεπιδράσεις κατά τη διάρκεια της πορείας μοριακής προσομοίωσης. Τα αποτελέσματα δείχνουν ότι η ολμεσαρτάνη και το μεθυλιωμένο παράγωγο της έχουν παρόμοιες αλληλεπιδράσεις με τα κρίσιμα αμινοξέα εξηγώντας έτσι την σχεδόν πανομοιότυπη δραστηριότητα τους *in vitro*. Παρ' όλα αυτά μέσω των υπολογισμών μοριακής πρόσδεσης και μοριακής δυναμικής δεν ήταν εφικτό να εξηγηθούν τα αποτελέσματα μεταλλαξιγένεσης, δείχνοντας έτσι ότι το πραγματικό σύστημα είναι αρκετά περίπλοκο και πως η κρυσταλλική δομή και τα ομόλογα μοντέλα δεν δύναται να προσομοιώνουν το πολύπλοκο αυτό περιβάλλον επαρκώς. Πειράματα μοριακής κβαντικής χρησιμοποιήθηκαν για να υπολογισθούν οι χημικές μετατοπίσεις NMR για τις διάφορες διαμορφώσεις της ολμεσαρτάνης και του μεθυλιωμένου παραγώγου της. Οι τιμές αυτές συγκρίθηκαν με τις πειραματικές τιμές εξάγοντας χρήσιμες πληροφορίες για τις βιοδραστικές διαμορφώσεις της ολμεσαρτάνης και του μεθυλιωμένου παραγώγου της. Επιπλέον μέσω υπολογισμών Prime/MMGBSA συγκρίθηκαν οι πόζες και ενέργειες πρόσδεσης της ολμεσαρτάνης και του μεθυλαιθέρα της ολμεσαρτάνης στον AT₁R με τρία παράγωγα της ολμεσαρτάνης (R239470, R781253, R794847).

Στο δεύτερο μέρος της διατριβής έγινε εκτεταμένη χρήση μεθοδολογιών μοριακής δυναμικής και μοντελοποίησης σε διαφορετικά φυσικά προϊόντα στην προσπάθειά μας να αυξηθεί η βιοδιαθεσιμότητά και η υδατοδιαλυτότητά τους με ενώσεις εγκλεισμού και να χαρακτηρίσουμε την αρχιτεκτονική των αλληλεπιδράσεων στα σύμπλοκα εγκλεισμού. Συγκεκριμένα μελετήθηκαν σε μοριακό επίπεδο οι αλληλεπιδράσεις της σιλιμπινίνης, ενός φαρμάκου που προστατεύει κατά της ηπατοτοξικότητας, με την 2-υδροξυπροπυλο-β-

κυκλοδεξτρίνη (HP-β-CD). Το σύμπλοκο εγκλεισμού της σιλιμπινίνης με την HP-β-CD χαρακτηρίστηκε με Διαφορική Θερμιδομετρία Σάρωσης, και φασματοσκοπία NMR υγρής και στερεής κατάστασης. Οι μεταβολές στις χημικές μετατοπίσεις του συμπλόκου εγκλεισμού που χαρτογραφήσαμε, χρησιμοποιώντας ^{13}C CP/MAS, παρέχουν σημαντικές πληροφορίες για τις μοριακές αλληλεπιδράσεις και ήταν σε άριστη συμφωνία με τα αποτελέσματα 2D NOESY. Τα αποτελέσματα αυτά επισημαίνουν πως το μόριο έχει ενσωματωθεί εντός της κοιλότητας της HP-β-CD και αλληλεπιδρά με παρόμοιο τρόπο σε υγρή και στερεή μορφή. Τα θερμοδυναμικά χαρακτηριστικά του συμπλόκου σιλιμπινίνη-HP-β-CD και η σταθερότητα του μελετήθηκαν μέσω υπολογισμών μοριακής δυναμικής. Η διαλυτότητα του συμπλόκου σε νερό καθώς και τα χαρακτηριστικά της διαλυτότητας υπολογίστηκαν σε pH που προσομοιώνει το άνω γαστρεντερικό σύστημα, για να προσεγγισθούν οι φυσιολογικές συνθήκες. Η αντιπολλαπλασιαστική επίδραση του συμπλόκου σιλιμπινίνη-HP-β-CD συγκρίθηκε με εκείνη της σιλιμπινίνης σε ανθρώπινα καρκινικά κύτταρα MCF-7 μέσω δοκιμών MTT.

Επίσης, προς την ίδια κατεύθυνση, χρησιμοποιήθηκε το *p*-σουλφονατο καλιξ[4]αρένιο ως παράγοντας εγκλεισμού για την αύξηση της υδατοδιαλυτότητας και βιοδιαθεσιμότητα της κερκετίνης. Η στοιχειομετρία του συμπλόκου καλιξαρενίου-κερκετίνης επιβεβαιώθηκε πως είναι 1:1 με την χρήση διαφορετικών μεθόδων (φασματοσκοπία UV, Job plot, φασματοσκοπία NMR στερεής κατάστασης και μοριακής μοντελοποίησης).

Μέρος της παρούσας διδακτορικής διατριβής έχει δημοσιευθεί στα περιοδικά: *Molecules* [20(3):3868-3897, 2015], *Molecular Pharmaceutics* [12(3), 954-965, 2015], *Expert Opinion in Therapeutic Patents* [25(11), 1305-1317, 2015], *Current Medicinal Chemistry*, [23(1), 36-59, 2016], *Arabian Journal of Chemistry* [doi: <http://dx.doi.org/10.1016/j.arabjc.2016.11.014>]. Επίσης παράλληλα συμμετείχα σε άλλα ερευνητικά προγράμματα κατά τη διάρκεια των οποίων δημοσίευσα στα πιο κάτω περιοδικά: *BBA-Biomembranes*, *Comb. Chem. High Throughput Screen.*, *Carbohydrate Res.*, *BBA-General Subjects*, *Chemico-Biological Interactions*, *MedChemComm*, *Int. J. Pharm.*, *J. Agr. Food Chem.*, *J. Biomol. Struct. Dyn.*, *Bioinformatics*, *J. Mol. Str.*, *Arzneimittelforschung-Drug Research*, *Platelets*.

Acknowledgements

First and foremost, I would like to express my gratitude to my supervisor, Assistant Professor Dr. Andreas G. Tzakos for his support, and thoughtful advice.

I am particularly grateful to Prof. Dr. Thomas Mavromoustakos for his encouragement and his support in the computational studies.

I would like to thank, Prof. Dr. Ioannis Gerotheranassis, for his helpful advice and the comments and corrections of my thesis.

I wish to thank my examiners: Professor Sotirios Chatzikakou, Associate Professors Theodoros Tselios and Georgia Valsami and Assistant Professor Nikolaos Kourkoumelis, for their comments on my thesis and the interesting discussion during my viva.

I am grateful to Associate Professor Georgia Valsami and the members of her laboratory for the preparation of the silibinin:cyclodextrin complex as well as the solubility and dissolution rate experiments.

I would also like to acknowledge the help that I have received from my colleagues Dr. Dimitrios Ntountaniotis (solid state NMR), Maria V. Chatziathanasiadou (MSc.) (MTT assays), Alexandra V. Chatzikonstantinou (MSc.) (DOSY experiments), and Apostolos Karanastasis at the Department of Materials Science and Engineering (Electrophoretic light scattering and TEM).

I also would like to thank Prof. Clemens Glaubitz and Dr. Johanna Becker-Baldus for their help in the acquirement of the solid state NMR spectra in the Institute of Biophysical Chemistry, in the Goethe University, Frankfurt. The visits in their lab were financed by the programme for the promotion of the exchange and scientific cooperation between Greece and Germany IKYDA 2015.

Computational resources for this PhD thesis for a total of 100,000 GPU hours were provided by two grants awarded by the Cy-Tera Project (NEA ΥΠΟΔΟΜΗ/ΣΤΡΑΤΗΓ/0308/31), which is co-funded by the European Regional Development Fund and the Republic of Cyprus through the Research Promotion Foundation.

Finally, I would like to thank the European Union (European Regional Development Fund-ERDF) and Greek national funds through the Operational Program “THESSALY-MAINLAND GREECE AND EPIRUS-2007–2013” of the National Strategic Reference Framework (NSRF 2007–2013) for the financial support.

Table of Contents

1	Chapter 1: Introduction-Theoretical Framework	16
1.1	The angiotensin II type 1 receptor and its antagonists.....	16
1.2	Structural and conformational properties of AT ₁ R receptors and AT ₁ R antagonists 19	
1.3	Comparison of conformational properties in different environments.....	22
1.4	Homology models of AT ₁ R	23
1.5	Olmesartan	25
1.5.1	Docking of olmesartan to the AT ₁ R	25
1.6	The Role of Membrane Bilayers in the Binding of drugs to the AT Receptors ...	27
1.7	The use of cyclodextrins and calixarenes in pharmaceutical formulations	29
1.7.1	Cyclodextrins.....	29
1.7.2	A brief history of the cyclodextrins.....	29
1.7.3	Cyclodextrins in pharmaceutical formulations.....	31
1.7.4	Characterization of drug:CD complexes	34
1.7.5	Computational studies of drug:CD inclusion complexes	41
1.8	Calixarenes.....	44
2	Chapter 2: Objectives and Scope of the Thesis.....	48
2.1	The dynamic properties of angiotensin II type 1 receptor inverse agonists in solution and in the receptor site	48
2.2	Investigation of the interactions of silibinin with 2-hydroxypropyl- β -cyclodextrin through biophysical techniques and computational methods	50
2.3	Cancer delivery of quercetin through pH responsive calixarene-gold nanoparticles	52
3	Chapter 3: Methodology	55
3.1	Computational methods for investigating the dynamic properties of olmesartan	55
3.2	Materials and Methods for the investigation of the interactions of silibinin with HP- β -CD	61
3.3	Material and methods for the investigation of the interactions between quercetin and p-sulphonato[4]calixarene.....	66
4	Chapter 4: The dynamic properties of angiotensin II type 1 receptor inverse agonists in solution and in the receptor site.....	70
4.1	Conformational analysis of olmesartan and olmesartan methyl ether in solution using NMR and theoretical calculations	70

4.2	Induced Fit Docking calculations	78
	<i>Olmesartan methyl ether in the crystal structure and the two homology models</i>	85
4.3	Molecular Dynamics Simulations.....	86
4.4	Comparison between NMR data and predicted ¹³ C NMR chemical shifts.....	95
4.5	The interactions of R239470, R794847 and R781253 with the crystal structure 4ZUD 103	
4.6	Conclusions.....	106
5	Chapter 5: Interactions of silibinin with 2-hydroxypropyl-β-cyclodextrin.....	109
5.1	DSC analysis to characterize the SLB–HP-β-CD complex.....	109
5.2	¹³ C solid state CP/MAS NMR spectra.....	110
5.3	¹ H- ¹ H 2D NOESY spectra of the complexes.....	113
5.4	Solubility experiments	115
5.5	Dissolution rate experiments.....	115
5.6	Diffusion Ordered NMR Spectroscopy.....	117
5.7	MD Simulations.....	118
5.8	MTT assay.....	120
5.9	Conclusions.....	121
6	Chapter 6: Cancer delivery of quercetin through a pH responsive calixarene–gold nanoparticle	122
6.1	Determination of the Binding constant of the quercetin –calixarene complex...	122
6.2	Job’s plot.....	122
6.3	Solid State NMR spectroscopy	123
6.4	Molecular modeling.....	125
6.5	Electrophoretic light Scattering and TEM	127
7	Conclusions	129
8	Abbreviations	131
9	Permission/License	133
10	PUBLICATIONS-PRESENTATIONS	134
10.1	Publications in International Journals.....	134
10.2	Publications in Greek Journals	136
10.3	Poster Presentations	136
11	References	138

Legend of Figures

Figure 1-1. The RAS and representative drugs that target this system ³	17
Figure 1-2. (top, left) A 3D proposed model of Ang II. (top, right) A 3D structure of losartan. Circled or squared segments of the two molecules illustrate common pharmacophores. Circled common pharmacophores are shown for the 2D structures of Ang II (top, left) and losartan (bottom, right) ³	19
Figure 1-3. Structures of AT ₁ R antagonists. Almost all of them contain three structural features: biphenyl tetrazole or acidic bioisostere (colored in blue), heterocyclic segment (colored in green) and small alkyl chain (colored in red) ⁵⁵	23
Figure 1-4. A) Superimposition of the crystal structure (green) with the homology model derived from the rhodopsin structure (blue) and the homology model derived from the CXCR4 structure (red). B) The second extracellular loop in the two homology models (blue and red) and the crystal structure (green). C) Superimposition of the four key residues Arg167, Lys199, Tyr35 and Ile288 (in green are shown the residues in the crystal structure, in blue the residues in the rhodopsin homology model and in red the residues in the CXCR4 homology model) ⁵⁵	25
Figure 1-5. A) Crystal structure of olmesartan (CSD reference code: ZOGSOD); B) Low energy conformers of olmesartan in methanol optimized using the HF/6.31G** basis set (RMSD between the crystal structure A and B is 0.2 Å.) ⁵⁵	26
Figure 1-6. A) Docking of olmesartan in the homology model of AT ₁ R based on CXCR4. Blue lines represent hydrogen bonds, cyan lines represent π -cation interactions and green lines represent π - π interactions. B) Docking of olmesartan in the crystal structure of AT ₁ R ⁵⁵	27
Figure 1-7. A. Candesartan cilexetil (left) and olmesartan (right) positioned in one leaflet of membrane bilayers. As it can be observed candesartan cilexetil is positioned deeper in membrane bilayers owing to its more hydrophobic nature. However, both molecules as they are amphipathic adopt polar and non-polar interactions. B. Two step mechanism of action for ARBs. In the first step ARBs are postulated to embed themselves in the lipid matrix and in the second step are laterally diffused to the active site of AT ₁ R ³	28
Figure 1-8. (Top) The structures of α -CD, β -CD and γ -CD. (Middle) Geometric dimensions of the cyclodextrins. (Bottom) The glycopyranose unit and a spacefilling model of β -CD	31
Figure 1-9. Structural representation of p-tert-butylcalix[n]arene ¹⁷⁵	45
Figure 1-10. The four limiting conformations of calix[4]arenes (cone, partial cone, 1,3-alternate and 1,2-alternate). For R = Methyl or Ethyl, conformational interconversion takes place even at room temperature, whereas when the R groups are larger than ethyl, the structure is fixed by the conditions used during lower rim (phenolic oxygen) functionalization process. Pure conformers of calix[4]arene can be isolated only in case of sterically hindered rotation around the bridging methylene group like in the case of p-tert-butylcalix[4]arenes and is generally unknown for n>4 ¹⁷⁵	46
Figure 2-1. Chemical structures of olmesartan medoxomil, olmesartan and olmesartan methyl ether as well as their critical dihedral angles and the derivatives of olmesartan R239470, R781253, and R794847.	48
Figure 2-2. Structure of SLB (top, left) and the cyclic HP- β -CD (right) consisting of seven D-glycopyranose units (bottom, left). Numbers correspond to those referred in the NMR tables.....	50
Figure 2-3: A) Tumor sites create larger gaps in the endothelium. Disorganised angiogenic tumor vessels are developed that supply nutrients and oxygen. The EPR effect causes the accumulation of molecules of high molecular weight. The cancer cells create an acidic environment around them. B)	

The anionic gold nanoparticle enters the cell through a process of endocytosis. Quercetin is mainly released in the acidic environment of the liposome. C) The structures of quercetin, p-sulfonato-calix[4]arene, the Calix-Qrc complex and the Calix-Qrc-Au nanoparticle..... 54

Figure 4-1. ¹H NMR spectra for a) olmesartan dissolved in CD₃OD b) olmesartan methyl ether dissolved in CD₃OD and c) olmesartan methyl ether dissolved in CD₃CN ³⁰³. 72

Figure 4-2. Representative low energy conformations of (a) olmesartan in methanol and olmesartan methyl ether in: (b) methanol and (c) acetonitrile as derived from MacroModel ³⁰³. 73

Figure 4-3. Representative low energy conformers of olmesartan in methanol without using constraints. 73

Figure 4-4. Representative low energy conformers of olmesartan methyl ether in methanol without the use of constraints. 74

Figure 4-5. Representative low energy conformers of olmesartan methyl ether in acetonitrile. 75

Figure 4-6. Coordinate scan for the dihedral τ_8 using molecular mechanics and the OPLS3 force field 75

Figure 4-7. Potential energy surface scan of the dihedral τ_8 using DFT level of theory and the B3LYP/6-31G** hybrid functional..... 76

Figure 4-8. a) Crystal structure of olmesartan (CSD reference code: ZOGSOD); b) Low energy conformers of olmesartan in methanol optimized using the HF/6.31G** basis set; c) Optimized lowest energy conformer of olmesartan methyl ether in methanol; d) Optimized lowest energy conformer of olmesartan methyl ether in acetonitrile ³⁰³. 77

Figure 4-9. Most energetically favorable poses of olmesartan (left) and olmesartan methyl ether (right) in the AT₁R after applying induced fit docking in the a) crystal structure (PDB ID 4YAY), b) CXCR4 homology model, c) rhodopsin homology. Blue lines represent hydrogen bonds, cyan lines represent π -cation interactions 79

Figure 4-10. Most energetically favorable poses of olmesartan in the AT₁R crystal structure 4ZUD (in three dimensions and two dimensions) after the induced fit docking in a) mutant Y113F; b) mutant K199Q; c) mutant H256A and d) mutant Q257A. 81

Figure 4-11. Most energetically favorable poses of olmesartan (in three dimensions and two dimensions) after the induced fit docking in implicit membrane in the AT₁R homology model based on CXCR4: a) mutant Y113F; b) mutant K199Q; c) mutant H256A; and d) mutant Q257A. 83

Figure 4-12. Most energetically favorable poses of olmesartan (in three dimensions and two dimensions) after the induced fit docking in the AT₁R homology model based on rhodopsin: a) mutant Y113F; b) mutant K199Q; c) mutant H256A and d) mutant Q257A..... 85

Figure 4-13: Protein and ligand RMSD during the time of simulation for: (a) olmesartan in the crystal structure with PDB ID 4ZUD; (b) olmesartan in the Y113F mutant; (c) olmesartan in the K199Q mutant; (d) olmesartan in the H256A mutant; (e) olmesartan in the Q257A mutant and (f) olmesartan methyl ether. 87

Figure 4-14: Protein-ligand interactions during the whole simulation time for: (a) olmesartan; (b) olmesartan methyl ether ³⁰³. 90

Figure 4-15. Modification of olmesartan's dihedral angles as a function of time during MD simulations in the crystal structure 4ZUD surrounded by DPPC bilayers. 90

Figure 4-16. a) Distances between H9 and H4 (blue) and H19-H12 (red) for olmesartan b) Distances between H19-H12 (blue), H9-H4 (red), H9-H5 (green) in olmesartan methyl ether c) Distance between H9-H23 (blue), H10-H23 (red) in olmesartan methyl ether 91

Figure 4-17. Protein-ligand interactions during the whole time of simulation for (a) olmesartan in the Y113F mutant (b) olmesartan in the K199Q mutant (c) olmesartan in the H256A mutant (d) olmesartan in the Q257A mutant.	93
Figure 4-18. RMSD of the backbone and interactions fraction for the mutation Y113A.	94
Figure 4-19. Modification of τ_8 during the trajectory for (a) olmesartan; (b) olmesartan in the Y113F mutant; (c) olmesartan in the K199Q mutant; (d) olmesartan in the H256A mutant; (e) olmesartan in the Q257A mutant; (f) olmesartan methyl ether and (g) olmesartan in the Y113A mutant.	94
Figure 4-20. Interactions fraction and binding modes of (a) R239470; (b) R794847; (c) R781253	105
Figure 5-1: Thermal scans of A) SLB, B) HP- β -CD, C) their mixture (molar ratio 1:1) and D) the complex with the same ratio ³¹⁹	110
Figure 5-2: ¹³ C CP/MAS spectra of (A) silibinin, (B) HP- β -CD, (C) mixture of SLB-HP- β -CD and (D) complex of SLB-HP- β -CD ³¹⁹	113
Figure 5-3: 2D NOESY of the complex of SLB-HP- β -CD using mixing time of 150 ms.	114
Figure 5-4. Solubility of SLB-HP- β -CD complex (top) and pure SLB (bottom).	116
Figure 5-5. pH effect on SLB dissolution from the SLB-HP- β -CD lyophilized.	116
Figure 5-6. Overlapping of the same spectral region from a DOSY spectrum of 0.5 mM of SLB-HP- β -CD lyophilized product (in black), and free HP- β -CD (1.8 mM) (in red). The spectra were recorded in D ₂ O at room temperature.	117
Figure 5-7. RMSD values versus trajectory time of the modified cyclodextrin (red), and all atoms of silybin (in blue).	118
Figure 5-8. The SLBA-HP- β -CD complex: A) as predicted initially by GlideXP (hydrogen bonds are shown in green), B) after 100 ns of MD simulation, C) after 200 ns, and D) at the end of the simulation.	119
Figure 5-9. Effects of SLB-HP- β -CD (in green) and SLB (in blue) on cell proliferation determined by MTT assay. Data are the result of 2 independent experiments performed in triplicates. The standard error of each measurement is also presented ³¹⁹	120
Figure 6-1 Benesi-Hildebrand plot for the complex formation of <i>p</i> -sulphonatocalix[4]arene/Quercetin.	122
Figure 6-2. Job's plot for <i>p</i> -sulphonatocalix[4]arene-quercetin complex (Conc. 1×10^{-4} M).....	123
Figure 6-3. ¹ H- ¹³ C CPMAS (a) and ¹ H MAS (b) NMR spectra of quercetin (Q), calixarene (C), simple mixture of Q and C, Q:C complex, and GNPs@Calix-Qrc complex.	125
Figure 6-4: The quercetin-calixarene complex: A) as predicted initially by GlideXP (hydrogen bonds are shown in blue and π - π interactions in cyan), B) after the optimization using the X3LYP/6-31G** basis set, C) quercetin completely included in the calixarene, and D) quercetin detached from the calixarene but still interacting with it.	127
Figure 6-5: A) HR-TEM Image of finely dispersed GNPs@Calix-Qrc Complex and B) ultra-high magnification image of an isolated particle where the distance between two successive 200 crystal planes is highlighted ³⁴⁰	128

Legend of Tables

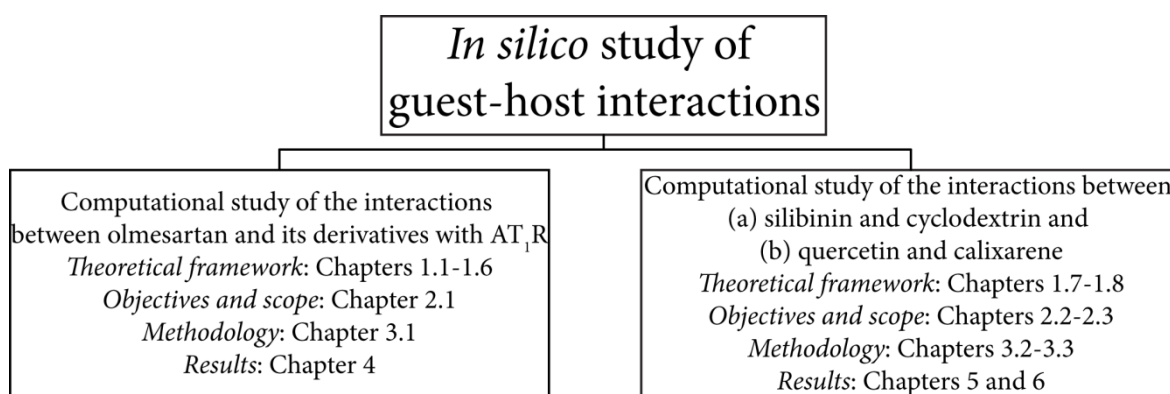
Table 1-1: List of CD containing drug products with their tradenames ^{99, 101}	33
Table 1-2: Examples of the recent bibliography involving MD simulations of cyclodextrin complexes.	42
Table 3-1: NOE derived distances obtained after integration of the cross-peaks obtained from 2D NOESY spectra.	57
Table 4-1: Interactions of olmesartan with the residues of AT ₁ R in the crystal structures and the two homology models.	85
Table 4-2: Interactions of olmesartan methyl ether with the residues of AT ₁ R in the crystal structure and the two homology models.	86
Table 4-3: Predicted chemical shifts for olmesartan's eight representative conformations and the crystal structure (CSD reference code ZOGSOD).	97
Table 4-4: Predicted chemical shifts for olmesartan methyl ether's four representative conformations in CD ₃ OD.	98
Table 4-5: Predicted chemical shifts for olmesartan methyl ether's four representative conformations in CD ₃ CN.	99
Table 4-6: Predicted NMR chemical shifts for olmesartan in the two receptors (PDB ID codes 4YAY and 4ZUD) as were calculated using QSite.	100
Table 4-7: Predicted NMR Chemical Shifts for olmesartan methyl ether in the two receptors (PDB ID codes 4YAY and 4ZUD) as were calculated using QSite.	101
Table 4-8: % deviations of various conformers in the ¹³ C chemical shifts versus the experimental for olmesartan and its methyl ether.	102
Table 4-9: Prime MM-GBSA energies for olmesartan, binding at the wild type AT ₁ R and its four mutated structures Y113F, K199Q, H256A and Q257A, olmesartan methyl ether, R781253, R794847 and R239470 binding at the wild type of AT ₁ R.	103
Table 5-1: <i>T_m</i> , <i>T_{onset}</i> and ΔH values for the samples SLB, HP- β -CD, the mixture SLB-HP- β -CD 1:1 and the complexes SLB-HP- β -CD using ratios 1:1, 1:2 and 1:4. (Values are subjected to 5% error for three consecutive runs.)	109
Table 5-2: ¹³ C chemical shifts of SLB, HP- β -CD, mixture of SLB and HP- β -CD, and complex SLB-HP- β -CD.	111
Table 5-3: Binding free energy analysis for the SLBA-HP- β -CD complex as obtained by the MM-PBSA calculations.	119
Table 6-1: Binding free energy analysis for the quercetin-calixarene complex as obtained by the MM-PBSA calculations.	126

Legend of Schemes

Scheme 1-1: Organization of the thesis.....	16
Scheme 3-1. Computational workflow.....	56

1 Chapter 1: Introduction-Theoretical Framework

The main scope of the present thesis is the *in silico* study of guest-host interactions of bioactive compounds. In the first chapter is summarized the theoretical framework of the principles governing the *in silico* study (see Scheme 1-1). The objectives and scope of the thesis dissertation are explained in the second chapter. The methodologies applied are described in the third chapter. Chapter 4 is devoted to the results of the interactions between olmesartan and its derivatives with AT₁R. In the last two subsequent chapters are discussed the results of the interactions between silibinin and cyclodextrin (chapter 5) and quercetin with calixarene (chapter 6).



Scheme 1-1: Organization of the thesis.

1.1 The angiotensin II type 1 receptor and its antagonists

The renin angiotensin system (RAS) is the main target for regulating the body's blood pressure¹. This is a bioenzymatic system where angiotensinogen, through the two enzymes renin and angiotensin converting enzyme (ACE), produces the octapeptide hormone angiotensin II (Ang II: a compound word of Greek origin composed of the words «αγγείο» (vessel) and «τάση» (tension)) that in pathological conditions causes vasoconstriction. ACE inhibitors were the first drugs designed and synthesized to block the detrimental effects of Ang II (Figure 1-1)².

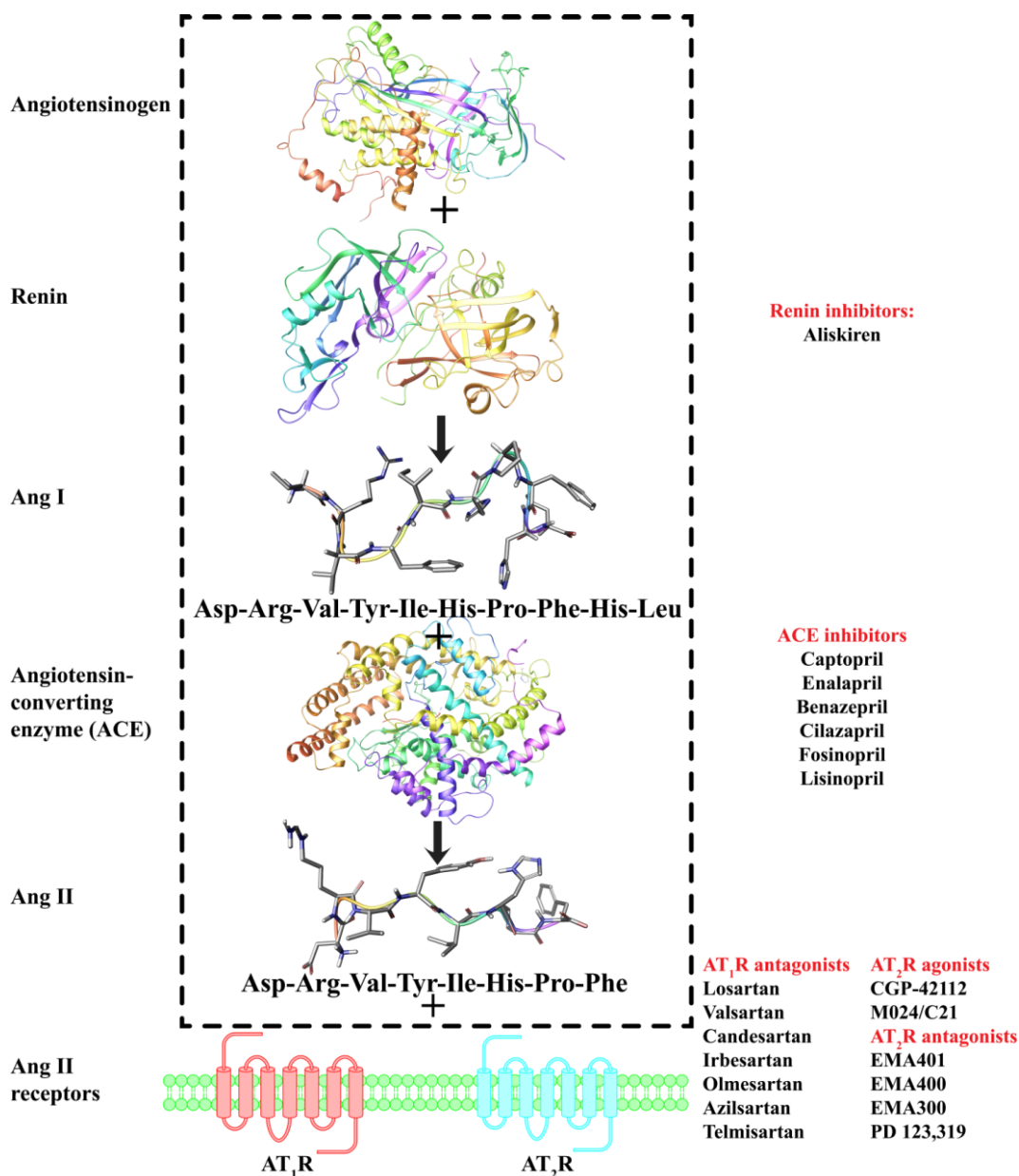


Figure 1-1. The RAS and representative drugs that target this system ³.

Recently, the efforts to design and synthesize renin inhibitors were met with success with the discovery of the drug aliskiren ⁴. Today, more knowledge has been gained on RAS. First, it is known that more biochemical pathways are affecting the conversion of angiotensinogen to Ang II; second, although Ang II affects mainly two GPCR receptor subtypes, namely AT₁R and AT₂R, at least four different subtypes have been identified (designated as AT₁R, AT₂R, AT₃R and AT₄R ⁵). Also, the different metabolites of Ang II, which are formed after proteolytic degradation of the parent molecule, exert biological activities. In addition, Ang II has high binding affinity to neurolysin which in turn may affect significantly the activity on RAS ⁶⁻⁸. The action of Ang II on AT₁R was the first to be

studied in detail, while the mode of action of AT₂R remained elusive for a long time owing to the lack of ligands that selectively target this receptor as also due to its low expression⁹⁻¹². The recent discovery of novel ligands that selectively target these receptor subtypes has paved the way to deconvolute the functions of AT₁R and AT₂R. Furthermore, new functions of the two receptors have been revealed. It is now shown that AT₁R and AT₂R present opposing biological functions, e.g., AT₂R has anti-proliferative properties^{13, 14}, while AT₁R facilitates angiogenesis and cellular proliferation^{13, 15}. Furthermore, besides the classical functions mediated by the AT₁R like vasoconstriction, proliferation of vascular smooth muscle and cardiac cellular growth, a direct correlation has been identified between the up-regulation of AT₁R and the immunosuppression and invasiveness state in many cancer types, establishing AT₁R as a potential cancer drug target¹⁶⁻²⁰. Respectively, the discovery of new ligands that selectively target AT₂R has encouraged the scientific community to explore in detail functions orchestrated and associated by AT₂R. For instance, AT₂R adopts a protective role in pathological conditions such as tissue injury and inflammation²¹, diabetic neuropathy²², stroke damage²³, diabetes type 2²⁴, spinal cord injury²⁵ and cancer^{26, 27}. The accumulating body of evidence highlights the enhanced potential of both AT₁R and AT₂R to act as important pharmaceutical targets for a diverse array of pathologies. In light of this, it is worth collating the principles that govern selectivity on these two subtype receptors and utilize these to design and develop the new generation of more selective compounds.

As with renin and ACE inhibitors, extensive rational design plans had to be implemented by researchers working both in industry and academia to discover AT₁R antagonists. Initially, efforts were mainly focused on peptides, but owing to the known disadvantages that peptides encounter they could not enter clinical trials or the market as drugs. However, these studies provided valuable SAR knowledge. From peptides, the scientists have been led to small organic molecules that mimicked the C-terminal segment of Ang II (Figure 1-2).

The first AT₁R antagonist that entered the market was losartan [IC₅₀ = 5.5 nM²⁸ (binding to human AT₁R using as radioligand ¹²⁵I[Sar¹-Ile⁸]Ang II), 150 nM²⁹ (inhibition of [¹²⁵I]Ang II (0.2 nM) binding to bovine adrenal cortical membranes), 6.7 nM³⁰ (displacement of [¹²⁵I]Sar¹,Ile⁸-Ang II specifically bound to AT₁R in rat hepatic membranes)]. The success of losartan followed eight more derivatives constituting the class of SARTANs or angiotensin receptor blockers (ARBs) (Figures 1-3).

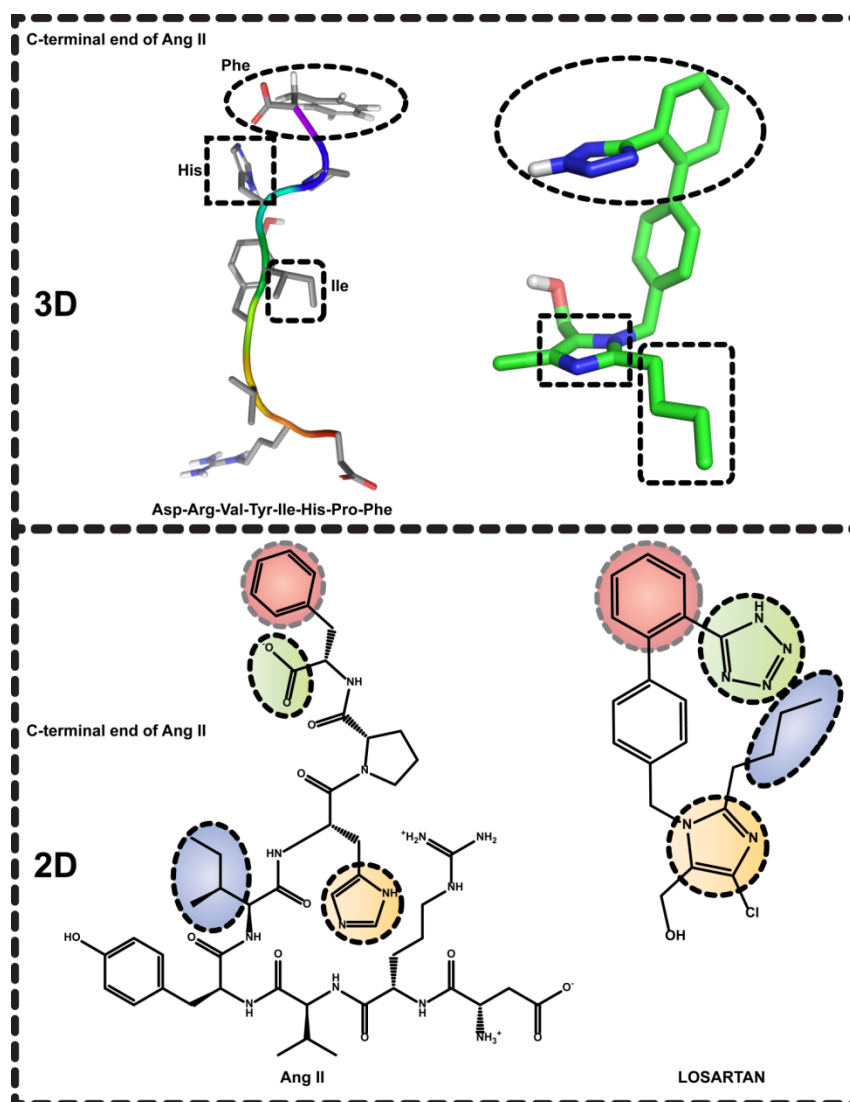


Figure 1-2. (top, left) A 3D proposed model of Ang II. (top, right) A 3D structure of losartan. Circled or squared segments of the two molecules illustrate common pharmacophores. Circled common pharmacophores are shown for the 2D structures of Ang II (top, left) and losartan (bottom, right) ³.

1.2 Structural and conformational properties of AT₁R receptors and AT₁R antagonists

Angiotensin II (AngII) is an octapeptide hormone generated in the Renin Angiotensin System (RAS), through a biocascade of enzymatic reactions and it is responsible for the regulation of the blood pressure. AT₁R antagonists are molecules that antagonize the action of peptide hormone Angiotensin II that is implicated in causing hypertension in the case of RAS overexpression, by acting on the AT₁R ^{1, 2, 5, 31-39}.

The AT₁R belongs to family A of G-protein coupled receptors (GPCRs) and, like other GPCRs, is consisted of an amino terminal extracellular region, a carboxy-terminal

intracellular tail and seven, mostly hydrophobic, membrane-spanning segments (TMs), connected by alternating intracellular (IL) and extracellular loops (EL)⁴⁰. The intracellular regions of AT₁R are most likely involved in receptor/G-protein coupling, whereas the extracellular regions interact with AngII and its analogues. The interaction of AngII with AT₁R induces conformational changes that are associated with the receptor activation. These conformational changes are transmitted through the TMs of AT₁R to its intracellular regions and are responsible for receptor interaction and stimulation of G-proteins, thus eliciting a biological effect. Combining molecular dynamics (MD) simulations and a mutagenesis approach, Cabana, *et al.*⁴¹, illustrated that activation of AT₁R is associated with a reorientation of D74^{2.50} in the second TM (TM2) and N295^{7.46} in the seventh TM (TM7) of AT₁R from the third TM (TM3) toward the first TM (TM1). The superscripts refer to a generalized numbering system that indexes TM residues of family A GPCRs relative to the most conserved amino acid in the TM in which it is located⁴². Specifically, in the inactive AT₁R, the D74^{2.50} in TM2 interacts with the N111^{3.35} in the TM3 and N295^{7.46} in TM7 through a H-bond network. Receptor activation is associated with a reorientation of these residues, and the formation of a new H-bond network involving D74^{2.50}, N295^{7.46} and N46^{1.50}. These conformational changes are associated with a change in the water accessibility within an area of AT₁R, which is located between the upper portions of TM3 and TM7, approximately up to two helical turns above N295^{7.46}. This area contains a hydrophobic cluster consisted of V108^{3.33} and L112^{3.36} in TM3, I288^{7.39}, A291^{7.42} and Y292^{7.43} in TM7, and F77^{2.53} in TM2. These residues form a tight hydrophobic core, which is disrupted during AT₁R activation. Specifically, there is a gain in water accessibility during receptor activation, which is associated with TM movements that result in a 3Å increase in the average distance between portions of TM3 (V108^{3.33} to L112^{3.36}) and TM7 (I288^{7.39} to Y292^{7.43}). The receptor activation-associated disruption of the hydrophobic cluster and the increase of the solvent accessibility in that area of AT₁R, possibly influences the orientation of the side chain of W253^{6.48} in the sixth TM (TM6) of receptor⁴¹. The W253^{6.48}, a conserved tryptophan residue in family A GPCRs, also known as the “rotamer toggle switch”, has been shown to play a key role in the activation of GPCRs^{43, 44}. Interestingly, the recent crystal structure of the AT₁R in complex with an antagonist, and a thorough mutagenesis study^{45, 46}, have shown that along with Arg167 in the second extracellular loop of the AT1, V108^{3.33} and Ser109^{3.33} in the TM3, Gln257^{6.52} in the TM6, as well as, Tyr292^{7.43} and Asn295^{7.46} in the TM7 interact with AT₁R antagonists.

It is therefore tempting to speculate that the molecular mechanism underlying AT₁R antagonism involves ligand interaction with these residues and stabilization of the tight hydrophobic network between TM3 and TM7, thus impeding the TM movements that are responsible for the increase in the distance between TM3 and TM7 during receptor activation^{47,48}.

The crystal structures of commercially available AT₁R antagonists that provide information on the conformational properties in the solid state was studied. In addition, literature will be reported referring to the conformational properties of AT₁R antagonists in solution using mainly high resolution NMR spectroscopy and *in silico* calculations using molecular and quantum mechanics approaches.

The human receptor AT₁R in complex with its selective antagonist ZD7155 at 2.9 Å resolution was crystallized in 2015 by applying the recently developed method of serial femtosecond crystallography at an X-ray free-electron laser⁴⁶. AT₁R antagonists are structurally similar to the prototype losartan. At the moment in the market there are eight molecules, whose structures are shown in Figure 1-3. These molecules that were originally developed to illustrate therapeutic potential for hypertension were recently found to exert a broader therapeutic window for many other diseases³. Valsartan and telmisartan are among the top 30 blockbuster drugs in 2013 with sellings of \$3.5 and \$3 billion respectively⁴⁹.

The interesting conformational properties of commercially available AT₁R antagonists are attributed to the fact that they bear the following structural features:

- (a) aromatic segments suitable to form π - π stacking interactions. Such aromatic segments include biphenyl tetrazole or biphenyl carboxylate and various heterocyclic rings;
- (b) acidic moieties as tetrazole or carboxylate groups that can be ionized and form various complexes with metals;
- (c) alkyl aliphatic chain responsible for its hydrophobic interactions with the active site of the AT₁R;
- (d) other groups such as hydroxyl or halogen that are also essential for specific interactions with the AT₁R;

All the above signalizations pinpoint that these molecules encompass flexible regions and the molecular basis of their action, at the target site, is directly linked to their conformational properties that consequently set the basis for the rational drug design.

1.3 Comparison of conformational properties in different environments

The conformational properties of drugs are not only important to be studied in isolation (solid state, solution state or *in silico*) but it is of paramount importance to reveal their architecture in a simulating or the real biological environment, that is the active site of the AT₁R receptor. Thus, the conformational properties of the AT₁R antagonists in lipid bilayers as also in their bound state to the AT₁R receptor (derived from homology modeling or the crystal structure), will be exploited and compared with those structures that have been determined from *in silico* studies, from crystal structures or structural studies in organic solvents⁵⁰⁻⁵⁴.

As the AT₁R antagonists target the transmembrane region of AT₁R, lipid bilayers are considered to play a judicious role in the molecular basis of their action. Hitherto, it is not known if AT₁R antagonists approach directly the AT₁R receptor or they are embedded first in the lipid bilayers and through diffusion reach the active site of the AT₁R.

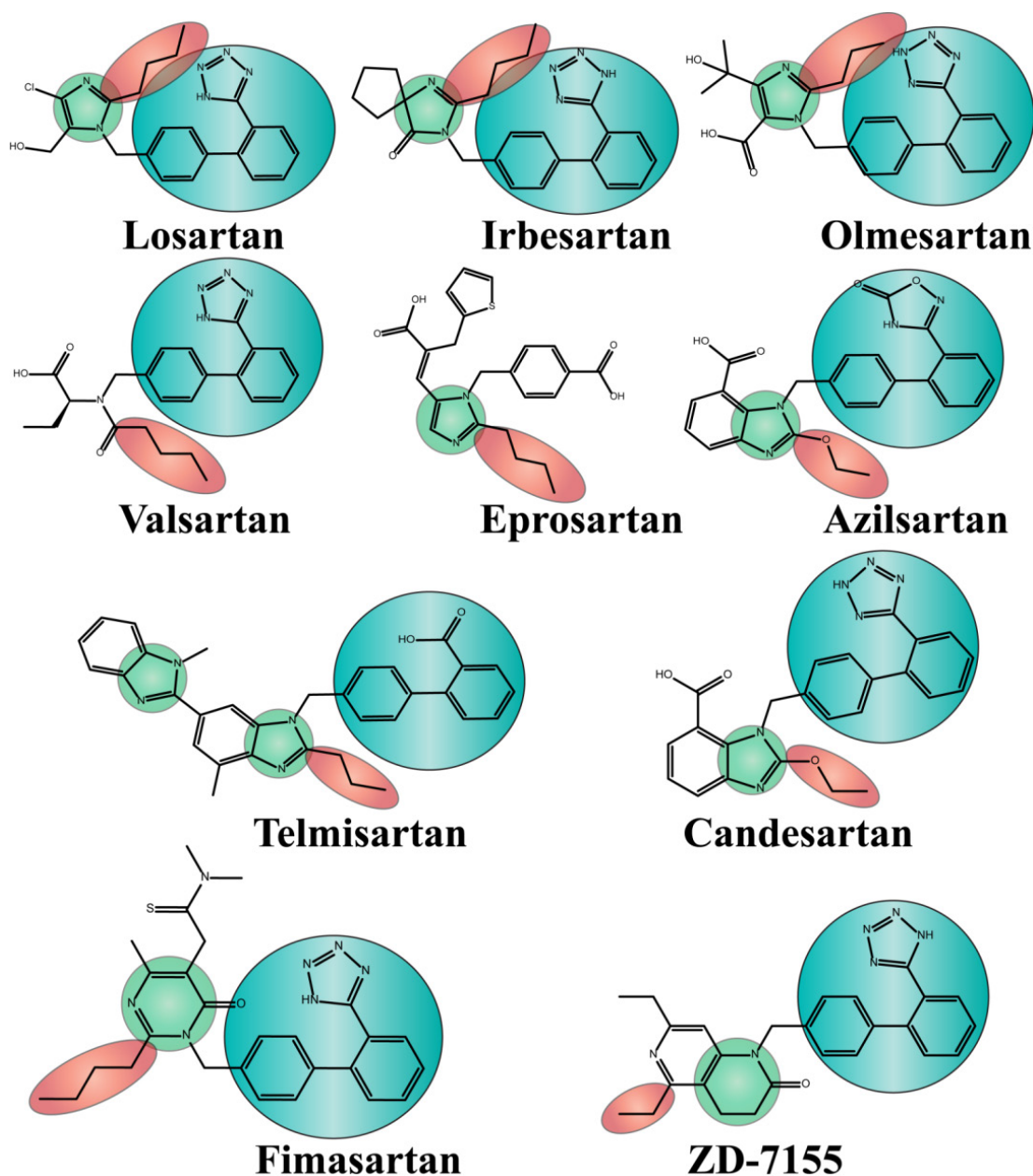


Figure 1-3. Structures of AT₁R antagonists. Almost all of them contain three structural features: biphenyl tetrazole or acidic bioisostere (colored in blue), heterocyclic segment (colored in green) and small alkyl chain (colored in red) ⁵⁵.

1.4 Homology models of AT₁R

Three dimensional experimental structures of GPCRs (either derived from NMR studies or X-ray crystallography) are limited in number ^{56, 57}. As a result, homology modeling, the prediction of the 3D structure of a protein based on templates with very similar amino acid sequences, is an important tool for drug design and discovery ⁵⁸. The process of homology modeling includes: the selection of one or more templates, the structural alignment and model building, the refinement, and in the end the validation and assessment of the model

⁵⁷. The predictive ability of the model and as a result the success of the method depends on the similarity between the templates and the target sequence ⁵⁹. The conformations and binding modes of the AT₁R antagonists in the X-ray crystal structure are compared with those provided by two representative homology models.

The first model was developed by Tuccinardi *et al.* ⁶⁰, using the bovine rhodopsin crystal structure as a template (PDB ID: 1U19). Losartan was docked in the AT₁R using as important residues the ones defined from mutagenesis data. The model was refined using molecular dynamics in DPPC bilayers. The second model was built by Matsoukas *et al.* ⁶¹, using as a template the Chemokine Receptor type 4 (CXCR4) (PDB ID: 3ODU). AngII was docked in the model using Glide and the Induced Fit Protocol. The model was refined using molecular dynamics in POPC lipid bilayers. As can be seen in Figure **1-4A** the transmembrane domains of the two homology models with the crystal structure are in good alignment. The alignment of the second extracellular loop (EL2) reveals that while the homology model based on the CXCR4 structure has a good alignment with the crystal structure, the homology model based on rhodopsin has a different secondary structure (Figure **1-4B**). Another major difference between the two homology models is the position of Arg167. While in Tuccinardi's model Arg167 is positioned at a great distance from the binding site, in the CXCR4 model Arg167 is introduced in the binding site. Other key residues such as Lys199, Tyr35 and Ile288 are placed in the homology models very near to their actual site in the crystal structure (Figure **1-4C**). These differences will be further analyzed in the following sections.

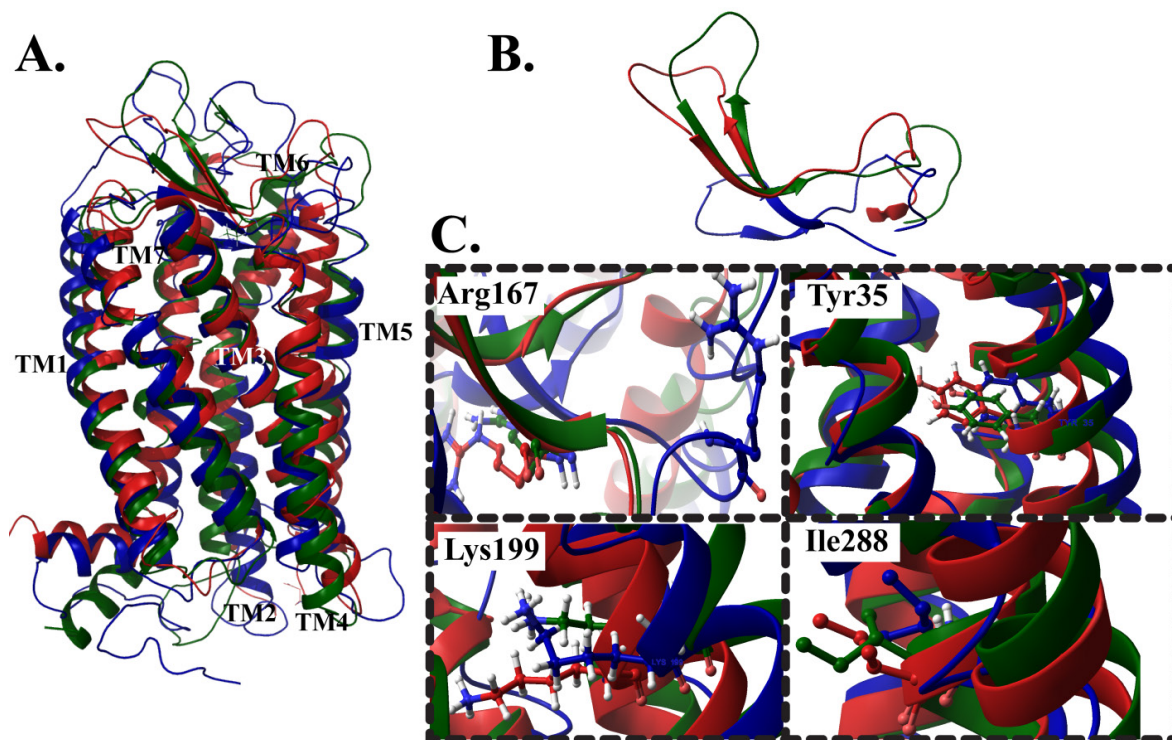


Figure 1-4. A) Superimposition of the crystal structure (green) with the homology model derived from the rhodopsin structure (blue) and the homology model derived from the CXCR4 structure (red). B) The second extracellular loop in the two homology models (blue and red) and the crystal structure (green). C) Superimposition of the four key residues Arg167, Lys199, Tyr35 and Ile288 (in green are shown the residues in the crystal structure, in blue the residues in the rhodopsin homology model and in red the residues in the CXCR4 homology model) ⁵⁵.

1.5 Olmesartan

The crystal structure of olmesartan ⁶² and its low energy conformers using NMR and theoretical data are shown in Figure 1-17. As it can be seen one of the low energy NMR conformers resembles that of the crystal structure. Thus, tetrazole, carboxylate group and alkyl chain are located in the same side, although there are some differences in torsion angles with those in the X-ray structures.

1.5.1 Docking of olmesartan to the AT₁R

Miura *et al.* ⁶³, reported the docking of olmesartan to a homology model of AT₁R based on the rhodopsin structure. The tetrazole moiety was shown to interact with the key aminoacids His256, Lys199 and Glu257. Another key polar interaction referred in the model was that between the hydroxymethyl group of olmesartan and that of the phenyl hydroxyl group of Tyr113. The docking results were imposed to be in harmony with the mutation studies ^{64, 65}. Olmesartan was also docked in the homology model of AT₁R based

on the CXCR4 structure⁶¹. The tetrazole moiety interacts with Arg167 predicting correctly the importance of this residue. Other key interactions include hydrogen bonding with Lys199, Tyr184 and Pro192 (Figure 1-18A). The conformation of olmesartan in these docking studies deviates from that observed by X-ray crystallography and NMR studies. The alkyl chain in both X-ray and NMR results, points towards the biphenyl tetrazole system, while in the docking experiments a similar interaction is not observed. An extended conformation of olmesartan was observed in the newest reported docking study based on the crystallographic data of AT₁R. In addition the crucial interactions differ considerably. The key interactions of olmesartan in the crystallized receptor are those between its tetrazole and carboxylate groups with Arg167⁴⁶ (Figure 1-18B).

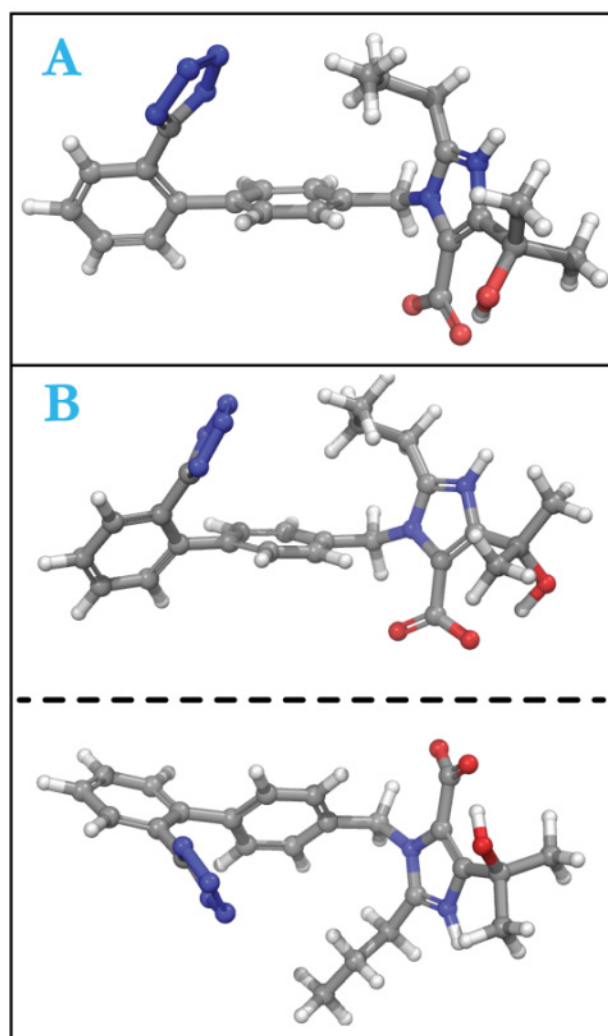


Figure 1-5. A) Crystal structure of olmesartan (CSD reference code: ZOGSOD); B) Low energy conformers of olmesartan in methanol optimized using the HF/6.31G** basis set (RMSD between the crystal structure A and B is 0.2 Å.)⁵⁵

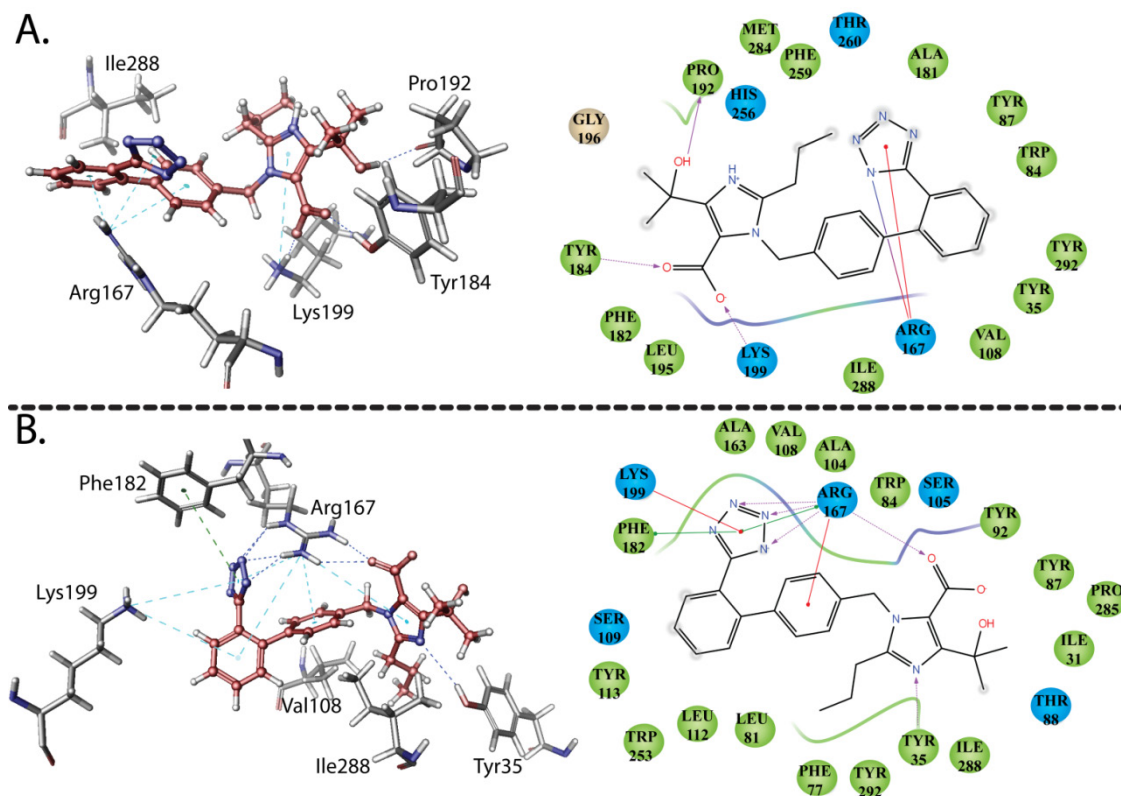


Figure 1-6. A) Docking of olmesartan in the homology model of AT₁R based on CXCR4. Blue lines represent hydrogen bonds, cyan lines represent π -cation interactions and green lines represent π - π interactions. B) Docking of olmesartan in the crystal structure of AT₁R

1.6 The Role of Membrane Bilayers in the Binding of drugs to the AT Receptors

AT₁R antagonists act on the transmembrane region of the receptor site while Ang II interacts with both extracellular and intracellular sites. The way that AT₁R antagonists interact with their active site, however, remains uncharted. A critical question is whether they directly approach the receptor or they are intercalated into the membrane core and then diffuse to the active site of the receptor (Figure 1-7B). How crucial is the membrane bilayer core for their action? Drug-membrane interactions along with drug-AT₁R interactions are investigated to dissect the roles of these two components. The drug-membrane interactions show subtle but distinct differences between the thermal and dynamic properties of AT₁R antagonists. The data suggest that each AT₁R antagonist has a unique action on the membrane⁶⁶⁻⁷⁸. In the following figure, the interactions of candesartan cilexetil and olmesartan are illustrated as revealed from a combination of NMR spectroscopy, molecular modeling, Raman spectroscopy and Differential Scanning Calorimetry⁷⁹. The study of the mechanism of losartan as it embeds in the lipid bilayers

and approaches the AT₁R has been recently studied⁸⁰. Further work is needed to elaborate the issue of the preference of losartan into the two sites by using new models of AT₁R as the one described by Matsoukas⁸¹. In our recent study, the application of 2D NOESY experiment led to the finding of the localization of AT₁R antagonists (Figure 1-7A).

Molecular modeling enhances and promotes the field since it offers a better understanding of the interactions of drugs with AT₁R and AT₂R. The non-crystallized receptors demand the use of modeling to generate 3D low energy conformers of AT₁R and AT₂R. New approaches in the modeling of these receptors have recently been reported. Molecular Dynamics simulations are used to differentiate between the two step mechanism for drugs to reach the transmembrane active site of AT₁R. The role of lipid bilayers in the AT₁R antagonism is also studied using various biophysical methods.

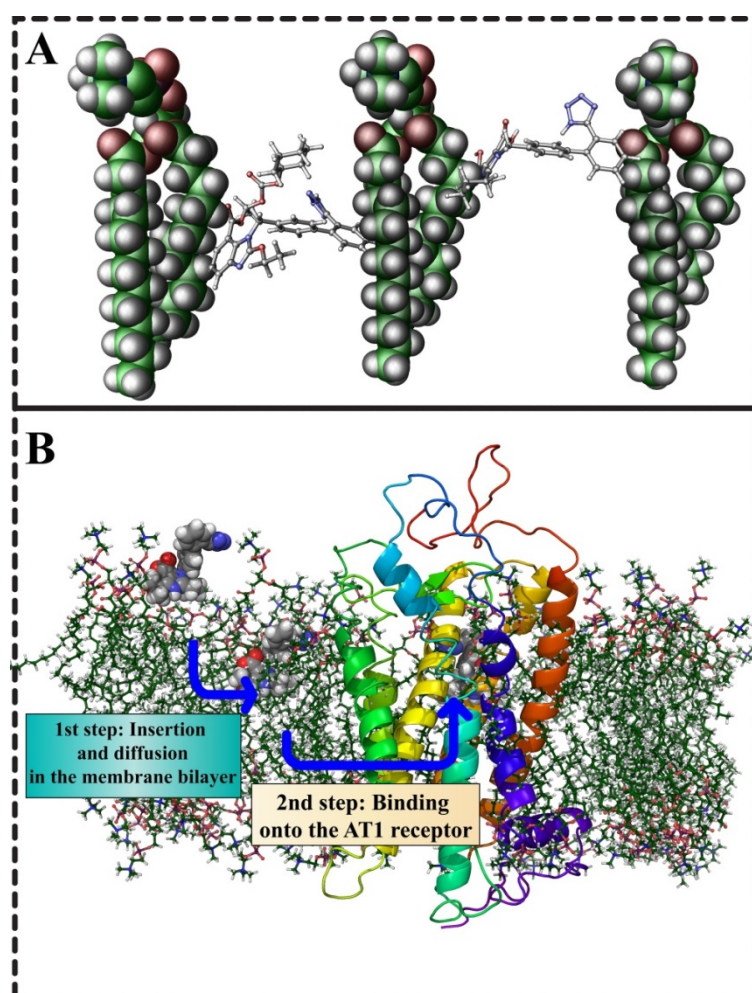


Figure 1-7. A. Candesartan cilexetil (left) and olmesartan (right) positioned in one leaflet of membrane bilayers. As it can be observed candesartan cilexetil is positioned deeper in membrane bilayers owing to its more hydrophobic nature. However, both molecules as they are amphipathic adopt polar and non-polar interactions. B. Two step mechanism of

action for ARBs. In the first step ARBs are postulated to embed themselves in the lipid matrix and in the second step are laterally diffused to the active site of AT₁R³.

1.7 The use of cyclodextrins and calixarenes in pharmaceutical formulations

1.7.1 Cyclodextrins

1.7.2 A brief history of the cyclodextrins

The history of cyclodextrins (CD) begins with the work of the pharmacist and chemist Antoine Villiers who first described cellulosines. In 1891, in the Proceedings of the Académie des Sciences, Villiers observed that potato starch can ferment to mainly yield dextrins⁸²⁻⁸⁴. The term dextrins had already been used at the time to describe the degradation products and/or the intermediate decomposition products of starch (note that the production of dextrins by the degradation of starch through heating was discovered in 1821^{84,85}).

The Austrian chemist and bacteriologist Franz Schardinger, in 1903, discovered that a type of extremely heat resistant microorganism was able to dissolve starch and form crystalline byproducts remarkably similar to the cellulosine reported by Villiers^{86,87}. He distinguished two types of polysaccharides, and named them crystalline dextrin A and crystalline dextrin B. The B form resembled Villiers' cellulosine. Schardinger gave the first description of the preparation, separation, and purification of the two cellulosines first described by Villiers⁸⁸⁻⁹⁰.

In 1942, French and Rundle, using the X-ray diffraction technique and crystal density measurements, determined the molecular weights of α - and β -dextrins and discovered the exact number of glucose units per dextrin, that is, six and seven, respectively (Figure 1-8)⁹¹. They demonstrated that molecular weights were integral multiples of the value 162.1 for a glucose residue⁸⁴.

In 1967, Professor Friedrich Cramer showed that the inclusion complex between sodium p-nitrophenolate and α -CD and was able to detail the mechanism of formation of this inclusion complex giving the first scientific explanation⁹². He noted that the formation of a CD/substrate inclusion complex includes five elementary steps:

- (1) the guest molecule approaches the cyclodextrin. Afterwards, water molecules escape from the inside cavity of the host. The van der Waals interactions and the number of hydrogen bonds decrease, whereas the degrees of freedom of translation and rotation of the freed water molecules increase.

- (2) the guest molecule becomes released from the layer of water that envelops it and also acquires a different state; the layer of water becomes dispersed and rearranges;
- (3) the guest molecule, considered to be in a perfect gas state, enters the cavity, and the complex formed is stabilized by van der Waals forces and/or hydrogen bonds;
- (4) the expelled water molecules are rearranged and form hydrogen bonds between each other;
- (5) the structure of the water is restored around the part of the substrate that remains in contact with the solvent and that is integrated into the hydration shell around the CD.^{93, 94}

In the mid-1970s, the German biochemist and crystallographer Wolfram Saenger demonstrated that CDs are macrocyclic structures that form a cavity shaped like a truncated cone^{95, 96}. In 1976, Saenger gave three explanations for the formation of an inclusion complex with α -CD in aqueous solution:

- (1) the guest molecule directly replaces the water molecules in the cavity;
- (2) the CD molecules absorb the energy of the water molecules retained in the cavity and take on a relaxed conformation (in this state the water molecules can be easily substituted by another guest);
- (3) the guest becomes associated with the outer surface of the CD and only enters the cavity once it has absorbed the activation energy (transfer of the conformation from a state of high energy of the CD–water complex to a state of lower energy of the CD–guest molecule complex).

Saenger mentions the release of the tension energy within the CD molecule upon formation of the complex. The same year, Bergeron and Rowan,⁹⁷ performing an NMR study, showed that the London forces and the release of high-energy water molecules from the cavity are the main contributors to the inclusion of p-nitrophenolate into α -CD and β -CD without demonstrating the involvement of Saenger's tension energy. Saenger's description (like that of Bender two years later) of the formation of an inclusion complex mainly involved hydrophobic interactions.

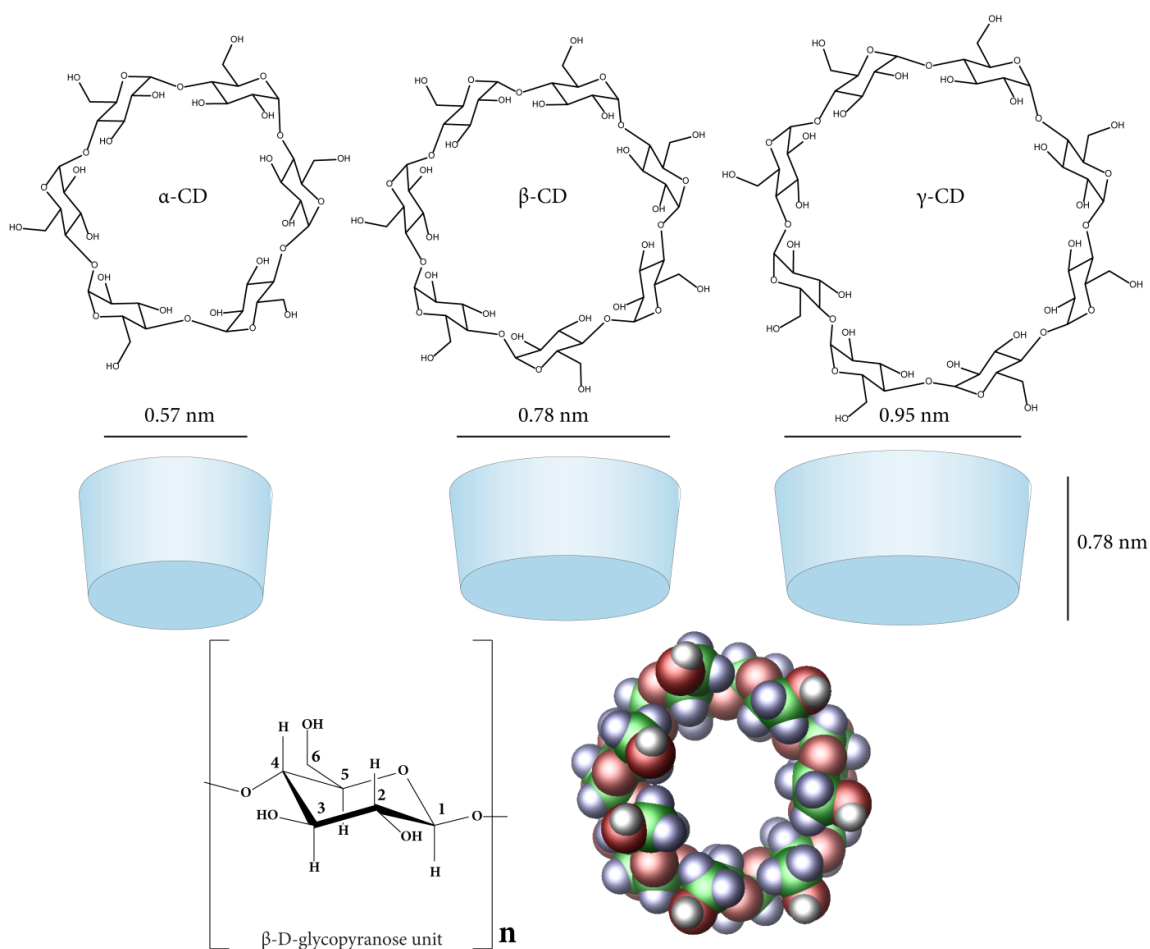


Figure 1-8. (Top) The structures of α -CD, β -CD and γ -CD. (Middle) Geometric dimensions of the cyclodextrins. (Bottom) The glycopyranose unit and a spacefilling model of β -CD.

1.7.3 Cyclodextrins in pharmaceutical formulations

Formulation is a complex process in which the active pharmaceutical components along with the excipients are targeted together towards the organ or the cell for exerting beneficial effects in the human health. Formulations constitute compositions that can be prepared in a capsule, tablet, an emulsion, or other form according to a specific procedure⁹⁸. Drug formulations are very important since they are essential to ensuring that the active ingredient is spatiotemporally delivered at the correct rate, concentration and part of the body⁹⁹. Optimized pharmaceutical formulations are essential to be established since they: (i) enhance the drug delivery process helping the drug to pass the physiological, biochemical and chemical barriers; (ii) improve the drug's solubility, stability and dissolution rates; (iii) establish a controlled delivery rate; (iv) provide improved therapeutic outcome; (v) exhibit more favorable side effect profile, (vi) foster patient compliance through ease of use or by reducing the dosing⁹⁸.

The chemical structure of the drug reflects its physicochemical properties and therefore the proper formulation is required for its effective spatiotemporal delivery and optimal action. Several general formulations have been proposed for drug delivery, suitable for various classes of drug molecules. None of the formulations provide a universal platform to control drug release as none of these are devoid of problems⁹⁸.

CDs have been used as drug delivery systems to enhance efficacy of hydrophobic drugs, by entrapping them¹⁰⁰⁻¹⁰². Due to the chair structure of the glucopyranose rings, CD molecules are shaped like cones with secondary hydroxy groups extending from the wider edge and the primary groups from the narrow edge (Figure 1-8). This gives the CD molecule a hydrophilic outer surface. The central cavity is lipophilic¹⁰³. Although the natural CDs and their complexes are hydrophilic, their aqueous solubility can be rather limited, especially in the case of β -CD. This is thought to be due to relatively strong binding of the CD molecules in the crystal state (i.e. relatively high crystal lattice energy)¹⁰⁴. Random substitution of the hydroxy groups, even by hydrophobic moieties like methoxy functions, will result in dramatic improvements in their solubility. The main reason for the solubility enhancement is that the random substitution transforms the crystalline cyclodextrins into amorphous mixtures of isomeric derivatives¹⁰². Most CDs are hydrophilic and, due to their bacterial digestion, high molecular weight, large number of hydrogen donors and acceptors, and high hydrophilicity (logKo/w between -8 and -12), their oral bioavailability is generally below 4%¹⁰². The oral bioavailability of 2-hydroxypropyl-cyclodextrin (HP- β -CD) in humans is between 0.5 and 3.3%, with 50–65% of the oral dose excreted intact in the faeces and the rest is mainly metabolized by bacteria in the colon. CD absorbed intact is rapidly excreted in the urine. Toxicological studies have demonstrated that orally administered CDs are practically nontoxic due to lack of absorption from the gastrointestinal tract¹⁰⁵.

The first CD-related patent was issued in Germany in 1953¹⁰⁶. In this patent, the basic properties of the natural α -CD, β -CD and γ -CD are described and how, through complex formation, these CDs can enhance aqueous solubility and chemical stability of biologically active compounds. The marketed drug prostaglandin E2/ β -CD in the form of sublingual tablets (Prostarmon E, Ono), was the first one to be an inclusion complex with cyclodextrin and was sold in Japan in 1976. Worldwide there are currently about 35 different CD containing drug products on various world markets (Table 1-1).

Table 1-1: List of CD containing drug products with their tradenames^{102, 104}.

Drug/cyclodextrin	Trade name	Formulation	Company (country)
α -CD			
Alprostadil	Caverject Dual	Intravenous solution	Pfizer (Europe)
Cefotiam-hexetil HCl	Pansporin T	Tablet	Takeda (Japan)
Limaprost	Opalmon	Tablet	Ono (Japan)
PGE1	Prostavastin	Parenteral solution	Ono (Japan); Schwarz (Europe)
β -CD			
Benexate HCl	Ulgut, Lonmiel	Capsule	Teikoku (Japan); Shionogi (Japan)
Cephalosporin	Meiact	Tablet	Meiji Seika (Japan)
Cetirzine	Cetrizin	Chewable tablet	Losan Pharma (Germany)
Chlordiazepoxide	Transillium	Tablet	Gador (Argentina)
Dexamethasone	Glymesason	Ointment, tablet	Fujinaga (Japan)
Dextromethorphan	Rynathisol	Synthelabo (Europe)	
Diphenhydramine and chlortheophylline	Stada-Travel	Chewable tablet	Stada (Europe)
Ethinylestradiol and drospirenone	Yaz	Tablet	Bayer (Europe, USA)
Iodine	Mena-Gargle	Solution	Kyushin (Japan)
Meloxicam	Mobitil	Tablet and suppository	Medical Union (Egypt)
Nicotine	Nicorette	Sublingual tablet	Pfizer (Europe)
Nimesulide	Nimedex	Tablets	Novartis (Europe)
Nitroglycerin	Nitropen	Sublingual tablet	Nihon Kayaku (Japan)
Omeprazole	Omebeta	Tablet	Betafarm (Europe)
PGE2	Prostarmon E	Sublingual tablet	Ono (Japan)
Piroxicam	Brexin, Flogene, Cicladon	Tablet, suppository	Chiesi (Europe); Aché (Brazil)
Tiaprofenic acid	Surgamyl	Tablet	Roussel-Maestrelli (Europe)
HP- β -CD			
Cisapride	Propulsid	Suppository	Janssen (Europe)
Indometacin	Indocid	Eye drop solution	Chauvin (Europe)
Itraconazole	Sporanox	Oral and intravenous solution	Janssen (Europe, USA)
Mitomycin	MitoExtra, Mitozytrex	Intravenous infusion	Novartis (Europe)
<i>Sulfobutylether β-cyclodextrin sodium salt</i>			
Aripiprazole	Abilify	Intramuscular solution	Bristol-Myers Squibb (USA); Otsuka Pharm. (USA)
Maropitant	Cerenia	Parenteral solution	Pfizer Animal Health (USA)
Voriconazole	Vfend	Intravenous solution	Pfizer (USA, Europe,

			Japan)
Ziprasidone mesylate	Geodon, Zeldox	Intramuscular solution	Pfizer (USA, Europe)

1.7.4 Characterization of drug:CD complexes

A variety of techniques have been employed to confirm the formation and utility of CD complexes. Selecting the most appropriate technique to use depends on the complexation process as well as the inherent properties of the drug, CD molecule, and their resultant complex. It is important for characterization to be able to distinguish between formed complexes and any “free” drug or CD. Drug-CD complexes may be characterized in the solid state or in solution. Both a simple physical mixture of the raw materials (drug and CD) as well as the raw materials independently subjected to processing conditions need to be simultaneously characterized in most instances in order to conclusively confirm complex formation.

1.7.4.1 Thermo-Analytical Methods

Thermo-analytical methods are commonly employed to characterize inclusion complexes¹⁰⁷. Differential Scanning Calorimetry (DSC) or differential thermal analysis (DTA) may be used to compare thermal profiles of drugs before and after CD complexation.

Molecular changes such as melting, oxidation, or decomposition are manifested as characteristic peaks or troughs on the derived thermograms¹⁰⁸. Peak shifts and/or the gain and loss of features on the thermogram can confirm complex formation. Various therapeutics including salbutamol and famotidine have demonstrated the loss of characteristic peaks on thermograms when complexed with CD molecules^{108, 109}. Thermograms may be further used to quantitatively determine the extent of drug complexation¹⁰⁷. Such characterization requires a comparison of the area under the DSC curve of a physical mixture of drug-CD with that under the DSC curve of a formed complex. The proportional change in area can be correlated with the apparent degree of complex formation.

1.7.4.2 Microscopic Methods

Scanning electron microscopy (SEM) and transmission electron microscopy (TEM) can be used to image the crystalline state of the raw materials and the final product following complexation^{110, 111}. The observed differences in structure can be used to indicate the formation of inclusion or non-inclusion complexes. Although the methods have been routinely used to characterize CD complexes, they are considered inconclusive in

confirming complexation and should only be used as adjuncts to more robust characterization techniques.

1.7.4.3 Wettability/Solubility Studies

In wettability studies, powdered drug-CD complex is analyzed with regard to its contact angle and sedimentation and dissolution rates when exposed to water. While simple CD addition to a powder can enhance its cumulative wettability, the conduction of dissolution studies of the powder can give a better indication of whether drug-CD complexation has indeed occurred^{112, 113}. Solid CD formulations may be pressed into tablets and subjected to a dissolution test. Following collection of media at preset intervals and subsequent analysis of drug content within the media, one can determine whether the CD complexation has improved a drug's dissolution property. Dissolution rates of complexes prepared via different methods can be compared to determine which method is most efficient at enhancing drug dissolution. Solubility studies using varying CD concentrations may also be assessed. If drug solubility is increased with increasing CD concentration, this can be taken as a clear indication of CDs interaction resulting in enhanced drug solubility.

1.7.4.4 Spectroscopic Methods

Spectroscopic characterization via ¹H-NMR is a robust technique for confirming the formation of inclusion complexes. The technique can also assist in determining the precise molecular groups of the drug and CD that are interacting during complex formation¹¹⁴. For example, spectra of hydrogen atoms located on the interior of the CD molecule show significant shifts when inclusion complexation occurs. The spectrum of the included molecule may also change, with relevant hydrogen peaks shifting to indicate their involvement in the interaction. When varying ratios of drug and CD are used, the extent of peak shift can help determine the ratio at which complexation is at a maximum.

1.7.4.4.1 Solid state NMR

Conventional utilization of solution phase NMR data acquisition techniques on solid samples yields broad, featureless spectra. The broad nature of the signal is due primarily to dipolar interactions which do not average out to zero in the solid state, and chemical shift anisotropy (CSA), which again is a function of the fact that our compound of interest is in the solid state. The principal interaction developed by a nucleus with a magnetic moment with a magnetic field in the solid state is the Zeeman interaction (H_z).

Dipole-dipole interaction is the direct magnetic coupling of two nuclei through space. This interaction may involve two nuclei of equivalent spin, or nonequivalent spin, and is dependent upon the internuclear distance and dipolar coupling tensor. The total interaction, labeled H_D is the summation of all possible pairwise interactions (homo- and heteronuclear). It is important to note that the interaction is dependent on the magnitude of the magnetic moments which is reflected in the magnetogyric ratio and on the angle (θ) that the internuclear vector makes with B_0 . Therefore, this interaction is significant for spin $1/2$ nuclei with large magnetic moments such as ^1H and ^{19}F . Also, the interaction decreases rapidly with increasing internuclear distance (r), which generally corresponds to contributions only from directly bonded and nearest neighbor nuclei. Equation 1-1 describes the dipolar interaction for a pair of nonequivalent, isolated spins I and S .

$$H_D^{IS} = \frac{\gamma^I \gamma^S \hbar}{r^3} \vec{I} \hat{D} \vec{S} \quad \text{Equation 1-1}$$

Since the dipolar coupling tensor, D , contains a $(1-3 \cos^2\theta)$ term, this interaction is dependent on the orientation of the molecule. In solution-phase studies where the molecules are rapidly tumbling, the $(1-3\cos^2\theta)$ term is integrated over all angles of θ and subsequently disappears. Within solid-state NMR, the molecules are fixed with respect to B_0 , thus the $(1-3\cos^2\theta)$ term does not approach zero. This leads to broad resonances within the solid-state NMR spectrum since dipole-dipole interactions typically range from 0 to 105 Hz in magnitude. In the case of pharmaceutical solids which are dominated by carbon and proton nuclei, the dipole-dipole interactions may be simplified. The carbon and proton nuclei may be perceived as "dilute" and "abundant" based upon their isotopic natural abundance, respectively. Homonuclear ^{13}C - ^{13}C dipolar interactions essentially do not exist because of the low concentration of ^{13}C nuclei (natural abundance of 1.1%). On the other hand, ^1H - ^{13}C dipolar interactions contribute significantly to the broad resonances, but this heteronuclear interaction may be removed through simple high-power proton decoupling fields, similar to solution phase techniques.

The three-dimensional magnetic shielding by the surrounding electrons is an additional interaction that the nucleus experiences in either the solution or the solid state. This *chemical shift interaction* (H_{cs}) is the most sensitive interaction to changes in the immediate environment of the nucleus and provides the most diagnostic information in a measured NMR spectrum. The effect originates from the small magnetic fields that are generated about the nucleus by currents induced in orbital electrons by the applied field.

These small perturbations upon the nucleus are reflected in a change in the magnetic field experienced by the nucleus. Therefore, the field at the nucleus is not equal to the externally applied field and hence the difference is the nuclear shielding, or chemical shift interaction [Eq. (1-2)].

$$H_{CS} = \gamma_I \hbar \vec{I} \cdot \hat{\sigma} \cdot \vec{B}_0 \quad \text{Equation 1-2}$$

It is important to note the orientation dependence of the shielding constant, σ , and the fact that shielding is proportional to the applied field, hence the need for chemical shift reference materials such as tetramethylsilane. Solution-state NMR spectra yield "average" chemical shift values which are characteristic of the magnetic environment for a particular nucleus. The average signal is due to the isotropic motion of the molecules in solution. In other words, B_0 "sees" an average orientation of a specific nucleus. For solid-state NMR, the chemical shift value is also characteristic of the magnetic environment of a nucleus, but normally, the molecules are not free to move. It must be kept in mind that the shielding will be characteristic of the nucleus in a particular orientation of the molecule with respect to B_0 . Therefore, a specific functional group oriented perpendicular to the magnetic field will give a sharp signal characteristic of this particular orientation. Analogously, if the functionality is orientated parallel to B_0 , then a sharp signal characteristic of that orientation will be observed. For most polycrystalline pharmaceutical samples, a random distribution of all orientations of the molecule will exist. This distribution produces all possible orientations and is thus observed as a very broad NMR signal. The magnitude of the chemical shift anisotropy is typically between 0 and 105 Hz. Two additional interactions experienced by the nucleus in the solid state are *spin-spin couplings* to other nuclei and *quadrupolar interactions*, which involve nuclei of spin greater than 1/2. Spin-spin (H_{sc}), or *J coupling*, originates from indirect coupling between two spins by means of their electronic surroundings and are several orders of magnitude smaller (possibly 0-10⁴ Hz, typically only several kHz) than dipole interactions. Summarizing the interactions, the isotropic motions of molecules in the solution state, yield a discrete average value for the scalar spin-spin coupling and chemical shift interactions. For the dipolar term, the average obtained is zero, and the interaction is not observed in solution-phase studies. In sharp contrast, interactions in the solid state are orientation dependent, subsequently producing a more complicated spectrum, but one that contains much more information. In order to

yield highly resolved, "solution-like" spectra of solids, a combination of three techniques is used: dipolar decoupling¹¹⁵, magic-angle spinning^{116,117}, and cross-polarization¹¹⁸.

Dipolar Decoupling

High-powered proton decoupling fields can eliminate the heteronuclear ¹H-¹³C dipolar interactions that may dominate a solid-state NMR spectrum. The concept of decoupling is familiar to the solution-phase NMR spectroscopist but needs to be expanded for solid-state NMR studies. In solution-phase studies, the decoupling eliminates the scalar spin-spin coupling, not the dipole-dipole interactions. Irradiation of the sample at the resonant frequency of the nucleus to be decoupled (B_2 field) causes the z component of the spins to flip rapidly compared to the interaction one wishes to eliminate. Scalar interactions usually require 10 W of decoupling power or less. In pharmaceutical solids work, decoupling is used primarily to remove the heteronuclear dipolar interactions between protons and carbons. The magnitude of the dipolar interaction (-50 kHz) usually requires decoupling fields of 100 W and subsequently removes both scalar and dipole interactions. Even with the use of high-power decoupling, broad resonances still remain, due principally to chemical shift anisotropy.

Magic-Angle Spinning

Molecules in the solid state are in fixed orientations with respect to the magnetic field. This produces chemical shift anisotropic powder patterns for each carbon atom since all orientations are possible. It was shown as early as 1958 that rapid sample rotation of solids narrowed dipolar broadened signals¹¹⁵. A number of years later, it was recognized that spinning could remove broadening caused by CSA yet retain the isotropic chemical shift¹¹⁶. The concept of magic-angle spinning arises from the understanding of the shielding constant, σ [Eq. (1-2)]. This constant is a tensor quantity and, thus, can be related to three principal axes where σ_i is the shielding at the nucleus when B_0 aligns along the i^{th} principal axis, and θ_i is the angle this axis makes with B_0 .

$$\sigma_{zz} = \sum_{i=1}^3 \sigma_i \cos^2 \theta \quad \text{Equation 1-3}$$

Under conditions of mechanical spinning, this relationship becomes time dependent and a $(3\cos^2\theta-1)$ term arises. By spinning the sample at the so-called "magic angle" of 54.7° , or $54^\circ44'$, this term becomes zero and thus removes the spectral broadening due to CSA, providing that the sample rotation (kHz) is greater than the magnitude of the CSA (kHz). CSA may range from 0 to 20 kHz so our spin rates must exceed this value or spinning side

bands are observed. Although fast enough spin rates may not be achieved to remove CSA totally for specific compounds, slower than optimal rates will still narrow the resonances. Spinning side bands, at multiples of the spin rate, will complicate the spectrum, but they can be easily identified by varying the spin rate and observing which signals change in frequency. In addition, specific pulse sequences may be used to minimize the spinning side bands. While increasing the magnetic field strength increases the signal to-noise ratio (Zeeman interaction), it also increases the CSA, since this interaction is field dependent. Utilizing today's high-field spectrometers (>4.7 T), spinning side bands may exist but can be identified and used to gain additional information or be potentially eliminated if necessary. The techniques of magic-angle spinning and heteronuclear dipolar decoupling produce solid-state NMR spectra which approach the linewidths and appearance of solution phase NMR spectra. Unfortunately, there is an inherent lack of sensitivity in the general NMR experiment because of the nearly equivalent population of the two spin states for spin 1/2 nuclei. In addition, the sensitivity of the experiment is decreased with pharmaceutical compounds since they are composed primarily of carbon atoms where the ^{13}C observable nuclei have a natural abundance of only 1%. The long relaxation times of specific carbon nuclei also pose a problem since quick, repetitive pulsing cannot occur. The technique of cross-polarization provides a means of both signal enhancement and reduction of long relaxation times.

Cross-Polarization

The concept of cross-polarization as applied to solid state NMR was implemented by Pines *et al.*¹¹⁸. A basic description of the technique is the enhancement of the magnetization of the rare spin system by transfer of magnetization from the abundant spin system. Typically, the rare spin system is classified as ^{13}C nuclei and the abundant system as ^1H spins. This is especially the case for pharmaceutical solids and the remaining discussion of cross-polarization focuses on these two spin systems only.

1.7.4.4.2 The application of solid state NMR in characterizing cyclodextrin complexes

Although solid state NMR is not as widely used technique as liquid state NMR, X-Ray crystallography or Raman spectroscopy in the investigation and characterization of cyclodextrin complexes, it has been implemented more often in the recent years. One of the most recent applications is presented in the article by Inoue *et al.* in which ^{13}C CP MAS NMR was used to characterize the complex between limaprost and α and β -CD¹¹⁹.

The differences that were detected in solid state NMR spectra between the complexes in α - and β -cyclodextrin brought them to the conclusion that the small cavity of α -CD predominantly included the ω -chain of limaprost, whereas β -CD included the five-membered ring in the solid state ¹¹⁹. Li *et al.* used solid state NMR in order to explore the effect of the preparation processes on the physicochemical properties of inclusion complexes between β -CD and bisacodyl ¹²⁰. Arrúa *et al.* have elucidated the guest-host interactions between praziquantel and β -CD and its derivatives using ¹³C CP MAS and ¹⁵N solid state NMR ¹²¹. These experiments provided evidence that most complexes have a 2:1 host-guest molar ratio ¹²¹. The interactions of benznidazole and methyl β -CD or HP- β -CD have been evaluated by Priotti *et al.* ¹²² The ¹³C CP MAS data showed that the benzene ring of the benznidazole is positioned inside the cyclodextrin cavity while the imidazole of the drug molecule interacts with hydroxypropyl groups of the CD ¹²². Karoyo *et al.* have used ¹³C and ¹⁹F MAS solid state NMR in order to investigate the inclusion complex of sodium perfluorooctanoate with β -CD ¹²³⁻¹²⁵. ¹³C and ¹⁵N solid state NMR studies have also been used by Ferreira *et al.* in order to study the complexes of albendazole, an anthelmintic agent, with β -CD ¹²⁶. Pajzderska *et al.* used ¹H solid state NMR in order to characterize the mixture and complex of diazepam with β -CD ¹²⁷. ¹³C CP MAS, ¹H and ¹⁹F NMR experiments were conducted by Koito *et al.* in order to study the hydrofluoroether/ β -CD inclusion complex ¹²⁸. Abbate *et al.* characterized the complexes that are formed between cyclic siloxanes and α -, β -, γ -CD using ¹³C CP MAS NMR ¹²⁹. Hasegawa *et al.* used a combination of molecular dynamics and ¹³C solid state NMR in order to study the complex polyaniline/ β -CD ¹³⁰.

1.7.4.5 X-Ray Techniques

X-Ray diffraction (XRD) involves identifying complex formation by analyzing the crystal structure of a formed complex. Complex formation leads to changes in diffraction peaks based on the impact of formation on drug and CD crystallinity ¹³¹. A decrease in peak sharpness on the diffractogram corresponds with a loss in crystallinity. Molecules including warfarin, quercetin, and celecoxib all demonstrate losses in crystalline peaks following complexation with various CDs, which indicates the amorphous nature of these complexes ¹³¹⁻¹³³. The crystal structures of some common CD molecules and the guest-CD complexes have appeared in the Cambridge Structural Database.

1.7.5 Computational studies of drug:CD inclusion complexes

Molecular modeling is a characterization strategy which employs the use of computational methods to mimic the behavior of molecules. The distinguishing feature of the technique is its ability to characterize molecular systems at the atomic level ¹³⁴. Currently there are hundreds of reports describing theoretical calculations of drug-CD complexes.

1.7.5.1 Quantum Mechanics

QM mathematically describes the spatial positions of all electrons and nuclei. It is able to predict the structural and electronic characteristics of molecules. Recently the orientation and the developed interactions between cinnamic acid and β -CD were characterized using ONIOM ¹³⁵. The inclusion mechanism and the formation constants of chalcone and 2',4'-dihydroxychalcone with β -CD were also determined using QM methods ¹³⁶.

1.7.5.2 Molecular Dynamics

Molecular dynamics is a simulation of the time dependent behavior of a molecular system, such as vibrational motion or Brownian motion. It requires a way to compute the energy of the system, most often using a molecular mechanics calculation. This energy expression is used to compute the forces on the atoms for any given geometry ¹³⁷. The first step in every MD simulation is the choice of the initial positions for the atoms. The system should be in an optimized geometry in order to avoid clashes. For solvent+solute systems, the solute is often placed in the center of a collection of solvent molecules, with positions obtained from a simulation of the neat solvent. An initial set of atom velocities is then chosen. The velocities usually obey to a Boltzmann distribution for some temperature. The momentum of each atom and then the forces on each atom are calculated from the velocity, the mass and the chosen MM force field. New positions for the atoms are then computed a short time later, called the time step, along with new velocities and accelerations. This is a numerical integration of Newton's equations of motion using the information obtained in the previous steps. The iterations are repeated long enough for the system to reach equilibrium. Equilibrium is not the lowest energy configuration; it is a configuration that is reasonable for the system with the given amount of energy. Once the system has reached equilibrium, the atomic coordinates are saved every few iterations. This list of coordinates over time is called a trajectory. At the end the trajectories are analyzed in order to obtain information on the system.

In order for this system to work, the force field must be designed to describe intermolecular forces and vibrations away from equilibrium. If the purpose of the simulation is to search conformation space, a force field designed for geometry optimization is often used. For simulating bulk systems, it is more common to use a force field that has been designed for this purpose, such as the AMBER, GROMOS or OPLS force fields. There are several algorithms available for performing the numerical integration of the equations of motion. The Verlet and velocity Verlet algorithms are widely used because they require a minimum amount of computer memory and CPU or GPU time. It uses the positions and accelerations of the atoms at the current time step and positions from the previous step to compute the positions for the next time step. The Verlet algorithms often have a step in which the velocities are rescaled in order to correct for minor errors in the integration, thus simulating a constant-temperature system. The choice of a time step is important. A time step that is too large will cause atoms to move too far along a given trajectory, thus poorly simulating the motion. A time step that is too small will make it necessary to run more iterations, thus taking longer the simulation run. One general rule of thumb is that the time step should be one order of magnitude less than the timescale of the shortest motion (vibrational period or time between collisions). This gives a time step on the order of tens of femtoseconds for simulating a liquid of rigid molecules and tenths of a femtosecond for simulating vibrating molecules.

1.7.5.2.1 Applications of MD simulations in studying CD complexes

The binding free energy between CD and guest molecule can be calculated by the MM/PBSA, free energy perturbation and thermodynamic integration methods. A recent example is the calculation of the formation constant of the complex between quercetin and HP- β -CD using the MM-PBSA method¹³⁸. Examples of the usage of molecular dynamics in the investigation of guest-host complexes involving cyclodextrins are shown in Table 1-2.

Table 1-2: Examples of recent literature involving MD simulations of cyclodextrin complexes.

Authors	Application	Reference
Nutho et al.	QM and MM-PBSA/GBSA methods and molecular dynamics are used in order to establish the binding mode and the system stability of the fisetin/ β -CD complex.	¹³⁹
Sangpheak et al	MD and free energy calculations based on MM- and QM-PBSA/GBSA were applied in order to study the naringenin/ β -CD or 2,6 dimethyl β -CD (DM- β -CD) complex. The study suggested that the phenyl ring of naringenin preferentially dipped in the hydrophobic cavity of the	¹⁴⁰

	cyclodextrins. The free energy calculations showed that the complex naringenin/DM- β -CD is more stable than the one with β -CD.	
Nagaraju and Sastry	The guest host inclusion complexes of small molecules such as H ₂ O, NH ₃ , NH ₄ ⁺ , C ₆ H ₆ , and bisimidazolyl compounds with α -, β - and γ -CDs were investigated using both ab initio methods and MM-PBSA. The stoichiometry of the complexes is provided. The study also shows that QM and molecular dynamics show that benzene forms a more stable complex with β -CD than α - or γ -CD.	141
El-Barghouthi et al.	The complexes of benzanilide, benzoin, phenyl benzoate, benzoic acid, diphenylacetic acid with β -CD are explored using free energy perturbation, thermodynamic integration and MM-PBSA methods.	142
Oda and Kuroda	The inclusion complex of glycyrrhizic acid with β -, and γ -CD was studied using molecular dynamics and isothermal titration calorimetry.	143
Mayer et al.	The complexes of β -CD with four fentanyl-based compounds were studied using NMR and MM-GBSA. The stoichiometry of the complexation is determined using Job plot.	144
Kicuntod et al.	The inclusion complex of pinostrobin with various β -CD derivatives (DM- β -CD, HP- β -CD) are explored using QM and MM-PBSA/GBSA.	145
Zhang et al.	The encapsulation of satraplatin inside β -CD is studied using analytical and biophysical methods as well as molecular modelling. Molecular docking and binding energy calculations were used in order to rationalize the geometry of the supramolecular complex.	146
Shi et al.	The inclusion mechanism of the S- and R-ketoprofen in β -CD was investigated using molecular dynamics simulations. The binding free energy was calculated using MM-GBSA.	147
Tidemand et al. Schönbeck et al.	The complexation of glycoldeoxycholate and glycochenodeoxycholate with β -CD and HP- β -CD was investigated using ITC and molecular dynamics.	148, 149
Gannamani et al.	The inclusion complex of antipyrine with α -, β - and γ -CD was explored using MD simulations and the binding free energies for the complexes were calculated using the MM-PBSA method.	150
Figueiras et al.	In this study is investigated the complexation of fenbufen with methyl β -CD. The conformational space of the complex was studied using MD simulations with the GROMOS forcefield.	151
Ali <i>et al.</i>	The complexation of (RS)-benzhexol was studied using MD studies in vacuo with Allinger's force field.	152
Uccello-Barretta et al.	The encapsulation of the two enantiomers of methyl-2-chloropropionate with Lipodex E [octakis (3-O-butanoyl-2,6-di-O-pentyl)- γ -cyclodextrin] was explored using both MD and steered MD simulations. Binding energy was calculated using the MM-GBSA method in AMBER 12.	153
Nascimento et al.	The orientation of the two enantiomers of 4-hydroxypropranolol in carboxymethyl β -CD using MD simulations with the AMBER force field. The energetic parameters for the inclusion complexes at a molecular level were found to be in good agreement with the experimental findings concerning the elution order of guest 4-hydroxypropranolol enantiomers.	154
Fernandes et al.	MD simulations were used in order to establish the preferred conformation of cyanidin-3-O-glucoside with β -CD. The simulations were run in AMBER 10.0 with the GLYCAM2004 force field for the CD and GAFF for the small molecule.	155
Liu et al.	The study aims to provide evidence that CDs can form stable complexes with polychlorinated biphenyls. In particular, MD simulations were run for the complex 3,3',4,4',5-pentachlorobiphenyl/ β -CD using GROMACS and the GROMOS force field. The calculated results have showed that the guest molecule forms a stable 1:1 inclusion complex with the CD.	156
Jana et al.	In this study the atomistic MD simulations of the 1:1 inclusion complex formed between β -CD and the zwitterionic form of phenylalanine using GROMACS and the general GROMOS force field are presented.	157
Troche-Pesqueira	The inclusion complex of resveratrol with β -CD was studied using MD	158

et al.	simulations in AMBER 11 with the GAFF and GLYCAM06g force field.	
Ali et al.	The structure elucidation of the complex xylazine/ β -CD is achieved using ^1H - ^1H ROESY and MD simulations.	¹⁵⁹
Martini et al.	The interactions between 1-indanone-thiosemicarbazone/5,6-dimethoxy-1-indanone-thiosemicarbazone and HP- β -CD are explored using MD simulations in GROMACS with the GROMOS96 force field.	¹⁶⁰
Minea et al.	The inclusion complexes between propiconazole nitrate (an antifungal pesticide) with sulfobutylether- β -CD, sulfated- β -CD, and monochlorotriazinyl- β -CD are investigated using MD simulations in GROMACS.	¹⁶¹

1.7.5.3 Docking Studies

Docking is a simulation method for the prediction of one “ligand” molecule binding to a “receptor” molecule to form the “ligand–receptor” complex by scoring the functions with the association or binding affinity between two molecules. In rational drug design, docking is a popular approach for predicting the spatial orientation of drug candidates to their target protein or predicting the binding affinity between them. Recently the inclusion mechanism between phloridzin and HP- β -CD was investigated by Zhang *et al.* ¹⁶². The use of Autodock concluded that the substitution distribution of HP- β -CD influences both the orientation and the binding constant of the drug. The inclusion complexes between luteolin and five variants of CD molecules were previously studied using docking techniques ¹⁶³. Experimental results showed that the 1:1 luteolin/G β CD complex had the highest stability constant. Molecular docking results were in agreement with the experimental data ¹⁶³.

1.8 Calixarenes

Calix[n]arenes (CAs) constitute a fascinating class of macrocycles that have found a broad spectrum of applications in supramolecular chemistry and molecular recognition ¹⁶⁴⁻¹⁶⁸. They are cyclic conjugated oligomers of phenolic groups and are characterized by conformational plasticity (Figure 1-9). For instance, the calix[4]arene has four “up-down” conformers which have been designated as partial cone, cone, 1,3-alternate and 1,2-alternate ^{169, 170}, as illustrated in Fig. 1-10. Their conformational flexibility is attributed to the rotation around α -bonds of the Ar-CH₂-Ar groups ¹⁷⁰. Calixarenes can offer building blocks that can be exploited both as receptors, for guest-host type interactions, and catalysts via suitable functionalization of the two available characteristic upper and lower rim edges. The feasibility to customize the architectural orientation of the ligating arms of calixarenes, by shaping their scaffold conformation, offers the possibility to be explored as scaffolds for the construction of multivalent ligands. Calixarenes can be functionalized

following electrophilic substitutions either to the *lower rim* side through Williamson-type OH- modifications or to the *upper rim* side (see Fig. 1-9).

Calixarenes provide a unique category of macrocycles broadly used in supramolecular chemistry. They are synthesized through base or acid catalyzed electrophilic aromatic substitutions via condensation of formaldehyde with p-substituted phenols (Fig. 1-9). Through selection of appropriate reaction conditions (i.e. temperature, catalytic amount of base) a specific number of phenolic units (tetrameric, hexameric and octameric) can be selectively linked with methylene (-CH₂-) spacers. Their cyclo-oligomeric scaffold enables them to operate as host molecules due to the formed hydrophobic cavities¹⁷¹. The diverse structures adopted by calixarenes make them extremely useful in the study of molecular recognition and supramolecular processes^{172, 173}.

By fine tuning different reaction parameters and the appropriate utilization of molar ratios, bases, solvents, of protecting groups, reactants, etc., it is feasible to synthesize in a selective way an array of different calixarene variants^{164, 165} that can be utilized in diverse applications. For instance, calixarenes have become ideal scaffolds for complexation studies, especially for the sequestration of inorganic ions¹⁶⁶. Modification of the *lower or upper rims* has led to the construction of appropriate hosts able to transferring cationic, anionic and/or neutral molecules from aqueous to the organic layer¹⁷⁴.

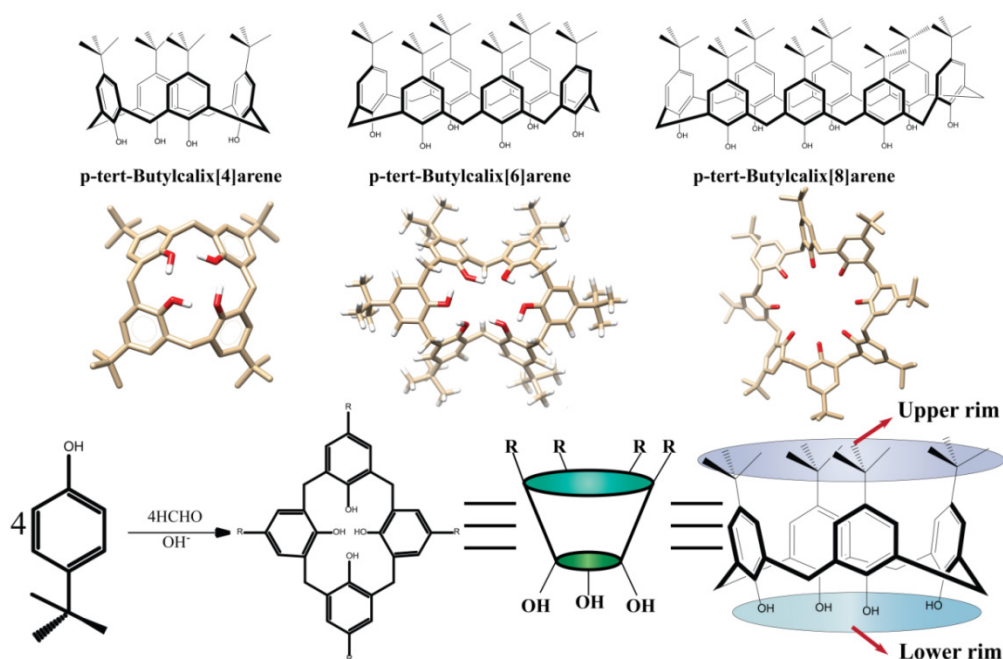


Figure 1-9. Structural representation of p-tert-butylcalix[n]arene¹⁷⁵.

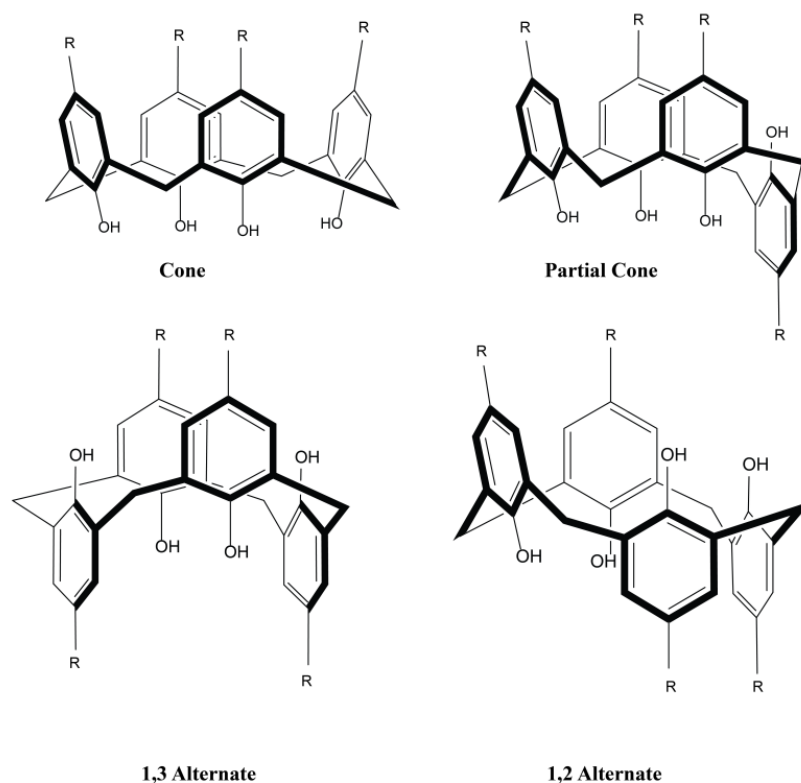


Figure 1-10. The four limiting conformations of calix[4]arenes (cone, partial cone, 1,3-alternate and 1,2-alternate). For R = Methyl or Ethyl, conformational interconversion takes place even at room temperature, whereas when the R groups are larger than ethyl, the structure is fixed by the conditions used during lower rim (phenolic oxygen) functionalization process. Pure conformers of calix[4]arene can be isolated only in case of sterically hindered rotation around the bridging methylene group like in the case of p-tert-butylcalix[4]arenes and is generally unknown for $n > 4$ ¹⁷⁵.

Supramolecular host-guest inclusion complexes were formed by hydrophobic interactions, hydrogen bonding, p-p stacking, charge-transfer, and others, which have provoked lots of interest because of their reversible nature (complexation and decomplexation) ¹⁷⁶⁻¹⁸⁰. Numerous research groups have reported Calixarene-based drug delivery systems by loading drugs in different inclusion complexation forms. In 2009, Wheate et al. ¹⁸¹ constructed a vehicle for anticancer drug delivery based on p-sulphonatocalix[4]arene and dinuclear platinum compound by side-on binding of the two parts. The system would release dinuclear platinum upon in vivo administration, due to high content of blood serum existing in body. In order to amplify the applicability of water-soluble CAs in complex systems, Liu et al. ^{182, 183} reported the complexation of topotecan and irinotecan with p-sulphonatocalix[4]arene under 1:1 molar ratio, and the inclusion modes were confirmed by means of ¹H NMR, DSC, 2D NMR and UV-vis spectroscopy. And then Song et al. ¹⁸⁴

constructed the inclusion complex using p-sulphonatocalix[6]arene and vitamin B6 in acidic and alkaline media. The complex systems could release cargo through disaggregation of the inclusion complexes under certain conditions, which means they can act as an excellent candidate for drug delivery. For the sake of loading larger cargo, such as norfloxacin and ciprofloxacin, calix[8]arene was chosen as host macrocyclic compound to encapsulate drug into its cavity^{185, 186}. Luo et al.¹⁸⁵ reported a smart delivery system, which was composed of p-sulfocalix[8]arene and antimicrobial agent in aqueous solutions and could respond to competitive agent, i.e., bovine serum albumin.

2 Chapter 2: Objectives and Scope of the Thesis

The objectives and scopes of the thesis are presented in this chapter. These include: (a) study of the conformational properties of olmesartan in solution and receptor site; (b) exploration of the host guest interactions between silibinin and cyclodextrin and quercetin with calixarene. A detailed analysis of the objectives and scopes follows.

2.1 The dynamic properties of angiotensin II type 1 receptor inverse agonists in solution and in the receptor site

Olmesartan (Figure 2-1) exhibits potent inverse agonist activity and is the latest drug appeared in the market before azilsartan. It possesses a unique structure, bearing a hydroxyl group in the imidazole ring and a carboxyl group. For this reason it has received a considerable interest for its pharmacological and biophysical properties. In particular, studies have been already conducted in order to clarify olmesartan's thermal, dynamic and structural properties in lipid bilayers and comprehend its distinct pharmacological profile^{187, 188}. In addition, olmesartan's impurities and degradation products were identified¹⁸⁹⁻¹⁹². Recently, the crystal structure of the human AT₁R in complex with olmesartan was reported by Zhang *et al.*¹⁹³.

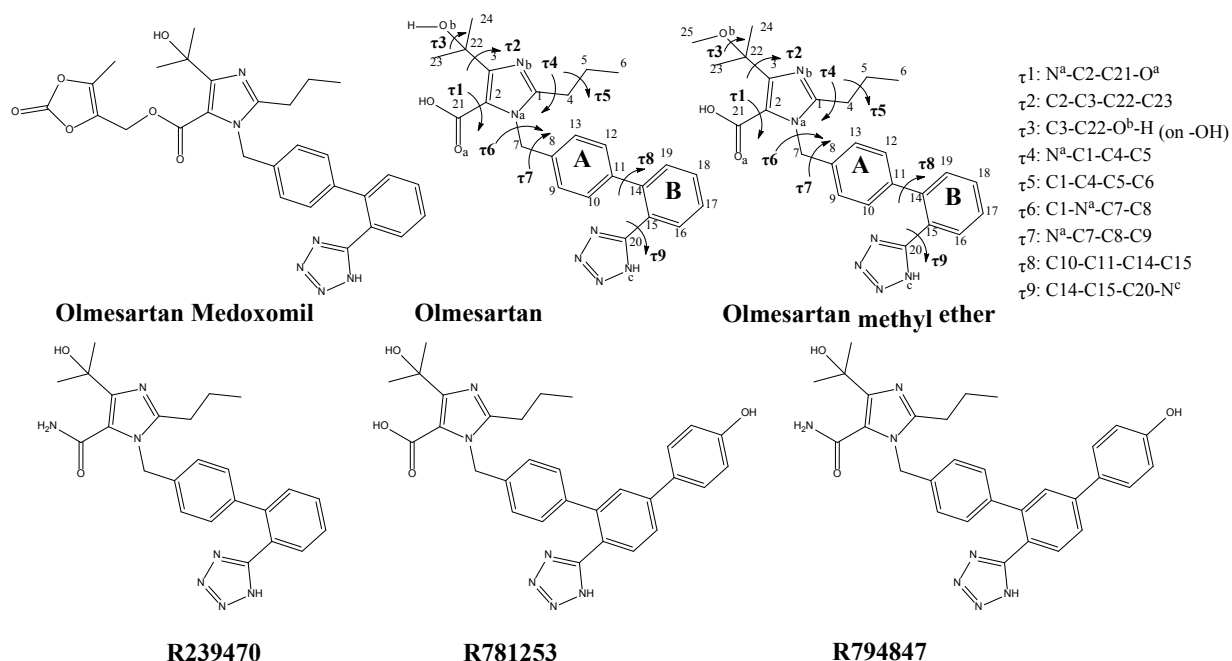


Figure 2-1. Chemical structures of olmesartan medoxomil, olmesartan and olmesartan methyl ether as well as their critical dihedral angles and the derivatives of olmesartan R239470, R781253, and R794847.

The *in situ* formation of olmesartan methyl ether from olmesartan, when the latter is dissolved in methanol was identified using various spectroscopic methodologies and its mechanism of formation was explored using theoretical studies¹⁹⁴. In the same study¹⁹⁴, olmesartan methyl ether demonstrated *in vitro* equal AT₁R inverse agonism with that of the prototype drug of this class of molecules, losartan.

It is reported that conformations based on NMR spectroscopy explain better the coherent biological activities of the drug molecules^{55, 195}. This statement is examined in the present study for the cases of olmesartan and its methyl ether analogue. The Nuclear Overhauser Effect (NOE) effect was utilized to acquire distance constraints. The recent literature on the role of methyl groups in medicinal chemistry^{196, 197} urged us to compare the conformational properties of olmesartan and its methyl ether analogue.

Miura *et al.*⁶⁵ have reported that mutations in the AT₁R such as Y113F, K199Q, H256A and Q257A lower the binding affinity of olmesartan 25, 15, 16 and 103 –folds, respectively. Moreover the Y113A mutation did not exert any impact on the binding affinity of olmesartan. In marked contrast these mutations did not affect the binding of olmesartan for the AT₁R in a recent study in which different experimental conditions and different expression systems of receptor have been used¹⁹³. These residues did not appear to develop direct interactions with the ligand in the cryo-cooled crystal structure of the AT₁R-olmesartan complex¹⁹³. Docking and MD studies for olmesartan have been performed in an effort to project a putative explanation of its biological effects and to interpret the impact of the mutations in its binding affinity. Crystallographic data of co-crystallized selective AT₁R antagonist ZD7155 with AT₁R⁴⁶ and the more recent crystal structure of AT₁R with olmesartan¹⁹³ were used for the *in silico* calculations. Induced fit docking calculations were also performed in two homology models of the AT₁R in order to evaluate if these models provide a better explanation of the biological data. New theoretical approaches to study the molecular docking of drug molecules in the active site of the receptor^{198, 199} allow further accuracy in the results. In addition, comparisons have been conducted with olmesartan derivatives presenting different biological profiles: olmesartan methyl ether, R239470 (a neutral antagonist^{65, 200}), R781253 (a new inverse agonist²⁰⁰) and R794847 (a weak partial agonist^{193, 200}). All these compounds were docked in the AT₁R and then MD simulations were performed in dipalmitoylphosphatidylcholine (DPPC) bilayers.

Finally, statistical treatment of experimental ^{13}C NMR chemical shifts of olmesartan/olmesartan methyl ether and the calculated isotropic shielding constants of their respective conformers has been carried out. This was performed in order to assess whether calculated chemical shifts can predict which conformers are the major ones in the conformational equilibrium^{201, 202}.

2.2 Investigation of the interactions of silibinin with 2-hydroxypropyl- β -cyclodextrin through biophysical techniques and computational methods

Milk thistle has been used since ancient times to treat a range of liver and gallbladder disorders, such as hepatitis, cirrhosis, as well as other gastrointestinal problems²⁰³⁻²⁰⁹. The bioactive phytochemical of this plant is silymarin, which is composed of a mixture of four isomeric flavonolignans, namely silibinin, isosilibinin, silidianin and silichristin, their diastereoisomers and one flavonoid^{207, 210-212}. The flavonolignan silibinin or silybin (SLB) is the main active component of silymarin complex, which is derived from silymarin extract as an approximately 1:1 mixture of two diastereoisomers, namely, silybin A (SLBA) and silybin B (SLBB)^{207, 211} (Figure 2-2). Silybin A, silybin B, isosilybin A, and isosilybin B have been distinguished and assigned using quantum mechanical driven ^1H iterative Full Spin Analysis²¹³.

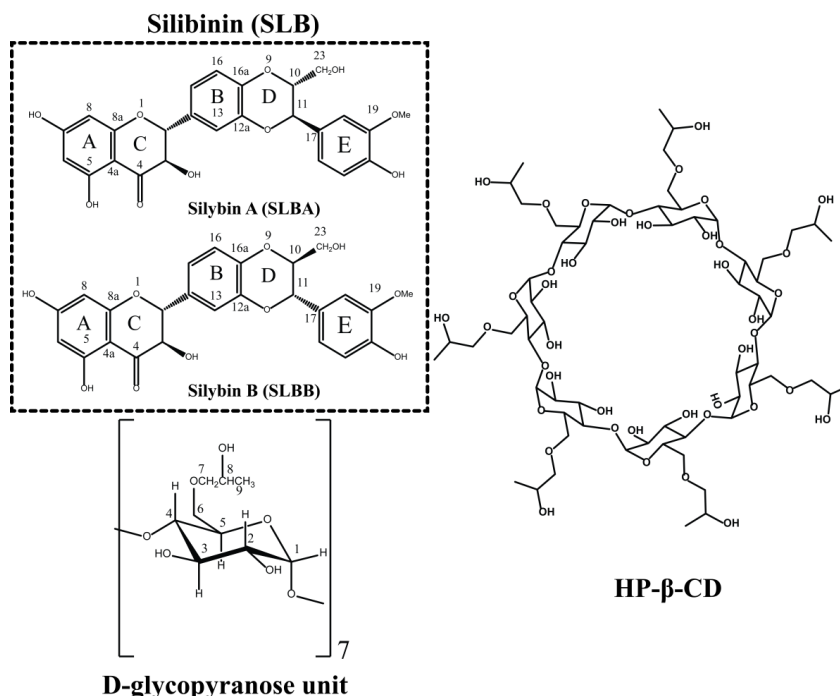


Figure 2-2. Structure of SLB (top, left) and the cyclic HP- β -CD (right) consisting of seven D-glycopyranose units (bottom, left). Numbers correspond to those referred in the NMR tables.

Nowadays, SLB has been widely used in the treatment of hepatic disorders of varying origin ²⁰⁷⁻²⁰⁹. Moreover, in recent studies, SLB has shown strong anticancer efficacy against advanced human PCA cells ^{207, 214, 215}, intestinal carcinogenesis ^{207, 216}, colorectal cancer growth ^{207, 217, 218} and lung tumors ^{207, 219}. Also, the hypocholesterolemic ²⁰⁷ and the cardioprotective effect of silymarin and its constituents in the context of the established mechanisms of preconditioning have been discussed ²²⁰.

The therapeutic properties of SLB are associated with different mechanisms of action at the cellular level: (a) it acts as a radical scavenger ^{221, 222}; (b) it possesses cell-regenerating activity associated with its ability to activate protein synthesis by stimulation of DNA-dependent RNA-polymerase I ^{208, 223}; (c) it is a potent inhibitor of human intestinal β -glucuronidase ^{205, 206} that contributes to neonatal jaundice.

Intestinal absorption of SLB is rapid but incomplete and its oral bioavailability from silymarin extract is very low and variable ^{205, 209, 224, 225}, mainly due to its limited aqueous solubility ⁹ (430 mg/L), leading to incomplete *in vivo* dissolution and poor intestinal absorption. In conjunction to the extensive first pass metabolism from the liver, these are the two limiting factors for the oral use of silibinin in therapeutics. About 10-50% of silibinin contained in silymarin standardized extract (Legalon) is absorbed following oral administration in humans and about 80% is excreted in the bile, while about 10% enters the enterohepatic circulation ^{205, 208, 224}. However, apart from the observed rapid but incomplete SLB intestinal absorption, the systemic exposure to silymarin extract components was found linear and dose proportional ^{224, 225}. Most of the SLB present in plasma, after administration, is in its conjugated form, consisting mainly of sulfates and glucuronides ^{224, 226}. In the recent study by Jancova *et al.* ²²⁷, the predominant formation of the 7-O- β -D-glycuronides and the preferential glucuronidation of silybin B were confirmed *in vitro* while, the contribution of specific UDP-glucurotransferases to the metabolism of SLB diastereomers was also identified.

Cyclodextrins (CDs), as described in chapter 1.8, have been widely used to protect drugs against conjugation and metabolic inactivation ²²⁸⁻²³⁰ as well as to enhance the aqueous solubility and hence to ameliorate the oral bioavailability of sparingly soluble drug molecules ²³¹⁻²³⁸. Therefore, the complexation of SLB with CD can solve the abovementioned two problems regarding the use of SLB as a drug. SLB is known as a drug that complexes with β -cyclodextrins (see Figure 1), but detailed physicochemical studies on the SLB-CD interactions at the molecular level were lacking ²³⁹.

In the present work, a lyophilized SLB–HP- β -CD complex was prepared and evaluated *in vitro*. Differential Scanning Calorimetry and mass spectrometry have been used for the complex characterization. 2-hydroxypropyl- β -cyclodextrin (HP- β -CD) is a water soluble derivative of the parent β -cyclodextrin (β -CD). It has been approved by the European Medicine Agency (EMA) and the American Food and Drug Administration (FDA) as safe for both oral and intravenous (*i.v.*) administration to humans, since it is not associated with the serious adverse effects (e.g., irreversible nephrotoxicity) of the parent β -CD after *i.v.* administration. For the first time, both solid state and high resolution liquid NMR spectroscopy have been applied to detect the molecular interactions of silibinin with HP- β -CD. 2D NOESY spectra showed correlations between the host and guest molecules. In addition, chemical shift changes on the complexing of the guest with the host, provide significant information on their molecular interactions. The aqueous solubility and dissolution characteristics of the complex at pH conditions simulating those of the upper gastrointestinal tract have been applied.

Finally, molecular dynamics (MD) calculations have been performed (a) to reveal the thermodynamic characteristics associated with the drug interactions with HP- β -CD and (b) to study the stability of the drug upon complexation with HP- β -CD.

Investigation of the SLB–HP- β -CD effect in MCF-7 cancer cells growth was carried out using the MTT assay. From these assays it became evident that the SLB–HP- β -CD complex pinpointed superior attributes with respect to the free silibinin.

2.3 Cancer delivery of quercetin through pH responsive calixarene–gold nanoparticles

Quercetin (Qrc), a flavonoid, has been extensively studied and its efficacy has been evidenced in a broad therapeutic window of diseases probably due to its ability to orchestrate a polypharmacology profile. Recently the direct binding of quercetin to the BH3 domain of Bcl-2 and Bcl-xL proteins has been revealed, thereby inhibiting their activity and promoting cancer cell apoptosis²⁴⁰. To take advantage of the full therapeutic capacity of quercetin in tumors one has to enhance its solubility as also to achieve a selective and spatiotemporal controlled release in cancer cells. To succeed this, tumor microenvironment characteristics have to be exploited. Tumor sites create gaps or defects in the tumor vessels architecture that supply nutrients and oxygen to these tissues (Figure 2-3A)²⁴¹ and result to the accumulation of high-molecular weight compounds to the tumor site, the so-called enhanced permeability and retention (EPR) effect²⁴². Circulating

nanoparticles can thus passively accumulate in tumor tissue once they extravasate through these large vascular pores. We therefore targeted to construct gold (Au) nanoparticles (AuNPs) due to their unique ability to combine chemical, electronic, optical, physical properties with respect to other biomedical nanotechnologies. However, deeper penetration and delivery of the nanoparticles within the tumor mass is hampered due to malformed lymphatic system as also due the dense extracellular matrix found in most tumors. In our design strategy and in order to overcome such deficiencies and to achieve a deeper tumor penetration through an independent release and diffusion of the therapeutic drug cargo we took advantage of the acidic extracellular pH found in tumor tissue (Figure **2-3B**)²⁴³. This happens mainly due to lactate secretion from anaerobic glycolysis²⁴³. We thus aimed to obtain a pH responsive and acidic release of the drug cargo from the nanoparticle. To this we therefore decorated the gold nanoparticle with appropriate calixarene derivative onto which quercetin was engulfed-loaded (Figure **2-3C**). We selected calixarene due to their exceptional advantages in the construction of molecular recognition systems with variety of steric structure, and the diversity of functioning and relative availability²⁴⁴⁻²⁴⁶. We especially used the water soluble *p*-sulfonatocalixarene (Calix) due to their high solubility in water, stability and lower toxicity with a number of potential biological activities and inclusion behavior^{247, 248}. To achieve the characterization of the calixarene-quercetin complex as also of the Quercetin-calixarene-AuNP we recruited an array of different techniques including in silico studies, solid state and solution NMR, fluorimetry, Dynamic - TEM - Electrophoretic Light Scattering, FTIR, DSC. To assay the mechanism of cell entrance we used FACS and confocal microscopy and we also assayed the cytotoxic activity.

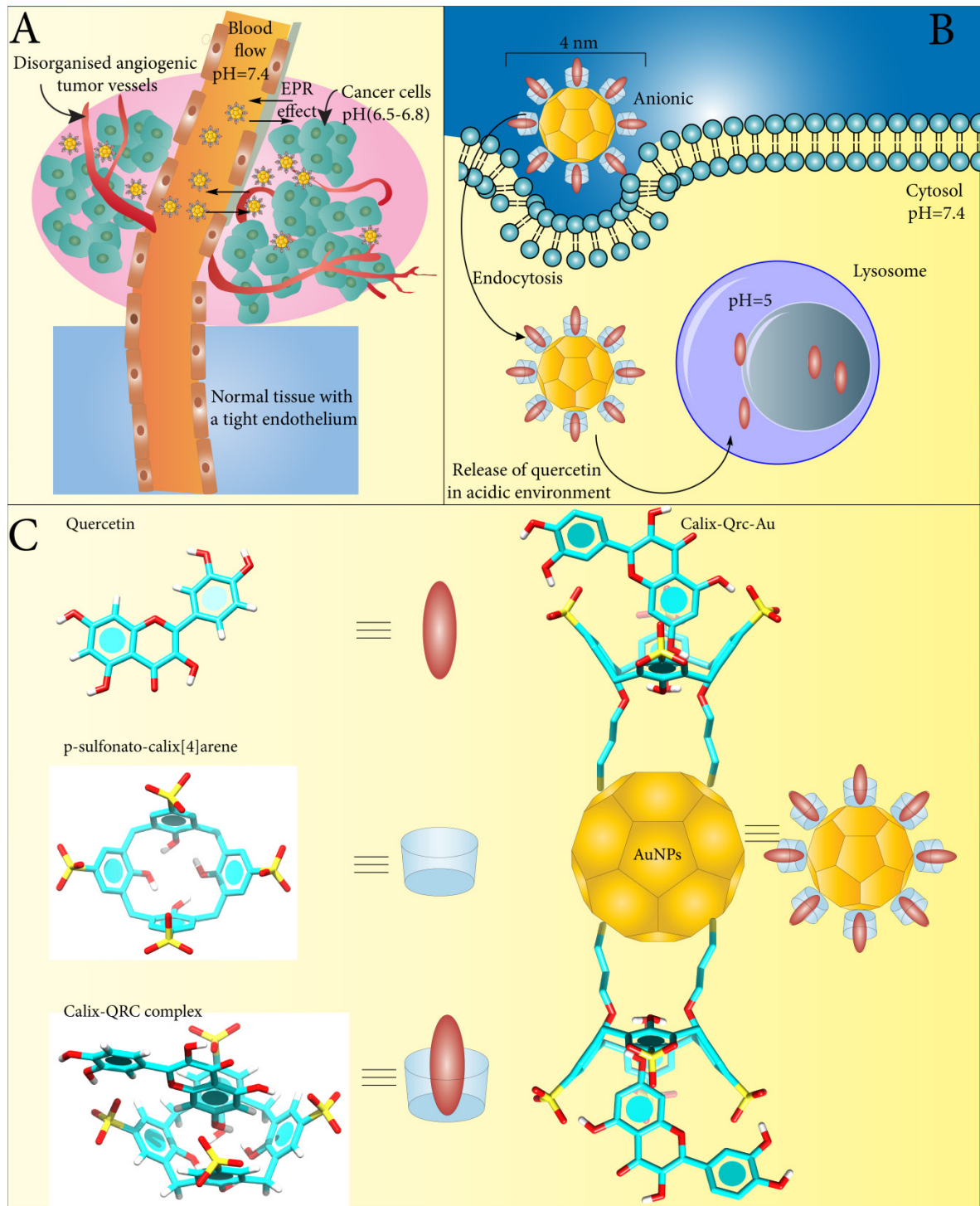


Figure 2-3: A) Tumor sites create larger gaps in the endothelium. Disorganised angiogenic tumor vessels are developed that supply nutrients and oxygen. The EPR effect causes the accumulation of molecules of high molecular weight. The cancer cells create an acidic environment around them. B) The anionic gold nanoparticle enters the cell through a process of endocytosis. Quercetin is mainly released in the acidic environment of the lysosome. C) The structures of quercetin, p-sulfonato-calix[4]arene, the Calix-Qrc complex and the Calix-Qrc-Au nanoparticle.

3 Chapter 3: Methodology

3.1 Computational methods for investigating the dynamic properties of olmesartan
Materials. Olmesartan was kindly provided by Daiichi Sankyo Pro Pharma. CD₃CN 99.80% was purchased from Euriso-Top, Gif-sur-Yvette, Essone, France and CD₃OD (99%+) from Sigma Aldrich, St. Louis, MO.

NMR spectroscopy. 2 mg of olmesartan were dissolved in CD₃OD and 2 mg of olmesartan methyl ether were dissolved in either CD₃OD or CD₃CN. The high-resolution NMR spectra were obtained on a Bruker Avance III spectrometer (Bruker Biospin GmbH, Reinsteten, Germany) operating at 600.11 MHz for ¹H and at 150.11 MHz for ¹³C, with a 5 mm inverse detection probe. The residual ¹H signals (3.33 ppm for CD₃OD and 1.94 ppm for CD₃CN) were used as internal standards. 1D and 2D NMR spectra were acquired using the pulse sequences included in the Bruker library of pulse programs.

Experimental data were processed using MestReC software.

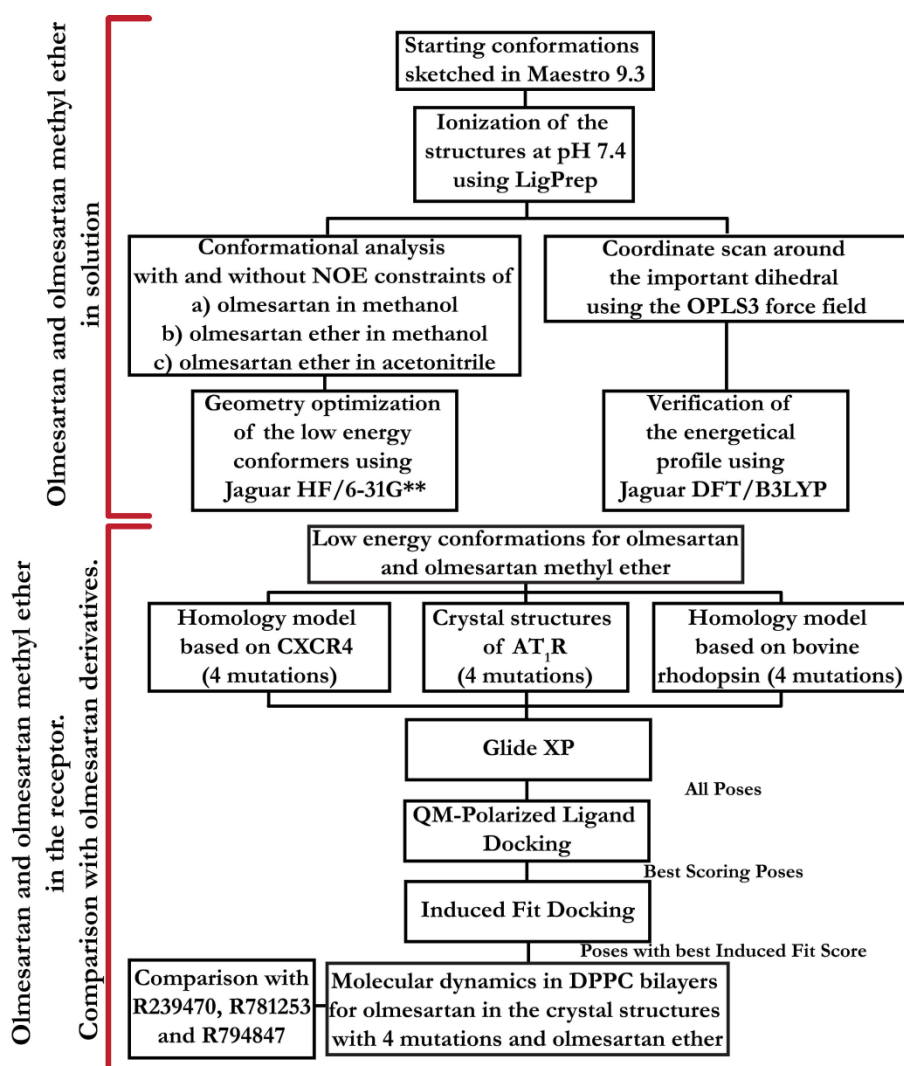
The complete NMR data (¹H, ¹³C, COSY, HSQC, HMBC) have been assigned for both, olmesartan (in CD₃OH) and olmesartan methyl ether (in CD₃CN). It must be pointed out that in case of olmesartan methyl ether, dissolved in CD₃OD, the signal of the methoxy group protons overlaps with the residual solvent peak. This necessitated the recording of 1D ¹H and 2D NOESY NMR experiments for olmesartan and olmesartan methyl ether in CD₃OD and CD₃CN solvents.

The NOEs signals observed (for olmesartan in CD₃OD and for olmesartan methyl ether in CD₃CN and CD₃OD) were quantified. The proton distances (Table 1) were calculated via the mathematical formula (3-1):

$$R = R_{REF} \sqrt[6]{\frac{V_{REF}}{V}} \quad (\text{Equation 3-1})$$

V_{REF} , R_{REF} represent the reference volume and the reference distance, respectively and V , R , the volume and the distance for each signal. The average distance between the hydrogens H4-H5 ($\approx 2.80 \text{ \AA}$) was implemented as R_{REF} . Upper and lower limit values of constraints were allowable (15% of tolerance).

Software. All the computational studies were performed in the Schrödinger 2015.2 suite. The starting structures were sketched in Maestro 10.2 and subsequently ionized at a pH of 7.4 using Epik 3.2, as implemented in Ligprep 3.4²⁴⁹. Calculations were performed for both neutral and ionized forms. A schematic representation of the computational workflow is shown in Scheme 3-1.



Scheme 3-1. Computational workflow

Conformational Analysis. The Macromodel 10.8 module²⁵⁰, was used for the conformational analysis of olmesartan and olmesartan ether. The dielectric constant (ϵ) was set at 35.85 for the simulations in acetonitrile and 33.62 for methanol (at 298 K). The conformational search was performed with distance constraints. The ten distances derived from the NOE (shown in Table 3-1) were used as constraints during the simulations for

olmesartan in methanol. In addition, thirteen distances shown in Table 1 were used as constraints during the simulations for olmesartan ether in methanol. Fourteen distances were used as constraints for the simulation of olmesartan methyl ether in acetonitrile. To account for NOE-derived distance flexibility, a margin of $\pm 0.5 \text{ \AA}$ was used for every constraint and a force constant of $10 \text{ kJ mol}^{-1} \text{ \AA}^{-2}$. All the conformational searches were carried out using the torsional sampling method (a Monte Carlo multiple minimum method). A 21 kJ mol^{-1} energy cutoff was used to remove the highest energy conformers. Every conformer was minimized using the Polak–Ribiere conjugate gradient (PRCG) method for a maximum of 2000 steps, to a convergence threshold for the gradient of $0.001 \text{ kJ mol}^{-1} \text{ \AA}^{-1}$ and the OPLS3 force field^{251, 252}, since it provides accurate energy minimization potential functions for small molecules. In order to work with a manageable set of representative conformers, the resulting structures were clustered using the conformer_cluster.py script. The atomic RMSD matrix was calculated using all the heavy atoms, while the clustering was calculated using an average linkage method.

Table 3-1: NOE derived distances obtained after integration of the cross-peaks obtained from 2D NOESY spectra.

	Olmesartan	Olmesartan methyl ether	
	Solvents		
	CD ₃ OD	CD ₃ OD	CD ₃ CN
Olmesartan/olmesartan methyl ether protons	NOE derived distance (Å)		
H5-H4	2.8	2.8	2.8
H9-H4	3.6	3.5	3.3
H5-H7	4.3	3.9	3.6
H4-H7	3.0	3.3	2.6
H6-H4	3.5	3.3	3.1
H6-H5	2.8	2.7	2.6
H7-H9,H13	2.8	2.6	2.6
H19-H10,H12	2.8	2.3	2.6
H19-H18	2.2	1.9	2.3
H16-H17	2.3	1.8	2.4
H5-H9,H13		3.8	3.7
H6-H9,H13		4.5	
H9,H13-H23,H24		5.5	
H25-H23,H24			3.4
H10,H12-H23,H24			4.9
H9,H13-H10,H12			2.5

Geometry Optimization. The lowest energy conformers of olmesartan in methanol and olmesartan methyl ether in methanol and acetonitrile were then subjected to further geometry optimization. The optimization was carried out using the Jaguar 8.8 module²⁵³. The DFT/B3LYP level of theory and the 6-31G** basis set were used for the geometry optimization, while the Poisson–Boltzmann model (PBF) was used as solvent²⁵⁴. The SCF accuracy level was set to ultrafine. NMR chemical shieldings were calculated for all the representative conformers of olmesartan and olmesartan ether and the crystal structure of olmesartan using the GIAO method^{253, 255}. The chemical shifts were then calculated using the following formula:

$$\delta_{\text{calculated}}^x = \frac{\sigma^0 - \sigma^x}{1 - \sigma^0 / 10^6} \quad \text{Equation 3-2}$$

where $\delta_{\text{calculated}}^x$ is the calculated shift for nucleus x (in ppm), σ^x is the shielding constant for nucleus x and σ^0 is the shielding constant for the carbon or proton nuclei in tetramethylsilane (TMS), which was obtained from a B3LYP/6-31G** calculation on TMS.

Dihedral scan. In order to estimate the flexibility of the τ_8 dihedral angle a relaxed conformational scan was performed using both molecular mechanics and *ab initio* methods. The coordinate scan was achieved in MacroModel 10.8 using the OPLS3 force field and setting the dielectric constant to 35.85 for acetonitrile and 33.62 for methanol. The structures were minimized using the Polak Ribiere Conjugated Gradient method with a convergence threshold of 0.05. The initial coordinate was set at 0° and the final at 360° with an increment of 1°.

The relaxed potential energy surface (PES) scan was performed using the Jaguar 8.8²⁵³ module of Schrödinger for the τ_8 dihedral angle for both olmesartan and olmesartan methyl ether. The dihedral was incremented by 5 degrees in each step. The DFT level of theory and the B3LYP/6-31G** hybrid functional were used for the optimization of the structures during the coordinate scan for all the intermediate steps. The calculations were performed *in vacuo* and in methanol or acetonitrile solvents for olmesartan and olmesartan methyl ether respectively using the Poisson–Boltzmann finite element solvent model. Vibrational frequencies and IR intensities were calculated for all the intermediate conformations.

Docking procedure. The crystal structures and two homology models of the AT₁R were used for the docking procedure. The first model was kindly provided by Prof. T. Tuccinardi and was generated using the bovine rhodopsin crystal structure as template (PDB ID 1U19)⁶⁰. The second model, kindly provided by Dr. M. Matsoukas, was based on the CXCR4 crystal structure with PDB ID 3ODU^{61, 256}. The crystal structures (PDB IDs 4YAY (XFEL structure with resolution 2.9 Å)⁴⁶ and 4ZUD (resolution 2.8 Å)¹⁹³) and the homology models were prepared using the Protein Preparation Wizard²⁵⁷, were ionized at a pH of 7.4 using PROPKA²⁵⁸, and were minimized using the OPLS3 force field²⁵¹. Receptor grids for the homology models were generated centroid of the residues Tyr113, Lys199, Tyr253 and His256. The receptor grid for the crystal structure was generated centroid to the co-crystallized ligand ZD7155. The four important mutations according to Miura *et al.*⁶⁵, for each 3D structure of the protein (Y113F, K199Q, H256A, Q257A) were generated using the “Residue and Loop mutation” facility in Bioluminate 1.9. All residues within 5 Å of the mutation were minimized. Firstly, Schrödinger’s docking algorithm Glide was used to predict the binding geometries for the ligand-receptor complexes. The docking calculations were performed with GlideXP (extra precision mode)^{259, 260}, using standard van der Waals scaling of 0.8. All the resulting poses were used as starting conformations for the QM-Polarized Ligand Docking approach (QPLD)^{261, 262}. In this workflow, accurate quantum mechanical charges are generated from the electrostatic potential energy surface of the ligand using the density functional theory (DFT), the B3LYP/6-31G* basis set and the ultrafine SCF accuracy level within the Jaguar module. Ligands were redocked using GlideXP. The final selection was based on the Emodel score. Since Emodel combines the GlideScore and the internal energy of the ligand conformation, it is a more suitable score to rank the best poses of the same ligand. The five QPLD conformers with best Emodel scores were submitted as starting geometries for the Induced Fit Docking calculations with implicit membrane^{263, 264}. At the initial stage of docking side chains of residues that are within 5 Å of the ligand were trimmed. Three residues that are within 5 Å of the ligand and have the highest B-factors (above 40) were refined using Prime 4.0²⁶⁵. The ligands were redocked using the extra precision mode. The implicit membrane is a low-dielectric slab-shaped region, which is treated in the same way as the high-dielectric implicit solvent region. Hydrophobic groups, which normally pay a solvation penalty for creating their hydrophobic pocket in the high dielectric region, do not pay the same penalty while in the membrane slab. Conversely, hydrophilic groups lose any

short ranged solvation energy from the high dielectric region when moving into the low dielectric region. The implicit membrane model is intended for use with proteins that span the membrane^{263, 265}.

MD simulations : The poses in the two crystal structures with best Induced Fit Score were subjected to molecular dynamics simulations using Desmond 4.2²⁶⁶. The receptor was immersed in the DPPC bilayer. The SPC solvent model was used with an orthorhombic box shape. The OPLS3 force field was used during the building of the system²⁵¹. The system was minimized using steepest descent for 2500 maximum iterations until a gradient threshold of 25 kcal mol⁻¹ Å⁻¹ was reached. The simulation time for the molecular dynamics was set at 300 ns in the NPT ensemble class. The temperature and the pressure were set at 325 K and 1.01325 bar correspondingly. The RESPA integrator was used with a timestep of 2.0 fs²⁶⁷. The thermostat method used was the Nose-Hoover chain²⁶⁸, while the Martyna-Tobias-Klein method was used as barostat²⁶⁹. The cutoff radius was set at 9.0 Å. MD simulations were run for olmesartan in both crystal structures (4YAY and 4ZUD) and the four mutated structures, while for olmesartan methyl ether and the compounds R239470, R781253 and R794847 MD simulations were run in both crystal structures and repeated twice.

MM-GBSA calculations: The MM-GBSA calculations were performed using Prime. The water and DPPC molecules were removed from the trajectories using the delete_atoms.py utility. The binding energy was calculated for a total of 4151 frames of the MD trajectory starting from the 100th ns until the end of the trajectory at the 300th ns. The binding free energy was calculated by equation (3-3).

$$\Delta G_{\text{Bind}} = \Delta E_{\text{MM}} + \Delta G_{\text{Solv}} + \Delta G_{\text{SA}} \quad \text{Equation 3-3}$$

where ΔE_{MM} is the difference in the minimized energies between the protein–ligand complexes. ΔG_{Solv} is the difference in the GBSA solvation energy of the protein–ligand complex and sum of the solvation energies for the protein and ligand. ΔG_{SA} is the difference in the surface area energies for the complex and sum of the surface area energies in the protein and ligand.

Prediction of the chemical shielding constants of olmesartan and olmesartan methyl ether in their binding sites: From the MD trajectories of olmesartan and olmesartan methyl ether in the receptor, a snapshot closest to the calculated average structure for each trajectory of

the protein-ligand complex was created. Chemical shielding constants were calculated using QSite²⁷⁰. The QM region consisted of the ligands which were treated using the DFT/B3LYP/6-31G** basis set. The rest of the protein was treated using molecular mechanics and the OPLS-2005 force field with the maximum number of iterations set to 100 cycles and all calculations were converged before this limit using the conjugated gradient algorithm. The NMR shifts were calculated from the shielding constants using the formula (2).

3.2 Materials and Methods for the investigation of the interactions of silibinin with HP- β -CD

Silibinin (MW = 482.44), and HP- β -CD (MW ~1540) were purchased from Sigma Aldrich (Steinheim, Germany, purity > 99%). We determined the percentage of the two diastereoisomers present in silibinin on the basis of solution ¹H-NMR spectroscopy after following a recent report by Napolitano *et al.*²¹³. On the basis of this report a fingerprint has been extracted for the two diastereomers A and B of silibinin that present minor alteration on their ¹H chemical shifts. Through our solution ¹H-NMR studies we were able to determine the presence of the two diastereomers (resonances of the H13 protons of silybin A and silybin B) which after integration resulted to a 1:1 molar ratio for the two diastereomers of silybin A and silybin B, respectively.

Preparation of the lyophilized SLB-HP- β -CD product. A freeze-drying procedure was applied for the preparation of SLB-HP- β -CD lyophilized product. For the preparation of SLB-HP- β -CD aqueous solutions for freeze-drying in a molar ratio of 1:2, optimized in preliminary experiments, the neutralization method was used²⁷¹. More specifically, 0.300 g of SLB and 1.860 g of HP- β -CD were weighed accurately, transferred in a 300 mL volumetric flask and suspended with 200 mL of water. Small amounts of ammonium hydroxide were then added under continuous stirring and pH monitoring until complete dissolution and pH adjustment to a value between 9 and 10 has been obtained. The resulting solution at molar ratio of 1:2 was thereafter freeze-dried using a Kryodos-50 model Telstar lyophilizer. SLB-HP- β -CD aqueous solutions for freeze-drying in molar ratio of 1:1 and 1:4 were similarly prepared for comparative purposes using 0.930 g and 3.720 g of HP- β -CD, respectively.

Differential scanning calorimetry. The samples were obtained as described above, and were transferred to stainless steel capsules obtained from Perkin-Elmer and sealed. Thermal scans were obtained on a Perkin-Elmer DSC-4 instrument (Norwalk, CT).

Samples (*ca.* 5-10 mg) were scanned from 40 to 230 °C using a scanning rate of 10 °C/min under nitrogen atmosphere. The following diagnostic parameters were used for the study of drug:CD complexation: T_m (maximum position of the recorded heat capacity), T_{onset} (start of the phase transition), and the enthalpy change, ΔH .

MS studies. Mass spectrometry was performed using an ESI-LTQ-ORBITRAP XL unit (Thermo Fisher Scientific) at the full scan positive mode. The ESI LTQ ORBITRAP XL unit was operated with a spray voltage of 3.4 kV. The sheath gas flow rate and auxiliary gas flow rate were adjusted to 30 and 8 arbitrary units. The capillary voltage and the tube lens voltage were set to 40 and 110 V, respectively. The mass resolution was set to 60000, while the scan ranged from m/z : 150 up to m/z : 1200. The MS data were analyzed by the Xcalibur 2.1.0 software.

NMR studies. Pure SLB and HP- β -CD, a physical mixture of SLB and HP- β -CD and the SLB-HP- β -CD lyophilized product were prepared as described above, and were analyzed by both solid state and high resolution liquid NMR spectroscopy to detect the molecular interactions of SLB with HP- β -CD.

Liquid State NMR: Diffusion ordered NMR spectroscopy (DOSY) spectra were recorded using a Bruker AV-500 spectrometer equipped with a pulsed field gradient unit capable of producing magnetic field pulse gradients in the z -direction of 53 G cm^{-1} , at room temperature. Samples were dissolved in 0.5 mL D_2O and transferred to 5 mm NMR tubes. The NMR system was controlled by the software TopSpin 2.1. All spectra were acquired with an acquisition time of 1.09 s and relaxation delay $4 T_1$. T_1 values were determined by the inversion recovery time pulse sequence and were calculated from 2 to 3.5 s²⁷². DOSY experiments were performed with the bipolar pulse longitudinal eddy current delay (BPPLD) pulse sequence. More specific, 16 BPPLD spectra with 16 K data points were collected and the eddy current delay (T_e) was set to 5 ms. The duration of the pulse field gradient, δ_g , was optimized in order to obtain 5% residual signal with the maximum gradient strength. The pulse gradient was increased from 2 to 95% of the maximum gradient strength using a linear ramp. After Fourier transformation and baseline correction, the diffusion dimension was treated with the Topspin 2.1 suite.

Solid State NMR. 850 MHz ^1H experiments were performed on a Bruker 850WB Avance III spectrometer equipped with a 3.2 mm MAS HCN probe. 23 kHz magic angle spinning was applied and the temperature was set to 310 K. 600 MHz ^1H and ^{13}C experiments were performed on a Bruker 600WB Avance I spectrometer equipped with an HX 4 mm MAS

probe. 12 kHz magic angle spinning was applied and the temperature was set to 310 K. Cross polarization was used for ^{13}C excitation using an 80% linear ramp²⁷³⁻²⁷⁵. During ^{13}C detection, 100 kHz Spinal-64 [Fung 2000] proton decoupling was applied.

All samples were referenced to the CH group ^{13}C signal in natural abundance adamantane at 38.48 ppm. ^1H was referenced indirectly from ^{13}C .

High resolution NMR spectroscopy: 2D NOESY experiments have been performed using a Bruker 400 MHz Avance spectrometer and a BBI z-gradient probe at ambient temperature and using CD_3OD solvent. The relaxation delay used during the experiment was 1.5 s and the mixing time was 400 ms.

Solubility studies: Solubility studies for SLB and the SLB–HP- β -CD lyophilized product were performed using a thermostated shaking bath (Unitronic orbital J.P. Selecta) with adapted thermostating unit, while a Shimadzu UV-1700 Pharma Spec UV/VIS spectrometer was used for spectrophotometric measurements. Measurement of the solubility of pure SLB and that of SLB obtained from the lyophilized SLB–HP- β -CD product was conducted at pH 2.0, 4.5, and 6.8 at 37 °C. An excess amount of SLB or SLB–HP- β -CD lyophilized product was added to 10 mL of phosphate buffer pH 2.0, 4.5 or 6.8. After equilibration for 0, 3, 6, 15, 24 and 48 h at the thermostated shaking bath (37 \pm 0.5 °C, 50 rpm) suspensions were filtered through regenerated cellulose syringe filters of 0.45 μm pore size and the SLB concentration was determined spectrophotometrically after dilution with mixed MeOH-aqueous medium solution (50:50 v/v).

Dissolution experiments: Dissolution experiments for SLB and SLB–HP- β -CD lyophilized product were performed using a USP dissolution apparatus I (Pharma test Type PTW S III). All experiments were performed in triplicate at pH 2.0, 4.5 and 6.8, at 37 °C and 100 rpm. An accurately weighed amount of SLB (25 mg) or an equivalent amount of the lyophilized SLB–HP- β -CD product was placed into an empty capsule (in triplicate). The filled capsules were placed in the vessels of a USP dissolution apparatus II (Pharma test Type PTW S III) and were kept at the bottom with the help of metal spirals. The dissolution medium was 500 mL phosphate buffer pH 2.0, 4.5 or 6.8 and dissolution was performed at 37 \pm 0.5 °C and at 100 rpm rotation speed. Samples (2.5 mL) were withdrawn at appropriate time intervals (5, 10, 15, 20, 30, 45, 60, 120 and 180 min) after the beginning of the experiment, they were filtered through regenerated cellulose syringe filters (pore size 0.45 μm), and were assayed spectrophotometrically for SLB.

Molecular modeling. The initial structures of SLBA and SLBB were sketched in the Maestro utility of the Schrödinger Suite 2012.2 ²⁷⁶. A crystal structure of β -CD (CSD reference code BUVSEQ02 ²⁷⁷) was modified in the same utility to HP- β -CD. The OPLS-2005 force field ²⁷⁸ was used to minimize the structure of SLBA, SLBB and HP- β -CD. Docking programs have been used to predict the binding modes and the affinities between cyclodextrins and drugs ²⁷⁹⁻²⁸². In our case, GlideXP, which is an algorithm that identifies binding poses for ligands inside a macromolecule, was used ²⁶⁰. HP- β -CD was considered as the receptor and SLBA or SLBB as the ligand. The resulting initial structure was thoroughly checked using the data given by the NOE and solid-state NMR. Next, the complex was subjected to MD simulations. Since, docking and MD results for the one diastereomer were very similar to the other the analysis in the results and discussion section will be only referred to the SLBA diastereomer.

The MD simulations were carried out with the PMEMD module from the AMBER 12 simulation package ^{283, 284}. The geometry of the drug was optimized with the HF/6-31G* basis set (Gaussian 09) ²⁸⁵. The general AMBER force field (GAFF) was used to obtain force field parameters for silibinin with RESP charges ^{286, 287}. The force field GLYCAM_06i-12SB ²⁸⁸ was utilized to represent the behavior of the cyclodextrin part of the host molecule, while GAFF was used for the 2-hydroxypropyl groups. Overall, RESP charges were calculated for the modified cyclodextrin. The system was next solvated using the TIP3P water model ²⁸⁹ in a truncated octahedron with 3841 water molecules. The minimum distance between the edge of the periodic box and each atom of the system was set at 18 Å. The minimization of the complex was carried out for 5000 steps, using a nonbonded cutoff of 18 Å in constant volume. The solvated complex was then heated under constant volume for 100 ps. The temperature was gradually increased from 0 to 300 K using a Langevin thermostat ²⁹⁰. Restraints of 10 kcal mol⁻¹ Å⁻² were applied to HP- β -CD SLBA. Next, the system was equilibrated under constant pressure in two steps of 100 ps each. In the first one, constraints of 10 kcal mol⁻¹ Å⁻² were applied to the complex, while in the second step all restraints were removed. Two independent MD calculations of 190 and 250 ns were run at 300 K under constant pressure. The bonds involving hydrogen atoms were constrained at their equilibrium distance using SHAKE ²⁹¹. The collision frequency (γ) was set at 2 ps⁻¹. The analysis of the trajectories was done with the ptraj module of AMBER ²⁹².

MM-PBSA. The molecular mechanics Poisson–Boltzmann Surface Area (MM-PBSA) method was used for the calculation of the binding energy between the modified cyclodextrin and SLBA²⁹³⁻²⁹⁶.

25000 MD snapshots from each MD run of the complex were considered for the calculation of the enthalpy contribution (ΔH). 6250 snapshots (equally spaced in the last 125 ns of the MD simulation) were used for the calculation of the entropy contribution ($-T\Delta S$). The entropy term (eq. 2) was calculated by normal-mode analysis using the NMODE module of AMBER.

Topology files for the complex (stripped of water), the ligand, and HP- β -CD were created using the ante-mmpbsa utility. For each snapshot, a free energy for the complex, silibinin, and 2-hydroxypropyl-cyclodextrin is calculated, and the total binding free energy (ΔG_{bind}) is computed using the following equation:

$$\Delta G_{\text{bind}} = G_{\text{complex}} - (G_{\text{SLBA}} + G_{\text{HP-}\beta\text{-CD}}) \quad \text{Equation 3-4}$$

G_{complex} , $G_{\text{HP-}\beta\text{-CD}}$ and $G_{\text{SLBA/B}}$ are the free energies for the complex, the receptor (2-hydroxypropyl- β -cyclodextrin in this case), and the ligand (silibinin), respectively. The binding free energy can be expressed as a combination of enthalpy and entropy contributions:

$$\Delta G_{\text{bind}} = \Delta H - T\Delta S \quad \text{Equation 3-5}$$

The enthalpy term in eq. (3-5) is calculated as:

$$\Delta H = \Delta E_{\text{gas}} + \Delta G_{\text{solv}}, \quad \text{Equation 3-6}$$

where ΔE_{gas} is defined as the molecular mechanical (MM) free energy change upon complexation of HP- β -CD with SLBA in the gas phase, while ΔG_{solv} is the solvation free energy. ΔE_{gas} is further divided into Coulomb interactions (ΔE_{ele}) and van der Waals interaction terms (ΔE_{vdW}):

$$\Delta E_{\text{gas}} = \Delta E_{\text{ele}} + \Delta E_{\text{vdW}} \quad \text{Equation 3-7}$$

The solvation term of eq. 3-6 is defined as a sum of polar (ΔE_{PB}) and nonpolar (ΔE_{cavity}) contributions:

$$\Delta G_{\text{solv}} = \Delta G_{\text{PB}} + \Delta G_{\text{cavity}} \quad \text{Equation 3-8}$$

MTT assay. MCF-7 human breast cancer line was cultured in DMEM high glucose, supplemented with 10% FBS, antibiotics Penicillin/Streptomycin (100 U/mL Penicillin and 100 $\mu\text{g/mL}$ Streptomycin), non-essential aminoacids (1x) at 37 °C in humidified atmosphere of 5% CO₂. Silibinin and complex stock solutions were prepared in MeOH.

20000 cells were plated in each well at a 96-well plate and after 24 h were treated with various silibinin and complex concentrations (0-100 μ M). 24 h after the induction, MTT solution (from 5 mg/1 mL in PBS) was added in each well and incubated for additional 3 h. The supernatant from each well was removed and cells were washed with PBS buffer. Stop mix solution (20% SDS in 50% dimethyl formamide in water) was then added (100 μ L in each well) and remained in darkness for 2 h. The absorbance of each well was measured at 550 nm with a microplate ELISA reader (Awareness Technology Inc), with a reference at 650 nm. Results from two independent experiments in triplicates were counted in and the final value was calculated with the respective standard deviation.

3.3 Material and methods for the investigation of the interactions between quercetin and p-sulphonato[4]calixarene

Materials: All starting materials and reagents used were of standard analytical grade from Merck or Aldrich and used without further purification. Quercetin (Qrc) (purity 98%) was purchased from Sigma–Aldrich (St. Louis, MO, USA). All commercial grade solvents were distilled, and then stored over molecular sieves. All reactions, unless otherwise noted, were conducted under a nitrogen atmosphere. TLC was performed on DC AlufolienKieselgel 60 F₂₅₄ (Merck). All aqueous solutions were prepared with deionized water that was obtained via a Millipore milli-Q Plus water purification system and 100/ATR Sampling Accessory. Melting points were determined on a Gallenkamp apparatus in a sealed capillary glass tube and are uncorrected. pH was measured through Orion 410A+ pH meter. CEM-MDS 2000 closed vessel microwave system was used in this study to prepare real and certified samples. Shimadzu 1700 UV-Vis spectrophotometer was used for absorbance measurement.

Methods

Binding constant: Binding constant for p-sulphonatocalix[4]arene-quercetin (Calix-Qrc) complex was determined via UV spectroscopy through titrating a fixed concentration of p-sulphonatocalix[4]arene with varying concentrations of quercetin at pH 7.5. The value of the binding constant (K_a) of Qrc with Calix was evaluated with the aid of the Benesi–Hildebrand equation²⁹⁷.

$$\frac{[D]_o}{Abs} = \left(\frac{1}{[A]_o} \right) \cdot \left(\frac{1}{\epsilon k_a} \right) + \frac{1}{\epsilon} \quad \text{Equation 3-9}$$

Where $[D]_o$ is the concentration of quercetin, Abs is the absorbance of complex at wavelength, $[A]_o$ is the concentration of p-sulphonatocalix[4]arene, K_a is the equilibrium constant for complex and ϵ is the molar absorptivity of complex at λ . A plot of $1/[A]_o$ vs $[D]_o/Abs$ gives a intercept ($1/\epsilon$) and slope ($1/K_a\epsilon$) from which value of k_a was calculated.

Stoichiometric ratio of the p-sulphonatocalix[4]arene and QRC complex: Job's method (continual variation method) was used to determine the stoichiometric ratio between the p-sulphonatocalix[4]arene and the quercetin for their complexation by mixing solutions of both components of equimolar concentration (1×10^{-4} M) in different ratios varying from 1:9 to 9:1.

Solid State NMR spectroscopy: 1H and ^{13}C NMR spectra were recorded on a 600 MHz Varian system equipped with a 3.2 mm Varian Double Resonance HX MAS probe. Larmor frequencies were 599.556 MHz for 1H nuclei and 150.744 MHz for ^{13}C nuclei. Chemical shifts were reported relatively to the signals of 1H and ^{13}C nuclei in tetramethylsilane. 1H echo MAS spectra were recorded at 20 kHz sample rotation frequency with 50 s of relaxation delay. 1H - ^{13}C CPMAS spectra were recorded at 16 kHz sample rotation frequency with 20 s of relaxation delay. Polarization transfer was achieved with RAMP cross-polarization (ramp on the proton channel) with contact time of 5 ms. High-power XiX heteronuclear proton decoupling was applied during acquisition.

High Resolution Transmission Electron Microscopy Study: HR-TEM imaging was realized with a JEOL JEM-2100 instrument operating at 200 KV. Samples were prepared by casting a minute drop of a 0.1% w/v gold nanoparticle (GNP) dispersion onto carbon coated grids followed by gentle solvent evaporation under ambient conditions.

Light Scattering Study: Dynamic and Electrophoretic Light Scattering measurements were performed using a Malvern Instruments Zetasizer Nano ZS in order to assess the colloidal stability and determine the mean hydrodynamic diameter and surface potential of the organic modified GNPs.

Molecular Modeling

Building of the initial complex: The structure of *para*-sulphonatocalix[4]arene was downloaded from the Cambridge Structural Database (CSD reference code PEMYUC²⁹⁸) while that of quercetin was sketched in Maestro 10.2²⁹⁹. The initial docking of quercetin in the calixarene was accomplished using the standard protocol in Glide (a module in the Schrodinger Suite that predicts the binding poses of a ligand within a macromolecule). All results were optimized using molecular mechanics and the OPLS3 force field²⁵¹.

Quantum mechanics study: In order to assess the stability of the complex and the binding energy *ab initio* calculations were performed using the Jaguar 8.8³⁰⁰ program as incorporated in the Schrodinger 2015.2 suite. The Hydrogen Bond workflow was used to calculate the accurate binding energy²⁵³. The geometry optimizations for quercetin, calixarene and the complex were carried out using X3LYP/6-31G** since this density functional gives very good geometries for hydrogen bonded complexes. The energy calculations were then carried out using LMP2 with the cc-pVTZ(-f) and cc-pVQZ(-g) basis sets²⁵³.

Molecular Dynamics: The optimized geometry of the complex from the QM step was then used as starting structure in the molecular dynamics simulations. The geometries of quercetin and calixarene were optimized using Gaussian 09 and the HF/6-31G* basis set²⁸⁵. Force field parameters and RESP charges were determined using the General Amber Force Field (GAFF)³⁰¹. The quercetin-calixarene complex was solvated using the TIP3P water model in a truncated octahedron²⁸⁹. The distance between the edge of the box and the atoms of the system was set at 18 Å. The system was minimized using 2000 steps of steepest descent minimization followed by 2000 steps of conjugate gradients minimization. Constraints of 10 kcal mol⁻¹ Å⁻² were applied to the complex. The temperature of the system was gradually increased in 5000 steps from 0 to 300 K using a Langevin thermostat²⁹⁰. The system was then equilibrated in constant pressure. The SHAKE algorithm³⁰² was applied to all hydrogen bonds. A 2 fs time step was used and a cutoff of 9 Å. The PMEMD Molecular Dynamics engine available in AMBER14 was used. Three independent MD simulations of 400 ns were run under constant pressure. The analysis of the trajectories was performed using ptraj²⁹². The molecular mechanics Poisson Boltzmann surface area (MM-PBSA) methodology was used to evaluate the relative interaction energies for the complex using an ionic strength of 150 mM and implicit solvation constants of $\epsilon = 1.0$ for

dielectric solute and $\epsilon = 80$ for the solvent ²⁹³. 40000 snapshots were used for the determination of the binding energy.

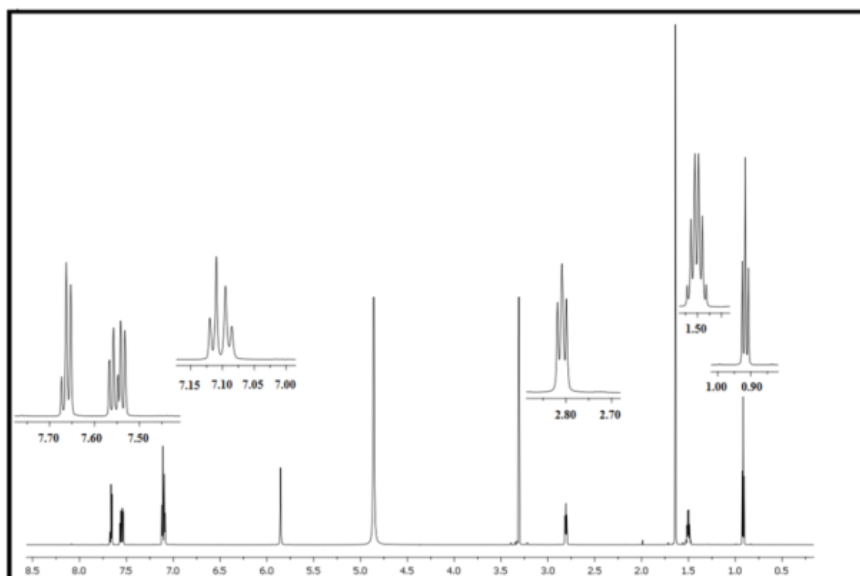
4 Chapter 4: The dynamic properties of angiotensin II type 1 receptor inverse agonists in solution and in the receptor site

In the present chapter are presented the conformational properties of olmesartan and olmesartan methyl ether in solution. Furthermore, are described the results of the induced fit docking calculations and the molecular dynamics simulations. These results were compared with those obtained by the olmesartan derivative compounds R239470, R794847, and R781253. Finally, concluding remarks are made in the end of the chapter.

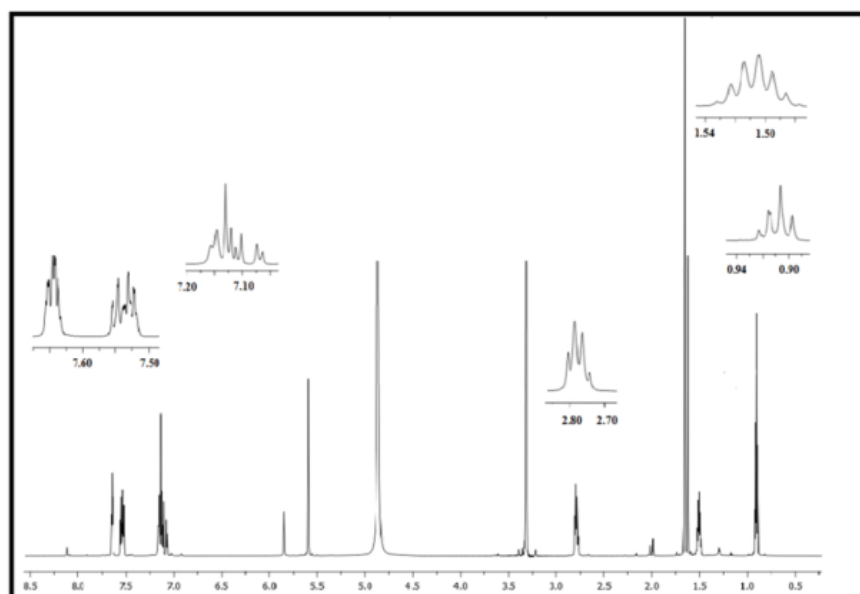
4.1 Conformational analysis of olmesartan and olmesartan methyl ether in solution using NMR and theoretical calculations

¹H NMR spectra of olmesartan in CD₃OD and olmesartan methyl ether in CD₃CN have been previously reported ¹⁹⁴. The ¹H NMR spectrum of olmesartan methyl ether in CD₃OD is illustrated in the Figure 4-1.

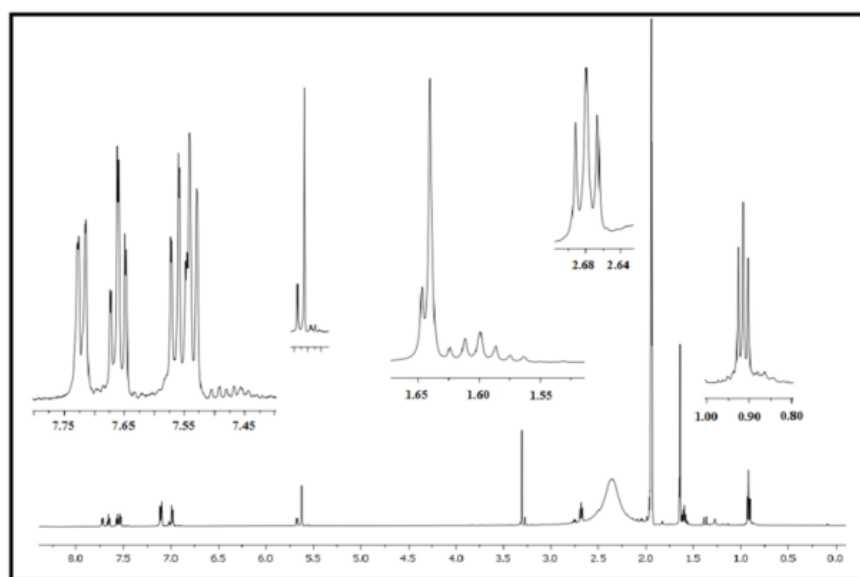
Distance NOE constraints are reported in Table 3-1 and were obtained after integration of the contour cross-peaks from the three 2D NOESY spectra.



a



b



c

Figure 4-1. ¹H NMR spectra for a) olmesartan dissolved in CD₃OD b) olmesartan methyl ether dissolved in CD₃OD and c) olmesartan methyl ether dissolved in CD₃CN³⁰³.

The representative conformations of olmesartan in methanol, derived using NOE constraints described in Table 3-1 are shown in Fig. 4-2a. In the article by Musafia and Senderowitz¹⁹⁵ it is stated that NMR derived structures were more appropriate for ligand based drug design. We have evaluated this hypothesis by applying conformational analysis on olmesartan and its methyl ether by considering the NOE data and compare the resulted conformations with those obtained without implementing NOE constraints. We are aware that the use of NOE constraints for structure determination has limitations on the basis that flexible molecules adopt a plethora of conformations that are projected on the finally recorded NOEs. However, if all NOEs are counted together, this dynamic process of the various conformations is lost. As can be observed by comparing the conformations in figure 4-2 and the ones in figures 4-3, 4-4 and 4-5, conformational analysis with and without NOE constraints provided almost identical results. Five of the eight representative conformations are *syn*, thus the tetrazole and imidazole moieties adopt the same orientation with respect to the ring plane of phenyl A. Half of the representative conformations of olmesartan methyl ether, in both solvents, are *anti*, thus the tetrazole and imidazole moieties adopt the opposite orientation with respect to the A phenyl ring plane (Fig. 2b and 2c). In order to understand which conformation (*syn* or *anti*) possesses a lower energy a relaxed PES (Potential Energy Surface) scan was performed around the τ_8 dihedral using both force field and *ab initio* methods (Fig. 4-6 and 4-7). Both techniques showed that for olmesartan in methanol the *syn* conformation is more stable (by 0.3 kcal/mol) while for olmesartan methyl ether the *anti* conformation is more stable (0.18 kcal/mol).

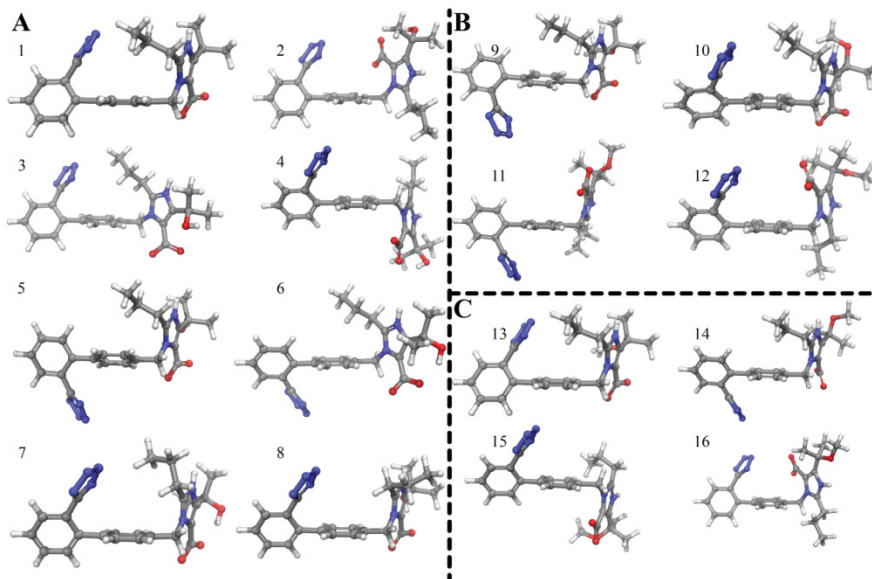


Figure 4-2. Representative low energy conformations of (a) olmesartan in methanol and olmesartan methyl ether in: (b) methanol and (c) acetonitrile as derived from MacroModel 303

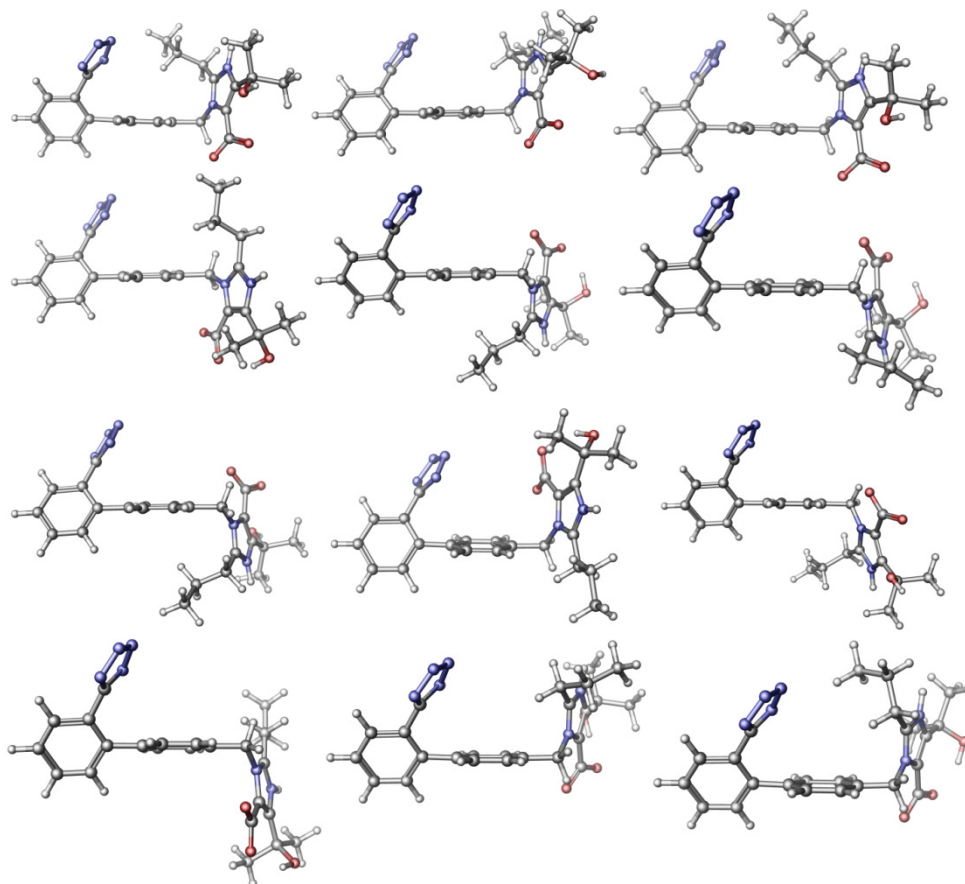


Figure 4-3. Representative low energy conformers of olmesartan in methanol without using constraints.

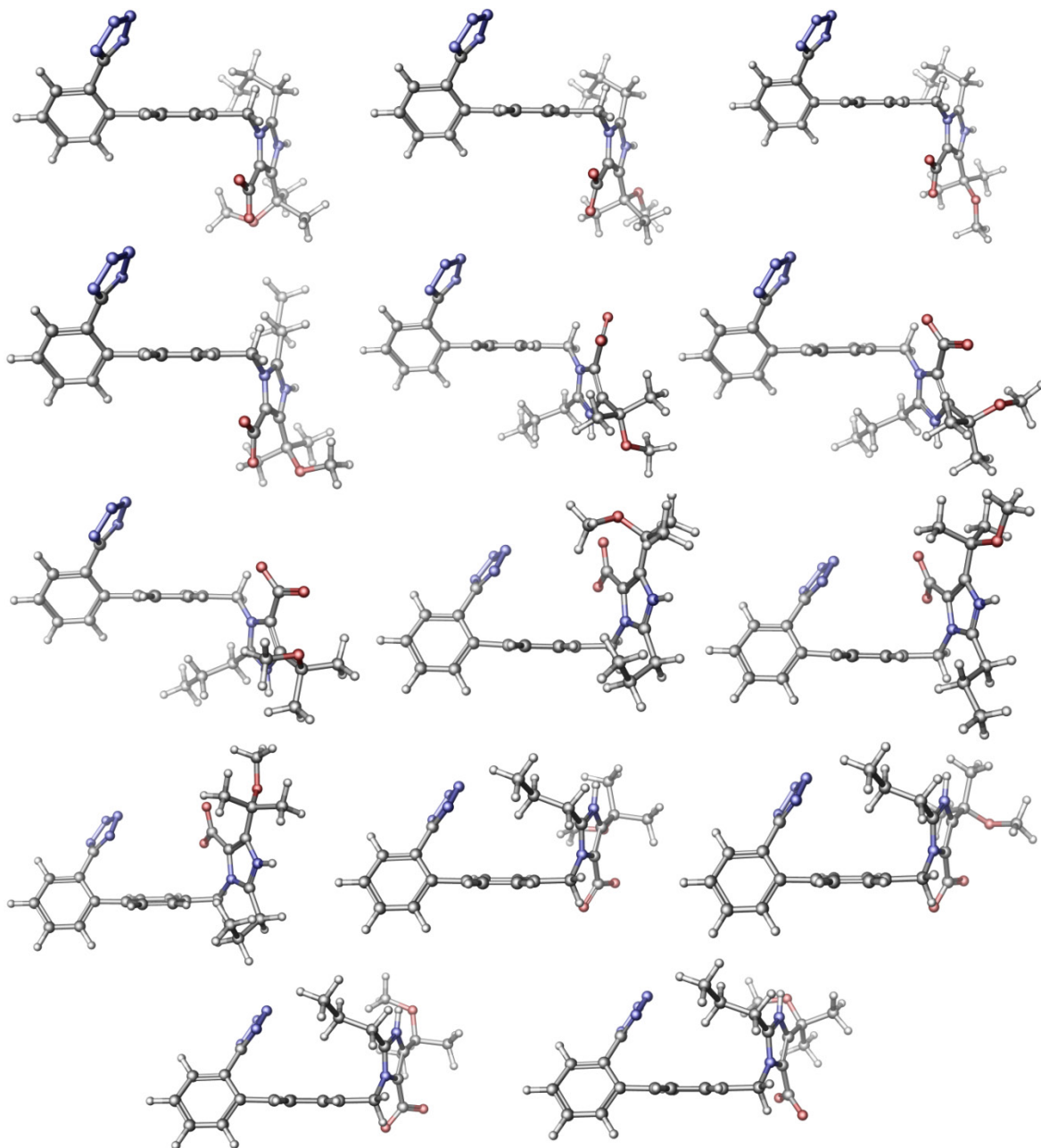


Figure 4-4. Representative low energy conformers of olmesartan methyl ether in methanol without the use of constraints.

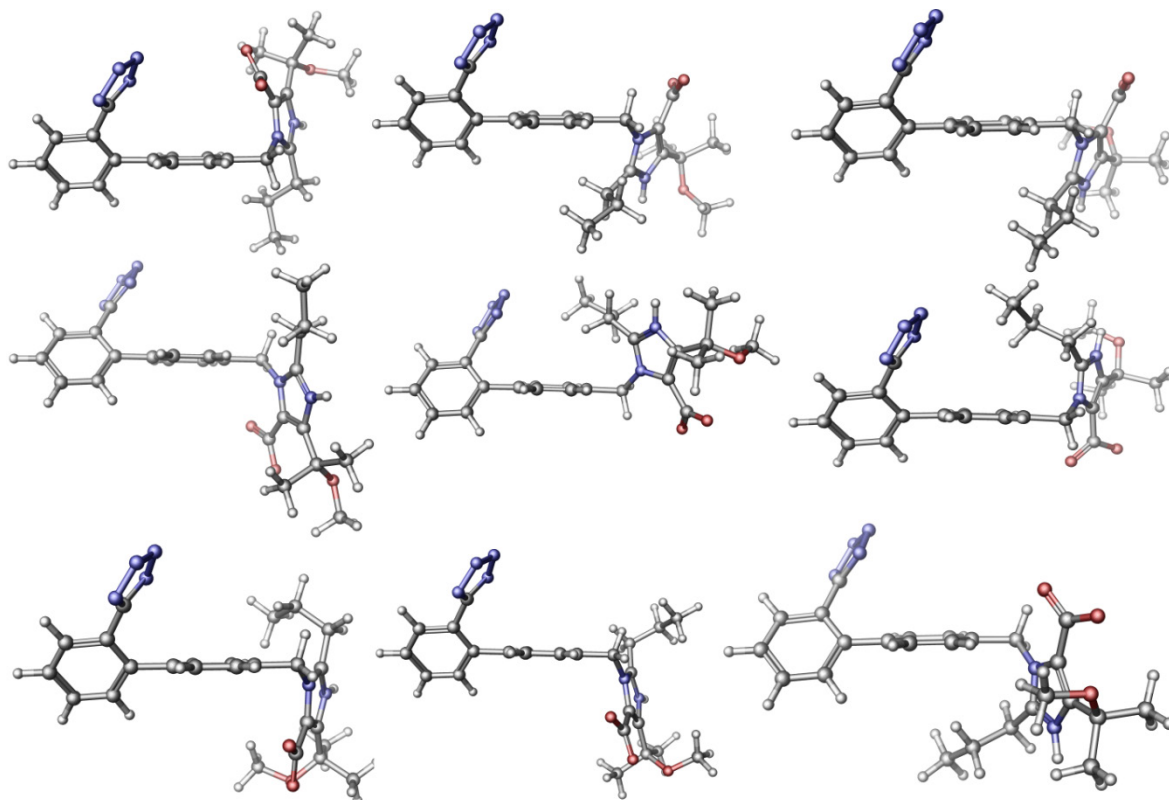


Figure 4-5. Representative low energy conformers of olmesartan methyl ether in acetonitrile.

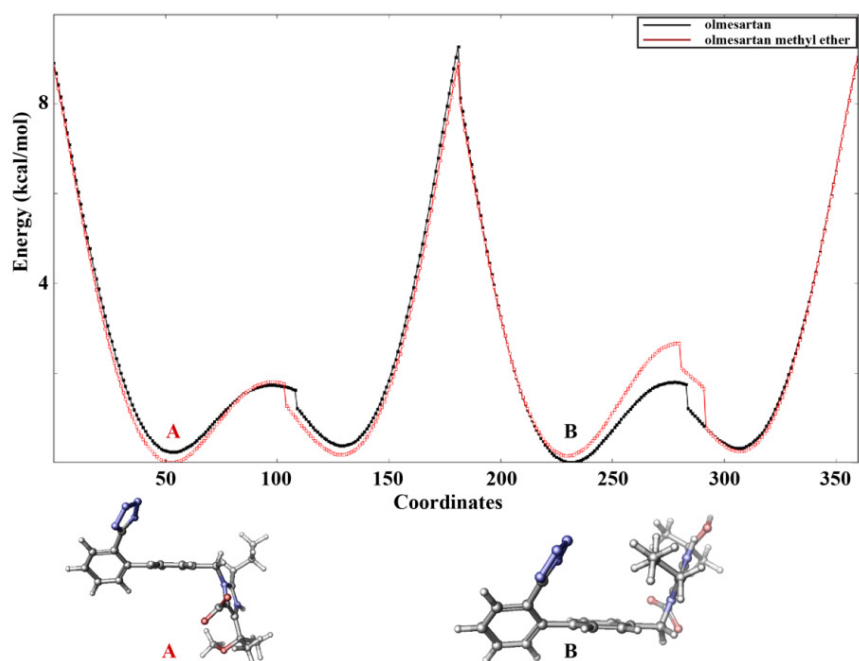


Figure 4-6. Coordinate scan for the dihedral τ_8 using molecular mechanics and the OPLS3 force field

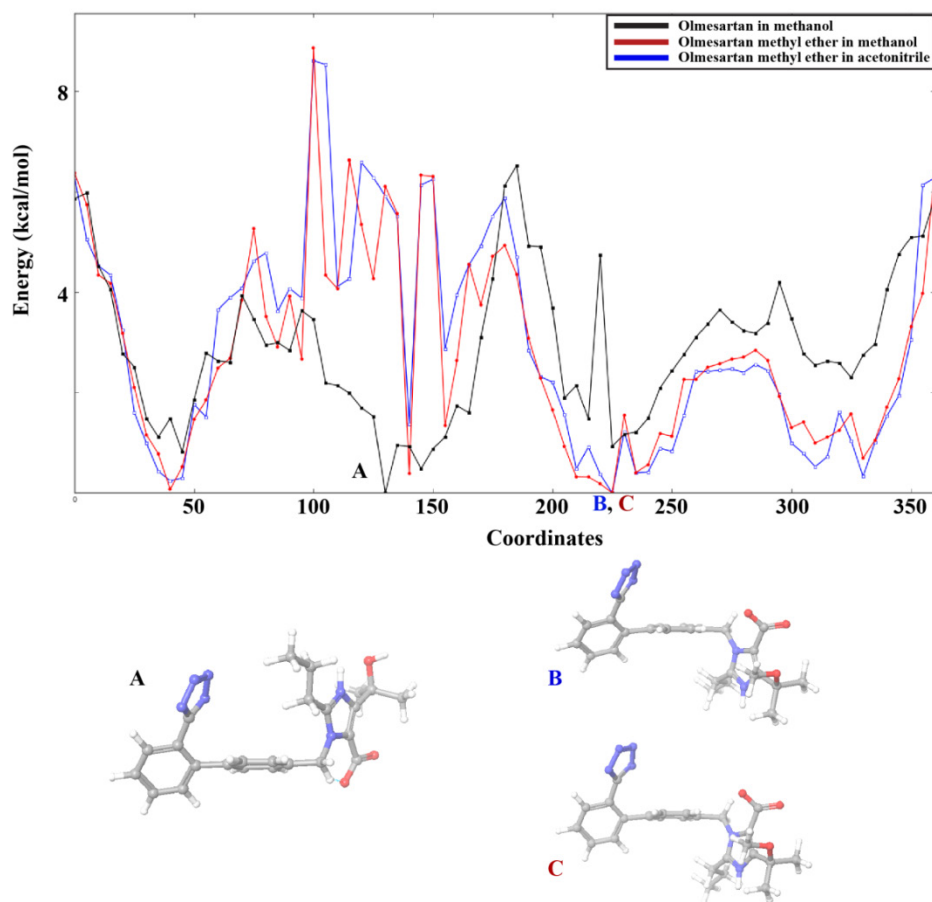


Figure 4-7. Potential energy surface scan of the dihedral τ_8 using DFT level of theory and the B3LYP/6-31G** hybrid functional

The optimized low energy structure of olmesartan using NOE constraints is compared with the crystal structure of olmesartan crystallized from ethanol by Yanagisawa *et al.*⁶² (CSD reference code: ZOGSOD). The RMSD between the crystal structure and the lowest energy conformer in olmesartan was found to be 0.2 Å (Fig. 4-8a and b). Another low energy structure was found for olmesartan which is the conformational enantiomer of the lowest energy conformer. The optimized lowest energy structure of olmesartan methyl ether in methanol as shown in Fig. 4-8c adopts an *anti* conformation as opposed to that of olmesartan that adopts a *syn* conformation in the same solvent. Olmesartan methyl ether in acetonitrile adopts a *syn* conformation (Fig. 4-8d). These results indicate that the *syn-anti* interconversion in the two solvents is achieved without a significant energy cost.

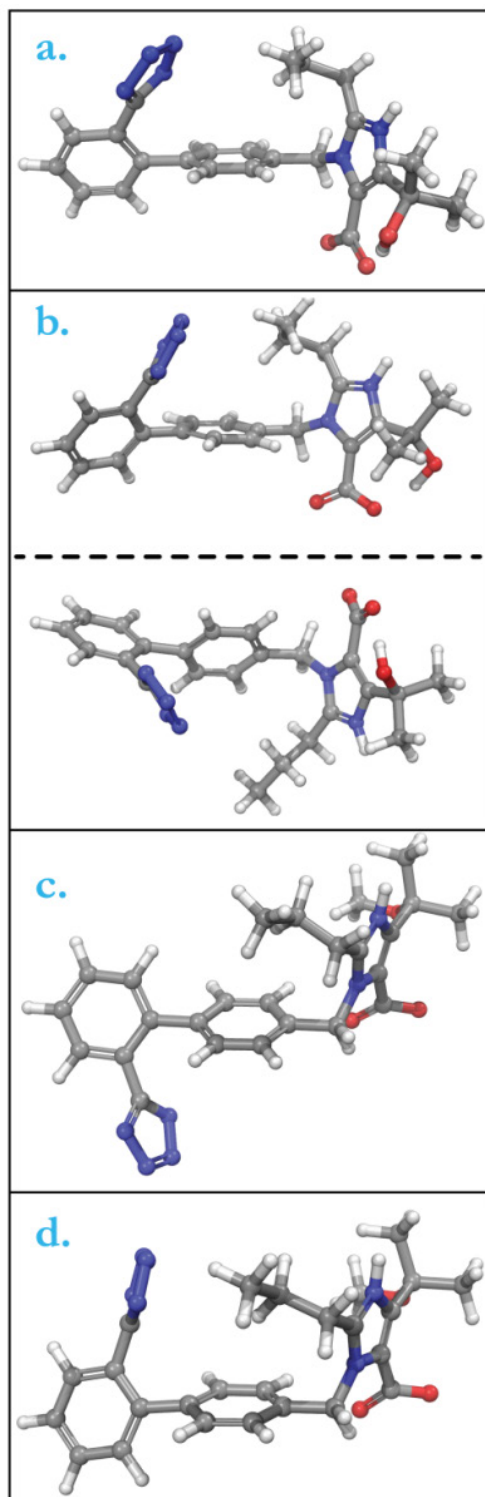


Figure 4-8. a) Crystal structure of olmesartan (CSD reference code: ZOGSOD); b) Low energy conformers of olmesartan in methanol optimized using the HF/6.31G** basis set; c) Optimized lowest energy conformer of olmesartan methyl ether in methanol; d) Optimized lowest energy conformer of olmesartan methyl ether in acetonitrile³⁰³.

4.2 Induced Fit Docking calculations

Olmesartan docked in the crystal structure 4YAY: As it can be predicted, most interactions of olmesartan are developed with Arg167. Both the tetrazole and the carboxyl moiety of the molecule develop hydrogen bonds with Arg167. Furthermore, π -cation interactions are developed between Arg167 and the A phenyl group of olmesartan. The hydroxyl group and the imidazole group of olmesartan develop hydrogen bonds with Tyr35 (Fig. 4-9a left). The imidazole group is also implicated in π - π interactions with Trp84. Polar interactions are also observed between the tetrazole group and Ser105, Ser109 and Lys199. The alkyl group develops hydrophobic interactions with Ile288, Phe77 and Tyr292. The RMSD between the docked structure of olmesartan in the crystal structure 4YAY and the crystallized structure of olmesartan in the AT₁R receptor (PDB ID 4ZUD) was found to be 0.3 Å. This pinpoints that the crystal structure 4YAY produces reliable poses and that the selected virtual workflow is suitable. As can be observed in Fig. 4-10a, b, c and d and Table 4-1 the mutations Y113F, K199Q, H256A and Q257A do not modify the binding mode of olmesartan at the AT₁R receptor. Olmesartan in all these cases adopts an *anti* configuration. Occasionally, the tetrazole moiety develops hydrogen bonds with Ser105 (Y113F, K199Q and Q257A). Also the hydroxyl group occasionally develops hydrogen bonds with Thr88 (Y113F, H256A).

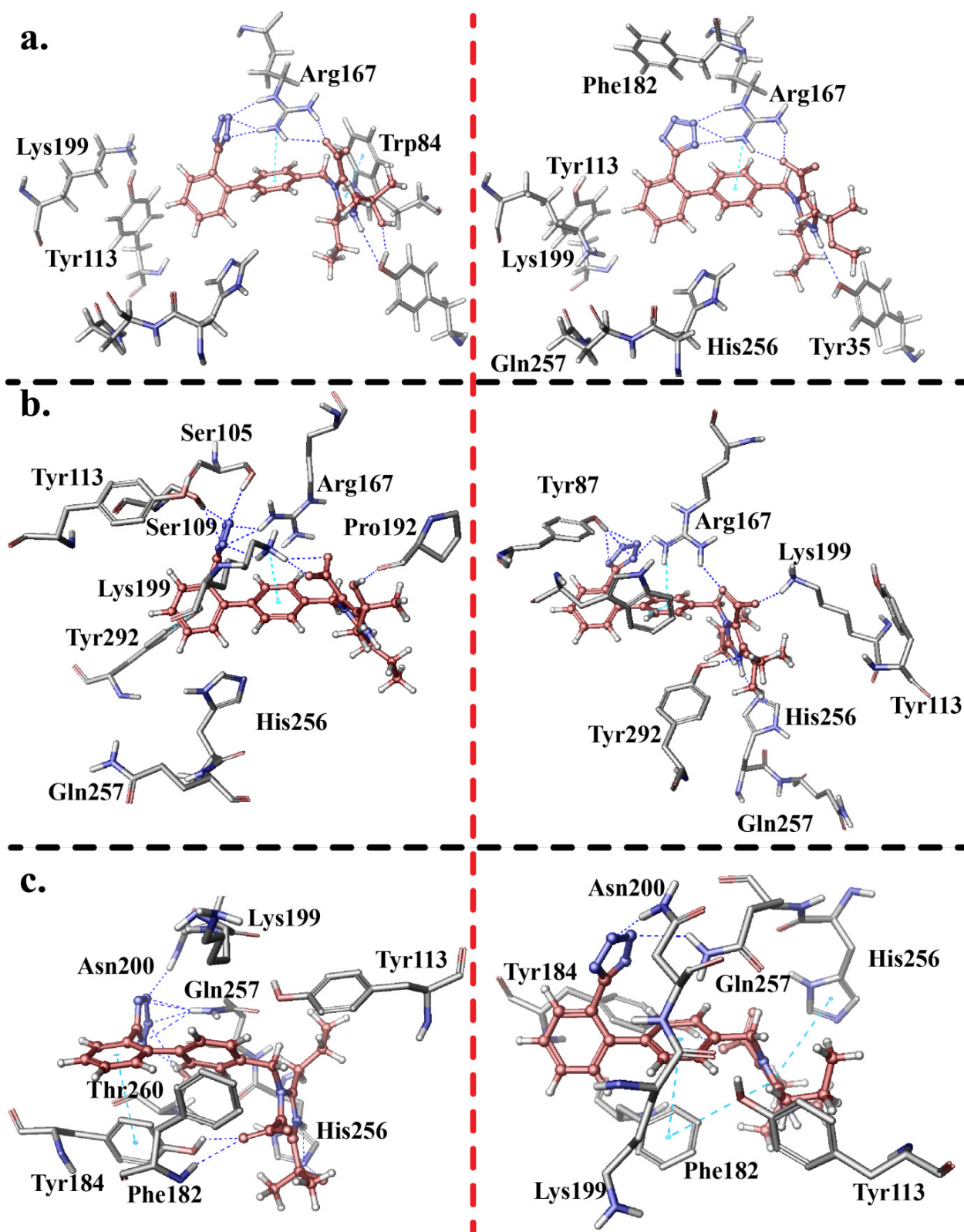
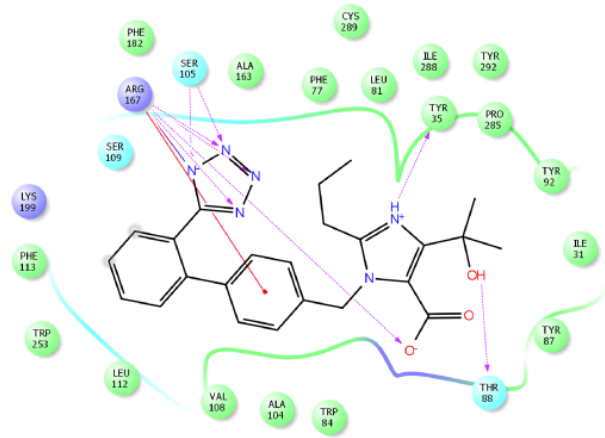
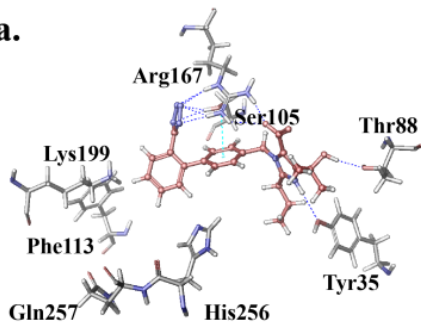
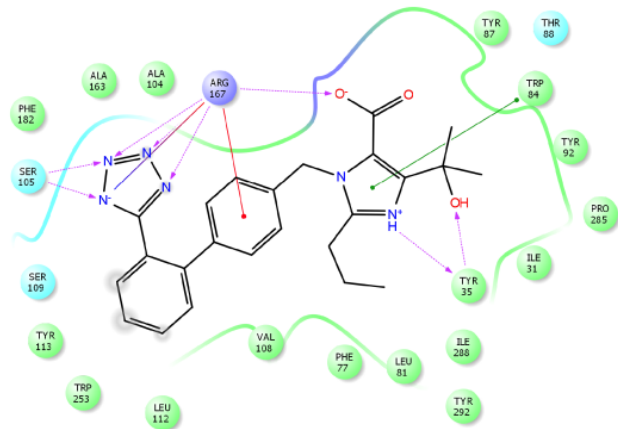
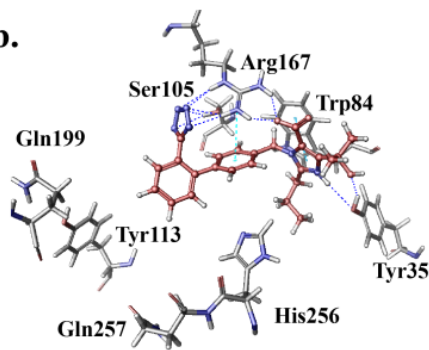


Figure 4-9. Most energetically favorable poses of olmesartan (left) and olmesartan methyl ether (right) in the AT₁R after applying induced fit docking in the a) crystal structure (PDB ID 4YAY), b) CXCR4 homology model, c) rhodopsin homology. Blue lines represent hydrogen bonds, cyan lines represent π -cation interactions

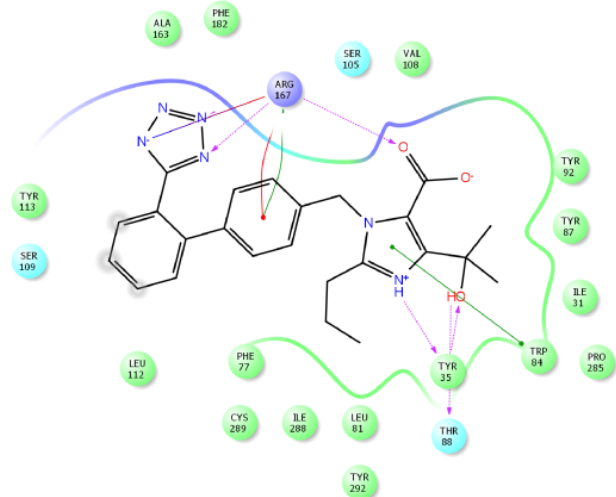
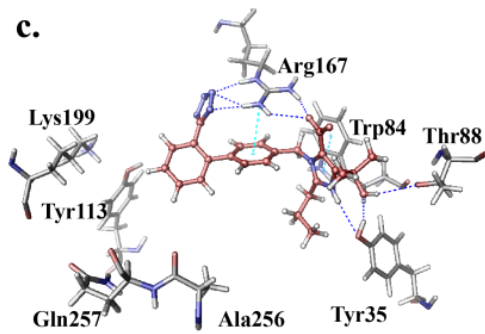
a.



b.



c.



d.

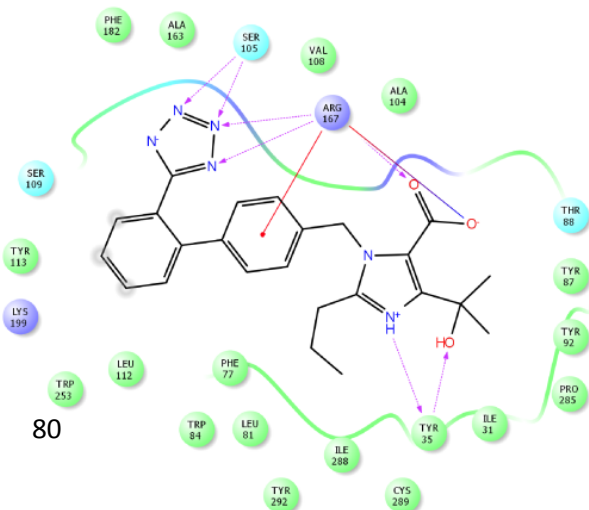
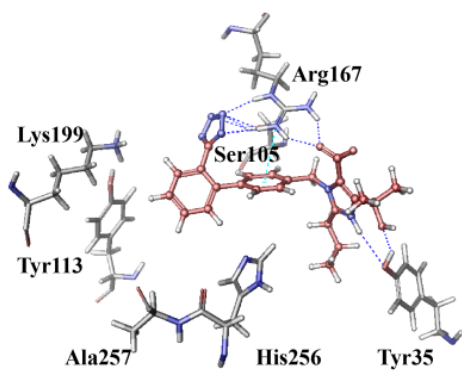


Figure 4-10. Most energetically favorable poses of olmesartan in the AT₁R crystal structure 4ZUD (in three dimensions and two dimensions) after the induced fit docking in a) mutant Y113F; b) mutant K199Q; c) mutant H256A and d) mutant Q257A.

Olmесartan in two homology models: Although the mutations reported by Miura *et al.*⁶⁵ cause significant effects on the biological activity of olmesartan and were explained based on the bovine rhodopsin crystal structure, they do not result in important differences in the Induced Fit Docking scores. In their reported findings, olmesartan was manually docked in the model and then the system was minimized using the CHARMM force field. The tetrazole moiety was suggested to interact with Gln257, the carboxyl group to interact with Lys199 and the hydroxyl group to interact with Tyr113⁶⁵. Miura *et al.* in a more recent model based on the CXCR4 structure (PDB ID 3OE0)⁶⁴ found that both His256 and Gln257 develop hydrogen bonds with the tetrazole moiety, Lys199 develops hydrogen bonds with both the tetrazole and carboxyl groups and Tyr113 develops a hydrogen bond with the hydroxyl group. In order to evaluate if AT₁R homology models based on rhodopsin and CXCR4 explain in a more optimized way the impact of these mutations, IFD calculations were performed in two reliable models already published^{60, 256}.

(a) Olmesartan in the CXCR4 homology model: The most remarkable feature observed is the fact that the predicted binding pose of olmesartan in the homology model is very similar to the one that olmesartan adopts in the crystal structure. Olmesartan adopts the *anti* configuration. The tetrazole moiety develops hydrogen bonds with Arg167, Ser105, Ser109 and Lys199 and π - π interactions with Phe182. One of the differences with the crystal model is the crucial role that Lys199 plays in this model. Lys199 develops hydrogen bonding with the carboxyl group and cation- π interactions with the A phenyl group. Hydrogen bonds are also observed between the hydroxyl group of olmesartan and Pro192 and the imidazole group and Asp263 (Fig. 4-9b left). The mutations here also do not cause modification in the binding pose of olmesartan in the homology model (Fig. 4-11a, b, c, d). Even the mutation K199Q, that was expected to have a great impact on the binding mode due to the importance of Lys199 in this model, does not affect drastically the binding mode. A hydrogen bond is developed between Gln199 and the tetrazole moiety. The application of unconstrained IFD calculations did not reveal the pose reported by Miura *et al.*⁶⁴. Since in this model, Arg167 has been located in the ligand binding site olmesartan consistently forms hydrogen bonds with it.

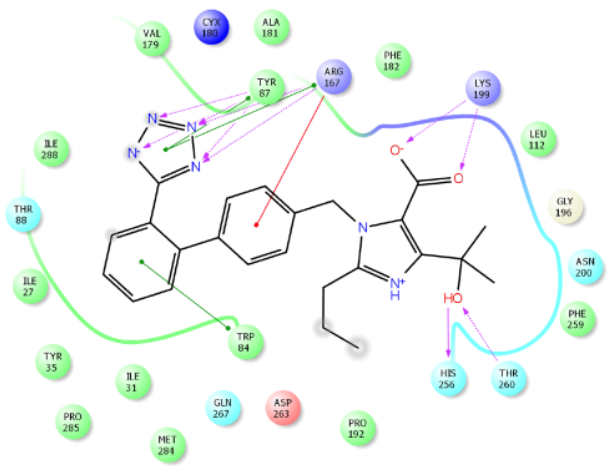
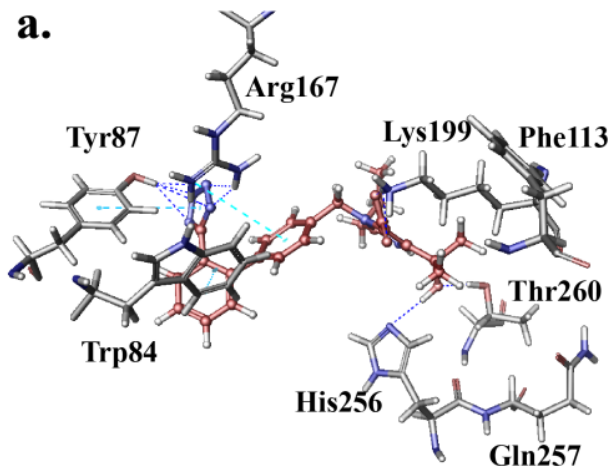
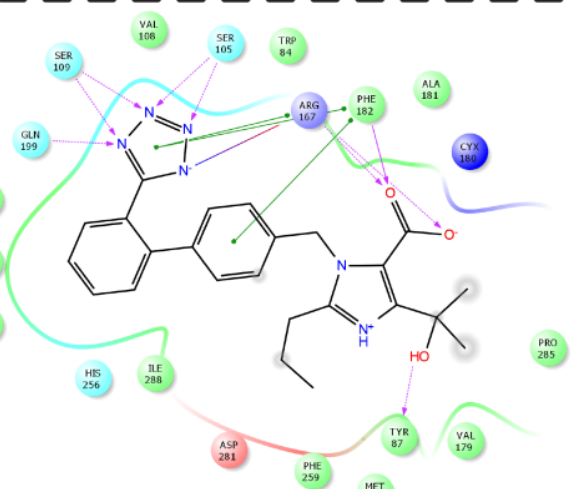
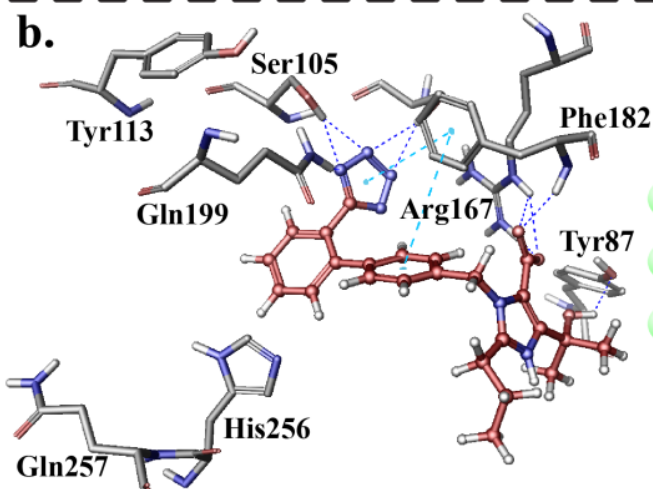
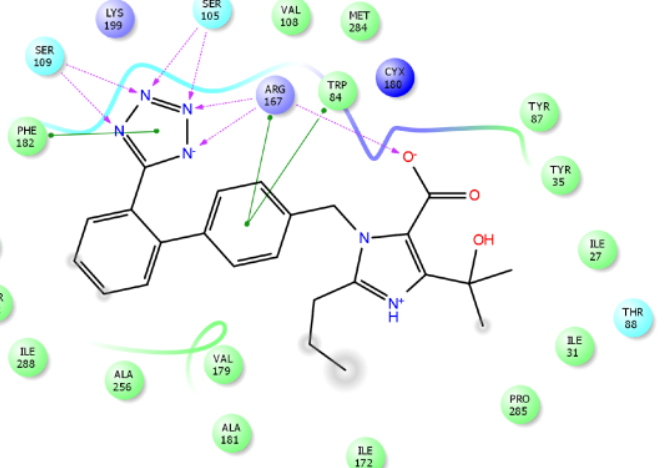
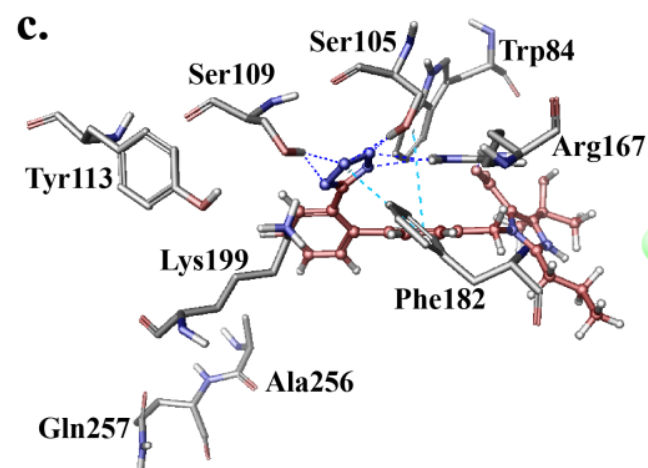
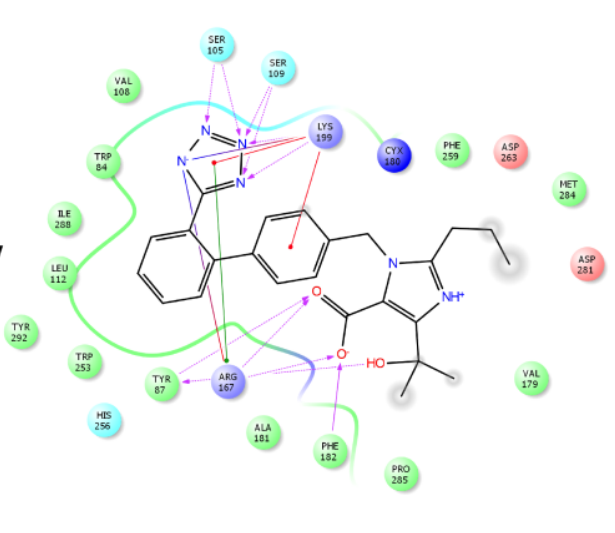
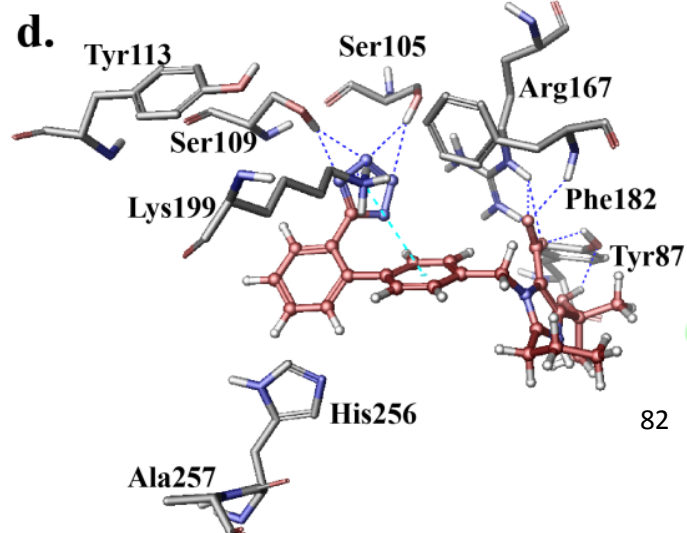
a.**b.****c.****d.**

Figure 4-11. Most energetically favorable poses of olmesartan (in three dimensions and two dimensions) after the induced fit docking in implicit membrane in the AT₁R homology model based on CXCR4: a) mutant Y113F; b) mutant K199Q; c) mutant H256A; and d) mutant Q257A.

(b) Olmesartan in the rhodopsin homology model: In this homology model the residues Gln257, His256, Phe182, Tyr184, Thr260 and Asn200 play a crucial role while the residues Lys199 and Tyr113 are in the vicinity of the binding site. More specifically, the tetrazole moiety develops hydrogen bonds with the residues Gln257, Thr260 and Asn200. The carboxyl group develops hydrogen bonds with Tyr184 and Phe182. The imidazole and hydroxyl groups develop hydrogen bonds with His256 (Fig. 4-9c left). The mutations Y113F and K199Q do not modify the binding mode of olmesartan or the Induced Fit Scores (Fig. 4-12a, b). The mutation H256A seems to cause some changes in the interactions developed by olmesartan. The hydrogen bond between Gln257 and Ser109 is interrupted. The two hydrogen bonds developed by His256 (Fig. 4-9c) are substituted by one hydrogen bond with Ala256 (Fig. 4-12c). Changes are also observed with the mutation Q257A. The tetrazole moiety develops hydrogen bonds only with Asn200. In addition the carboxyl group of olmesartan develops hydrogen bonds with Phe182, Tyr184, Ser109 and Tyr113. Although the interactions seem to change for olmesartan in these two mutations, the binding conformation is always the *anti*-.

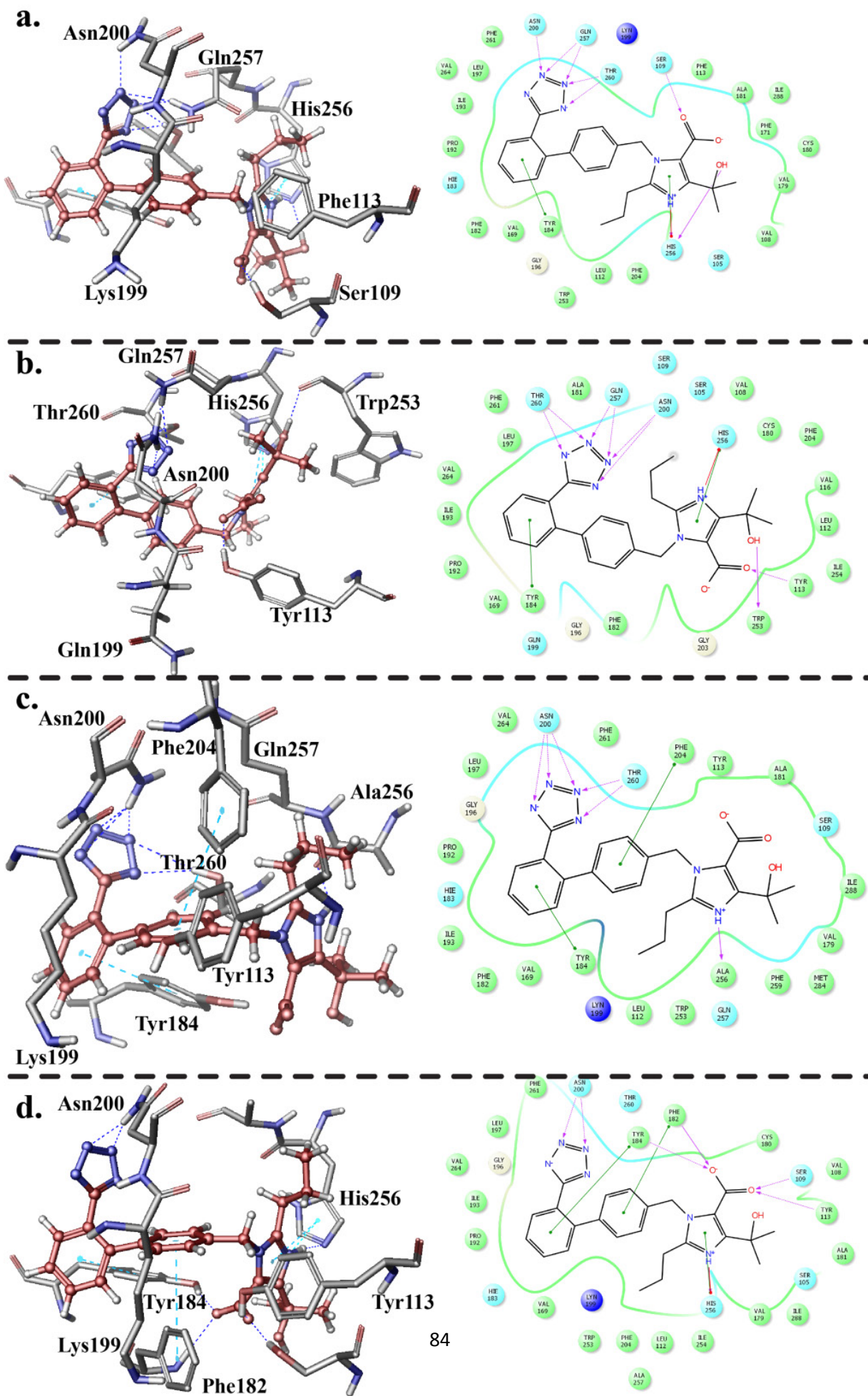


Figure 4-12. Most energetically favorable poses of olmesartan (in three dimensions and two dimensions) after the induced fit docking in the AT₁R homology model based on rhodopsin: a) mutant Y113F; b) mutant K199Q; c) mutant H256A and d) mutant Q257A.

Olmesartan methyl ether in the crystal structure and the two homology models.

Olmesartan's methyl ether adopts a very similar conformation to that of olmesartan inside the crystal structure. The *anti* conformation is favored. Both the tetrazole and carboxyl moieties of the molecule form hydrogen bonds with Arg167. π - π interactions are developed between tetrazole and the residue Phe182 and between the imidazole group and Trp84. The imidazole group also forms a hydrogen bond with Tyr35 (Fig. 4-9a right). The methyl ether moiety of olmesartan develops hydrophobic contacts with the residues Pro285, Tyr35, Ile31 and Ile288 (Table 4-2).

The homology model based on CXCR4 predicts the *anti* conformation of olmesartan methyl ether. The residue Arg167 forms hydrogen bonds with both the tetrazole and the carboxyl groups. The tetrazole moiety develops multiple hydrogen bonds with Tyr87. The carboxyl group develops a hydrogen bond with Lys199. The imidazole group forms a hydrogen bond with His256 and the oxygen of the methyl ether group develops a hydrogen bond with Tyr292 (Fig. 4-9b right).

The homology model based on the rhodopsin structure predicts the formation of hydrogen bonds between tetrazole and Asn200 and Gln257 (Fig. 4-9c right). The carboxyl group is predicted to develop hydrogen bond with Tyr184. The imidazole moiety forms π - π interactions with His256 and Phe182.

Table 4-1: Interactions of olmesartan with the residues of AT₁R in the crystal structures and the two homology models

Interactions	Hydrophobic	H-bonds	π - π / π -cation interactions
Rhodopsin model	Phe261, Tyr184, Phe182, Tyr113, Ala181, Phe171, Val108, Val179, Cys180, Ile288, Ile254, Leu112, Phe204, Val116, Pro192, Val169, Ile193, Leu197, Val264	Gln257x4, Thr260, Asn200, Tyr184, Phe182, His256x3	Tyr184
CXCR4	Pro192, Trp84, Ile193, Leu195,	Lys199x3, Ser109x2,	Lys199,

model	Val280, Phe259, Met284, Val108, Tyr292, Trp253, Ile288, Leu112	Ser105x2, Arg167, Asp263	Phe182, Tyr292
Crystal structure	Phe182, Ala163, Val108, Ala104, Tyr35, Pro285, Tyr92, Ile31, Tyr87, Trp84, Ile288, Phe77, Tyr292, Leu81, Leu112, Trp253	Arg167x3, Tyr35x2	Arg167, Trp84

Table 4-2: Interactions of olmesartan methyl ether with the residues of AT₁R in the crystal structure and the two homology models.

Interactions	Hydrophobic	H-bonds	π - π / π -cation
Rhodopsin model	Phe261, Tyr184, Phe182, Ala181, Val108, Tyr292, Phe171, Ile288, Cys180, Val179, Phe204, Val116, Trp253, Tyr113, Leu112, Val169, Pro192, Ile193, Val264	Asn200, Gln257, Tyr184	Phe182x2, His256
CXCR4 model	Ala181, Val179, Tyr87, Trp84, Phe182, Tyr292, Val108, Leu112, Trp253, Ile288, Phe259, Met284, Phe259, Ile31, Pro285, Tyr35, Ile27, Thr88	Tyr87x4, Arg167x2, Lys199, Tyr292, His256	Trp84
Crystal structure	Val108, Trp84, Tyr92, Tyr87, Ile31, Pro285, Tyr35, Tyr292, Ile288, Leu81, Cys289, Phe77, Trp253, Leu112, Tyr113, Phe182, Ala163	Arg167x3, Tyr35	Trp84, Phe182

4.3 Molecular Dynamics Simulations

MD simulations have been performed as it is well established that calculations are affected by the environment surrounding the studied system. The following reasons favoured the use of DPPC bilayers exclusively in this computational study: (a) DPPC's partition coefficient with respect to its aqueous environment, especially in the fluid state, resembles that of natural plasma membranes of the vasculature^{304, 305}; (b) Phosphatidylcholines (PCs) are the most abundant lipid species in the plasma membranes of the vascular smooth muscle cells³⁰⁴ and sarcolemma cardiac membranes³⁰⁵. The RMSDs for the C α of the receptor (in blue) and for the ligand (in red) are shown for: (i) olmesartan in the crystal

structure (Fig. 4-13a), (ii) the four mutations (Fig. 4-13b-e) and (iii) olmesartan methyl ether in the crystal structure (Fig. 4-13f). As can be seen after 100 ns the protein's structure has been stabilized.

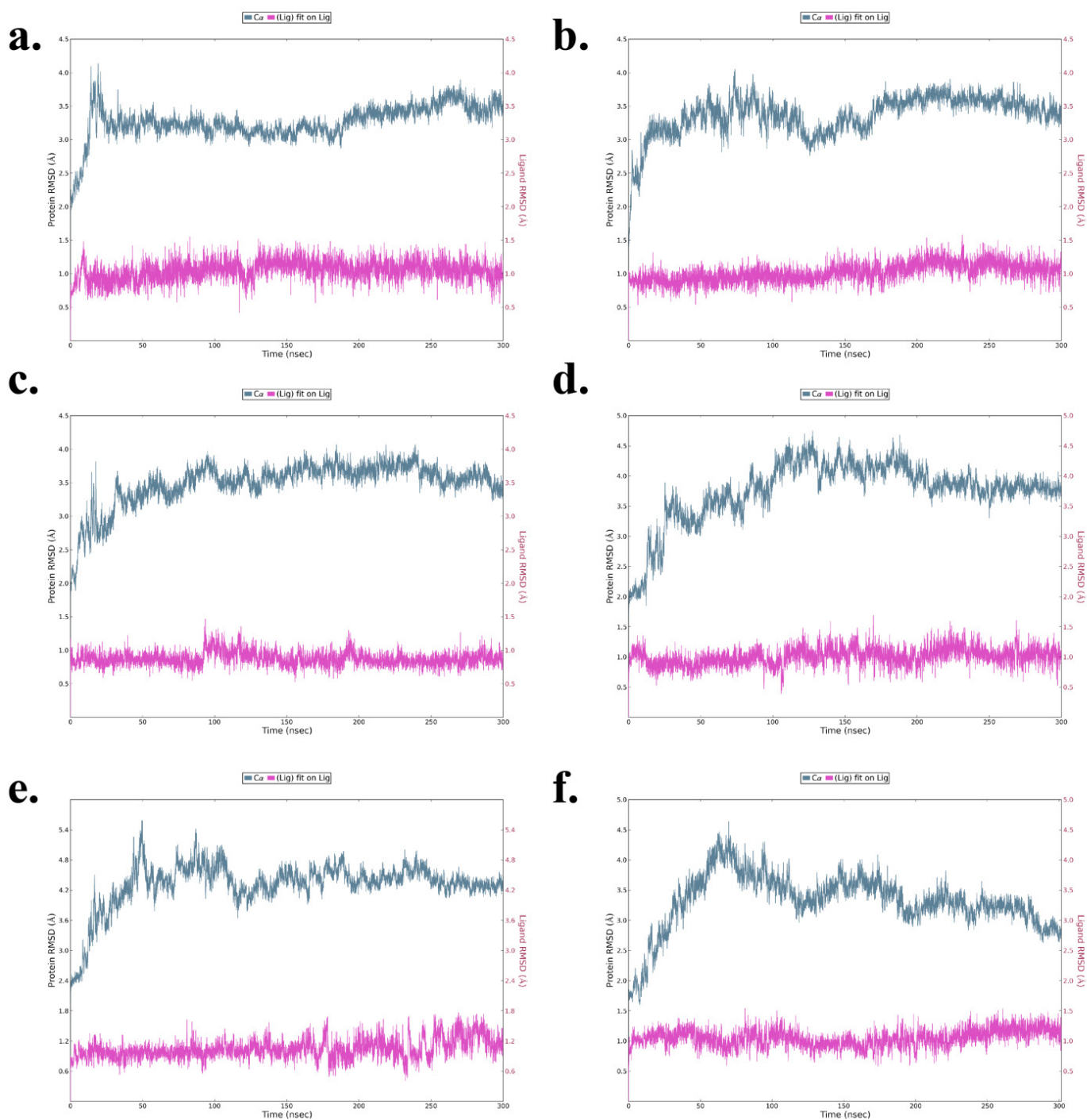
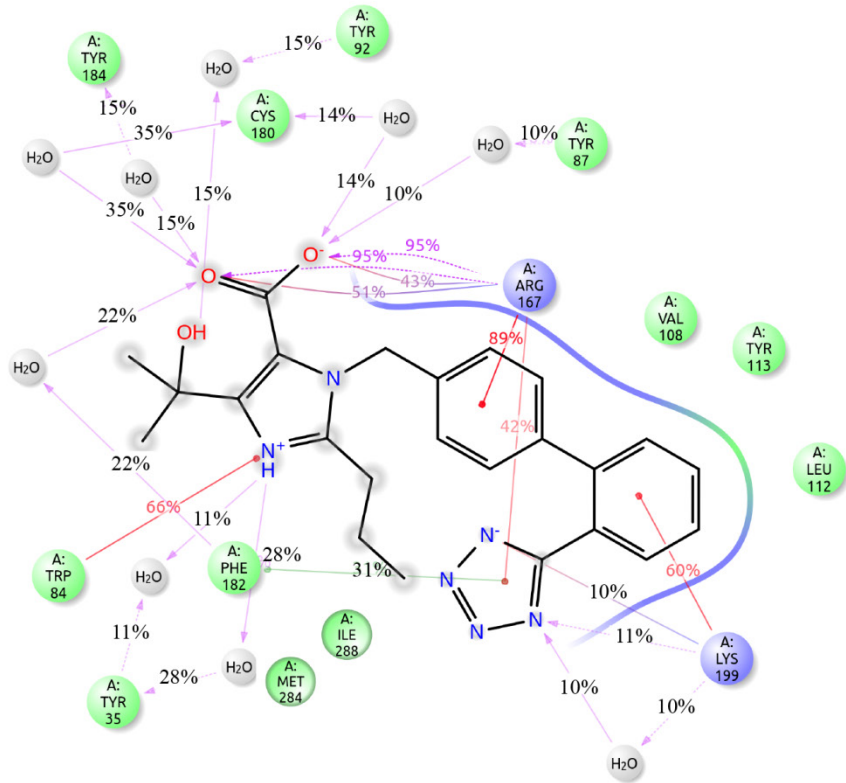


Figure 4-13: Protein and ligand RMSD during the time of simulation for: (a) olmesartan in the crystal structure with PDB ID 4ZUD; (b) olmesartan in the Y113F mutant; (c)

olmesartan in the K199Q mutant; (d) olmesartan in the H256A mutant; (e) olmesartan in the Q257A mutant and (f) olmesartan methyl ether.

Olmesartan's interactions in the crystal structure 4ZUD: As can be observed in Fig. 4-14a olmesartan develops hydrogen bonds with Arg167 during the trajectory time of the simulation. Hydrogen bonds between Arg167 side chain and the carboxyl group of olmesartan occur 95% of the simulation time, while those with tetrazole occur 35% of the simulation time. Interactions such as π -cation occur for 89% of the time with the second phenyl group and 42% of the time with the tetrazole group. Ionic interactions are also developed with the carboxyl group for 41% of the simulation time. The other key residue in the interaction diagram is Lys199. Hydrogen bonds are formed between Lys199 side chain and two nitrogen atoms of the tetrazole group for 11% of the simulation time. Hydrophobic interactions such as π -cation are also developed between Lys199 and the first phenyl group. Water bridges are formed by Lys199 as well as ionic interactions with the negatively charged nitrogen atom in tetrazole. Another important residue is Trp84. It develops π -cation interactions with the positively charged nitrogen atom of the imidazole aromatic ring for 66% of the simulation time. The residue Tyr35 is mainly involved in water bridges establishing connections with the imidazole ring. The residue Phe182 develops mainly π - π interactions with the tetrazole moiety of the drug as well as water bridges that connect it with the carboxyl moiety. The residues Cys180, Tyr184, Tyr92 and Tyr87 are implicated in water bridges that allow them to interact with the carboxyl group (although these contacts are only observed for 10-15% of the simulation time importantly they occur periodically). The residues Leu81, Val108, Leu112, Tyr113, Met284, Ile288 and Tyr292 develop hydrophobic interactions with olmesartan.

a.



b.

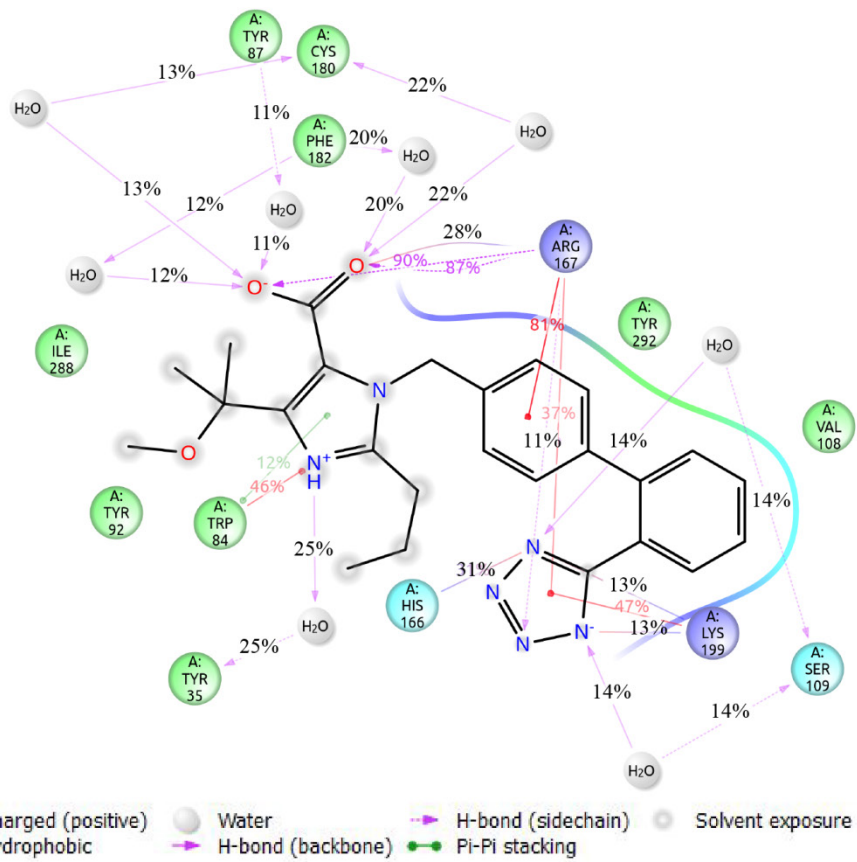


Figure 4-14: Protein-ligand interactions during the whole simulation time for: (a) olmesartan; (b) olmesartan methyl ether ³⁰³.

In order to reveal the preferred conformation of olmesartan in the receptor, the torsional angles of olmesartan were analyzed (Fig. 4-15). The dihedrals τ_6 , τ_7 , τ_8 constrain the molecule to an *anti* conformation during the whole time of simulation. This is probably due to three important interactions: (i) cation – π interaction of tetrazole with Lys199 and Arg167 that constrains the dihedral τ_8 , (ii) salt-bridge between the carboxyl group with Arg167 and (iii) π - π interactions of the imidazole group with Trp84 that forces the dihedrals τ_6 and τ_7 to adopt a narrow range of values.

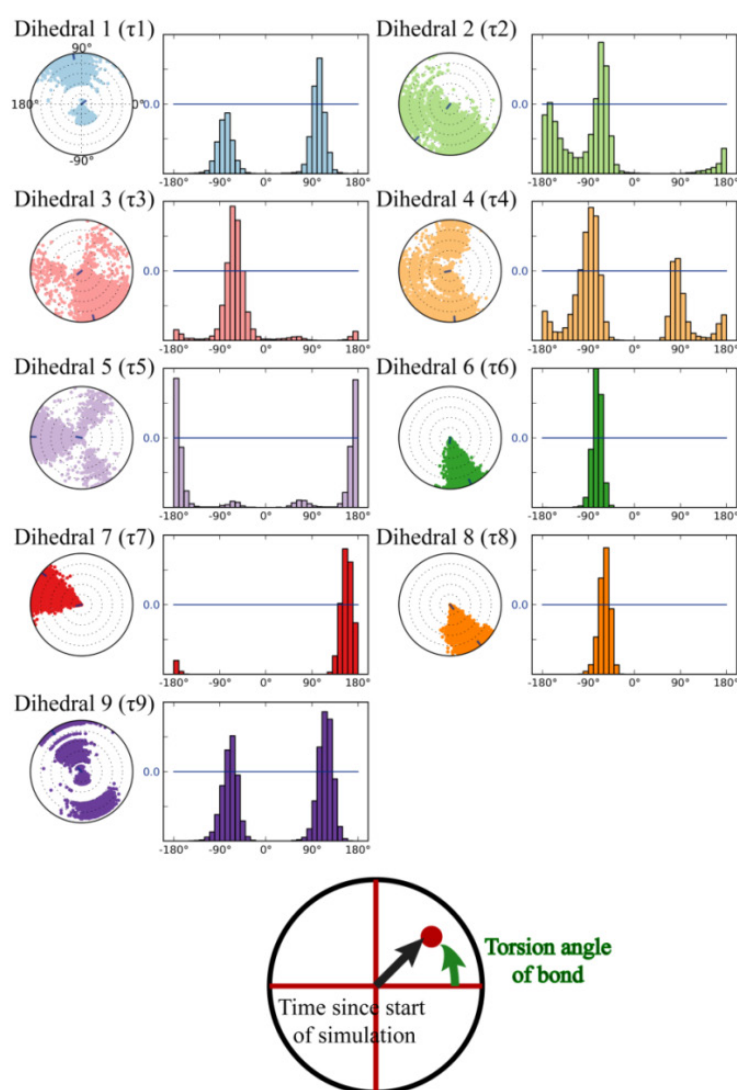


Figure 4-15. Modification of olmesartan's dihedral angles as a function of time during MD simulations in the crystal structure 4ZUD surrounded by DPPC bilayers.

The results obtained from the MD calculations have been compared with those obtained with the most important experimental NOEs (H9-H4 and H19-H12) (Fig. 4-16). The average values for the distance H9-H4 was found to be 4.07 Å and for the distance H19-H12 2.70 Å. These values are in accordance with those obtained from the NOE.

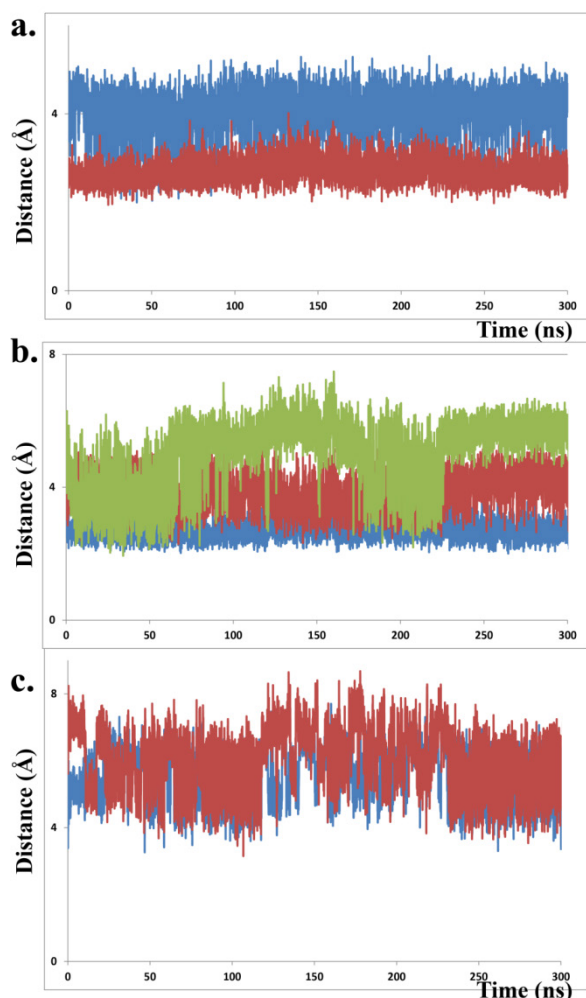


Figure 4-16. a) Distances between H9 and H4 (blue) and H19-H12 (red) for olmesartan b) Distances between H19-H12 (blue), H9-H4 (red), H9-H5 (green) in olmesartan methyl ether c) Distance between H9-H23 (blue), H10-H23 (red) in olmesartan methyl ether

Olmesartan's interactions in the mutated crystal structures Y113F, Y113A, H256A, Q257A: The protein ligand interactions of olmesartan in the receptor mutants Y113F, H256A and Q257A are shown in Fig. 4-17a, c and d, respectively. These three mutations do not seem to affect the conformation of the drug inside the active site or the developed interactions with the key residues.

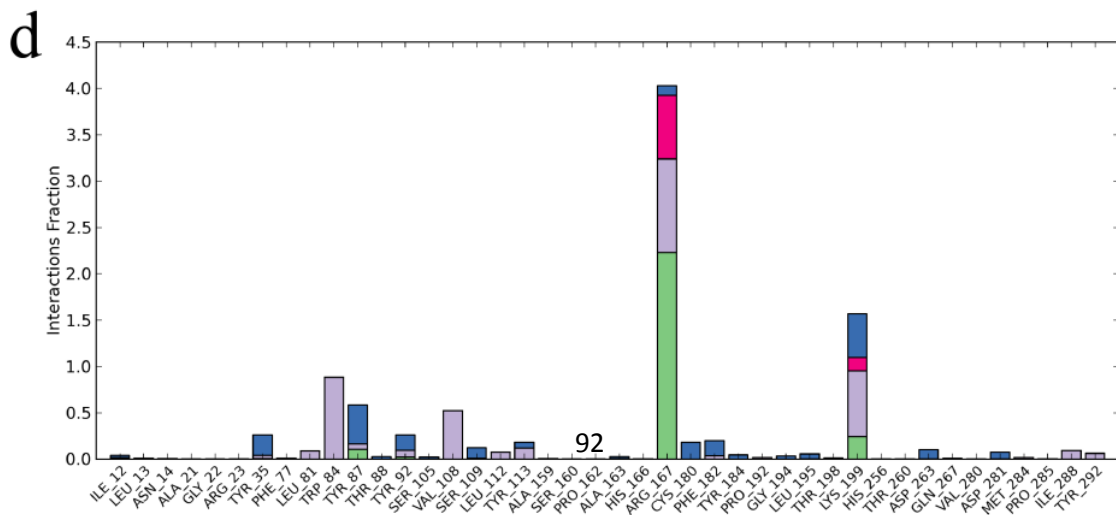
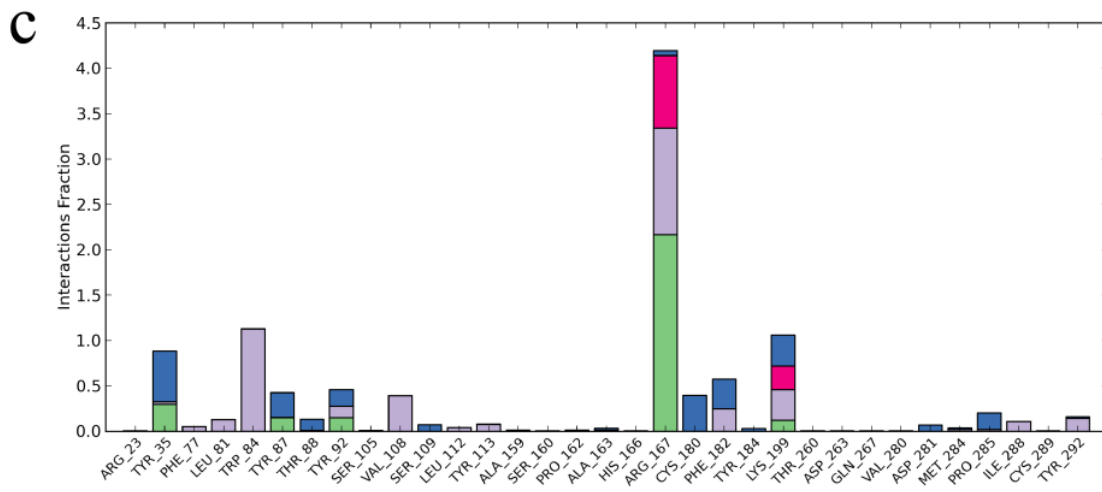
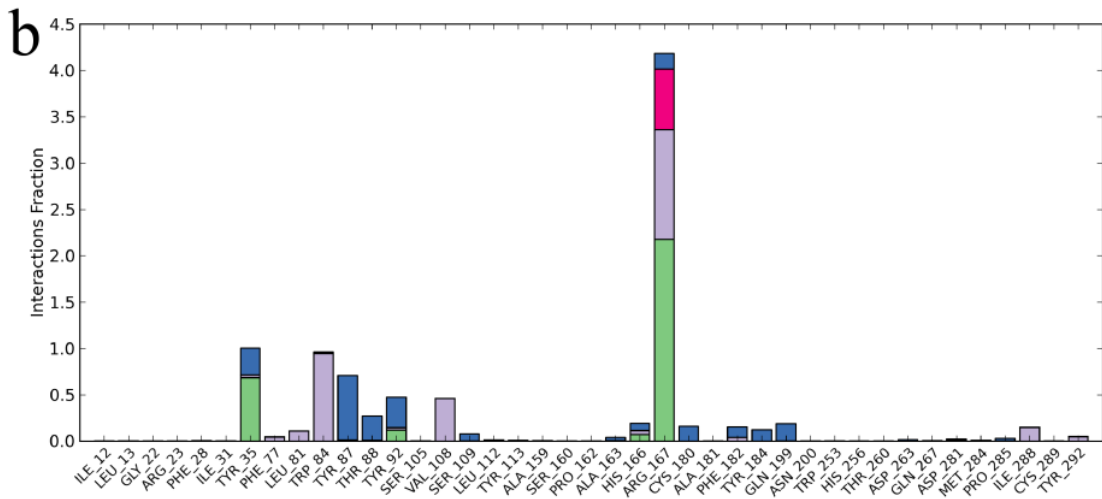
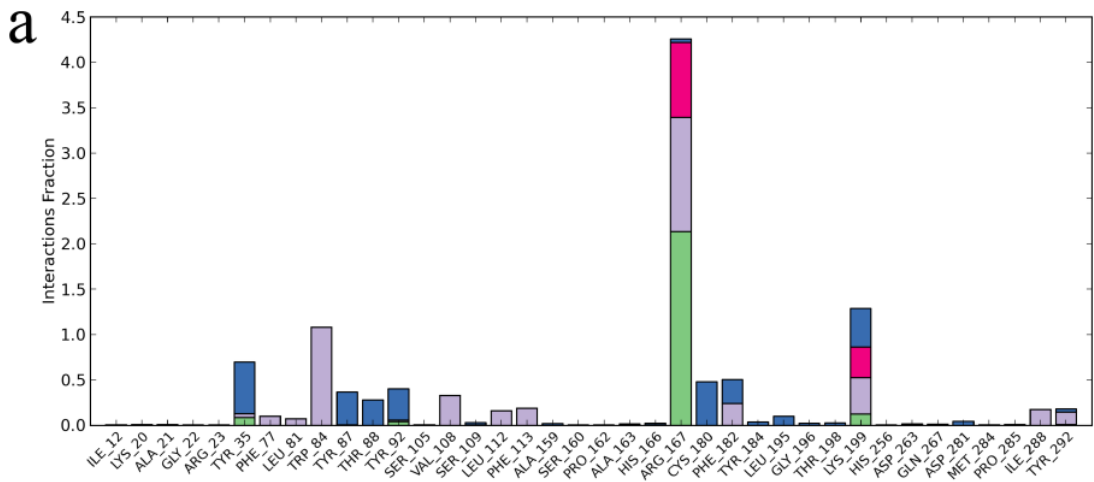


Figure 4-17. Protein-ligand interactions during the whole time of simulation for (a) olmesartan in the Y113F mutant (b) olmesartan in the K199Q mutant (c) olmesartan in the H256A mutant (d) olmesartan in the Q257A mutant.

More specifically, in these three mutations the most important interactions with residues such as Arg167, Lys199, Tyr35, Trp84, Tyr87, Thr88, Tyr92, Val108, Ile288 and Tyr292 remain intact. The same interactions were observed for the mutated structure Y113A (Figure 4-18).

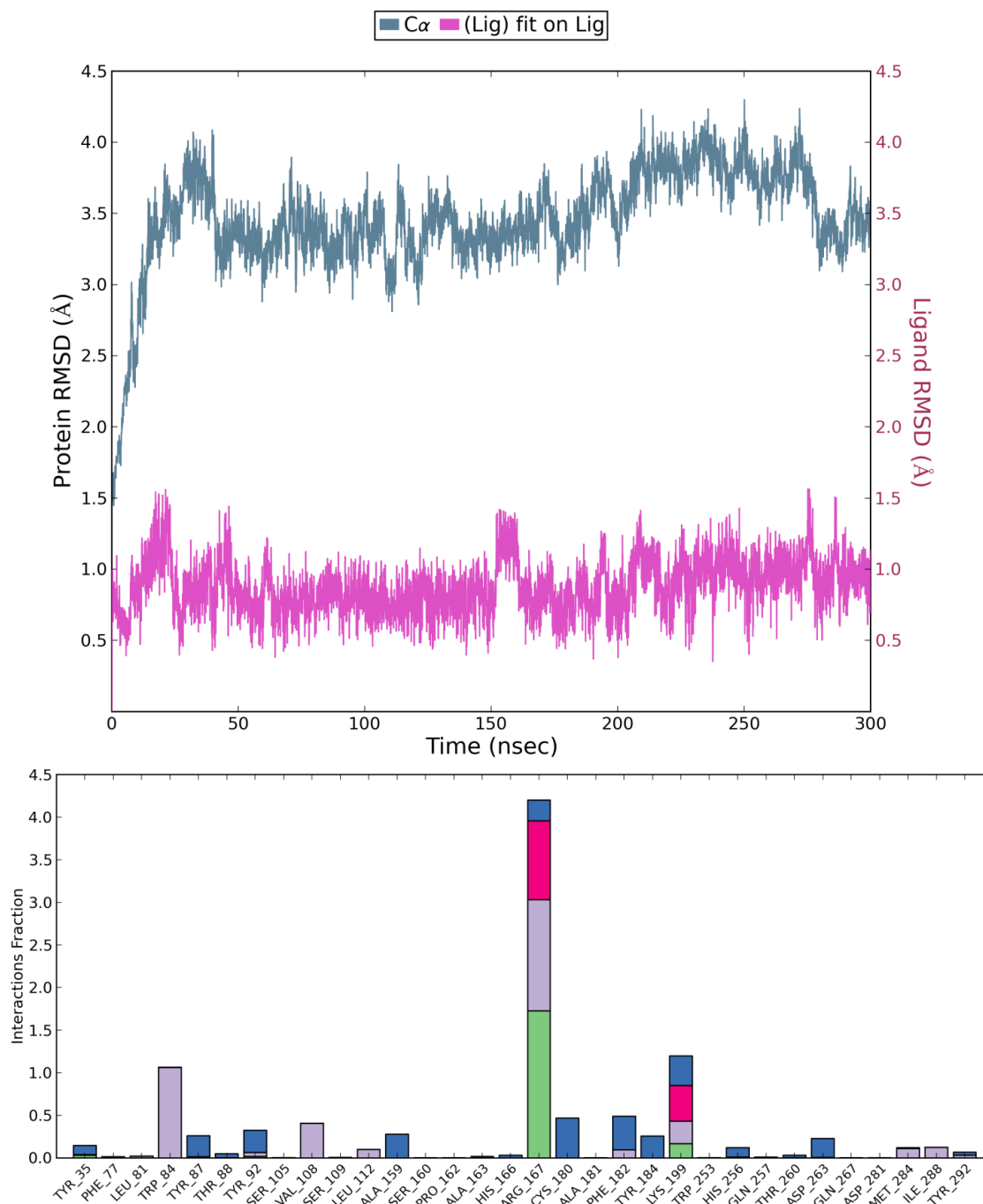


Figure 4-18. RMSD of the backbone and interactions fraction for the mutation Y113A.

For all critical dihedral angles that define olmesartan only τ_8 has been useful for further elaboration. All other dihedral angles remained constant during the trajectory in both the wild type and the mutated form. In order to show this fact, the evolution of the critical dihedral τ_8 for all the simulations is shown in Fig. 4-19b (Y113F), 4-19d (H256A), 4-19e (Q257A) and 4-19f (Y113A).

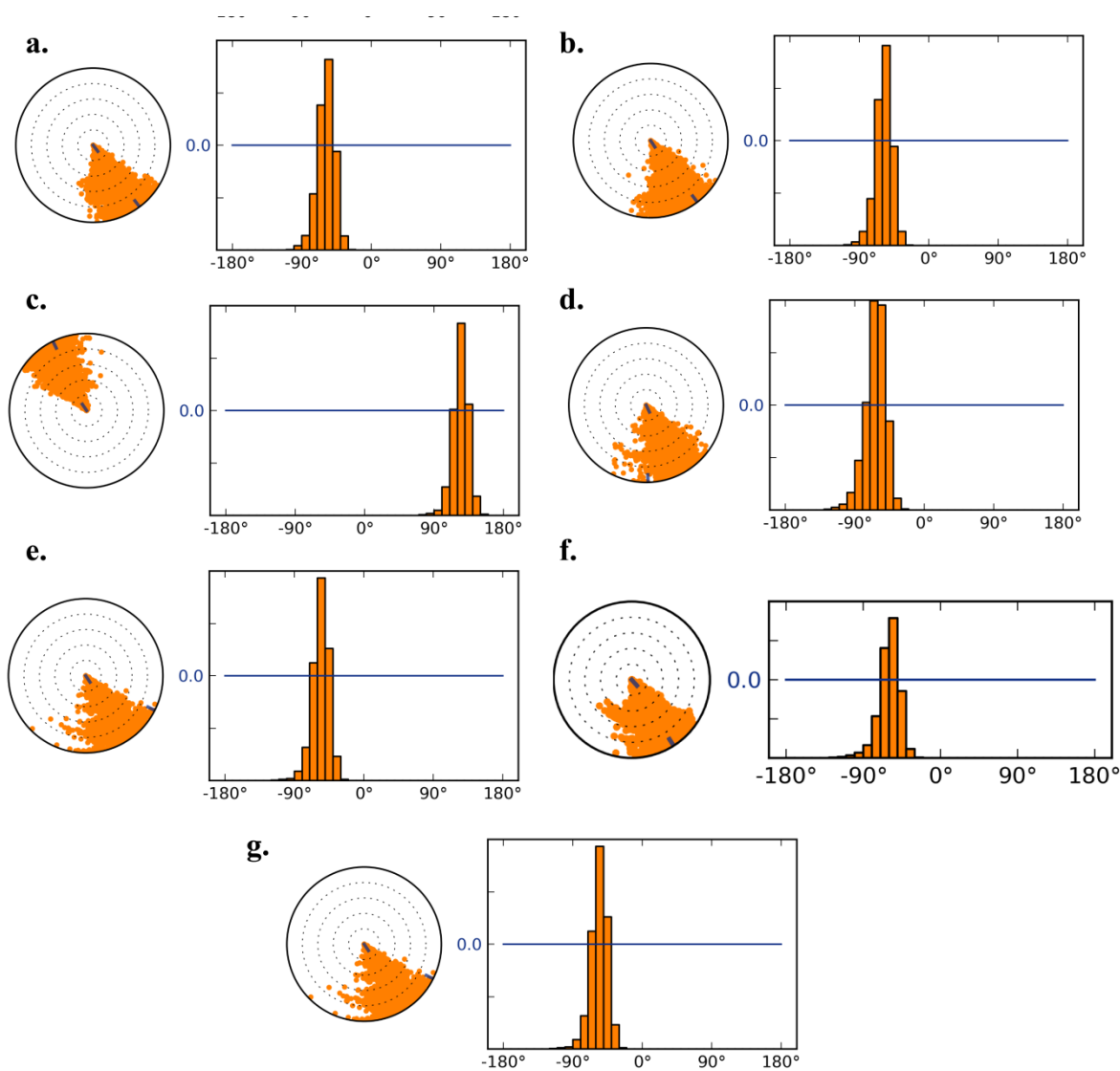


Figure 4-19. Modification of τ_8 during the trajectory for (a) olmesartan; (b) olmesartan in the Y113F mutant; (c) olmesartan in the K199Q mutant; (d) olmesartan in the H256A mutant; (e) olmesartan in the Q257A mutant; (f) olmesartan methyl ether and (g) olmesartan in the Y113A mutant.

Olmesartan's interactions in the mutated crystal structure K199Q: While in the previous cases the critical dihedrals remained the same, in the case of K199Q the values

for the torsional angle τ_8 change drastically (Fig. 4-19c). It is clear that this mutation causes the greatest effect in the ligand orientation inside the receptor. Seemingly, it stabilizes the position of the tetrazole moiety of the molecule through hydrogen bonding and π -cation interactions. Also the interactions that are lost due to the replacement of Lys with Gln are not balanced by any other residue. This shows that a change to this particular residue causes simultaneously a substantial change in the conformation of olmesartan and the loss of critical interactions that could explain the reduction of its biological activity.

Olmesartan methyl ether in the crystal structure: Olmesartan methyl ether develops the same interactions as olmesartan (Fig. 4-14b). The carboxyl group forms hydrogen bonds with Arg167 for 90% of the simulation time, as well as ionic interactions. This moiety also develops water bridges with residues such as Tyr87, Cys180, and Phe182. The tetrazole group develops: hydrogen bonds with Arg167 (11% of the time) and Lys199 (13%), water bridges with Ser109 (14%), and π -cation interactions with Lys199 (47%) and Arg167 (37% of the time). The imidazole group interacts with Trp84 with π - π interactions (12%) and π -cation interactions (46%) and with Tyr35 mainly forming water bridges (25%). The residue Arg167 also develops π -cation interactions with the A phenyl group. The conformation that olmesartan methyl ether adopts in the binding site is always *anti*.

Also in this case, the distances H19-H12, H9-H4, H9-H5 H9-H23 and H10-H23 were monitored (Fig. 4-16). The average values were found to be 2.7 (+/- 0.3) Å, 4.0 (+/- 0.5) Å, 5.0 (+/- 0.5) Å, 5.6 (+/- 0.6) Å and 6.0 (+/- 0.6) Å in accordance with the NOEs.

4.4 Comparison between NMR data and predicted ^{13}C NMR chemical shifts

The comparative values between experimental NMR data and predicted chemical shifts of the representative low energy conformations of olmesartan in methanol and olmesartan methyl ether in methanol and acetonitrile as derived from MacroModel are presented in Tables 4-3, 4-4 and 4-5. Also, in Table 4-3, olmesartan's NMR data are compared with the predicted chemical shifts of the structure of olmesartan crystallized from ethanol by Yanagisawa *et al.*⁶².

In the case of olmesartan two low energy conformations (conformations 3 and 4 in Figure 4-1) and the conformation of the crystal structure led to acceptable comparative results (Table 4-3) using as a criterion the deviation of >10% from the experimental values (Table 4-8). Furthermore, in the case of olmesartan methyl ether only conformation 10 in

methanol and conformation 16 in acetonitrile led to acceptable comparative results. Jaguar algorithm had the most deviations from the experimental values of olmesartan carbons C4-C6 of alkyl chain and C18 of the aromatic ring B. For olmesartan methyl ether Jaguar algorithm had the most deviations from the experimental values at C2 and C3 of the imidazole ring and C5 of the aromatic ring B.

On the other hand, the predicted chemical shifts for the binding poses of olmesartan and olmesartan methyl ether in the two crystal structures of AT₁R resulted in not acceptable comparative values (Tables 4-6 and 4-7). Based on the latter result, it is obvious that there are a lot of differences between the binding conformation on the receptor and the low energy conformations in the solvents (both for olmesartan and its methylated analogue).

Table 4-3: Predicted chemical shifts for olmesartan's eight representative conformations and the crystal structure (CSD reference code ZOGSOD).

	Exp. NMR shifts in CD ₃ OD	Conf. 1	‡	Conf. 2	‡	Conf. 3	‡	Conf. 4	‡	Conf. 5	‡	Conf. 6	‡	Conf.7	‡	Conf. 8	‡	ZOGSOD	‡
C1	148.80	140.04	5.88	142.14	4.47	140.24	5.75	144.52	2.87	135.40	9.01	136.39	8.34	141.52	4.89	141.25	5.07	138.90	6.65
C2	124.78	127.70	-2.34	127.40	-2.10	127.36	-2.07	126.62	-1.47	129.17	-3.52	129.30	-3.62	128.34	-2.85	129.54	-3.81	127.50	-2.18
C3	146.92	138.36	5.82	136.57	7.05	137.76	6.24	142.64	2.91	137.96	6.10	137.47	6.43	135.96	7.46	136.30	7.23	138.41	5.79
C4	28.29	17.22	39.12	15.06	46.78	28.77	-1.69	16.02	43.39	15.78	44.24	15.18	46.36	14.62	48.30	15.09	46.68	28.76	-1.66
C5	22.44	28.73	-28.04	30.66	-36.63	26.11	-16.34	32.66	-45.56	29.45	-31.24	29.35	-30.79	28.71	-27.94	32.62	-45.38	23.56	-5.01
C6	13.97	26.33	-88.49	21.95	-57.14	17.50	-25.25	24.73	-77.06	24.86	-77.99	25.61	-83.29	21.03	-50.54	20.91	-49.68	13.99	-0.17
C7	49.13	49.97	-1.70	49.43	-0.61	50.76	-3.32	49.44	-0.63	51.70	-5.23	51.57	-4.97	49.90	-1.57	50.52	-2.83	50.16	-2.10
C8	137.43	129.50	5.77	129.49	5.78	129.47	5.79	133.67	2.73	126.41	8.02	126.07	8.27	127.64	7.13	127.45	7.26	129.63	5.68
C9	127.77	119.71	6.31	123.05	3.69	119.40	6.55	123.61	3.25	120.41	5.76	121.35	5.02	124.43	2.61	124.08	2.88	120.73	5.51
C10	130.66	130.67	-0.01	128.57	1.60	130.82	-0.12	122.36	6.35	132.76	-1.61	130.15	0.39	127.86	2.14	127.70	2.27	122.90	5.94
C11	140.48	144.09	-2.57	142.93	-1.75	144.85	-3.11	141.59	-0.79	147.23	-4.80	146.02	-3.94	142.55	-1.48	143.54	-2.18	144.74	-3.04
C12	130.66	122.93	5.91	123.60	5.40	122.90	5.94	126.24	3.39	122.84	5.98	124.31	4.86	125.19	4.19	126.18	3.43	130.95	-0.22
C13	127.77	120.83	5.43	123.73	3.16	120.93	5.35	125.31	1.93	122.09	4.44	122.78	3.90	122.01	4.51	121.15	5.18	120.47	5.71
C14	142.93	133.67	6.48	135.80	4.99	133.79	6.39	136.94	4.19	131.19	8.21	131.23	8.18	135.43	5.25	135.40	5.27	133.63	6.50
C15	124.71	134.02	-7.47	135.29	-8.48	134.20	-7.61	134.02	-7.47	134.45	-7.81	134.91	-8.18	135.23	-8.43	135.22	-8.42	133.80	-7.29
C16	131.85	125.40	4.89	125.65	4.71	125.08	5.14	125.63	4.72	125.53	4.80	126.05	4.40	126.12	4.35	125.23	5.02	125.25	5.01
C17	129.12	120.42	6.74	120.37	6.78	120.20	6.91	120.17	6.93	120.54	6.64	120.53	6.65	120.36	6.78	120.41	6.75	120.31	6.82
C18	132.45	115.75	12.61	116.14	12.32	115.56	12.76	116.96	11.70	114.20	13.78	114.90	13.25	116.49	12.05	115.96	12.45	115.90	12.50
C19	131.70	123.73	6.05	122.10	7.29	124.08	5.78	122.58	6.92	125.49	4.72	125.41	4.78	122.36	7.09	122.07	7.31	124.38	5.55
C20	157.04	155.59	0.93	155.85	0.76	155.51	0.98	156.04	0.64	154.71	1.48	155.16	1.20	156.46	0.37	155.65	0.89	155.49	0.99
C21	164.29	150.72	8.26	152.33	7.28	150.71	8.27	154.15	6.17	149.72	8.87	150.38	8.47	152.18	7.37	151.49	7.79	150.96	8.11
C22	70.30	67.37	4.17	67.29	4.29	67.79	3.57	67.92	3.39	67.56	3.90	67.23	4.37	67.07	4.60	66.99	4.71	67.05	4.63
C23	29.70	26.98	9.15	30.35	-2.19	30.55	-2.86	29.82	-0.40	27.12	8.70	27.28	8.16	30.69	-3.34	27.11	8.73	27.23	8.33
C24	29.70	31.04	-4.52	27.01	9.07	27.26	8.22	27.74	6.61	30.84	-3.84	30.28	-1.95	27.24	8.29	30.90	-4.04	30.84	-3.84

‡ [(Experimental values-Calculated values)/Experimental values] x100

Table 4-4: Predicted chemical shifts for olmesartan methyl ether's four representative conformations in CD₃OD.

	Experimental NMR chemical shifts (olmesartan ether in CD ₃ OD)	Conf. 9	‡	Conf. 10	‡	Conf. 11	‡	Conf. 12	‡
C1	149.59	135.55	9.39	142.73	4.58	145.80	2.54	135.86	9.18
C2	121.94	140.63	-15.33	129.67	-6.34	135.17	-10.85	131.37	-7.73
C3	147.44	121.88	17.33	134.02	9.10	128.51	12.84	131.27	10.97
C4	27.96	28.82	-3.07	32.48	-16.17	32.92	-17.75	29.33	-4.90
C5	22.04	30.09	-36.52	24.46	-11.00	25.17	-14.18	25.46	-15.50
C6	13.65	15.40	-12.79	16.12	-18.07	16.23	-18.95	15.54	-13.81
C7	49.36	53.78	-8.96	50.43	-2.17	51.90	-5.15	52.18	-5.72
C8	136.11	126.06	7.39	133.42	1.97	134.02	1.53	126.83	6.82
C9	128.23	120.45	6.07	123.24	3.89	123.26	3.87	121.49	5.26
C10	130.80	129.98	0.63	122.72	6.18	121.90	6.80	130.76	0.03
C11	140.87	146.45	-3.96	142.32	-1.03	142.12	-0.89	145.65	-3.39
C12	130.80	125.02	4.42	125.77	3.85	126.58	3.23	124.54	4.78
C13	128.23	124.16	3.17	125.98	1.76	126.83	1.09	121.39	5.33
C14	142.56	131.64	7.66	135.85	4.71	136.80	4.04	131.39	7.83
C15	125.26	134.49	-7.38	133.32	-6.44	133.74	-6.77	134.61	-7.47
C16	131.67	125.78	4.48	124.52	5.43	125.19	4.92	125.78	4.48
C17	129.19	120.32	6.87	119.88	7.21	120.01	7.16	120.36	6.83
C18	131.51	114.86	12.66	116.32	11.55	116.66	11.29	114.89	12.63
C19	131.42	125.68	4.37	122.90	6.48	122.76	6.59	125.46	4.54
C20	157.41	155.07	1.49	155.89	0.97	155.52	1.20	155.13	1.45
C21	163.79	148.40	9.40	152.20	7.07	153.12	6.51	148.37	9.42
C22	76.00	73.40	3.42	76.97	-1.27	73.74	2.97	80.08	-5.37
C23	25.62	22.44	12.40	30.62	-19.52	31.30	-22.18	29.65	-15.73
C24	25.62	30.09	-17.45	21.95	14.32	23.24	9.28	22.25	13.15
C25	49.84	50.60	-1.53	52.65	-5.64	51.96	-4.26	50.82	-1.97

‡ [(Experimental values-Calculated values)/Experimental values] x100

Table 4-5: Predicted chemical shifts for olmesartan methyl ether's four representative conformations in CD₃CN.

	Experimental NMR chemical shifts (olmesartan ether in CD ₃ CN)	Conf. 13	‡	Conf. 14	‡	Conf. 15	‡	Conf. 16	‡
C1	153.37	143.98	6.12	134.96	12.01	137.86	10.11	139.49	9.05
C2	151.36	128.75	14.94	130.74	13.62	124.00	18.07	133.75	11.63
C3	119.41	135.59	-13.55	131.90	-10.46	136.53	-14.33	127.74	-6.97
C4	29.70	32.98	-11.02	29.50	0.68	28.66	3.51	28.67	3.47
C5	21.76	25.36	-16.52	24.77	-13.85	24.19	-11.19	26.37	-21.17
C6	14.11	16.03	-13.58	15.78	-11.81	14.72	-4.36	16.69	-18.26
C7	48.62	51.34	-5.60	52.33	-7.64	51.44	-5.80	49.70	-2.22
C8	138.37	134.12	3.07	127.59	7.79	128.92	6.83	130.11	5.97
C9	127.1	127.29	-0.15	120.14	5.48	120.96	4.83	122.33	3.75
C10	130.43	126.11	3.32	132.41	-1.52	126.60	2.94	129.02	1.08
C11	139.64	141.73	-1.50	146.77	-5.10	144.88	-3.76	144.93	-3.79
C12	130.43	122.05	6.42	122.46	6.11	125.49	3.79	122.81	5.84
C13	127.10	123.04	3.19	121.56	4.36	126.43	0.53	120.85	4.92
C14	142.35	137.52	3.39	131.75	7.45	134.52	5.50	134.29	5.66
C15	125.80	133.60	-6.20	134.71	-7.09	133.70	-6.28	133.70	-6.28
C16	131.73	125.77	4.53	125.59	4.66	125.71	4.57	124.67	5.36
C17	128.91	120.04	6.88	120.30	6.68	120.19	6.76	120.16	6.79
C18	132.03	117.09	11.32	114.43	13.33	115.95	12.18	115.30	12.67
C19	131.79	122.71	6.89	125.58	4.72	124.53	5.51	123.90	5.99
C20	156.57	155.99	0.37	154.82	1.11	155.46	0.71	155.09	0.95
C21	161.02	151.31	6.03	148.87	7.55	149.05	7.43	149.74	7.01
C22	79.24	75.68	4.50	80.22	-1.24	73.94	6.68	79.20	0.05
C23	26.40	23.93	9.34	22.14	16.13	23.27	11.84	22.68	14.08
C24	26.40	31.02	-17.50	29.80	-12.88	30.04	-13.79	22.43	15.03
C25	49.98	49.48	1.00	50.70	-1.44	49.25	1.46	49.09	1.78

‡ [(Experimental values-Calculated values)/Experimental values] x100

Table 4-6: Predicted NMR chemical shifts for olmesartan in the two receptors (PDB ID codes 4YAY and 4ZUD) as were calculated using QSite.

	Experimental NMR chemical Shifts (olmesartan in CD ₃ OD)	Calculated NMR chemical shifts for olmesartan docked in the 4YAY crystal structure	‡	Calculated NMR chemical shifts for olmesartan in the 4ZUD crystal structure	‡
C1	148.80	136.00	8.60	132.88	10.70
C2	124.78	137.10	-9.87	134.90	-8.11
C3	146.92	138.77	5.55	125.20	14.79
C4	28.29	29.68	-4.91	26.81	5.25
C5	22.44	20.49	8.71	25.80	14.98
C6	13.97	16.97	-21.48	15.33	-9.76
C7	49.13	51.47	4.76	47.70	2.92
C8	137.43	144.56	-5.19	125.58	8.62
C9 or C13	127.77	122.88	3.82	115.17	9.87
C9 or C13	127.77	124.57	2.51	118.84	6.99
C10 or C12	130.66	118.72	9.14	125.89	3.65
C10 or C12	130.66	123.40	5.55	132.21	-1.19
C11	140.48	134.43	4.31	145.60	-3.64
C14	142.93	135.81	4.98	136.05	4.82
C15	124.71	130.03	-4.27	136.23	-9.23
C16	131.85	126.35	4.17	127.58	3.24
C17	129.12	119.71	7.29	120.23	6.88
C18	132.45	120.97	8.67	117.16	11.55
C19	131.70	127.20	3.53	124.26	5.648
C20	157.04	159.90	-1.82	159.48	-1.55
C21	164.29	157.49	4.16	152.18	7.37
C22	70.30	69.91	0.55	71.47	-1.66
C23 or C24	29.70	33.55	-12.96	30.53	-2.80
C23 or C24	29.70	25.83	13.02	28.78	3.09

‡ [(Experimental values-Calculated values)/Experimental values] x100

Table 4-7: Predicted NMR Chemical Shifts for olmesartan methyl ether in the two receptors (PDB ID codes 4YAY and 4ZUD) as were calculated using QSite.

	Experimental NMR chemical shifts (olmesartan ether in CD ₃ CN)	Calculated NMR chemical shifts for olmesartan docked in the 4YAY crystal structure	‡	Calculated NMR chemical shifts for olmesartan in the 4ZUD crystal structure	‡
C1	153.37	129.89	15.312	136.53	10.98
C2	119.41	136.56	-14.361	133.50	-11.80
C3	151.36	129.91	14.169	127.13	16.01
C4	29.70	26.58	10.295	25.47	14.23
C5	21.76	19.81	8.975	23.70	-8.90
C6	14.11	16.97	-20.277	16.31	-13.50
C7	48.62	52.13	-7.219	49.08	-0.95
C8	138.37	130.05	6.012	127.42	7.92
C9 or C13	127.10	119.29	6.141	116.00	8.73
C9 or C13	127.10	121.22	4.626	114.28	10.09
C10 or C12	130.43	126.44	3.061	133.62	-2.44
C10 or C12	130.43	123.56	5.268	124.90	4.24
C11	139.64	140.08	-0.313	146.06	-4.40
C14	142.35	135.29	4.96	137.99	3.07
C15	125.8	130.83	-4.002	137.97	-9.67
C16	131.73	123.76	6.052	120.69	8.38
C17	128.91	122.20	5.209	117.30	9.01
C18	132.03	118.84	9.992	114.23	13.48
C19	131.79	127.46	3.284	124.84	5.27
C20	156.57	154.61	1.25	156.60	0.00
C21	161.02	150.13	6.762	143.52	10.87
C22	79.24	76.79	3.097	75.18	5.13
C23 or C24	26.40	34.62	-31.138	21.48	18.63
C23 or C24	26.40	24.73	6.344	28.26	-7.03
C25	49.98	54.18	-8.404	48.92	2.45

‡ [(Experimental values-Calculated values)/Experimental values] x100

Table 4-8: % deviations of various conformers in the ^{13}C chemical shifts versus the experimental for olmesartan and its methyl ether.

Conformations	Percentage of atoms that deviate from the experimental NMR data >10%	Percentage of atoms that deviate from the experimental NMR data 5-10%	Percentage of atoms that deviate from the experimental NMR data <5%
<i>Olmesartan</i>			
Conformation 1	16.6	50	33.3
Conformation 2	16.6	33.3	50
Conformation 3	12.5	50	37.5
Conformation 4	16.6	25	58
Conformation 5	16.6	45.8	37.5
Conformation 6	16.6	33.3	50
Conformation 7	16.6	29.2	54.16
Conformation 8	16.6	41.66	41.66
ZOGSOD	4.1	54.1	41.6
<i>Olmesartan methyl ether in methanol</i>			
Conformation 9	28	28	44
Conformation 10	24	32	44
Conformation 11	28	28	44
Conformation 12	24	36	40
<i>Olmesartan methyl ether in acetonitrile</i>			
Conformation 13	28	32	40
Conformation 14	32	32	36
Conformation 15	28	28	44
Conformation 16	24	32	44
<i>Olmesartan docked in the 4YAY crystal structure</i>	12.5	33.3	54.1
<i>Olmesartan in the 4ZUD crystal structure</i>	16.7	37.5	45.83
<i>Olmesartan methyl ether docked in the 4YAY crystal structure</i>	24	40	36
<i>Olmesartan methyl ether docked in the 4ZUD crystal structure</i>	36	36	28

4.5 The interactions of R239470, R794847 and R781253 with the crystal structure 4ZUD

Zhang *et al.*¹⁹³ supposes that the carbamoyl moiety of R239470 forms additional hydrogen bond interactions with Tyr87 and Tyr92. In the MD simulation of R239470 a very stable intramolecular hydrogen bond is formed between the -NH₂ moiety of the carbamoyl group and the hydroxyl group of the molecule (Fig. 4-20a). This interaction seems to “lock” the structure in a slightly different position compared to the one that olmesartan adopts, and results in forming an additional stable interaction between the imidazole moiety and Tyr92 for 42% of the simulation time. The rest of the developed interactions are the same for both molecules of olmesartan and R239470. In the case of R794847 this intramolecular hydrogen bond does not occur. The -NH₂ group of the carbamoyl moiety forms a hydrogen bond with Tyr87 for 72% of the simulation time. The 4-hydroxybenzyl moiety develops interactions mainly with Thr260 (hydrogen bond for 81% of the simulation time), Lys199 (π -cation interactions for 68% of the simulation time), Gln257 (hydrogen bond for 20% of the simulation time) and Trp253 (π - π interactions for 15% of the simulation time) (Fig. 4-20b). On the other hand, the hydroxyl group of the 4-hydroxybenzyl moiety of R781253 forms stable hydrogen bonds with Gln257 (80% of the simulation time) and Trp253 (17% of the simulation time) and π -cation interactions with His256 (37% of the simulation time). The rest of the interactions that are developed by these molecules at their binding site on the AT₁R follow the same pattern of olmesartan and olmesartan methyl ether and need no further discussion (Fig. 4-20c).

Table 4-9: Prime MM-GBSA energies for olmesartan, binding at the wild type AT₁R and its four mutated structures Y113F, K199Q, H256A and Q257A, olmesartan methyl ether, R781253, R794847 and R239470 binding at the wild type of AT₁R.

	ΔG Binding	Coulomb	Covalent	Hbond	Lipo	Packing	Solv_GB	vdW	K _d (nM)
Olmesartan Wild Type	-94.94	-8.82	11.33	-7.05	-37.72	-4.62	6.58	-54.63	2.2 ± 0.7 ⁶⁵
Olmesartan Y113F	-96.35	3.93	11.24	-7.22	-39.48	-5.36	-2.01	-57.44	52 ± 7 ⁶⁵
Olmesartan K199Q	-101.40	-2.38	9.92	-7.15	-40.46	-4.75	-1.55	-55.02	33 ± 6 ⁶⁵
Olmesartan H256A	-84.23	37.69	9.92	-7.11	-38.03	-5.28	-26.38	-55.02	36 ± 4 ⁶⁵
Olmesartan Q257A	-83.49	-16.18	8.35	-7.15	-31.52	-3.34	16.87	-50.51	226 ± 4 ⁶⁵
Olmesartan methyl ether	-82.75	37.72	8.54	-6.40	-40.30	-4.10	-22.14	-56.07	pIC ₅₀ = 8.44 □ ± 0.04 * ¹⁹⁴
R781253	-121.48	-17.82	8.09	-7.87	-51.07	-3.32	20.57	-70.06	21 ± 10 ³⁰⁶
R794847	-110.63	-51.99	8.91	-3.72	-47.04	-4.03	57.06	-69.80	48 ± 12 ³⁰⁶

R239470	-80.03	9.78	7.22	-2.94	-31.84	-3.62	-8.57	-50.05	0.8 ± 0.3 ³⁰⁶
---------	--------	------	------	-------	--------	-------	-------	--------	------------------------------

Coulomb: Coulomb energy; Covalent: Covalent binding energy; vdW: Van der Waals energy; Lipo: Lipophilic energy; Solv_GB: Generalized Born electrostatic solvation energy; Hbond: Hydrogen-bonding energy; Packing: Pi-pi packing energy

*In reference ¹⁹⁴ is mentioned only the pIC₅₀ value.

From the MM-GBSA calculations the most favored binding was exerted by R781253 showing highly favored VdW and Coulombic interactions (Table 4-9). The favored binding of R794847 is attributed also to Coulombic and VdW interactions. Olmesartan shows similar binding to wild type and mutated Y113F and K199Q receptors. However, it shows less favored binding with the mutated receptors H256A and Q257A. In H256A the coulombic interactions are disfavored and in Q257A the Solv_GB. Coulombic interactions are responsible for the low binding of olmesartan methyl ether.

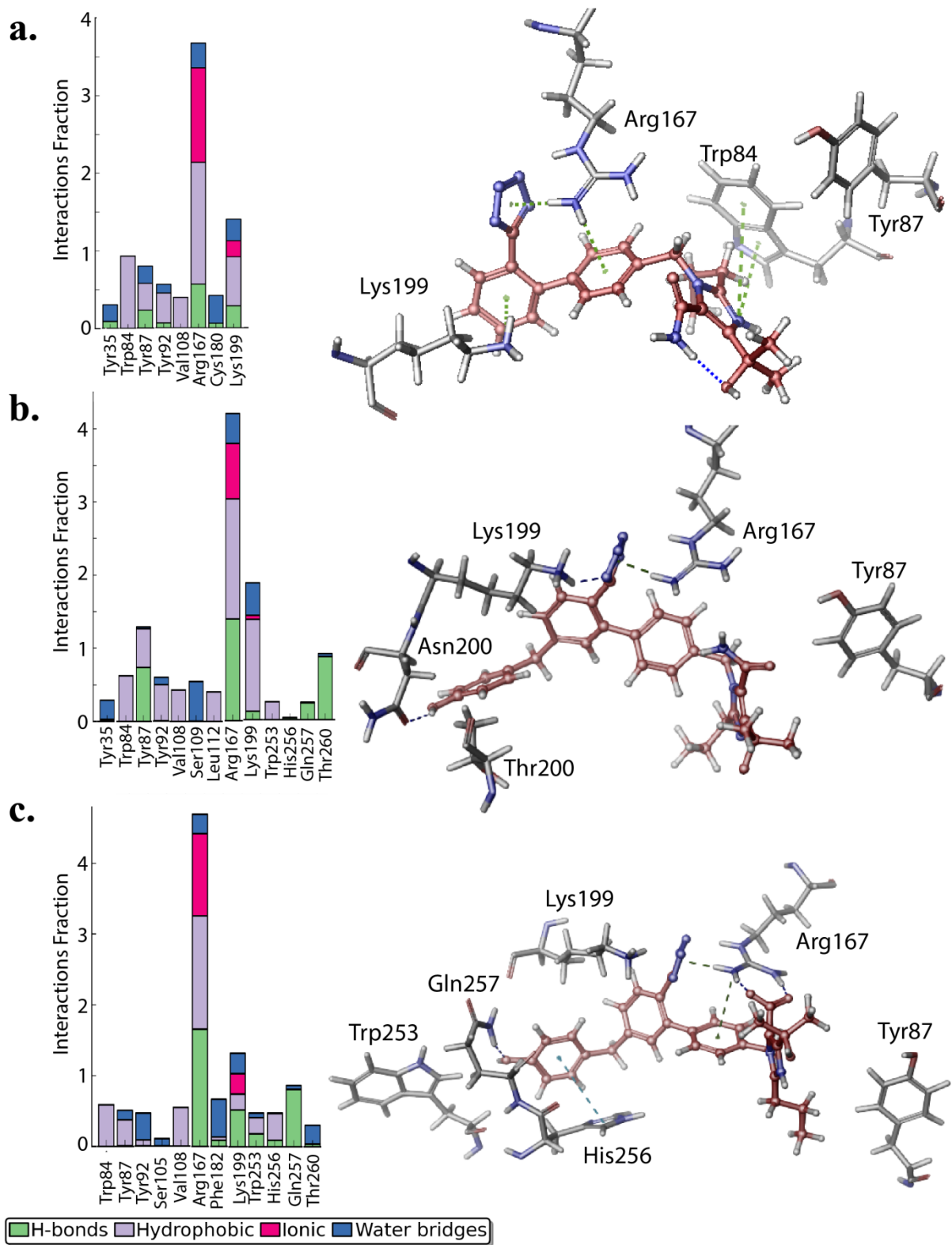


Figure 4-20. Interactions fraction and binding modes of (a) R239470; (b) R794847; (c) R781253

4.6 Conclusions

In a previous publication we found that olmesartan in a methanolic solution even at low temperatures is converted to its methylated ether analogue ¹⁹⁴. The *in vitro* experimental results showed that this methylated analogue possesses equipotent activity with AT₁R antagonist olmesartan. This finding triggered our interest to study the conformational properties both of olmesartan and its olmesartan methyl ether in the new co-crystallized AT₁R receptor with ZD7155. Indeed, the molecular docking and dynamics results can provide a plausible explanation for the *in vitro* results.

Miura *et al.* ⁶⁵ have reported that mutations in the AT₁R such as Y113F, K199Q, H256A and Q257A lower the binding affinity of olmesartan. It is possible that these residues do not contact the ligand and their mutation affect ligand binding indirectly, by altering the overall conformation of AT₁R. This could be supported by the fact that mutation of Y113F reduced olmesartan affinity, whereas the mutation Y113A substitution for this residue, did not affect ligand binding. Alanine mutation is a well-tolerated substitution that does not significantly affect receptor conformation ³⁰⁷. Alternatively the inconsistency between the results from mutagenesis studies and the crystal structure of AT₁R-olmesartan complex could be due to a possible conformational heterogeneity of Y113, K199, H256 and/or Q257 and to the fact that the crystal structure of a receptor represents only one single “snapshot” conformation. In specific, the crystal structure of the inactive β_2 adrenergic receptor revealed the absence of an electrostatic interaction between the intracellular ends of TM3 and TM6, which has been shown in mutagenesis and molecular modeling studies to stabilize the inactive state of this receptor and in the inactive crystal structure of rhodopsin ³⁰⁸. Dror *et al.* have suggested that the inactive β_2 adrenergic receptor exists in equilibrium between conformations with the electrostatic interaction formed and broken, and that the crystal structure of this receptor represents one single conformation ³⁰⁹. Interestingly, a previous study has shown that even different copies of the same crystal structure of the D3 dopamine receptor had different structures, thus highlighting particular areas of conformational flexibility. In specific the second intracellular loop of D3 dopamine receptor formed a 2.5 turn alpha helix in one copy whereas in the other was unstructured ³¹⁰. The presence of multiple conformations of a single receptor is further supported by the fact that even a single agonist could stabilize different conformations, and thus activating different signaling pathways. For example, the corticotropin releasing factor-related agonist, sauvagine, stimulated the adenylate cyclase activity in a bell-shaped manner, which could be partially due to that at subnanomolar

concentrations, the cAMP production was raised after activation of Gs, whereas at higher concentrations, the cAMP production was inhibited through the stimulation of Gi³¹¹. The concept of the presence of different receptor conformations that bind differentially the same agonist and activate differentially various signaling pathways has also been introduced by Maggi and Schwartz, based on their experimental findings³¹². Different AT₁R conformations stabilized by arrestin types 1 and 2 could be responsible for the 9-fold difference in the binding affinities of SII-Ang II to these entities³¹³. The complexity in the formation of different conformations of a receptor bound with the same ligand is further increased by the ability of ligands to change their conformations in their unbound and bound states. A previous study has shown that hydrophobic ligands unfold during binding³¹⁴. More interestingly, Stockwell *et al.* have shown that three of the most ubiquitous biological ligands in nature, ATP, NAD and FAD bind to proteins in widely varying conformations.³¹⁵ This is further supported by the fact that the retinal bound to rhodopsin upon light absorption is transformed from the 11-cis form into the all-trans retinal. During this process the receptor is transformed to its active state metarhodopsin, passing through several intermediate conformations, such bathorhodopsin and lumirhodopsin.

The above discussion brings to the point that the crystal structure and homology models of AT₁R do not simulate adequately the real environment of AT₁R. AT₁R is incorporated in the lipid bilayer which may interfere in the binding of AT₁R antagonists. Mutation of AT₁R may break the communication of the lipid bilayer core and AT₁R and thus affects significantly the binding of the AT₁R. The absence of a real lipid bilayer environment in docking and MD calculations make these inaccurate to simulate the biological results. An effort is under progress to increase the complexity of the study systems in order to examine if we can reconcile the discrepancy between the experimental and *in silico* results.

Prime MM-GBSA calculations for the five molecules studied (olmesartan, olmesartan methyl ether, R781253, R794847 and R239470) revealed similarities and differences in their binding energies and its components. Olmesartan methyl ether has less favoured $\Delta G_{\text{binding}}$. This is attributed to its disfavored Coulombic interactions. The interactions of olmesartan in the crystal structure of AT₁R (PDB ID 4ZUD) did not provide a certain trend. For example the interactions of olmesartan at the wild type and mutated type K199Q do not differ significantly. R239470 shows higher ΔG due to disfavored Coulombic interactions. In contrast R781253 and R794847 have more favored Coulombic interactions than olmesartan and this results in a better binding energy in respect to olmesartan. Thus, their favored

Coulombic interactions compensate successfully their Generalized Born electrostatic solvation energy.

The program Jaguar was used to compare the simulated chemical shifts obtained from different conformations with experimental NMR data. Such comparisons are useful to trigger the interest for using more accurate quantum mechanical calculations.

The ideal situation would be to study the interactions of drugs in a real environment. NMR methodologies applied also to AT₁R even in its crystal structure would be also very beneficial for the advancement of the field³¹⁶. There are currently in literature several discrepancies, especially in the field of membrane proteins, on defining their real structure (as was the case of the EmrE protein). Herein, we illustrated that a ligand-based approach can be used and is able to lead to logical results on the interaction of a ligand with its GPCR. Indeed, methods such as paramagnetic relaxation enhancement (PRE) and residual dipolar couplings (RDCs), could be utilized, however, as has been capitalized in a recent (2016) perspective in Nature Structural and Molecular Biology³¹⁷ “although membrane proteins constitute more than half of all drug targets, STD so far has seen only limited use for membrane proteins, probably because of the complicating presence of the membrane mimetic.” In the very same paper it was pinpointed that “nonphysiological constraints imposed by the crystal lattice rather than the micelle environment are problematic for these proteins.” The associated problems due to the presence of the membrane mimetic are not only due to the huge difficulties in the sample preparation (every batch could be different) but also that the recorded effects based on the technique suggested by the reviewer could be mediated due to complicated interactions of the ligand with the membrane mimetic, or the membrane proteins or both. Furthermore, saturation transfer difference (STD) or saturation transfer double difference (STDD) NMR, works best for weakly bound ligands, but not for tightly bound ligands. The message of this article to the scientific community is simple. Due to the fact that membrane proteins are a very important field of drug development, the suggested workflow, following appropriate validations, could assist on the determination of the ligand binding interaction poses.

5 Chapter 5: Interactions of silibinin with 2-hydroxypropyl- β -cyclodextrin

In this chapter are described the different analytical techniques and computational methods utilized to determine in molecular level the architecture of the silibinin-2-hydroxypropyl- β -cyclodextrin complex. In particular, DSC, high resolution solid state and liquid 2D NOESY and DOSY, MD simulations, MTT assays and solubility/dissolution rate experiments are applied.

5.1 DSC analysis to characterize the SLB–HP- β -CD complex.

DSC was used to characterize the SLB–HP- β -CD complex. In Table 5-1, the DSC values for SLB, HP- β -CD, a 1:1 mixture of SLB and HP- β -CD, and complexes of HP- β -CD with decreasing concentration of silibinin are shown. The DSC scan of HP- β -CD consists of a broad peak with $T_m = 114.66$ °C being in agreement with the reported data³¹⁸. Thermal scan of SLB shows a sharper peak with a higher T_m value of 173.93 °C (see Figure 5-1B). The mixture shows two distinct endothermic melting peaks of SLB and HP- β -CD (see Figure 5-1C) whereas only a single broad peak is observed in the lyophilized complex (see Figure 5-1D). This confirms the inclusion of the guest molecule into the cavity of the host^{204, 230}.

The DSC scan of the mixture shows ΔH values for each component to be less than those of the components obtained separately. For the three different complexes, an increase in ΔH is observed with the increase in the concentration of silibinin. This is expected because more interactions or displacement of water occurs as the concentration increases. The increase in ΔH is more evident between molar ratios 1:4 to 1:2 and less eminent between the ratios 1:2 to 1:1. This is an indication that complexation occurs at a ratio of 1:1.

Table 5-1: T_m , T_{onset} and ΔH values for the samples SLB, HP- β -CD, the mixture SLB–HP- β -CD 1:1 and the complexes SLB–HP- β -CD using ratios 1:1, 1:2 and 1:4. (Values are subjected to 5% error for the three consecutive runs.)

Samples	T_m (°C)	T_{onset} (°C)	ΔH (cal/g)
SLB	173.93	166.65	9.98
HP- β -CD	114.66	76.37	25.80
Mixture SLB–HP- β -CD 1:1	171.95	162.54	4.84
	114.66	88.66	20.72
Complex SLB–HP- β -CD 1:1	83.16	46.82	39.57

Complex SLB–HP-β-CD 1:2	91.90	51.94	38.20
Complex SLB–HP-β-CD 1:4	94.06	49.85	35.78

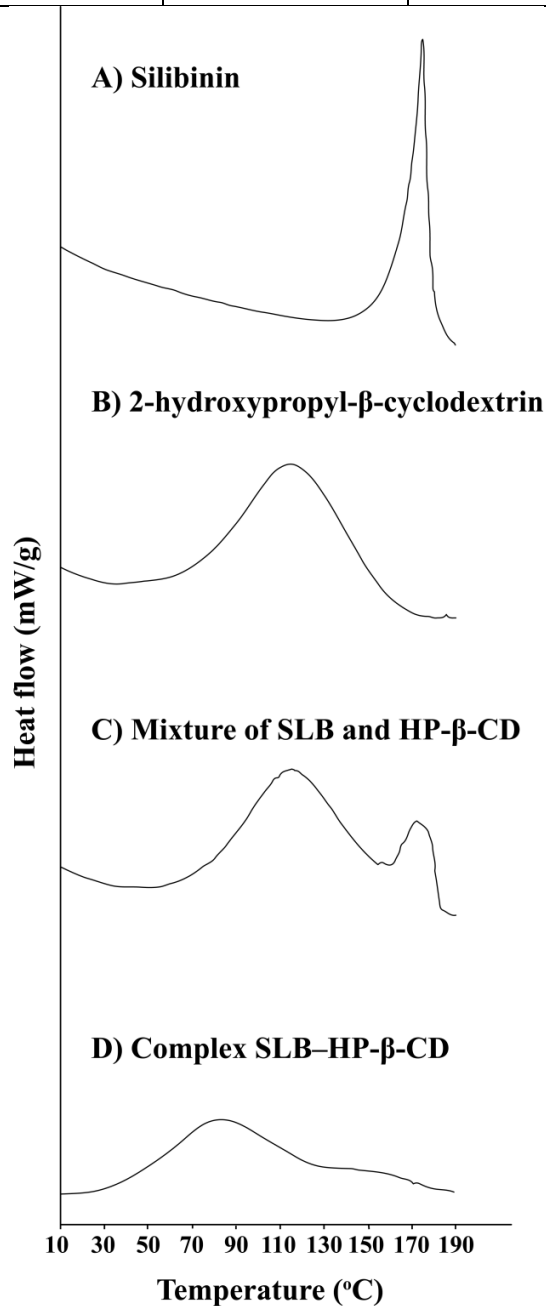


Figure 5-1: Thermal scans of A) SLB, B) HP-β-CD, C) their mixture (molar ratio 1:1) and D) the complex with the same ratio ³¹⁹.

5.2 ¹³C solid state CP/MAS NMR spectra

The ¹³C CP/MAS spectra of the solid silibinin, HP-β-CD, the mixture and the inclusion complex SLB–HP-β-CD are shown in Figure 5-2 and their chemical shifts are given in Table 5-2. Solid state NMR assignments were based on published high resolution NMR data in liquids ^{213, 320, 321} (see Table 5-2).

Table 5-2: ^{13}C chemical shifts of SLB, HP- β -CD, mixture of SLB and HP- β -CD, and complex SLB-HP- β -CD.

A. chemical shifts of SLB

Carbon atoms of SLB	DMSO-d ₆ 900 MHz 298 K ²¹³	(CD ₃) ₂ CO 300 MHz ³²⁰	CD ₃ OD 400 MHz 303 K ³²¹	Solid State NMR 600 MHz 298 K	Mixture	Complex
OMe	55.65	55.71	56.76	56.81	56.75	not observed
C23	60.15	61.01	62.37	62.65	nr*	nr
C3	71.35	72.32	73.94	72.58	nr	nr
C11	75.84	76.51	77.97	75.37	nr	nr
C10	78.08	78.88	80.29	81.65-83.55	nr	nr
C2	82.54	83.37	84.98	84.98 or 87.27	nr	nr
C8	95.09	96.51	96.82	98.7	nr	not observed
C6	96.04	95.54	97.83	100.05	nr	nr
C4a	100.43	100.50	101.95	103.66	nr	nr
C18	111.63	111.41	112.36	113.50	113.51	barely observed
C21	115.28	115.17	116.57	118.21-120.11	118.6-120.7	118.00-123.00
C13	116.28	116.74	117.84	118.21-120.11	118.6-120.7	118.00-123.00
C16	116.53	116.71	118.10	118.21-120.11	118.6-120.7	118.00-123.00
C22	120.51	120.89	121.98	124.22	nr	118.00-123.00
C15	121.37	121.38	122.50	127.59	nr	118.00-123.00
C17	127.44	128.45	129.71	130.37	130.00-130.85	128.99-132.28
C14	130.04	130.51	131.84	130.37	130.00-130.85	128.99-132.28
C12a	143.24	144.00	145.41	146.25-146.78	146.00-147.00	146.52
C16a	143.64	144.40	145.75	146.25-146.78	146.00-147.00	146.52
C19	146.98	147.94	149.49	148.07-149.25	148.09-149.43	150.53
C20	147.59	147.37	148.64	148.07-149.25	148.09-149.43	150.53
C8a	162.47	163.29	165.58	166.15-167.01	165.83-167.62	163.17-167.52
C5	163.27	164.06	164.65	166.15-167.01	165.83-167.62	163.17-167.52
C4	197.80	197.12	198.35	199.35	198.28-200.19	198.58-201.69
C7	nr	168.03	169.59	171.08	171.00-171.75	163.17-167.52

*nr = not resolved

B. Chemical shifts of HP- β -CD

Carbon atoms of HP- β -CD	Solid HP- β -CD	CD ₃ OD 250 MHz 298 K	Mixture	Complex
9	22.0190	20.92	21.98	barely observed
6	63.2987	63.11	62.893	62.78
8	69.1813	69.22	69.15	not observed
2	75.0652	74.51	75.147	75.09
5	75.0652	74.79	75.147	75.09
3	75.0652	75.63	75.147	75.09
7	78.55-84.51	79.50	80.00-87.00	81.41-86.60
4	78.55-84.51	83.21	80.00-87.00	81.41-86.60
1	104.3476	102.93	104.02	104.63

The chemical shifts of the mixture are almost identical to those of its components in contrast to the inclusion complex. The first eminent difference between the mixture of SLB-HP- β -CD and the complex of SLB-HP- β -CD is the absence of C8 and barely observable C9

of HP- β -CD in the complex. This indicates that C8 and C9 participate in the complexation. Furthermore, the absence of SLB peak attributed to the methoxy group in the spectrum of the complex SLB-HP- β -CD suggests that this structural segment of the drug participates in the complexation. C18 is barely seen in the complex and C7 and C4 are shifted upfield in comparison with the mixture. Once more, this evidences that the phenolic hydroxyl group region is participating in the complexation. An eminent feature of the aromatic region is that all peaks of the complex are broader in comparison to the corresponding ones observed for the mixture. This may be attributed to the complexation that imposes slower motions of the aromatic segment of SLB. From this analysis,³²² it is evident that inclusion of the drug occurs either through ring A or E as in these rings the most prominent chemical shift changes are observed.

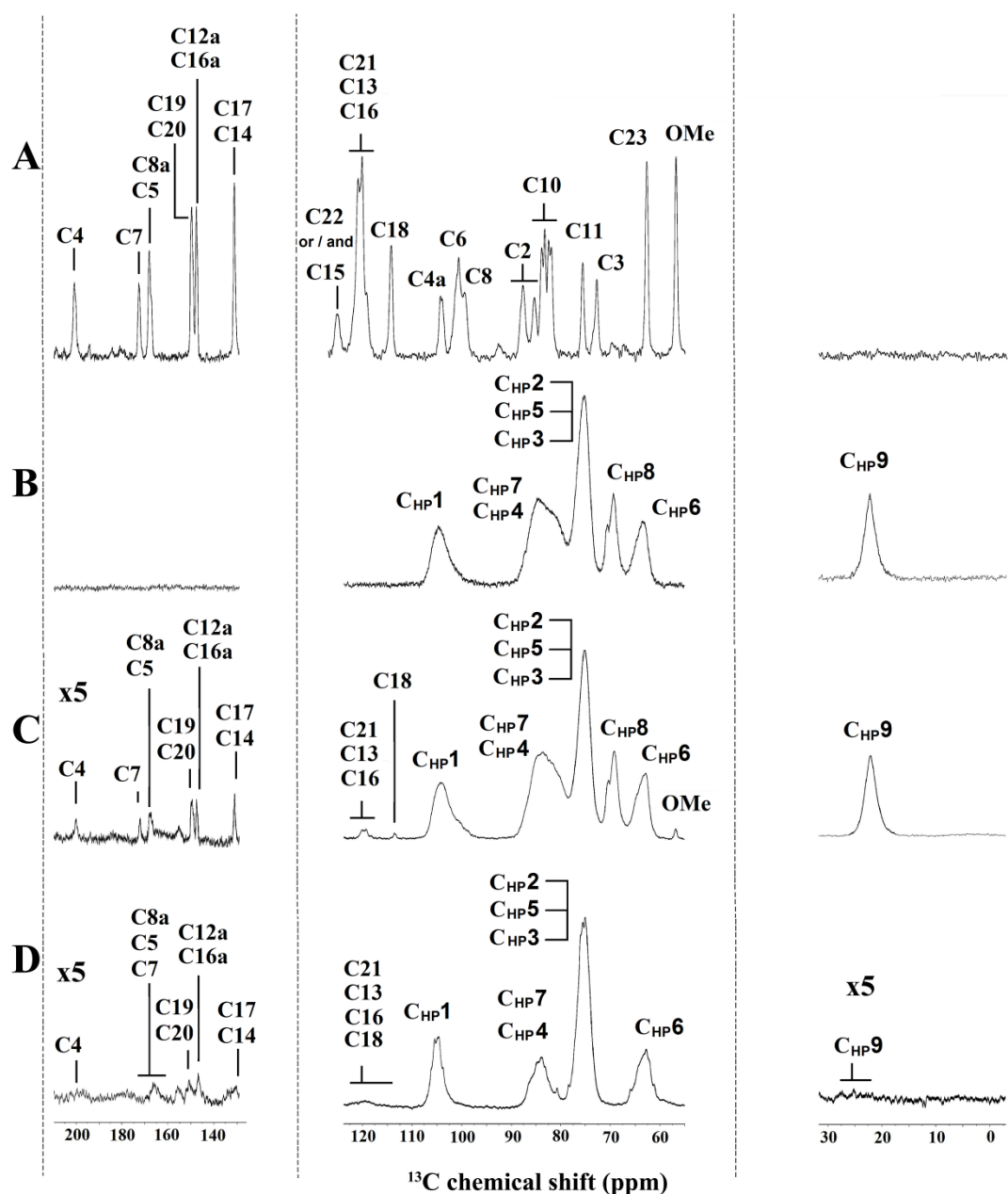


Figure 5-2: ^{13}C CP/MAS spectra of (A) silibinin, (B) HP- β -CD, (C) mixture of SLB-HP- β -CD and (D) complex of SLB-HP- β -CD ³¹⁹.

5.3 ^1H - ^1H 2D NOESY spectra of the complexes.

The NMR ^1H - ^1H 2D NOESY spectra of the complex 1:1 of SLB-HP- β -CD showed that the critical NOE was between the aromatic H22 of SLB and H7 of HP- β -CD (see Figure 5-3). This NOE complements the solid state NMR spectra proposing that SLB enters the hydrophobic core of HP- β -CD cavity through the A ring. Docking experiments of SLB into the HP- β -CD cavity confirm that the A ring is located in the vicinity of H3 and H5 in the hydrophobic core of HP- β -CD while the E ring interacts with the β -hydroxypropyl group as

well as with H2 and H4 protons. This NOE was used to build the initial complex for the MD experiment in order to get detailed information on the stability of the interactions between the two molecules. The ^1H - ^1H 2D NOESY spectrum of the mixture showed no intermolecular correlations, as expected.

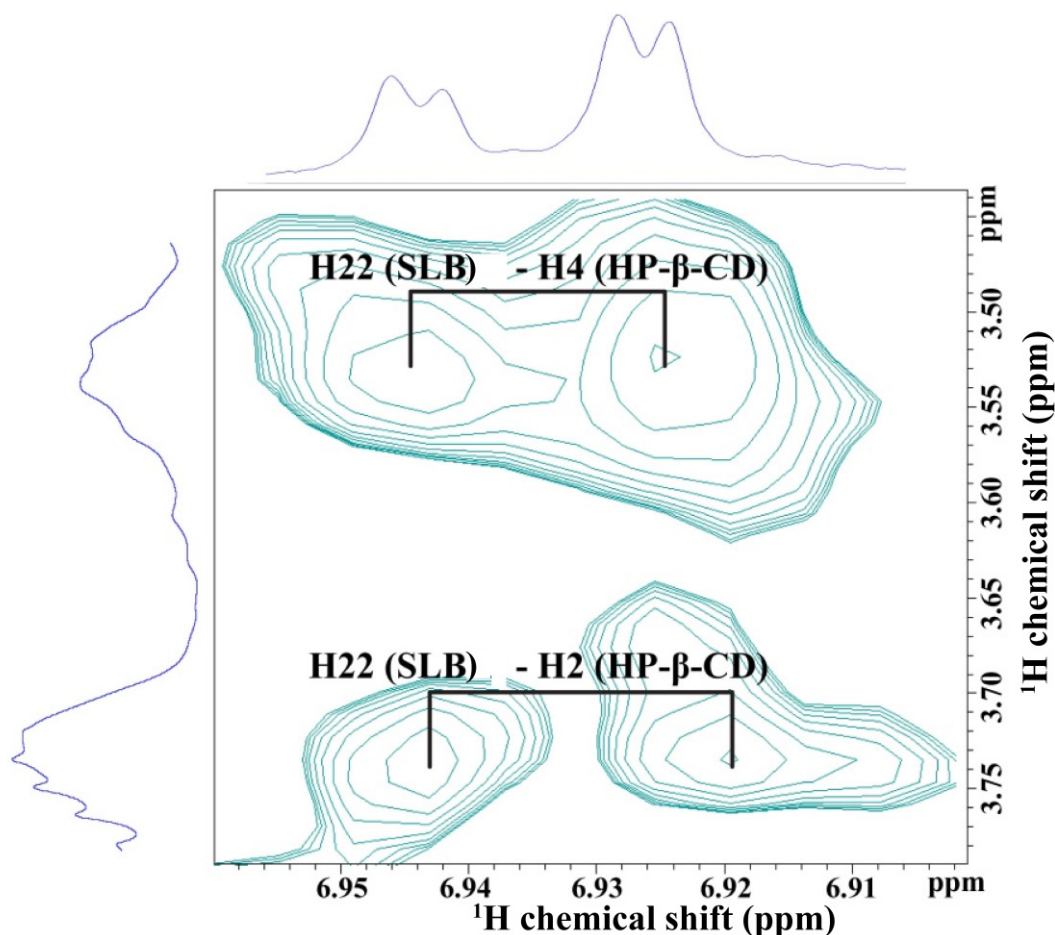


Figure 5-3: 2D NOESY of the complex of SLB–HP- β -CD using mixing time of 150 ms.

We have considered the mode of incorporation of various drugs in HP- β -CD, in an attempt to compare the bibliographic results with those obtained from our study. Sildenafil contains piperazine and an aromatic ring possessing a methoxy group. It was found that the hydrophobic core of HP- β -CD preferentially engulfed piperazine³²². These results are in agreement with ours, which show that the aromatic ring of SLB possessing a methoxy group is situated close to the HP- β -CD hydroxypropyl group. The aromatic ring of caffeic acid, which possesses two phenolic hydroxyl groups is found to locate itself in the interior core of HP- β -CD as depicted by 2D ROESY experiments³²³. The more polar –COOH group is oriented outside, towards the hydroxypropyl group. These results are again compatible with ours. Wang *et al.*³²⁴ studied scutellarein inclusion into HP- β -CD. They showed that its more

polar aromatic ring oriented outside of the core while the less polar aromatic ring possessing only one phenolic hydroxyl group was situated inside the hydrophobic core.

5.4 Solubility experiments

Results derived from solubility experiments for pure SLB and SLB/HP- β -CD lyophilized product at pH 2.0, 4.5 and 6.8 are presented in Figure 5-4. The solubility of pure SLB was 0.0033 ± 0.0018 mg/mL at pH 2.0, 0.005 ± 0.0008 mg/mL at pH 4.5 and 0.0023 ± 0.0003 mg/mL at pH 6.8. It is obvious that the interaction of SLB with HP- β -CD resulted in approximately 10 to 100 fold increase in SLB solubility with the solubilization effect being the most pronounced at pH 6.8.

5.5 Dissolution rate experiments

Results from dissolution studies are shown in Figure 5-5 for SLB-HP- β -CD lyophilized product at pH 2.0, 4.5 and 6.8. Dissolution of pure SLB in the same dissolution media should be considered negligible, since the measured UV absorbance values were lower than 0.005. At pH 4.5 and 6.8, dissolution of SLB from its SLB-HP- β -CD lyophilized product is rapid and the percentage of SLB dissolved reached 70-80% within 1 h. At pH 2.0, dissolution is slower reaching 50% of SLB dissolved within 3 h with no obvious trend for plateau.

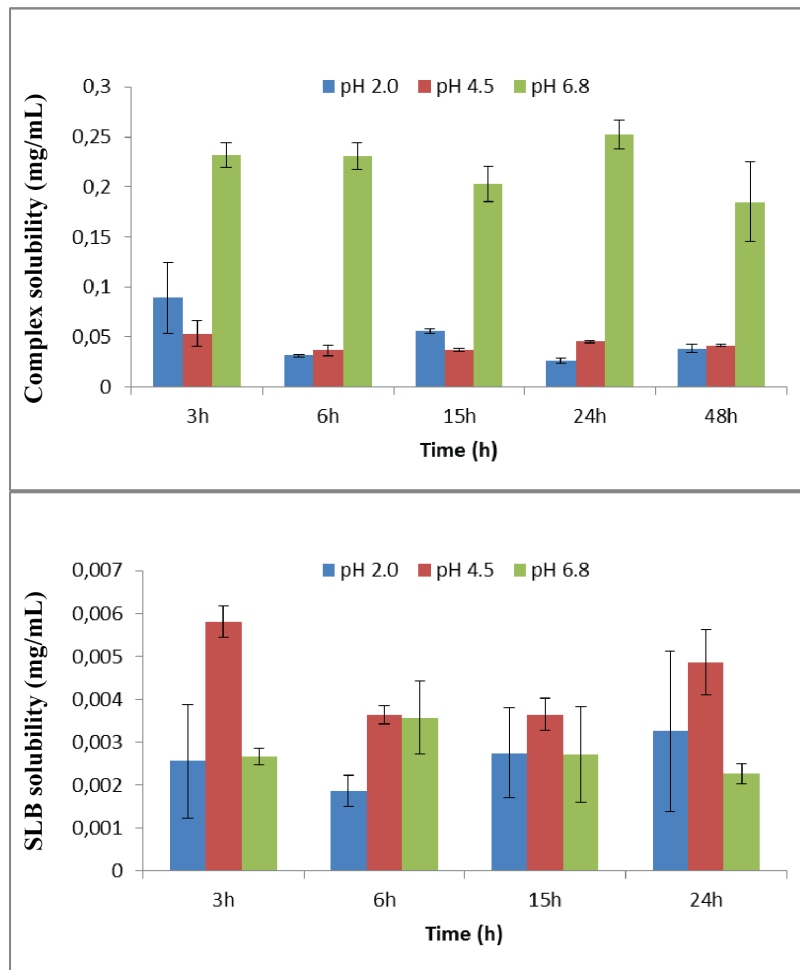


Figure 5-4. Solubility of SLB–HP- β -CD complex (top) and pure SLB (bottom).

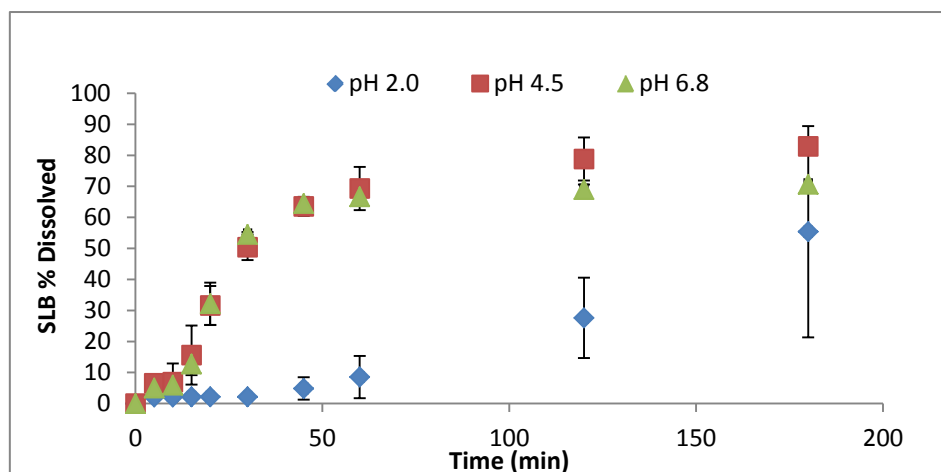


Figure 5-5. pH effect on SLB dissolution from the SLB–HP- β -CD lyophilized.

5.6 Diffusion Ordered NMR Spectroscopy.

Diffusion-ordered spectroscopy (DOSY) is a sensitive NMR technique that allows the determination of self-diffusion coefficients^{325, 326}. Thus, it provides information about the physical properties of the given molecular species like size, shape, and weight and, furthermore, allows determination of proton exchange rate, detection of intermolecular interactions, aggregation, and conformational changes. To study further the formation of the inclusion complex, in aqueous solution, between HP- β -CD and SLB we used DOSY NMR. The superposition of a selected DOSY region of the free HP- β -CD, colored in red, with the relevant DOSY region of the SLB-HP- β -CD lyophilized product, colored in black is illustrated In Figure 7. The diffusion coefficient of free HP- β -CD is $3.66 \times 10^{-10} \text{ m}^2\text{s}^{-1}$. The complex, as was expected, migrates as a single species (black dotted line). The SLB-HP- β -CD inclusion complex showed a decrease in diffusion rate, with respect to the free HP- β -CD, with a diffusion coefficient of $2.55 \times 10^{-10} \text{ m}^2\text{s}^{-1}$, clearly indicating the formation of a complex (Figure 5-6).

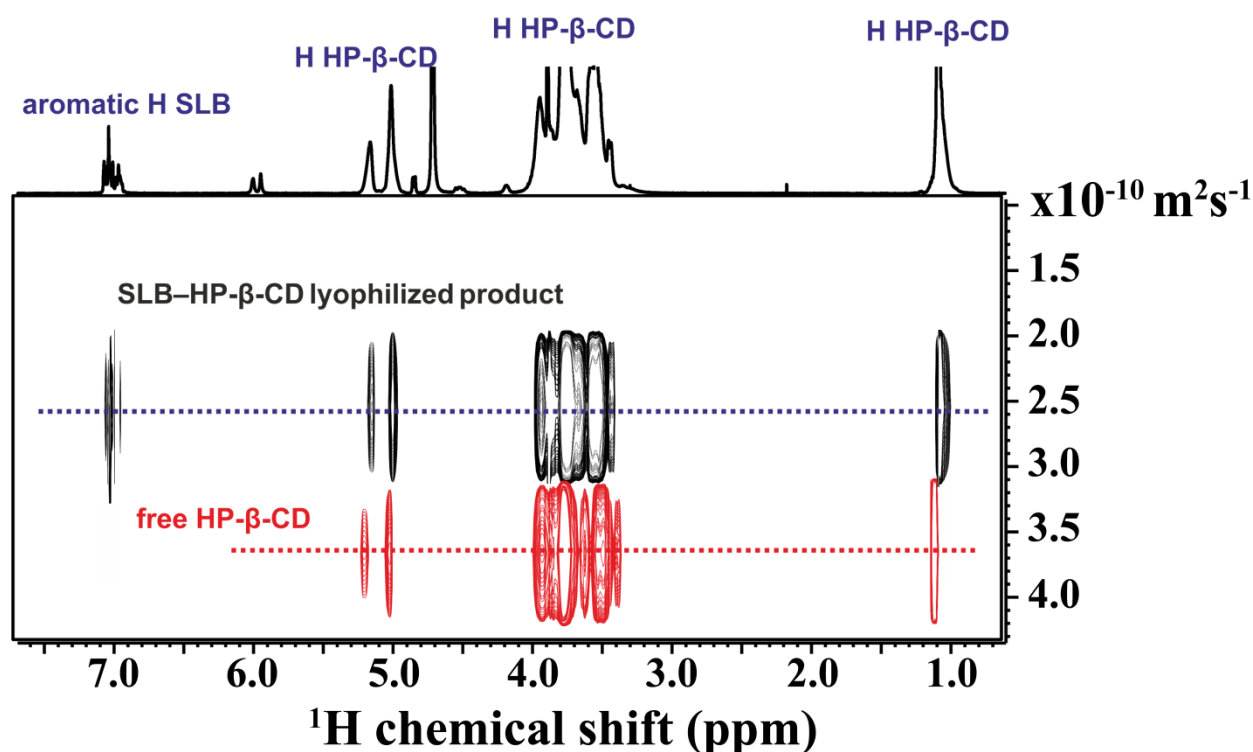


Figure 5-6. Overlapping of the same spectral region from a DOSY spectrum of 0.5 mM of SLB-HP- β -CD lyophilized product (in black), and free HP- β -CD (1.8 mM) (in red). The spectra were recorded in D_2O at room temperature.

5.7 MD Simulations.

The MD simulation performed on the complex of HP- β -CD with SLBA and SLBB showed a relatively stable system. During the 250 ns of the run, SLBA remains inside the ring of HP- β -CD. The RMSD values of cyclodextrin and SLBA during the simulation are shown in Figure 5-7. Despite the significant stability of the system, a conformational change for SLBA was observed at \sim 50 ns of the simulation. This change lasted for 90 ns before the drug stabilized its structure during the last part of the run. Analysis of the trajectories showed that the drug does not form any stable hydrogen bonds with HP- β -CD during the simulation. Instead, the system seems to be stabilized mainly through hydrophobic interactions.

Theoretical calculations, such as the MM-PBSA method have been used to calculate the binding energies of drugs inside cyclodextrin³²⁷⁻³²⁹. The total binding energy of the SLB–HP- β -CD complex, as it was calculated using equations 1-5 for the complete trajectory, was -4.2 kcal/mol, while the enthalpy of the system was -24.8 kcal/mol. This analysis (summarized in Table 5-3) shows that the binding of SLBA to HP- β -CD is energetically favorable. Moreover, it was shown that binding is mostly driven by van der Waals interactions, while the nonpolar solvation term also contributes favorably. A comparison with data reported in the literature^{328, 330} shows that the values reported herein are in qualitative agreement, however predicting less efficient binding than other studies.

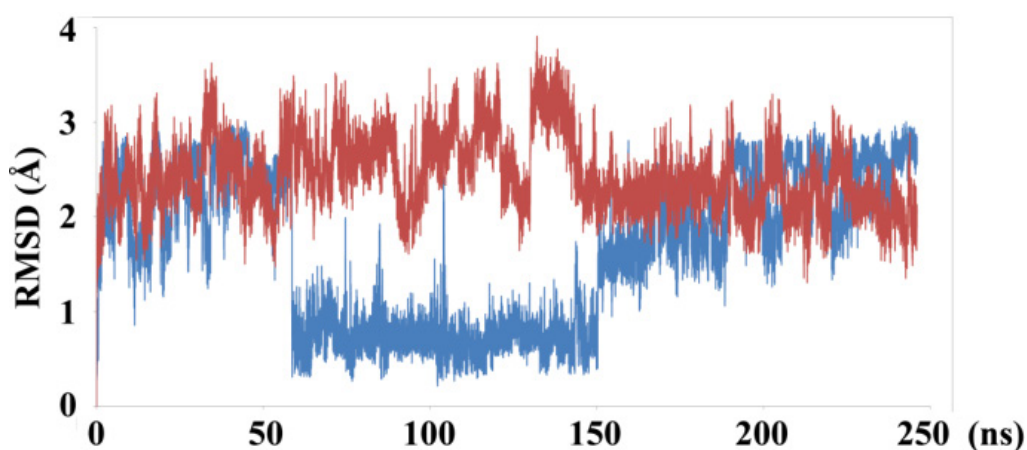


Figure 5-7. RMSD values versus trajectory time of the modified cyclodextrin (red), and all atoms of silybin (in blue).

Representative poses of the SLBA–HP- β -CD complex during the MD run are presented in Figure 5-8.

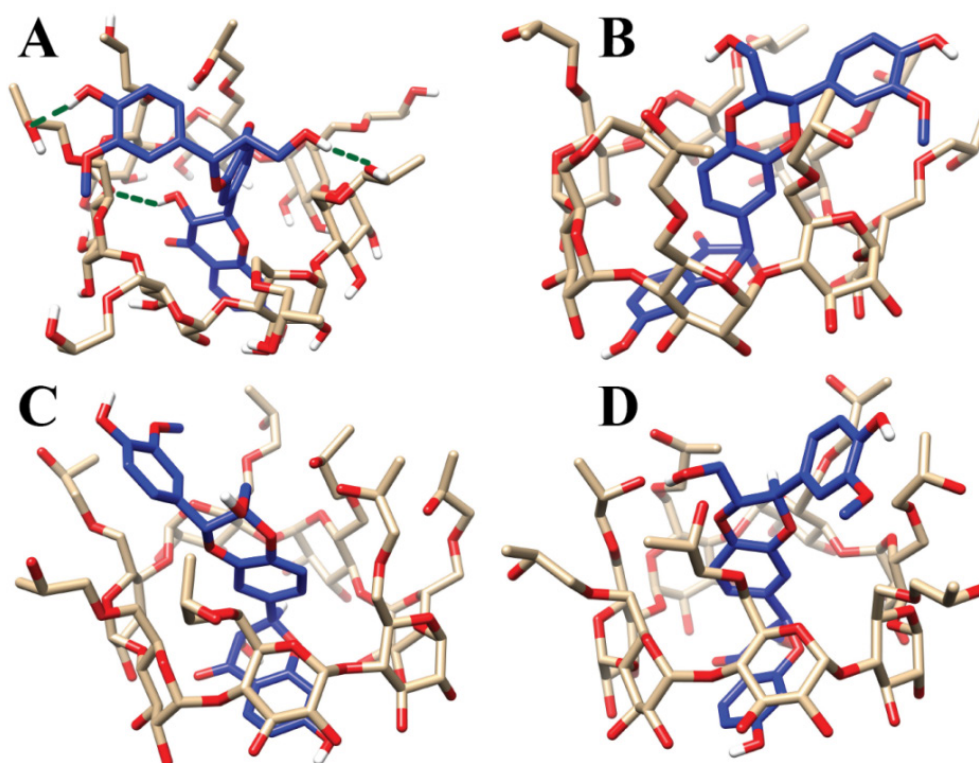


Figure 5-8. The SLBA–HP- β -CD complex: A) as predicted initially by GlideXP (hydrogen bonds are shown in green), B) after 100 ns of MD simulation, C) after 200 ns, and D) at the end of the simulation.

Table 5-3: Binding free energy analysis for the SLBA–HP- β -CD complex as obtained by the MM-PBSA calculations.

Energy Component	Average value	\pm SEM ¹
	(kcal/mol)	
ΔE_{vdw}	-46.74	0.02
ΔE_{elec}	-13.86	0.04
ΔG_{PB}	39.09	0.04
ΔG_{cavity}	-3.29	0.00
ΔE_{gas}	-60.60	0.04
ΔG_{solv}	35.80	0.04

$\Delta H = \Delta E_{\text{gas}} + \Delta G_{\text{solv}}$ (eq. 2)	-24.80	0.023
$-T\Delta S_{\text{total}}$	-20.58	0.023
$\Delta G_{\text{binding}}$	-4.22	0.023²

¹Standard error of the mean (SEM): SEM = Standard deviation/ \sqrt{N} . N is the number of trajectory frames used during the MM-PBSA calculations (6250 frames for entropy and 25000 frames for everything else). ²Pooled standard error of the mean.

5.8 MTT assay.

Recent publications have highlighted that silibinin induces cell death in MCF-7 human breast cancer cells either by activating caspase-8 and leading to apoptosis through mitochondrial pathway ³³¹ or by inhibiting phospho-ERK and phospho-Akt through the downregulation of Notch-1 ³³². It has, also, been reported the IC₅₀ of silibinin on MCF-7 cells (105 $\mu\text{M} \pm 18.5$) but not a direct comparison with the SLB-HP- β -CD complex ³³³. In the present work, MCF-7 cells have been exposed to various concentrations of SLB-HP- β -CD, free silibinin and drug free HP- β -CD in order to assess differences in their effect to cells' viability by MTT assay. Both silibinin and the complex decreased proliferation in a dose-dependent manner, with a higher reduction observed in those cells, which were treated with the complex, as shown in Figure 5-9. Cells treated with HP- β -CD showed an absorbance value equal to 96% of control, indicating that it's not toxic to cells.

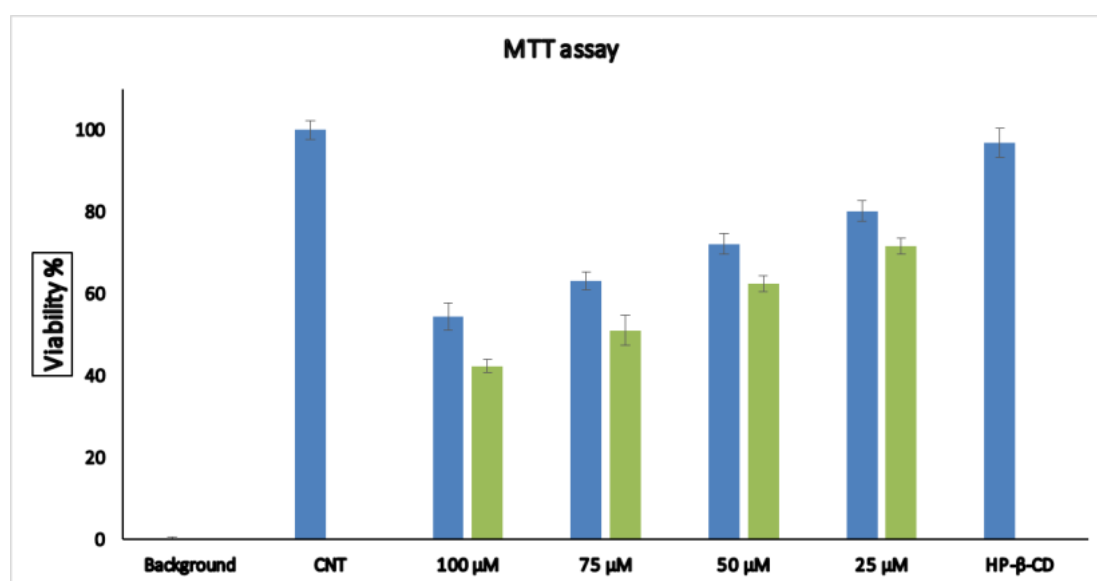


Figure 5-9. Effects of SLB-HP- β -CD (in green) and SLB (in blue) on cell proliferation determined by MTT assay. Data are the result of 2 independent experiments performed in triplicates. The standard error of each measurement is also presented ³¹⁹.

5.9 Conclusions

The DSC, mass spectrometry, DOSY and solid state ^{13}C CP/MAS results confirmed the complexation of SLB with HP- β -CD. High resolution 2D NOESY NMR spectroscopy combined with MD studies showed detailed information on the interactions of silibinin with HP- β -CD. This information was in agreement with solid state ^{13}C CP/MAS spectra utilizing the chemical shift changes during the complexation. The two condensed rings of SLB were incorporated in the lipophilic segment of HP- β -CD while the aromatic ring bearing a free phenolic hydroxyl and being methylated at ortho position is oriented outside the HP- β -CD, thus interacting with the hydroxypropyl segment. Examples of encapsulation of drugs from the literature possessing various aromatic rings are discussed and are in harmony with results obtained in the present study.

The observed 10 to 100 fold increase in SLB solubility upon interaction with HP- β -CD compared to pure SLB, as well as the rapid and more than 50% dissolution of SLB from the lyophilized SLB-HP- β -CD product at the entire pH range studied, suggest the possibility of enhanced *in vivo* dissolution and increased bioavailability of the SLB-HP- β -CD lyophilized product after oral administration. The observed enhanced cytotoxicity presented in the human breast cancer cell line MCF7 of the SLB-HP- β -CD with regards to the parent compound highlights the activity amplification that can be achieved with relevant formulations.

6 Chapter 6: Cancer delivery of quercetin through a pH responsive calixarene–gold nanoparticle

In the present chapter are reported the different analytical techniques and computational methods to investigate in molecular level the architecture of the quercetin-calixarene complex.

6.1 Determination of the Binding constant of the quercetin –calixarene complex

From the equation 3-9, plotting the values of $[\text{Calix}]/\text{abs}$ versus $1/[\text{Qrc}]$, a straight line was obtained from which the binding constant and correlation coefficient were obtained (Figure 6-1). The calculated binding constant (K_a) obtained from the ratio of the intercept to the slope is $K = 8.89 \times 10^3 \text{ l mol}^{-1}$. High value of binding constant suggests *p*-sulphonatocalix[4]arene possesses a compact framework and high π -electron density in the cavity leading to effective π -stacking interactions with guests and then forms stable complexes with Qrc.

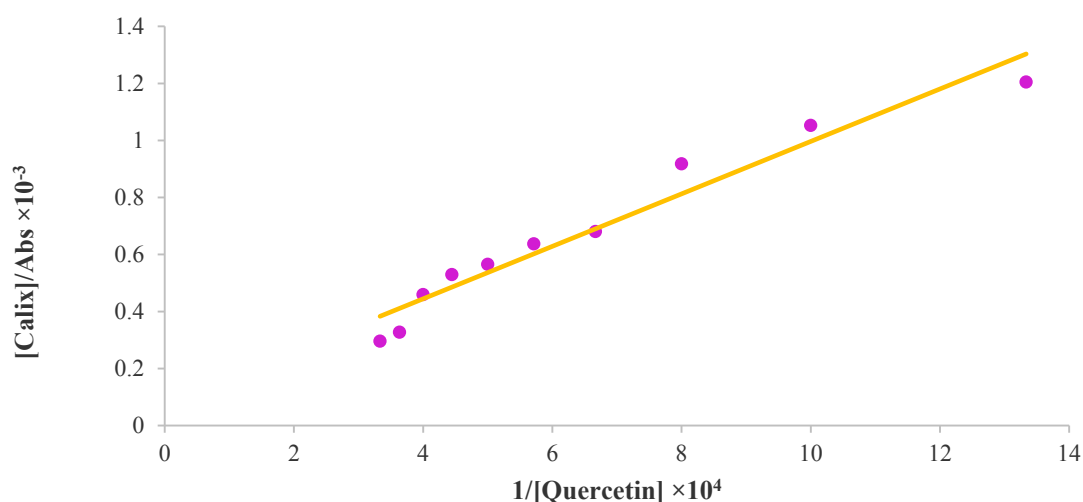


Figure 6-1 Benesi-Hildebrand plot for the complex formation of *p*-sulphonatocalix[4]arene/Quercetin.

6.2 Job's plot

Validation of the stoichiometric composition of Calix-Qrc complex was carried out by Job's method³³⁴. Figure 6-2 shows the relevant plot between the absorbance (274 nm) and the mole

fraction (X). The maximum absorbance was observed at 0.5, confirming the 1:1 stoichiometry for the complex.

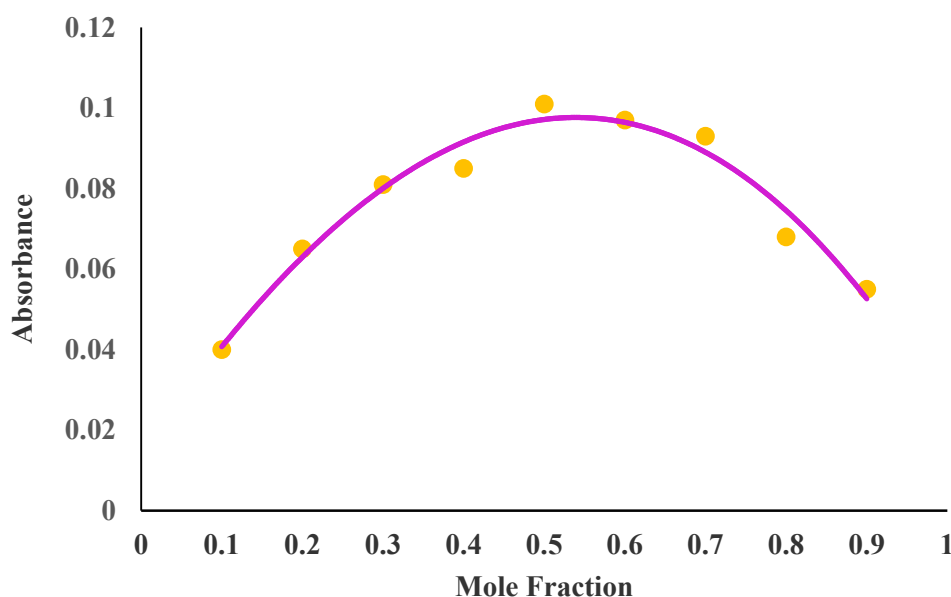


Figure 6-2. Job's plot for *p*-sulphonatocalix[4]arene-quercetin complex (Conc. 1×10^{-4} M)

6.3 Solid State NMR spectroscopy

^1H - ^{13}C CPMAS NMR spectra of Qrc, *p*-sulphonatocalix[4]arene sodium salt (Calix), mixture of Qrc and Calix with a molar ratio of 1:1, complex of Qrc and Calix with a molar ratio of 1:1 (Qrc:Calix complex), and complex of Qrc, Calix and Au-NPs (Qrc:Calix:Au-NPs complex) were recorded at 20 °C (Figure 6-3). The obtained spectrum for quercetin is in agreement with the one recorded by Wamer and Zielinski³³⁵ using a 300 MHz spectrometer. The spectrum obtained with our 600 MHz spectrometer and with faster sample rotation is characterized by better resolution and absence of many spinning bands interfering with the isotropic peaks. In both spectra, however, the multiplicity of the isotropic peaks indicates that quercetin either exhibits polymorphism or crystallizes with a crystallographic asymmetric unit that contains several quercetin molecules. The spectrum of Calix is almost identical to the one reported in the literature³³⁶. The spectrum of a simple mixture of the two compounds, Qrc and Calix, corresponds to a simple sum of two individual spectra of the two substances. This indicates that interactions among Qrc and Calix particles are negligible in the mixture.

The complexing of Qrc and Calix results in tremendously different spectrum compared to the spectrum of the simple mixture. All peaks in the spectrum of the complex are broadened, but

do not exhibit significant shifts in the resonance positions. The broadening can be attributed to the strong interactions between the two molecules leading to the formation of a less ordered (amorphous) material. The broadening is not localized to specific structural segments of the two molecules, suggesting the presence of amphipathic interactions. It is expected that the aromatic segment of quercetin is incorporated into the hydrophobic core of calixarene exerting aromatic-aromatic interactions, while the phenol hydroxyl groups of quercetin point to the phenolic and sulphate groups of calixarenes. Such entrapment of drug molecules is common and it has been observed for many amphiphilic drugs in other supramolecular structures such as cyclodextrins³³⁷. The broadening is so severe in the region of *cca* 80-100 ppm that assignment of quercetin peaks is no longer possible. Severe broadening is also observed in the region of *ca* 140-190 ppm and precludes the differentiation of the quercetin and the calixarene peaks.

Quercetin was also complexed with Au-NPs. Again, the complexation leads to broadening of the peaks in the ¹H-¹³C CPMAS NMR spectrum. Additional peaks in the region of 50-80 ppm can be assigned to HSCH₂CH₂O- and -CH₂O peaks. Quercetin's peaks in the region of 80-100 ppm are no longer observable, which is most probably due to very strong interactions with the gold nanoparticles. Calixarene peaks attributed to carbons 3 and 5 are no more resolved, thus indicating that the interactions between quercetin and calixarene are also stronger. The signals at about 180 ppm are narrower than the corresponding signals in the spectrum of the Qrc:Calix complex. They are also shifted to higher resonance frequencies. Overall, the differences between the spectra of the two different complexes (Qrc:Calix versus GNPs@Calix-Qrc) suggest that the interactions in the complexes with nanoparticles differ from the interactions in the Q:C complexes and show that there is specificity in the different supramolecular complexes.

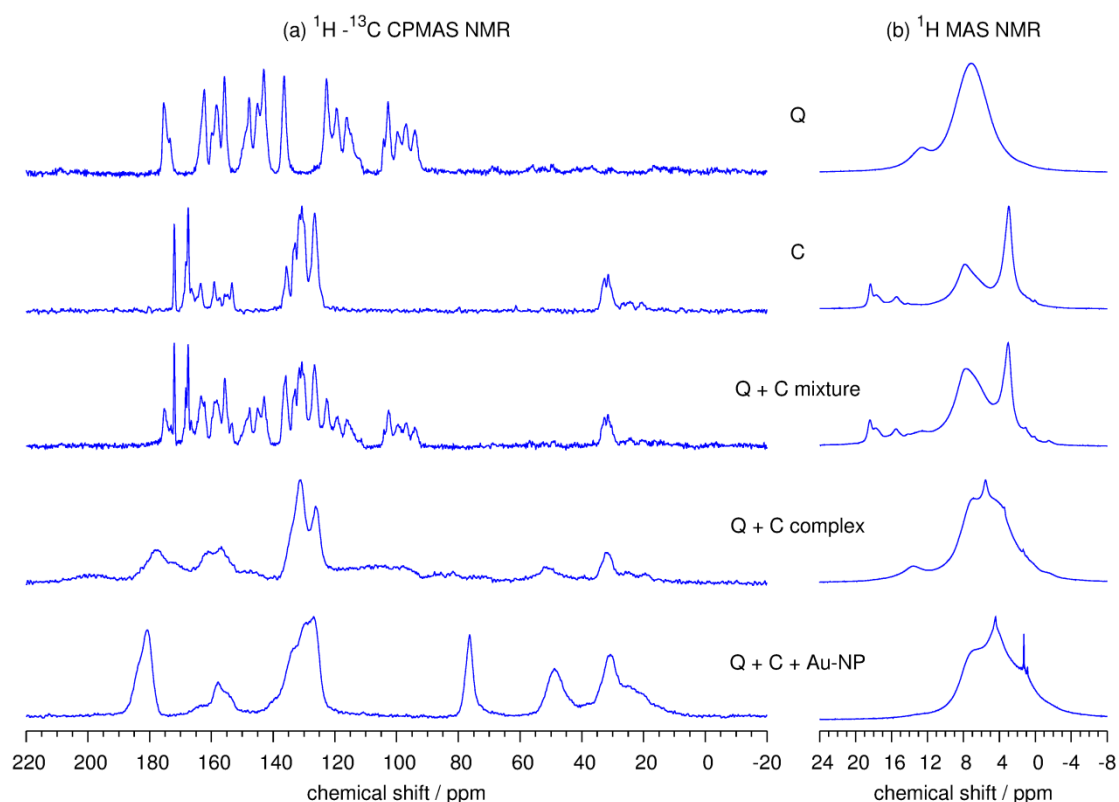


Figure 6-3. $^1\text{H}-^{13}\text{C}$ CPMAS (a) and ^1H MAS (b) NMR spectra of quercetin (Q), calixarene (C), simple mixture of Q and C, Q:C complex, and GNPs@Calix-Qrc complex.

^1H MAS NMR spectra (Figure 6-5b) provide some evidence of the hydrogen bondings in the samples. Hydrogen bonds can be clearly detected in the Q sample in the region of 12-15 ppm and in the C sample between 15 ppm and 20 ppm. In the Q:C complex only hydrogen bonds due to quercetin are preserved and in the GNPs@Calix-Qrc complex no hydrogen bonding is detected.

6.4 Molecular modeling

In Figure 6-4A is shown the result of the docking between calixarene and quercetin, while Figure 6-4B shows the optimized structure of the complex using the X3LYP/6-31G** density functional. As predicted by the solid state NMR data the complex is stabilized by both hydrogen bonds and π - π interactions. Quercetin is partially included within the host since it does not cross the calixarene ring. The BSSE-corrected cc-pVTZ(-f) binding energy was found to be -55.84 kcal/mol (cc-pVTZ(-f) BSSE correction: 3.49) while the cc-pVQZ(-g) binding energy was found to be -65.52 kcal/mol (cc-pVQZ(-g) BSSE correction: 1.75). The extrapolated binding energy was calculated at -72.11 kcal/mol. These values are in good agreement with those of found by Barroso-Flores *et al.*³³⁸ in their work on guest-host complexation of drugs with calixarenes and show a stable complex³³⁸. During the MD

simulations quercetin was for most of the time partially included in the calixarene and, fewer times, completely included within the calixarene (Figure 6-4C). In one of the simulations quercetin is detached from the calixarene molecule but still remains close developing mainly π - π interactions with the host. Analysis of the trajectories using ptraj shows that although quercetin develops many hydrogen bonds during the simulation with calixarene they do not tend to last long. The results from the MMPBSA calculations are shown in table 6-1. The binding energy of the complex was found to be -6.20 kcal/mol. The binding is driven mainly by van der Waals and electrostatic (Coulombic) interactions. This analysis shows that the complex is energetically favorable. The value of the binding constant between calixarene and quercetin in this study was determined to be $K= 8.89 \times 10^3 \text{ l mol}^{-1}$. If this value is used to find the molar Gibbs free energy of the complex via the equation $\Delta G = -RT \ln K_a$ (where R is the ideal gas constant and T the temperature set at 300K), the binding affinity of the complex is found to be -5.42 kcal/mol. A comparison of the experimental value and the one predicted using the MMPBSA method shows that they are quite close to each other.

Table 6-1: Binding free energy analysis for the quercetin-calixarene complex as obtained by the MM-PBSA calculations.

Energy Component	Average value (kcal/mol)	\pm SEM ¹
ΔE_{vdw}	-12.06	0.22
ΔE_{elec}	-8.31	0.06
ΔG_{PB}	14.08	0.06
ΔG_{cavity}	-1.13	0.00
ΔE_{gas}	-20.37	0.22
ΔG_{solv}	12.95	0.06
$\Delta H_{\text{total}} = \Delta E_{\text{gas}} + \Delta G_{\text{solv}}$	-7.42	0.21
$-T\Delta S_{\text{total}}$	-1.22	0.10
$\Delta G_{\text{binding}}$	-6.20	0.21

¹Standard error of the mean (SEM): SEM = Standard deviation/ \sqrt{N} . N is the number of trajectory frames used during the MM-PBSA calculations

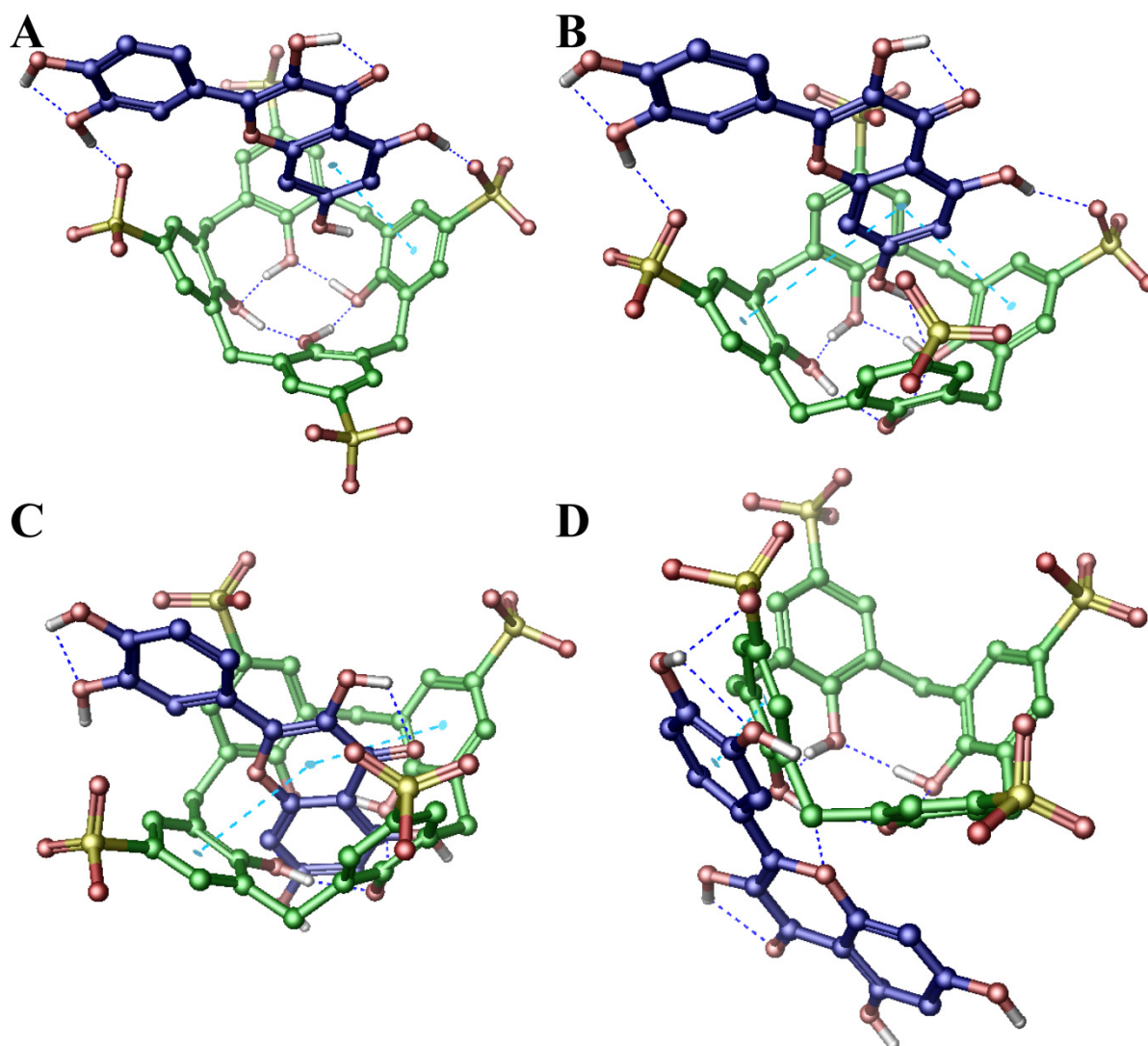


Figure 6-4: The quercetin-calixarene complex: A) as predicted initially by GlideXP (hydrogen bonds are shown in blue and π - π interactions in cyan), B) after the optimization using the X3LYP/6-31G** basis set, C) quercetin completely included in the calixarene, and D) quercetin detached from the calixarene but still interacting with it.

6.5 Electrophoretic light Scattering and TEM

The charge shape and size of the GNPs@Calix-Qrc Complex was also evaluated with dynamic & electrophoretic light Scattering and TEM. The mean hydrodynamic diameter (D_H) and surface charge of the GNPs@Calix-Qrc Complex was investigated in aqueous dispersions at pH=7 at a concentration of 0.4% w/v. The Number Averaged distribution of D_H (Figure 6-5) follows a monomodal profile with peak mean diameter at ~ 4.8 nm. Results are in very good agreement with images obtained from TEM. Electrophoretic mobility scattering allowed for the determination of zeta potential which in turn provides an estimate of the surface charge characteristics of the GNP³³⁹. The value of -13.9 mV corresponds to a negative surface charge and is ascribed to the sulfonic groups of the calixarene moiety

physisorbed on the GNPs@Calix-Qrc Complex surface, thus validating the successful organic modification. Furthermore, the presence of surface charge has been found to prolong the colloidal stability of the suspended GNPs through electrostatic repulsion mechanism.

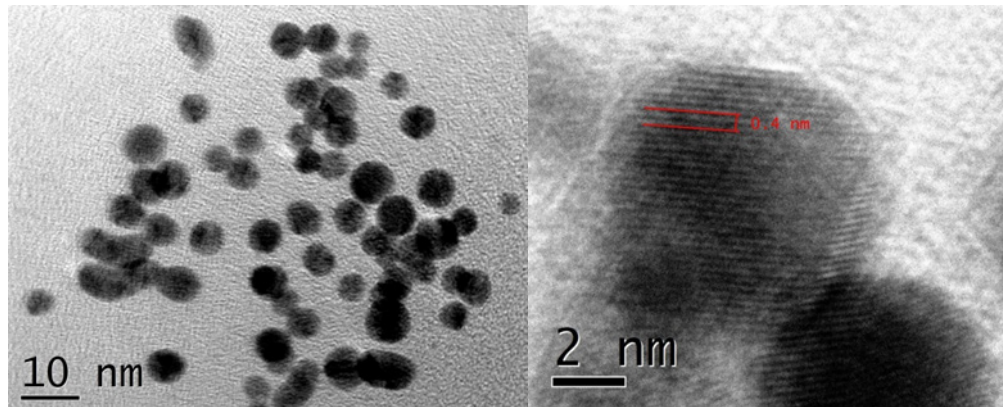


Figure 6-5: A) HR-TEM Image of finely dispersed GNPs@Calix-Qrc Complex and B) ultra-high magnification image of an isolated particle where the distance between two successive 200 crystal planes is highlighted³⁴⁰.

7 Conclusions

In the present thesis computational methods including molecular docking, induced fit docking, molecular dynamics and MM-PBSA calculations were used to characterize guest-host interactions.

In the first part of the thesis the conformational properties of both olmesartan and olmesartan methyl ether were studied in solution and in the receptor's site. The molecular docking and dynamics results provided a plausible explanation for the *in vitro* results. Mutations in the AT₁R such as Y113F, K199Q, H256A and Q257A lower the binding affinity of olmesartan. It is possible that these residues are not in direct contact with the ligand and their mutation affect ligand binding indirectly, by altering the overall conformation of AT₁R. Prime MM-GBSA calculations for the five molecules studied (olmesartan, olmesartan methyl ether, R781253, R794847 and R239470) revealed that olmesartan methyl ether has less favored $\Delta G_{\text{binding}}$ than olmesartan. This is attributed to its disfavored Coulombic interactions.

SLB-HP- β -CD complex was confirmed by DSC, mass spectrometry, DOSY and solid state ¹³C CP/MAS. High resolution 2D NOESY NMR spectroscopy combined with MD studies showed detailed information on the interactions of silibinin with HP- β -CD. This information was in agreement with solid state ¹³C CP/MAS spectra utilizing the chemical shift changes during the complexation. The two condensed rings of SLB were incorporated in the lipophilic segment of HP- β -CD while the aromatic ring bearing a free phenolic hydroxyl and being methylated at ortho position is oriented outside the HP- β -CD, thus interacting with the hydroxypropyl segment. Examples of encapsulation of drugs from the literature possessing various aromatic rings are discussed and are in harmony with results obtained in the present study. MM-PBSA calculations showed that the binding energy of the complex is a favorable one. All these results show that the complex SLB-HP- β -CD complex could be used as a new formulation for silibinin after Silipide (Siliphos®), a formulation of silibinin with phosphatidylcholine. In a recent study by Christodoulou *et al.*³⁴¹ pharmacokinetics and pharmacodynamics studies as well as *in vivo* experiments were performed. The results were quite promising and showed that the lyophilized product can overpass both solubility and absorption problems of pure silibinin.

The complexing agent *p*-sulphonatocalix[4]arene has been used to enhance the solubility and bioavailability for the poorly water soluble quercetin. The 1:1 complex formed between *p*-sulphonatocalix[4]arene and quercetin was confirmed by Job's plot, solid state NMR and

molecular modeling. A gold nanoparticle was then established on the basis of this architectural scaffold which presented enhanced potency against cancer cell lines. The nanoparticle was characterized to be of spherical shape, negative charge and bears a size of 4.8 nm. These facts show that natural products can be embedded on programmable drug delivery systems that can both enhance their aqueous solubility as also bioactivity.

8 Abbreviations

ACE	Angiotensin converting enzyme
AMBER	Assisted Model Building with Energy Refinement
Ang II	Angiotensin II
ARBs	Ang II receptor blockers
B3LYP	Becke, three-parameter, Lee-Yang-Parr Hybrid functionals
BPT	Biphenyltetrazole
Calix	<i>p</i> -sulphonatocalix[4]arene
CD	Cyclodextrin
CXCR-4	C-X-C chemokine receptor type 4
DFT	Density functional theory
DOSY	Diffusion-order spectroscopy
DPPC	Dipalmitoylphosphatidylcholine
DMSO	Dimethyl sulfoxide
DSC	Differential Scanning Calorimetry
EL	Extracellular loops
GAFF	General AMBER force field
GIAO	Gauge Including Atomic Orbital
GNP	Gold Nanoparticles
GPCR	G-protein coupled receptor
HF	Hartree-Fock
HP- β -CD	2-hydroxypropyl- β -cyclodextrin
IFD	Induced fit docking
IL	Intracellular loops
MD	Molecular Dynamics
MM	Molecular mechanics
MM-GBSA	Molecular mechanics generalized Born surface area
MM-PBSA	Molecular mechanics Poisson-Boltzmann surface area
MS	Mass Spectrometry
NOE	Nuclear Overhauser effect
OPLS	Optimized Potentials for Liquid Simulations
PES	Potential Energy Surface
PMEMD	Particle Mesh Ewald Molecular Dynamics

PRCG	Polak–Ribiere conjugate gradient
QM	Quantum mechanics
QPLD	QM-Polarized Ligand Docking
Qrc	Quercetin
RAS	Renin angiotensin system
RESP	Restrained electrostatic potential
RMSD	Root mean square deviation
ROE	Rotating Frame Overhauser Effect
SLB	Silybin/silibinin
TMs	Membrane-spanning segments
XRD	X-Ray Diffraction
XRPD	X-ray Powder Diffraction

9 Permission/License

Figures 1-1 and 1-2 in chapter 1 are reprinted from the article: Rational drug design and synthesis of molecules targeting the angiotensin II type 1 and type 2 receptors, *Molecules*, 20(3):3868-3897, 2015. The article is published under a CC BY-NC-SA 4.0 (Attribution-NonCommercial-ShareAlike 4.0 International) license. The material can be shared and adapted freely. Figures 1-3, 1-4, 1-5, 1-6 are reprinted from the article: Leveraging NMR and X-ray Data of the Free Ligands to Build Better Drugs Targeting Angiotensin II Type 1 G-Protein Coupled Receptor, *Current Medicinal Chemistry*, 23(1), 36-59, 2016. The publisher for this copyrighted material is Bentham Science Publishers Ltd. Publisher granted a non-exclusive license to use this material (License number 4053150529719). Figures 1-9 and 1-10 are reprinted from the article: Calixarenes in Biocatalysis and Cancer Therapy, *Current Organic Chemistry*, 20(10), 1043-1057, 2016. The publisher for this copyrighted material is Bentham Science Publishers Ltd. Publisher granted a non-exclusive license to use this material (License number 4053150073277).

Material and figures in chapter 4 are reprinted from the article: Understanding the bioactivity of olmesartan and its methyl ether by charting the conformational space through NMR and molecular modeling, *Arabian Journal of Chemistry*, doi: 10.1016/j.arabjc.2016.11.014. The article is published under a CC BY-NC-ND 4.0 (Attribution-NonCommercial-NoDerivatives 4.0 International) license by Elsevier Ltd. The material can be shared in any medium or format.

Material and figures in chapter 5 are reprinted with permission from the article: Investigation of the interactions of silibinin with 2-hydroxypropyl- β -cyclodextrin through biophysical techniques and computational methods *Molecular Pharmaceutics*, 12(3), 954-965, 2015. Copyright (2015) American Chemical Society.

10 PUBLICATIONS-PRESENTATIONS

10.1 Publications in International Journals

The underlined publications are presented in the thesis. In parentheses are shown the 2015 impact factors of the journals.

- 1) “The application of solid-state NMR spectroscopy to study Candesartan Cilxetil (TCV-116) membrane interactions. Comparative study with the AT₁R antagonist drug olmesartan”

Biochimica et Biophysica Acta-Biomembranes, 1838, 2439-2450, **2014** (I.F. 3.687)

Ntountaniotis D., **Kellici T.**, Tzakos A., Kolokotroni P., Tselios T., Becker-Baldus J., Glaubitz C., Makriyannis A., Mavromoustakos T.*.

- 2) “Rational drug design and synthesis of molecules targeting the angiotensin II type 1 and type 2 receptors”

Molecules (Basel, Switzerland), 20(3):3868-3897, **2015** (I.F. 2.465)

Kellici, T. F., Tzakos A. G., Mavromoustakos T.*

- 3) “Investigation of the interactions of silibinin with 2-hydroxypropyl- β -cyclodextrin through biophysical techniques and computational methods”

Molecular Pharmaceutics, 12(3), 954-965, **2015** (I.F. 4.342)

Kellici, T. F. et al., Tzakos A.G.*, Mavromoustakos T.*

- 4) “Branched-chain sugar nucleosides: Stereocontrolled synthesis and bioevaluation of novel 3'-C-trifluoromethyl and 3'-C-methyl pyranonucleosides”

Carbohydrate Research, 407, 170-178, **2015** (I.F. 1.817)

Kollatos, N., Manta, S., Dimopoulou, A., Parmenopoulou, V., Triantakostanti, V.V., **Kellici, T. F.**, Mavromoustakos, T., Schols, D., Komiotis, D.*

- 5) “A novel synthetic luteinizing hormone-releasing hormone (LHRH) analogue coupled with modified β -cyclodextrin: Insight into its intramolecular interactions”

Biochimica et Biophysica Acta - General Subjects, 1850 (1), 159-168, **2015** (I.F. 5.083)

Kordopati, G.G., Tselios, T.V., **Kellici, T.**, Merzel, F., Mavromoustakos, T., Grdadolnik, S.G., Tsivgoulis, G.M.*

- 6) “Rational drug design paradigms: the odyssey for designing better drugs”

Combinatorial Chemistry & High Throughput Screening, 18(3):238-256, **2015** (I.F. 1.041)

Kellici T.F., et al., Mavromoustakos T.*

- 7) “Rosemary tea consumption results to anxiolytic- and anti-depressant-like behavior of adult male mice and inhibits all cerebral area and liver cholinesterase activity; phytochemical investigation and *in silico* studies”
Chemico Biological Interactions, 237, 47-57, **2015** (I.F. 2.618)
 Ferlemi A. Katsikoudi A., Kontogianni V. G., **Kellici T. F.**, Iatrou G., Lamari F. N., Tzakos A. G.*, Margarity M.*
- 8) “Pharmaceutical compositions for antihypertensive treatments: a patent review.”
Expert Opinion in Therapeutic Patents. 25(11), 1305-1317, **2015** (I.F. 4.626)
Kellici T. F., Liapakis G., Tzakos A. G., Mavromoustakos T.*
- 9) “Leveraging NMR and X-ray Data of the Free Ligands to Build Better Drugs Targeting Angiotensin II Type 1 G-Protein Coupled Receptor”
Current Medicinal Chemistry, 23(1), 36-59, **2016** (I.F. 3.455)
Kellici T.F., *et al.*, Mavromoustakos T.*
- 10) “Calixarenes in Biocatalysis and Cancer Therapy”
Current Organic Chemistry, 20(10), 1043-1057, **2016** (I.F. 1.949)
Karakurt S., **Kellici T. F.**, Mavromoustakos T., Tzakos A. G.*, Yilmaz M.*
- 11) “New hydrazones of 5-nitro-2-furaldehyde with adamantanealkanohydrazides: synthesis, conformational analysis and trypanocidal activity”
Medicinal Chemistry Communications, 7, 1229–1236, **2016** (I.F. 2.319)
 Foscolos A., Papanastasiou I., Foscolos G.B.*, Tsoinias A., **Kellici T.F.**, Mavromoustakos T., Taylor M. C., Kelly J.M.
- 12) “Deconvoluting the synergistic antiplatelet activity of an olive leaf extract”
Journal of Agricultural and Food Chemistry, 64(22), 4511-4521, **2016** (I.F. 2.857)
 Kontogianni V. G., Tsoumani M. E., **Kellici T.F.**, Mavromoustakos T., Gerothanassis I. P., Tselepis A. D., Tzakos A. G.*
- 13) “PRESS: Protein S-sulfenylation Server”
Bioinformatics, (Oxford University Press), In Press (I.F. 5.766)
 Sakka M., Tzortzis G., N. Bekas, M. D. Mantzaris, **T. F. Kellici**, A. Likas, D. Galaris, I. P. Gerothanassis, A. G. Tzakos*
- 14) “NMR structural elucidation of 35-55 Myelin Oligodendrocyte Glycoprotein epitope implicated in the induction of Experimental Autoimmune Encephalomyelitis”
 Ntountaniotis D., Kordopati G. G., Vanioti M., **Kellici T. F.**, Mavromoustakos T.*, G. Spyroulias, Golic Grdadolnik S., Tselios T. V. *
Journal of Biomolecular Structure and Dynamics, In Press (I.F. 2.300)

15) “Molecular Basis of Interactions of Quercetin with 2-Hydroxypropyl-β-Cyclodextrin”
Kellici T. F., et al., A. G. Tzakos*

International Journal of Pharmaceutics, 511, 303–311, 2016 (I.F. 3.994)

16) “The use of J-coupling as a sole criterion to assign the total absolute stereochemistry of new pyrrolidinone class synthetic analogs, derived from S-pyroglutamic acid.”

Journal of Molecular Structure, 1129, 195-199, 2017 (I. F. 1.780)

Kellici T. F. et al. T. Mavromoustakos*

17) “Understanding the bioactivity of olmesartan and its methyl ether by charting the conformational space through NMR and molecular modeling”

Arabian Journal of Chemistry, doi: 10.1016/j.arabjc.2016.11.014 (I.F. 3.613)

Kellici T.F.*, Ntountaniotis D., Liapakis G., Tzakos A. G., Mavromoustakos T.*

18) “Controlled Release from Solid Pharmaceutical Formulations of two new Adamantane Aminoethers with Antitubercular Activity”

Arzneimittelforschung-Drug Research, Accepted (I.F. 0.701)

Vlachou, M.*; Siamidi A.; Diamantidi E.; Iliopoulou A.; Ioannidou V.; Kourbeli V.; Foscolos A-S.; Papanastasiou I.; Vocat A.; Cole S.T.; Karalis V.; **Kellici T.**; Mavromoustakos T.

19) “Molecular requirements involving human platelet protease-activated receptor-4 mechanism of activation by peptide analogues of its tethered ligand”

Platelets, Accepted (I.F. 3.213)

Moschonas, I.; **Kellici, T. F.**; Mavromoustakos, T.; Stathopoulos, P.; Tsikaris, V.; Magafa, V.; Tzakos, A. G.; Tselepis, A. D.*

10.2 Publications in Greek Journals

- «Νέα πολυστοχευμένα φάρμακα κατά των πολυπαραγοντικών ασθενειών», Ιατρικά Νέα, Τεύχος 50, Έτος 9^ο, σελ. 48-50, Διμηνιαίο Επιστημονικό Περιοδικό.

Θ. Μσυρομούστακος, Χ. Τζούπης, Αικ. Κουκουλίτσα, Τ. Κελίτσης, Γ. Λεώνης, Μ. Παπαδόπουλος.

- «Οι κυκλοδεξτρίνες ως υποστρώματα για την παρασκευή φαρμακευτικών προϊόντων», Ιατρικά Νέα, Τεύχος 59, Έτος 11, σελ. 32-37 Διμηνιαίο Επιστημονικό Περιοδικό
Μ. Πανοπούλου, Γ Σκουφάς, Δ. Ντουντανιώτης, Τ. Kellici, Θ. Μαυρομούστακος

10.3 Poster Presentations

2^ο Πανελλήνιο Συνέδριο Θρόμβωσης-Αντιθρομβωτικής Αγωγής

1. Μελέτη της επίδρασης πεπτιδικών αναλόγων του εκλεκτικού αγωνιστή του PAR-4 στα αιμοπετάλια και ερμηνεία της δράσης τους με τη χρήση λογισμικών προσομοίωσης και κρυσταλλικών δομών ευκρινείας.

H. X. Μοσχονάς, T. Kellici, Π.Τ. Σταθόπουλος, Β. Τσικάρης, Β. Μαγκαφά, Θ. Μαυρομούστακος, Α. Γ. Τζάκος, Α.Δ. Τσελέπης.

32nd Cyprus-Noordwijkerhout-Camerino Symposium (18-22 Μαΐου 2014 Κύπρος)

2. Hydrazones of 5-nitro-2-furanecarboxaldehyde with 1-adamantane-alkanoyhydrazides with probable trypanocidal activity.

Angeliki Sofia Foscolos, Ioannis Papanastasiou, Georgios Foscolos, Andrew Tsoinīs, Tahsin Kellici, Thomas Mavromoustakos

3. Interactions of Silybin-A with cyclodextrins derivatives using solid and liquid state NMR spectroscopy, differential scanning, and isothermal titration calorimetry as well as molecular dynamics simulations. Poster Prize from ChemMedChem.

T. Kellici, D. Ntountaniotis, G. Leonis, M. Chatziathanasiadou, A. Tzakos, J. Baldus, C. Glaubitz, G. Valsami, E. Archontaki, K. Viras, M. G. Papadopoulos, T. Mavromoustakos

4. Conformational studies of LHRH analogue conjugated with cyclodextrin using 2D NMR and molecular modeling.

Golfo Kordopati, Theodore Tselios, Tahsin Kellici, Franci Merzel, Thomas Mavromoustakos, Simona Golic-Grdadolnik, Gerasimos Tsivgoulis

IXth Joint Meeting in Medicinal Chemistry (7-10 Ιουνίου 2015 Αθήνα)

5. Preparation and investigation of the inclusion complex of silibinin with 2-hydroxypropyl-β-cyclodextrin

T. Kellici, D. Ntountaniotis, G. Leonis, M. Chatziathanasiadou, A. Tzakos, J. Baldus, C. Glaubitz, G. Valsami, E. Archontaki, K. Viras, M. G. Papadopoulos, T. Mavromoustakos

International Society On Thrombosis And Haemostasis Congress, 20-25 June 2015

6. Effect of PAR-4 tethered-ligand peptide analogs on human platelet activation

I. C. Moschonas, T. Kellici, V. Magafa, T. Mavromoustakos, A. G. Tzakos, A. D. Tselepis

Kinase 2016: Next Generation Inhibitors on Monday 16 – Tuesday 17 May 2016 at BioCity,

Nottingham, UK.

7. Design and Synthesis of Novel pyrimidinopyrimidines as VEGFR2/EGFR inhibitors

Paraskevas Konstantinos, Tahsin Kellici, Maria Michailidou, Thomas Mavromoustakos, Thomas Efferth, Heleni Loutrari, Alexios-Leandros Skaltsounis, Ioannis K. Kostakis.

11 References

1. De Gasparo, M.; Catt, K. J.; Inagami, T.; Wright, J. W.; Unger, T., International union of pharmacology. XXIII. The angiotensin II receptors. *Pharmacological Reviews* **2000**, *52*, 415-472.
2. Burnier, M.; Brunner, H. R., Comparative antihypertensive effects of angiotensin II receptor antagonists. *Journal of the American Society of Nephrology* **1999**, *10*, S278-S282.
3. Kellici, T. F.; Tzakos, A. G.; Mavromoustakos, T., Rational drug design and synthesis of molecules targeting the angiotensin II type 1 and type 2 receptors. *Molecules* **2015**, *20*, 3868-3897.
4. Wood, J. M.; Maibaum, J.; Rahuel, J.; Grütter, M. G.; Cohen, N. C.; Rasetti, V.; Rüger, H.; Göschke, R.; Stutz, S.; Fuhrer, W.; Schilling, W.; Rigollier, P.; Yamaguchi, Y.; Cumin, F.; Baum, H. P.; Schnell, C. R.; Herold, P.; Mah, R.; Jensen, C.; O'Brien, E.; Stanton, A.; Bedigian, M. P., Structure-based design of aliskiren, a novel orally effective renin inhibitor. *Biochemical and Biophysical Research Communications* **2003**, *308*, 698-705.
5. Unger, T.; Chung, O.; Csikos, T.; Culman, J.; Gallinat, S.; Gohlke, P.; Hohle, S.; Meffert, S.; Stoll, M.; Stroth, U.; Zhu, Y. Z., Angiotensin receptors. *Journal of hypertension. Supplement : official journal of the International Society of Hypertension* **1996**, *14*, S95-103.
6. Swindle, J. D.; Santos, K. L.; Speth, R. C., Pharmacological characterization of a novel non-AT1, non-AT2 angiotensin binding site identified as neurolysin. *Endocrine* **2013**, *44*, 525-531.
7. Wangler, N. J.; Santos, K. L.; Schadock, I.; Hagen, F. K.; Escher, E.; Bader, M.; Speth, R. C.; Karamyan, V. T., Identification of membrane-bound variant of metalloendopeptidase neurolysin (EC 3.4.24.16) as the non-angiotensin type 1 (non-AT 1), non-AT 2 angiotensin binding site. *Journal of Biological Chemistry* **2012**, *287*, 114-122.
8. Speth, R. C.; Carrera, E. J.; Bretón, C.; Linares, A.; Gonzalez-Reiley, L.; Swindle, J. D.; Santos, K. L.; Schadock, I.; Bader, M.; Karamyan, V. T., Distribution of Non-AT₁, Non-AT₂ Binding of ¹²⁵I-Sarcosine, Isoleucine⁸ Angiotensin II in Neurolysin Knockout Mouse Brains. *PLoS ONE* **2014**, *9*, e105762.
9. Unger, T., The angiotensin type 2 receptor: Variations on an enigmatic theme. *Journal of Hypertension* **1999**, *17*, 1775-1786.
10. Steckelings, U. M.; Rompe, F.; Kaschina, E.; Namsolleck, P.; Grzesiak, A.; Funke-Kaiser, H.; Bader, M.; Unger, T., The past, present and future of angiotensin II type 2 receptor stimulation. *JRAAS - Journal of the Renin-Angiotensin-Aldosterone System* **2010**, *11*, 67-73.
11. Alterman, M., Development of selective non-peptide angiotensin II type 2 receptor agonists. *JRAAS - Journal of the Renin-Angiotensin-Aldosterone System* **2010**, *11*, 57-66.
12. Unger, T.; Dahlöf, B., Compound 21, the first orally active, selective agonist of the angiotensin type 2 receptor (AT2): Implications for AT2 receptor research and therapeutic potential. *JRAAS - Journal of the Renin-Angiotensin-Aldosterone System* **2010**, *11*, 75-77.
13. Stoll, M.; Steckelings, U. M.; Paul, M.; Bottari, S. P.; Metzger, R.; Unger, T., The angiotensin AT2-receptor mediates inhibition of cell proliferation in coronary endothelial cells. *The Journal of clinical investigation* **1995**, *95*, 651-7.
14. Nouet, S.; Nahmias, C., Signal transduction from the angiotensin II AT2 receptor. *Trends in endocrinology and metabolism: TEM* **2000**, *11*, 1-6.
15. Li, P.; Kondo, T.; Numaguchi, Y.; Kobayashi, K.; Aoki, M.; Inoue, N.; Okumura, K.; Murohara, T., Role of bradykinin, nitric oxide, and angiotensin II type 2 receptor in imidapril-induced angiogenesis. *Hypertension* **2008**, *51*, 252-8.
16. Kim, S.; Toyokawa, H.; Yamao, J.; Satoi, S.; Yanagimoto, H.; Yamamoto, T.; Hirooka, S.; Yamaki, S.; Inoue, K.; Matsui, Y.; Kwon, A. H., Antitumor effect of angiotensin

II type 1 receptor blocker losartan for orthotopic rat pancreatic adenocarcinoma. *Pancreas* **2014**, 43, 886-90.

17. Peng, X.; Wang, F.; Li, L.; Bum-Erdene, K.; Xu, D.; Wang, B.; Sinn, A. A.; Pollok, K. E.; Sandusky, G. E.; Li, L.; Turchi, J. J.; Jalal, S. I.; Meroueh, S. O., Exploring a structural protein-drug interactome for new therapeutics in lung cancer. *Molecular bioSystems* **2014**, 10, 581-91.

18. Chen, X.; Meng, Q.; Zhao, Y.; Liu, M.; Li, D.; Yang, Y.; Sun, L.; Sui, G.; Cai, L.; Dong, X., Angiotensin II type 1 receptor antagonists inhibit cell proliferation and angiogenesis in breast cancer. *Cancer letters* **2013**, 328, 318-24.

19. Rhodes, D. R.; Ateeq, B.; Cao, Q.; Tomlins, S. A.; Mehra, R.; Laxman, B.; Kalyana-Sundaram, S.; Lonigro, R. J.; Helgeson, B. E.; Bhojani, M. S.; Rehemtulla, A.; Kleer, C. G.; Hayes, D. F.; Lucas, P. C.; Varambally, S.; Chinnaiyan, A. M., AGTR1 overexpression defines a subset of breast cancer and confers sensitivity to losartan, an AGTR1 antagonist. *Proceedings of the National Academy of Sciences of the United States of America* **2009**, 106, 10284-9.

20. Azevedo, H.; Fujita, A.; Bando, S. Y.; Iamashita, P.; Moreira-Filho, C. A., Transcriptional Network Analysis Reveals that AT1 and AT2 Angiotensin II Receptors Are Both Involved in the Regulation of Genes Essential for Glioma Progression. *PLoS One* **2014**, 9, e110934.

21. Dhande, I.; Ma, W.; Hussain, T., Angiotensin AT2 receptor stimulation is anti-inflammatory in lipopolysaccharide-activated THP-1 macrophages via increased interleukin-10 production. *Hypertension research : official journal of the Japanese Society of Hypertension* **2015**, 38, 21-9.

22. Castoldi, G.; di Gioia, C. R.; Bombardi, C.; Maestroni, S.; Carletti, R.; Steckelings, U. M.; Dahlof, B.; Unger, T.; Zerbini, G.; Stella, A., Prevention of diabetic nephropathy by compound 21, selective agonist of angiotensin type 2 receptors, in Zucker diabetic fatty rats. *American journal of physiology. Renal physiology* **2014**, 307, F1123-31.

23. McCarthy, C. A.; Vinh, A.; Miller, A. A.; Hallberg, A.; Alterman, M.; Callaway, J. K.; Widdop, R. E., Direct angiotensin AT2 receptor stimulation using a novel AT2 receptor agonist, compound 21, evokes neuroprotection in conscious hypertensive rats. *PLoS One* **2014**, 9, e95762.

24. Iwanami, J.; Mogi, M.; Tsukuda, K.; Jing, F.; Ohshima, K.; Wang, X. L.; Nakaoka, H.; Kan-no, H.; Chisaka, T.; Bai, H. Y.; Min, L. J.; Horiuchi, M., Possible synergistic effect of direct angiotensin II type 2 receptor stimulation by compound 21 with memantine on prevention of cognitive decline in type 2 diabetic mice. *European journal of pharmacology* **2014**, 724, 9-15.

25. Namsolleck, P.; Boato, F.; Schwengel, K.; Paulis, L.; Matho, K. S.; Geurts, N.; Thone-Reineke, C.; Lucht, K.; Seidel, K.; Hallberg, A.; Dahlof, B.; Unger, T.; Hendrix, S.; Steckelings, U. M., AT2-receptor stimulation enhances axonal plasticity after spinal cord injury by upregulating BDNF expression. *Neurobiology of disease* **2013**, 51, 177-91.

26. Kawabata, A.; Baoum, A.; Ohta, N.; Jacquez, S.; Seo, G. M.; Berkland, C.; Tamura, M., Intratracheal administration of a nanoparticle-based therapy with the angiotensin II type 2 receptor gene attenuates lung cancer growth. *Cancer research* **2012**, 72, 2057-67.

27. Magnani, F.; Pappas, C. G.; Crook, T.; Magafa, V.; Cordopatis, P.; Ishiguro, S.; Ohta, N.; Selent, J.; Bosnyak, S.; Jones, E. S.; Gerothanassis, I. P.; Tamura, M.; Widdop, R. E.; Tzakos, A. G., Electronic sculpting of ligand-GPCR subtype selectivity: the case of angiotensin II. *ACS chemical biology* **2014**, 9, 1420-5.

28. Agelis, G.; Resvani, A.; Durdagi, S.; Spyridaki, K.; Tűmová, T.; Slaninová, J.; Giannopoulos, P.; Vlahakos, D.; Liapakis, G.; Mavromoustakos, T.; Matsoukas, J., The discovery of new potent non-peptide Angiotensin II AT1 receptor blockers: A concise

synthesis, molecular docking studies and biological evaluation of N-substituted 5-butylimidazole derivatives. *European Journal of Medicinal Chemistry* **2012**, *55*, 358-374.

29. Kohara, Y.; Kubo, K.; Imamiya, E.; Wada, T.; Inada, Y.; Naka, T., Synthesis and angiotensin II receptor antagonistic activities of benzimidazole derivatives bearing acidic heterocycles as novel tetrazole bioisosteres. *J Med Chem* **1996**, *39*, 5228-35.

30. Cappelli, A.; Pericot Mohr Gl, G.; Gallelli, A.; Rizzo, M.; Anzini, M.; Vomero, S.; Mennuni, L.; Ferrari, F.; Makovec, F.; Menziani, M. C.; De Benedetti, P. G.; Giorgi, G., Design, synthesis, structural studies, biological evaluation, and computational simulations of novel potent AT(1) angiotensin II receptor antagonists based on the 4-phenylquinoline structure. *J Med Chem* **2004**, *47*, 2574-86.

31. Jeunemaitre, X.; Soubrier, F.; Kotelevtsev, Y. V.; Lifton, R. P.; Williams, C. S.; Charru, A.; Hunt, S. C.; Hopkins, P. N.; Williams, R. R.; Lalouel, J. M.; Corvol, P., Molecular basis of human hypertension: Role of angiotensinogen. *Cell* **1992**, *71*, 169-180.

32. Peach, M. J., Renin angiotensin system: Biochemistry and mechanisms of action. *Physiological Reviews* **1977**, *57*, 313-370.

33. Mehta, P. K.; Griendling, K. K., Angiotensin II cell signaling: Physiological and pathological effects in the cardiovascular system. *American Journal of Physiology - Cell Physiology* **2007**, *292*, C82-C97.

34. Burnier, M.; Brunner, H. R., Angiotensin II receptor antagonists. *Lancet* **2000**, *355*, 637-645.

35. Weir, M. R.; Dzau, V. J., The renin-angiotensin-aldosterone system: A specific target for hypertension management. *American Journal of Hypertension* **1999**, *12*, 205S-213S.

36. Mentz, R. J.; Bakris, G. L.; Waeber, B.; McMurray, J. J. V.; Gheorghide, M.; Ruilope, L. M.; Maggioni, A. P.; Swedberg, K.; Piña, I. L.; Fiuzat, M.; O'Connor, C. M.; Zannad, F.; Pitt, B., The past, present and future of renin-angiotensin aldosterone system inhibition. *International Journal of Cardiology* **2013**, *167*, 1677-1687.

37. Te Riet, L.; van Esch, J. H.; Roks, A. J.; van den Meiracker, A. H.; Danser, A. H., Hypertension: renin-angiotensin-aldosterone system alterations. *Circulation research* **2015**, *116*, 960-975.

38. Oparil, S.; Schmieder, R. E., New approaches in the treatment of hypertension. *Circulation research* **2015**, *116*, 1074-1095.

39. Robles, N. R.; Cerezo, I.; Hernandez-Gallego, R., Renin-angiotensin system blocking drugs. *Journal of Cardiovascular Pharmacology and Therapeutics* **2014**, *19*, 14-33.

40. Oliveira, L.; Costa-Neto, C. M.; Nakaie, C. R.; Schreier, S.; Shimuta, S. I.; Paiva, A. C., The angiotensin II AT1 receptor structure-activity correlations in the light of rhodopsin structure. *Physiol Rev* **2007**, *87*, 565-92.

41. Cabana, J.; Holleran, B.; Beaulieu, M. E.; Leduc, R.; Escher, E.; Guillemette, G.; Lavigne, P., Critical hydrogen bond formation for activation of the angiotensin II type 1 receptor. *The Journal of biological chemistry* **2013**, *288*, 2593-604.

42. Ballesteros, J. A.; Weinstein, H., Integrated methods for the construction of three-dimensional models and computational probing of structure-function relations in G protein-coupled receptors. *Methods in Neurosciences* **1995**, *25*, 366-428.

43. Nygaard, R.; Frimurer, T. M.; Holst, B.; Rosenkilde, M. M.; Schwartz, T. W., Ligand binding and micro-switches in 7TM receptor structures. *Trends in pharmacological sciences* **2009**, *30*, 249-59.

44. Shi, L.; Liapakis, G.; Xu, R.; Guarnieri, F.; Ballesteros, J. A.; Javitch, J. A., Beta2 adrenergic receptor activation. Modulation of the proline kink in transmembrane 6 by a rotamer toggle switch. *The Journal of biological chemistry* **2002**, *277*, 40989-96.

45. Takezako, T.; Unal, H.; Karnik, S. S.; Node, K., Structure-Function Basis of Attenuated Inverse Agonism of Angiotensin II Type 1 Receptor Blockers for Active-State Angiotensin II Type 1 Receptor. *Molecular pharmacology* **2015**, 88, 488-501.
46. Zhang, H.; Unal, H.; Gati, C.; Han, G. W.; Liu, W.; Zatsopin, N. A.; James, D.; Wang, D.; Nelson, G.; Weierstall, U.; Sawaya, M. R.; Xu, Q.; Messerschmidt, M.; Williams, G. J.; Boutet, S.; Yefanov, O. M.; White, T. A.; Wang, C.; Ishchenko, A.; Tirupula, K. C.; Desnoyer, R.; Coe, J.; Conrad, C. E.; Fromme, P.; Stevens, R. C.; Katritch, V.; Karnik, S. S.; Cherezov, V., Structure of the Angiotensin receptor revealed by serial femtosecond crystallography. *Cell* **2015**, 161, 833-44.
47. Venkatakrishnan, A. J.; Deupi, X.; Lebon, G.; Heydenreich, F. M.; Flock, T.; Miljus, T.; Balaji, S.; Bouvier, M.; Veprintsev, D. B.; Tate, C. G.; Schertler, G. F.; Babu, M. M., Diverse activation pathways in class A GPCRs converge near the G-protein-coupling region. *Nature* **2016**, 536, 484-7.
48. Flock, T.; Ravarani, C. N.; Sun, D.; Venkatakrishnan, A. J.; Kayikci, M.; Tate, C. G.; Veprintsev, D. B.; Babu, M. M., Universal allosteric mechanism for Galpha activation by GPCRs. *Nature* **2015**, 524, 173-9.
49. The Top 50 Drugs of 2014. *C&EN Supplement* **2014**, 39-42.
50. Blundell, C. D.; Packer, M. J.; Almond, A., Quantification of free ligand conformational preferences by NMR and their relationship to the bioactive conformation. *Bioorganic and Medicinal Chemistry* **2013**, 21, 4976-4987.
51. Fisette, O.; Lagüe, P.; Gagné, S.; Morin, S., Synergistic applications of MD and NMR for the study of biological systems. *Journal of Biomedicine and Biotechnology* **2012**, 2012.
52. Yamamoto, K.; Vivekanandan, S.; Ramamoorthy, A., Fast NMR data acquisition from bicelles containing a membrane-associated peptide at natural-abundance. *Journal of Physical Chemistry B* **2011**, 115, 12448-12455.
53. Huang, R.; Vivekanandan, S.; Brender, J. R.; Abe, Y.; Naito, A.; Ramamoorthy, A., NMR characterization of monomeric and oligomeric conformations of human calcitonin and its interaction with EGCG. *Journal of Molecular Biology* **2012**, 416, 108-120.
54. Porcelli, F.; Buck, B.; Lee, D. K.; Hallock, K. J.; Ramamoorthy, A.; Vegliai, G., Structure and orientation of pardaxin determined by NMR experiments in model membranes. *Journal of Biological Chemistry* **2004**, 279, 45815-45823.
55. Kellici, T. F.; Ntountaniotis, D.; Kritsi, E.; Zervou, M.; Zoumpoulakis, P.; Potamitis, C.; Durdagi, S.; Salmas, R. E.; Ergun, G.; Gokdemir, E.; Halabalaki, M.; Gerothanassis, I. P.; Liapakis, G.; Tzakos, A.; Mavromoustakos, T., Leveraging NMR and X-ray Data of the Free Ligands to Build Better Drugs Targeting Angiotensin II Type 1 G-Protein Coupled Receptor. *Curr Med Chem* **2016**, 23, 36-59.
56. Costanzi, S., Modeling G protein-coupled receptors and their interactions with ligands. *Current opinion in structural biology* **2013**, 23, 185-90.
57. Franca, T. C., Homology modeling: an important tool for the drug discovery. *Journal of biomolecular structure & dynamics* **2015**, 33, 1780-93.
58. Fanelli, F.; De Benedetti, P. G., Update 1 of: computational modeling approaches to structure-function analysis of G protein-coupled receptors. *Chem Rev* **2011**, 111, Pr438-535.
59. Yarnitzky, T.; Levit, A.; Niv, M. Y., Homology modeling of G-protein-coupled receptors with X-ray structures on the rise. *Current Opinion in Drug Discovery & Development* **2010**, 13, 317-25.
60. Tuccinardi, T.; Calderone, V.; Rapposelli, S.; Martinelli, A., Proposal of a new binding orientation for non-peptide AT1 antagonists: homology modeling, docking and three-dimensional quantitative structure-activity relationship analysis. *J Med Chem* **2006**, 49, 4305-16.

61. Matsoukas, M. T.; Potamitis, C.; Plotas, P.; Androutsou, M. E.; Agelis, G.; Matsoukas, J.; Zoumpoulakis, P., Insights into AT1 receptor activation through AngII binding studies. *Journal of chemical information and modeling* **2013**, 53, 2798-811.
62. Yanagisawa, H.; Amemiya, Y.; Kanazaki, T.; Shimoji, Y.; Fujimoto, K.; Kitahara, Y.; Sada, T.; Mizuno, M.; Ikeda, M.; Miyamoto, S.; Furukawa, Y.; Koike, H., Nonpeptide angiotensin II receptor antagonists: Synthesis, biological activities, and structure - Activity relationships of imidazole-5-carboxylic acids bearing alkyl, alkenyl, and hydroxyalkyl substituents at the 4-position and their related compounds. *Journal of Medicinal Chemistry* **1996**, 39, 323-338.
63. Miura, S.; Fujino, M.; Hanzawa, H.; Kiya, Y.; Imaizumi, S.; Matsuo, Y.; Tomita, S.; Uehara, Y.; Karnik, S. S.; Yanagisawa, H.; Koike, H.; Komuro, I.; Saku, K., Molecular mechanism underlying inverse agonist of angiotensin II type 1 receptor. *The Journal of biological chemistry* **2006**, 281, 19288-95.
64. Miura, S.; Nakao, N.; Hanzawa, H.; Matsuo, Y.; Saku, K.; Karnik, S. S., Reassessment of the unique mode of binding between angiotensin II type 1 receptor and their blockers. *PLoS One* **2013**, 8, e79914.
65. Miura, S. I.; Fujino, M.; Hanzawa, H.; Kiya, Y.; Imaizumi, S.; Matsuo, Y.; Tomita, S.; Uehara, Y.; Karnik, S. S.; Yanagisawa, H.; Koike, H.; Komuro, I.; Saku, K., Molecular mechanism underlying inverse agonist of angiotensin II type 1 receptor. *Journal of Biological Chemistry* **2006**, 281, 19288-19295.
66. Mavromoustakos, T.; Durdagi, S.; Koukoulitsa, C.; Simcic, M.; Papadopoulos, M. G.; Hodosecek, M.; Grdadolnik, S. G., Strategies in the rational drug design. *Current Medicinal Chemistry* **2011**, 18, 2517-2530.
67. Zoumpoulakis, P.; Mavromoustakos, T., Seeking the active site of the AT1 receptor for computational docking studies. *Drug Design Reviews Online* **2005**, 2, 537-545.
68. Mavromoustakos, T.; Zervou, M.; Zoumpoulakis, P.; Kyrikou, I.; Benetis, N. P.; Polevaya, L.; Roumelioti, P.; Giatas, N.; Zoga, A.; Moutevelis Minakakis, P.; Kolocouris, A.; Vlahakos, D.; Golic Grdadolnik, S.; Matsoukas, J., Conformation and bioactivity. Design and discovery of novel antihypertensive drugs. *Current Topics in Medicinal Chemistry* **2004**, 4, 385-401.
69. Mavromoustakos, T. M.; Zervou, M. V.; Zoumpoulakis, P. G., In *Frontiers in Medicinal Chemistry*; 2006; Vol. 3, pp 87-111.
70. Mavromoustakos, T.; Zoumpoulakis, I.; Kyrikou, I.; Zoga, A.; Siapi, E.; Zervou, M.; Daliani, I.; Dimitriou, D.; Pitsas, A.; Kamoutsis, C.; Laggner, P., Efforts to understand the molecular basis of hypertension through drug: Membrane interactions. *Current Topics in Medicinal Chemistry* **2004**, 4, 445-459.
71. Fotakis, C.; Megariotis, G.; Christodouleas, D.; Kritsi, E.; Zoumpoulakis, P.; Ntountaniotis, D.; Zervou, M.; Potamitis, C.; Hodzic, A.; Pabst, G.; Rappolt, M.; Mali, G.; Baldus, J.; Glaubitz, C.; Papadopoulos, M. G.; Afantitis, A.; Melagraki, G.; Mavromoustakos, T., Comparative study of the AT1 receptor prodrug antagonist candesartan cilexetil with other sartans on the interactions with membrane bilayers. *Biochimica et Biophysica Acta - Biomembranes* **2012**, 1818, 3107-3120.
72. Hodzic, A.; Zoumpoulakis, P.; Pabst, G.; Mavromoustakos, T.; Rappolt, M., Losartan's affinity to fluid bilayers modulates lipid-cholesterol interactions. *Physical Chemistry Chemical Physics* **2012**, 14, 4780-4788.
73. Ntountaniotis, D.; Mali, G.; Grdadolnik, S. G.; Maria, H.; Skaltsounis, A. L.; Potamitis, C.; Siapi, E.; Chatzigeorgiou, P.; Rappolt, M.; Mavromoustakos, T., Thermal, dynamic and structural properties of drug AT 1 antagonist olmesartan in lipid bilayers. *Biochimica et Biophysica Acta - Biomembranes* **2011**, 1808, 2995-3006.

74. Fotakis, C.; Christodouleas, D.; Zoumpoulakis, P.; Kritsi, E.; Benetis, N. P.; Mavromoustakos, T.; Reis, H.; Gili, A.; Papadopoulos, M. G.; Zervou, M., Comparative biophysical studies of sartan class drug molecules losartan and candesartan (CV-11974) with membrane bilayers. *Journal of Physical Chemistry B* **2011**, 115, 6180-6192.
75. Potamitis, C.; Chatzigeorgiou, P.; Siapi, E.; Viras, K.; Mavromoustakos, T.; Hodzic, A.; Pabst, G.; Cacho-Nerin, F.; Laggner, P.; Rappolt, M., Interactions of the AT1 antagonist valsartan with dipalmitoyl-phosphatidylcholine bilayers. *Biochimica et Biophysica Acta - Biomembranes* **2011**, 1808, 1753-1763.
76. Mavromoustakos, T.; Chatzigeorgiou, P.; Koukoulitsa, C.; Durdagi, S., Partial interdigitation of lipid bilayers. *International Journal of Quantum Chemistry* **2011**, 111, 1172-1183.
77. Fotakis, C.; Gega, S.; Siapi, E.; Potamitis, C.; Viras, K.; Moutevelis-Minakakis, P.; Kokotos, C. G.; Durdagi, S.; Grdadolnik, S. G.; Sartori, B.; Rappolt, M.; Mavromoustakos, T., Interactions at the bilayer interface and receptor site induced by the novel synthetic pyrrolidinone analog MMK3. *Biochimica et Biophysica Acta - Biomembranes* **2010**, 1798, 422-432.
78. Mavromoustakos, T.; Golic Grdadolnik, S.; Zervou, M.; Zoumpoulakis, P.; Potamitis, C.; Politi, A.; Mantzourani, E.; Platts, J. A.; Koukoulitsa, C.; Minakakis, P.; Kokotos, G.; Tselios, T.; Matsoukas, J.; Durdagi, S.; Papadopoulos, M. G.; Papahatjis, D. P.; Spyralanti, Z. S.; Dalkas, G. A.; Spyroulias, G. A. Putative Bioactive Conformers of Small Molecules: A Concerted Approach Using NMR Spectroscopy and Computational Chemistry. In *Medicinal Chemistry Research progress*, Ricci, G. P. C. a. S., Ed.; Nova Science Publishers: New York, 2008; Chapter 7, pp 175-207.
79. Ntountaniotis, D.; Kellici, T.; Tzakos, A.; Kolokotroni, P.; Tselios, T.; Becker-Baldus, J.; Glaubitz, C.; Lin, S.; Makriyannis, A.; Mavromoustakos, T., The application of solid-state NMR spectroscopy to study candesartan cilexetil (TCV-116) membrane interactions. Comparative study with the AT1R antagonist drug olmesartan. *Biochimica et Biophysica Acta - Biomembranes* **2014**, 1838, 2439-2450.
80. Zervou, M.; Cournia, Z.; Potamitis, C.; Patargias, G.; Durdagi, S.; Grdadolnik, S. G.; Mavromoustakos, T., Insights into the molecular basis of action of the AT1 antagonist losartan using a combined NMR spectroscopy and computational approach. *Biochimica et Biophysica Acta - Biomembranes* **2014**, 1838, 1031-1046.
81. Matsoukas, M. T.; Cordoní, A.; Ríos, S.; Pardo, L.; Tselios, T., Ligand binding determinants for angiotensin II type 1 receptor from computer simulations. *Journal of chemical information and modeling* **2013**, 53, 2874-2883.
82. Villiers, A., Sur la transformation de la fécule en dextrine par le ferment butyrique. *Compt. Rend. Fr. Acad. Sci* **1891**, 112, 435-438.
83. Villiers, A., Sur la fermentation de la fécule par l'action du ferment butyrique. *C. R. Acad. Sci.* **1891**, 112.
84. Crini, G., Review: A history of cyclodextrins. *Chemical Reviews* **2014**, 114, 10940-10975.
85. Maquenne, L.; Roux, E., Recherches sur l'amidon et sa saccharification diastasique. *Ann. Chim. Phys.* **1906**, 9, 179-220.
86. Schardinger, F., Über thermophile Bakterien aus verschiedenen Speisen und Milch - sowie über einige Umsetzungsprodukte derselben in kohlenhydrathaltigen Nährlösungen, darunter krystallisierte Polysaccharide (Dextrine) aus Stärke. *Zeitschrift für Untersuchung der Nahrungs- und Genußmittel* **1903**, 6, 865-880.
87. Schardinger, F., Über die Zulässigkeit des Warmhaltens von zum Gebuß bestimmten Nahrungsmittel mittelst Wärme speichernder Apparate, sog. Thermophore. *Wien. Klin. Wochenschr.* **1903**, 16, 468.

88. Schardinger, F., Bacillus macerans, ein Aceton bildender Rottebacillus. *Zentralbl. Bakteriol. Parasitenkd. Infektionskr. Hyg. Abt.* **1905**, 14, 772-781.
89. Schardinger, F., *Zentralbl. Bakteriol. Parasitenkd. Infektionskr. Hyg. Abt. II.* **1909**, 22, 98-103.
90. Schardinger, F., Bildung kristallisierter Polysaccharide (Dextrine) aus Stärkekleister durch Microben. *Zentralbl. Bakteriol. Parasitenkd.* **1911**, 29, 188-197.
91. French, D.; Rundle, R. E., The molecular weights of the schardinger alpha and beta dextrins. *Journal of the American Chemical Society* **1942**, 64, 1651-1653.
92. Cramer, F.; Hettler, H., Inclusion compounds of cyclodextrins. *Die Naturwissenschaften* **1967**, 54, 625-632.
93. Cramer, F., Cyclodextrin - A paradigmatic model. *Proceedings of the First International Symposium on Cyclodextrins (Budapest, 30 September - 2 October 1981)* **1981**, 3.
94. Cramer, F., Introductory remarks. *Proceedings of the Fourth International Symposium on Cyclodextrins. Advances in Inclusion Science* **1988**, 5, 1.
95. McMullan, R. K.; Saenger, W.; Fayos, J.; Mootz, D., Topography of cyclodextrin inclusion complexes. Part I. Classification of crystallographic data of α -cyclodextrin inclusion complexes. *Carbohydrate Research* **1973**, 31, 37-46.
96. McMullan, R. K.; Saenger, W.; Fayos, J.; Mootz, D., Topography of cyclodextrin inclusion complexes. Part II. The iodine-cyclohexa-amylose tetrahydrate complex; its molecular geometry and cage-type crystal structure. *Carbohydrate Research* **1973**, 31, 211-227.
97. Bergeron, R.; Rowan III, R., The molecular disposition of sodium p-nitrophenolate in the cavities of cycloheptaamylose and cyclohexaamylose in solution. *Bioorganic Chemistry* **1976**, 5, 425-436.
98. Kellici, T. F.; Liapakis, G.; Tzakos, A. G.; Mavromoustakos, T., Pharmaceutical compositions for antihypertensive treatments: A patent review. *Expert Opinion on Therapeutic Patents* **2015**, 25, 1305-1317.
99. Gibson, M., *Pharmaceutical Preformulation and Formulation: A Practical Guide from Candidate Drug Selection to Commercial Dosage Form*. CRC Press: 2009.
100. Semalty, A., Cyclodextrin and phospholipid complexation in solubility and dissolution enhancement: A critical and meta-analysis. *Expert Opinion on Drug Delivery* **2014**, 11, 1255-1272.
101. Arias, J. L., Liposomes in drug delivery: A patent review (2007 - present). *Expert Opinion on Therapeutic Patents* **2013**, 23, 1399-1414.
102. Loftsson, T.; Jarho, P.; Másson, M.; Järvinen, T., Cyclodextrins in drug delivery. *Expert Opinion on Drug Delivery* **2005**, 2, 335-351.
103. Frömmling, K. H.; Szejtli, J., In *Cyclodextrins in Pharmacy*; Kluwer Academic Publishers, Dordrecht: 1994.
104. Brewster, M. E.; Loftsson, T., Cyclodextrins as pharmaceutical solubilizers. *Advanced Drug Delivery Reviews* **2007**, 59, 645-666.
105. Irie, T.; Uekama, K., Pharmaceutical applications of cyclodextrins. III. Toxicological issues and safety evaluation. *Journal of Pharmaceutical Sciences* **1997**, 86, 147-162.
106. Freudenberg, K.; Cramer, F.; Plieninger, H., Verfahren Zur Herstellung von Einschlussverbindungen Physiologisch Wirksamer Organischer Verbindungen. **1953**.
107. Takahashi, A. I.; Veiga, F. J. B.; Ferraz, H. G., A literature review of cyclodextrin inclusion complexes characterization - Part III: Differential scanning calorimetry and thermogravimetry. *International Journal of Pharmaceutical Sciences Review and Research* **2012**, 12, 16-20.

108. Marques, H. M. C.; Hadgraft, J.; Kellaway, I. W., Studies of cyclodextrin inclusion complexes. I. The salbutamol-cyclodextrin complex as studied by phase solubility and DSC. *International Journal of Pharmaceutics* **1990**, 63, 259-266.
109. Hassan, M. A.; Suleiman, M. S.; Najib, N. M., Improvement of the in vitro dissolution characteristics of famotidine by inclusion in β -cyclodextrin. *International Journal of Pharmaceutics* **1990**, 58, 19-24.
110. Gong, L.; Li, T.; Chen, F.; Duan, X.; Yuan, Y.; Zhang, D.; Jiang, Y., An inclusion complex of eugenol into β -cyclodextrin: Preparation, and physicochemical and antifungal characterization. *Food Chemistry* **2016**, 196, 324-330.
111. Maestrelli, F.; González-Rodríguez, M. L.; Rabasco, A. M.; Mura, P., Preparation and characterisation of liposomes encapsulating ketoprofen-cyclodextrin complexes for transdermal drug delivery. *International Journal of Pharmaceutics* **2005**, 298, 55-67.
112. Patel, J. S.; Patel, R. P., Preparation, characterization and in vitro dissolution study of Nitrazepam: Cyclodextrin inclusion complex. *Journal of Pharmacy and Bioallied Sciences* **2012**, 4, 106-107.
113. Patel, R. P.; Patel, M. M., Solid-state characterization and dissolution properties of lovastatin hydroxypropyl- β -cyclodextrin inclusion complex. *Pharmaceutical Technology* **2007**, 31, 72-82.
114. Schneider, H. J.; Hacket, F.; Rüdiger, V.; Ikeda, H., NMR studies of cyclodextrins and cyclodextrin complexes. *Chemical Reviews* **1998**, 98, 1755-1785.
115. Farrar, T. C.; Becker, E. D., *Pulse and Fourier transform NMR; introduction to theory and methods*. Academic Press: New York., 1971; p xiv, 115 p.
116. Andrew, E. R., The narrowing of NMR spectra of solids by high-speed specimen rotation and the resolution of chemical shift and spin multiplet structures for solids. *Progress in Nuclear Magnetic Resonance Spectroscopy* **1971**, 8, 1-39.
117. Andrew, E. R.; Bradbury, A.; Eades, R. G., Removal of Dipolar Broadening of Nuclear Magnetic Resonance Spectra of Solids by Specimen Rotation. *Nature* **1959**, 183, 1802-1803.
118. Pines, A.; Gibby, M. G.; Waugh, J. S., Proton-Enhanced Nuclear Induction Spectroscopy. A Method for High Resolution NMR of Dilute Spins in Solids. *The Journal of Chemical Physics* **1972**, 56, 1776-1777.
119. Inoue, Y.; Iohara, D.; Sekiya, N.; Yamamoto, M.; Ishida, H.; Sakiyama, Y.; Hirayama, F.; Arima, H.; Uekama, K., Ternary inclusion complex formation and stabilization of limaprost, a prostaglandin E1 derivative, in the presence of alpha- and beta-cyclodextrins in the solid state. *Int J Pharm* **2016**, 509, 338-47.
120. Li, S.; Zhai, Y.; Yan, J.; Wang, L.; Xu, K.; Li, H., Effect of preparation processes and structural insight into the supermolecular system: Bisacodyl and beta-cyclodextrin inclusion complex. *Materials science & engineering. C, Materials for biological applications* **2016**, 58, 224-32.
121. Arrua, E. C.; Ferreira, M. J.; Salomon, C. J.; Nunes, T. G., Elucidating the guest-host interactions and complex formation of praziquantel and cyclodextrin derivatives by (^{13}C) and (^{15}N) solid-state NMR spectroscopy. *Int J Pharm* **2015**, 496, 812-21.
122. Priotti, J.; Ferreira, M. J.; Lamas, M. C.; Leonardi, D.; Salomon, C. J.; Nunes, T. G., First solid-state NMR spectroscopy evaluation of complexes of benzimidazole with cyclodextrin derivatives. *Carbohydr Polym* **2015**, 131, 90-7.
123. Karoyo, A. H.; Sidhu, P. S.; Wilson, L. D.; Hazendonk, P.; Borisov, A., Counterion Anchoring Effect on the Structure of the Solid-State Inclusion Complexes of β -Cyclodextrin and Sodium Perfluorooctanoate. *The Journal of Physical Chemistry C* **2015**, 119, 22225-22243.

124. Karoyo, A. H.; Sidhu, P.; Wilson, L. D.; Hazendonk, P., Characterization and Dynamic Properties for the Solid Inclusion Complexes of β -Cyclodextrin and Perfluorooctanoic Acid. *The Journal of Physical Chemistry B* **2013**, 117, 8269-8282.
125. Karoyo, A. H.; Borisov, A. S.; Wilson, L. D.; Hazendonk, P., Formation of Host-Guest Complexes of β -Cyclodextrin and Perfluorooctanoic Acid. *The Journal of Physical Chemistry B* **2011**, 115, 9511-9527.
126. Ferreira, M. J.; Garcia, A.; Leonardi, D.; Salomon, C. J.; Lamas, M. C.; Nunes, T. G., (^{13}C) and (^{15}N) solid-state NMR studies on albendazole and cyclodextrin albendazole complexes. *Carbohydr Polym* **2015**, 123, 130-5.
127. Pajzderska, A.; Mielcarek, J.; Wasicki, J., Complex and mixture of beta-cyclodextrin with diazepam characterised by (^1H) NMR and atom-atom potential methods. *Carbohydr Res* **2014**, 398, 56-62.
128. Koito, Y.; Yamada, K.; Ando, S., Solid-state NMR and wide-angle X-ray diffraction study of hydrofluoroether/ β -cyclodextrin inclusion complex. *Journal of Inclusion Phenomena and Macrocyclic Chemistry* **2013**, 76, 143-150.
129. Abbate, V.; Bassindale, A. R.; Brandstadt, K. F.; Taylor, P. G., Inclusion complexes between cyclic siloxanes and cyclodextrins: synthesis and characterization. *Journal of Inclusion Phenomena and Macrocyclic Chemistry* **2012**, 74, 223-230.
130. Hasegawa, Y.; Inoue, Y.; Deguchi, K.; Ohki, S.; Tansho, M.; Shimizu, T.; Yazawa, K., Molecular Dynamics of a Polyaniline/ β -Cyclodextrin Complex Investigated by ^{13}C Solid-State NMR. *The Journal of Physical Chemistry B* **2012**, 116, 1758-1764.
131. Sinha, V. R.; Anitha, R.; Ghosh, S.; Nanda, A.; Kumria, R., Complexation of celecoxib with β -cyclodextrin: Characterization of the interaction in solution and in solid state. *Journal of Pharmaceutical Sciences* **2005**, 94, 676-687.
132. Zingone, G.; Rubessa, F., Preformulation study of the inclusion complex warfarin- β -cyclodextrin. *International Journal of Pharmaceutics* **2005**, 291, 3-10.
133. Pralhad, T.; Rajendrakumar, K., Study of freeze-dried quercetin-cyclodextrin binary systems by DSC, FT-IR, X-ray diffraction and SEM analysis. *Journal of Pharmaceutical and Biomedical Analysis* **2004**, 34, 333-339.
134. Cai, W. S.; Wang, T.; Liu, Y. Z.; Liu, P.; Chipot, C.; Shao, X. G., Free energy calculations for cyclodextrin inclusion complexes. *Current Organic Chemistry* **2011**, 15, 839-847.
135. Liu, B.; Zeng, J.; Chen, C.; Liu, Y.; Ma, H.; Mo, H.; Liang, G., Interaction of cinnamic acid derivatives with β -cyclodextrin in water: Experimental and molecular modeling studies. *Food Chemistry* **2016**, 194, 1156-1163.
136. Sancho, M. I.; Andujar, S.; Porasso, R. D.; Enriz, R. D., Theoretical and Experimental Study of Inclusion Complexes of β -Cyclodextrins with Chalcone and 2',4'-Dihydroxychalcone. *The Journal of Physical Chemistry B* **2016**, 120, 3000-3011.
137. Young, D. C., *Computational chemistry : a practical guide for applying techniques to real world problems*. Wiley: New York, 2001; p xxiv, 381 p.
138. Kellici, T. F.; Chatziathanasiadou, M. V.; Diamantis, D.; Chatzikonstantinou, A. V.; Andreadelis, I.; Christodoulou, E.; Valsami, G.; Mavromoustakos, T.; Tzakos, A. G., Mapping the interactions and bioactivity of quercetin—(2-hydroxypropyl)- β -cyclodextrin complex. *International Journal of Pharmaceutics* **2016**, 511, 303-311.
139. Nutho, B.; Khuntawee, W.; Rungnim, C.; Pongsawasdi, P.; Wolschann, P.; Karpfen, A.; Kungwan, N.; Rungrotmongkol, T., Binding mode and free energy prediction of fisetin/ β -cyclodextrin inclusion complexes. *Beilstein journal of organic chemistry* **2014**, 10, 2789-99.
140. Sangpheak, W.; Khuntawee, W.; Wolschann, P.; Pongsawasdi, P.; Rungrotmongkol, T., Enhanced stability of a naringenin/2,6-dimethyl β -cyclodextrin inclusion complex:

molecular dynamics and free energy calculations based on MM- and QM-PBSA/GBSA. *Journal of molecular graphics & modelling* **2014**, 50, 10-5.

141. Nagaraju, M.; Sastry, G. N., Theoretical studies on inclusion complexes of cyclodextrins. *The journal of physical chemistry. A* **2009**, 113, 9533-42.

142. El-Barghouthi, M. I.; Jaime, C.; Akielah, R. E.; Al-Sakhen, N. A.; Masoud, N. A.; Issa, A. A.; Badwan, A. A.; Zughul, M. B., Free energy perturbation and MM/PBSA studies on inclusion complexes of some structurally related compounds with β -cyclodextrin. *Supramolecular Chemistry* **2009**, 21, 603-610.

143. Oda, M.; Kuroda, M., Molecular dynamics simulations of inclusion complexation of glycyrrhizic acid and cyclodextrins (1:1) in water. *Journal of Inclusion Phenomena and Macrocyclic Chemistry* **2016**, 85, 271-279.

144. Mayer, B. P.; Kennedy, D. J.; Lau, E. Y.; Valdez, C. A., Solution-State Structure and Affinities of Cyclodextrin:Fentanyl Complexes by Nuclear Magnetic Resonance Spectroscopy and Molecular Dynamics Simulation. *The journal of physical chemistry. B* **2016**, 120, 2423-33.

145. Kicuntod, J.; Khuntawee, W.; Wolschann, P.; Pongsawasdi, P.; Chavasiri, W.; Kungwan, N.; Rungrotmongkol, T., Inclusion complexation of pinostrobin with various cyclodextrin derivatives. *Journal of molecular graphics & modelling* **2016**, 63, 91-8.

146. Zhang, J.-Q.; Li, K.; Jiang, K.-M.; Cong, Y.-W.; Pu, S.-P.; Xie, X.-G.; Jin, Y.; Lin, J., Development of an oral satraplatin pharmaceutical formulation by encapsulation with cyclodextrin. *RSC Advances* **2016**, 6, 17074-17082.

147. Shi, M.; Zhang, C.; Xie, Y.; Xu, D., Stereoselective inclusion mechanism of ketoprofen into β -cyclodextrin: insights from molecular dynamics simulations and free energy calculations. *Theoretical Chemistry Accounts* **2014**, 133, 1556.

148. Tidemand, K. D.; Schönbeck, C.; Holm, R.; Westh, P.; Peters, G. H., Computational Investigation of Enthalpy–Entropy Compensation in Complexation of Glycoconjugated Bile Salts with β -Cyclodextrin and Analogs. *Journal of Physical Chemistry B* **2014**, 118, 10889-10897.

149. Schönbeck, C.; Westh, P.; Holm, R., Complexation Thermodynamics of Modified Cyclodextrins: Extended Cavities and Distorted Structures. *Journal of Physical Chemistry B* **2014**, 118, 10120-10129.

150. Gannimani, R.; Perumal, A.; Ramesh, M.; Pillay, K.; Soliman, M. E.; Govender, P., Antipyrine–gamma cyclodextrin inclusion complex: Molecular modeling, preparation, characterization and cytotoxicity studies. *Journal of Molecular Structure* **2015**, 1089, 38-47.

151. Figueiras, A.; Nunes, S. C. C.; Simões, S.; Pais, A. A. C. C.; Veiga, F., Molecular interaction governing solubility and release profiles in supramolecular systems containing fenbufen, pluronics and cyclodextrins. *Journal of Inclusion Phenomena and Macrocyclic Chemistry* **2015**, 81, 395-407.

152. Ali, S. M.; Shamim, S., Complexation of (RS)-benzhexol with β -cyclodextrin: structure elucidation of diastereomeric complexes by use of quantitative ^1H - ^1H ROESY and computational methods. *Monatshefte für Chemie - Chemical Monthly* **2015**, 146, 283-290.

153. Uccello-Barretta, G.; Schurig, V.; Balzano, F.; Vanni, L.; Aiello, F.; Mori, M.; Ghirga, F., Synergistic Effects of Trace Amounts of Water in the Enantiodiscrimination Processes by Lipodex E: A Spectroscopic and Computational Investigation. *Chirality* **2015**, 27, 95-103.

154. Nascimento, C. S.; Lopes, J. F.; Guimaraes, L.; Borges, K. B., Molecular modeling study of the recognition mechanism and enantioseparation of 4-hydroxypropranolol by capillary electrophoresis using carboxymethyl-beta-cyclodextrin as the chiral selector. *Analyst* **2014**, 139, 3901-10.

155. Fernandes, A.; Ivanova, G.; Bras, N. F.; Mateus, N.; Ramos, M. J.; Rangel, M.; de Freitas, V., Structural characterization of inclusion complexes between cyanidin-3-O-glucoside and beta-cyclodextrin. *Carbohydr Polym* **2014**, 102, 269-77.
156. Liu, P.; Xu, H.; Zhang, D.; Zhan, J., Molecular inclusion of PCB126 by beta-cyclodextrin: a combined molecular dynamics simulation and quantum chemical study. *Journal of Inclusion Phenomena and Macrocyclic Chemistry* **2013**, 76, 301-309.
157. Jana, M.; Bandyopadhyay, S., Molecular Dynamics Study of β -Cyclodextrin–Phenylalanine (1:1) Inclusion Complex in Aqueous Medium. *The Journal of Physical Chemistry B* **2013**, 117, 9280-9287.
158. Troche-Pesqueira, E.; Perez-Juste, I.; Navarro-Vazquez, A.; Cid, M. M., A β -cyclodextrin-resveratrol inclusion complex and the role of geometrical and electronic effects on its electronic induced circular dichroism. *RSC Advances* **2013**, 3, 10242-10250.
159. Ali, S. M.; Fatma, K.; Dhokale, S., Structure elucidation of beta-cyclodextrin-xylazine complex by a combination of quantitative (1)H-(1)H ROESY and molecular dynamics studies. *Beilstein journal of organic chemistry* **2013**, 9, 1917-24.
160. Martini, M. F.; Glisoni, R. J.; Sosnik, A.; Moglioni, A.; Pickholz, M., Insights on self-aggregation phenomena of 1-indanone thiosemicarbazones and the formation of inclusion complexes with hydroxypropyl- β -cyclodextrin by Molecular Dynamics simulations. *Journal of Molecular Liquids* **2016**, 222, 963-971.
161. Minea, B.; Marangoci, N.; Peptanariu, D.; Rosca, I.; Nastasa, V.; Corciova, A.; Varganici, C.; Nicolescu, A.; Fifere, A.; Neamtu, A.; Mares, M.; Barboiu, M.; Pinteala, M., Inclusion complexes of propiconazole nitrate with substituted [small beta]-cyclodextrins: the synthesis and in silico and in vitro assessment of their antifungal properties. *New Journal of Chemistry* **2016**, 40, 1765-1776.
162. Zhang, C. L.; Liu, J. C.; Yang, W. B.; Chen, D. L.; Jiao, Z. G., Experimental and molecular docking investigations on the inclusion mechanism of the complex of phloridzin and hydroxypropyl- β -cyclodextrin. *Food Chemistry* **2017**, 215, 124-128.
163. Liu, B.; Li, W.; Zhao, J.; Liu, Y.; Zhu, X.; Liang, G., Physicochemical characterisation of the supramolecular structure of luteolin/cyclodextrin inclusion complex. *Food Chemistry* **2013**, 141, 940-945.
164. Asfari, Z.; Bohmer, V.; Harrowfield, M., *Calixarenes 2001*. Kluwer Academic Publishers: Dordrecht ; Boston, 2001; p x, 683 p.
165. Böhmer, V., Calixarenes, macrocycles with (almost) unlimited possibilities. *Angew. Chem. Int. Ed.* **1995**, 34, 713-745.
166. Yilmaz, M.; Memon, S.; Tabakci, M.; Bartsch, R. A. In *New frontiers in polymer research*, Bregg, R. K., Ed.; Nova Science Publishers: New York, 2006, pp 125-171.
167. Giuliani, M.; Morbioli, I.; Sansone, F.; Casnati, A., Moulding calixarenes for biomacromolecule targeting. *Chemical communications (Cambridge, England)* **2015**, 51, 14140-59.
168. Casnati, A., Calixarenes and cations: a time-lapse photography of the big-bang. *Chemical Communications* **2013**, 49, 6827-6830.
169. Gutsche, C. D.; Reddy, P. A., Calixarenes. 25. Conformations and structures of the products of arylmethylation of calix[4]arenes. *Journal of Organic Chemistry* **1991**, 56, 4783-4791.
170. Jaime, C.; De Mendoza, J.; Prados, P.; Nieto, P. M.; Sánchez, C., ¹³C NMR chemical shifts. A single rule to determine the conformation of calix[4]arenes. *Journal of Organic Chemistry* **1991**, 56, 3372-3376.
171. Uyanik, A.; Sen, N.; Yilmaz, M., Improvement of catalytic activity of lipase from *Candida rugosa* via sol-gel encapsulation in the presence of calix(aza)crown. *Bioresource Technology* **2011**, 102, 4313-4318.

172. Yilmaz, M.; Erdemir, S., Calixarene-based receptors for molecular recognition. *Turkish Journal of Chemistry* **2013**, *37*, 558-585.
173. Gutsche, C. D., *Calixarenes : an introduction*. 2nd ed.; RSC Pub.: Cambridge, 2008; p xiii, 276 p.
174. Yilmaz, M.; Sirit, A.; Deligoz, H. In *Sorption Processes and Pollution: Conventional and Non-conventional Sorbents for Pollutant Removal from Wastewaters*, Badot, P.-M.; Crini, G., Eds.; Universitaires de Franche-Comté: Besançon, 2011, pp 401-417.
175. Karakurt, S.; Kellici, T. F.; Mavromoustakos, T.; Tzakos, A. G.; Yilmaz, M., Calixarenes in lipase biocatalysis and cancer therapy. *Current Organic Chemistry* **2016**, *20*, 1043-1057.
176. Yang, Y. W.; Sun, Y. L.; Song, N., Switchable host-guest systems on surfaces. *Accounts of Chemical Research* **2014**, *47*, 1950-1960.
177. Li, Q.; Guo, D. S.; Qian, H.; Liu, Y., Complexation of p-sulfonatocalixarenes with local anaesthetics guests: Binding structures, stabilities, and thermodynamic origins. *European Journal of Organic Chemistry* **2012**, 3962-3971.
178. Zhang, X.; Zhao, H.; Cao, X.; Feng, N.; Tian, D.; Li, H., Hg²⁺ wettability and fluorescence dual-signal responsive switch based on a cysteine complex of piperidine-calix[4]arene. *Organic and Biomolecular Chemistry* **2013**, *11*, 8262-8268.
179. De Assis, J. V.; Teixeira, M. G.; Soares, C. G. P.; Lopes, J. F.; Carvalho, G. S. L.; Lourenço, M. C. S.; De Almeida, M. V.; De Almeida, W. B.; Fernandes, S. A., Experimental and theoretical NMR determination of isoniazid and sodium p-sulfonatocalix[n]arenes inclusion complexes. *European Journal of Pharmaceutical Sciences* **2012**, *47*, 539-548.
180. Zhou, Y.; Li, H.; Yang, Y. W., Controlled drug delivery systems based on calixarenes. *Chinese Chemical Letters* **2015**, *26*, 825-828.
181. Wheate, N. J.; Abbott, G. M.; Tate, R. J.; Clements, C. J.; Edrada-Ebel, R.; Johnston, B. F., Side-on binding of p-sulphonatocalix[4]arene to the dinuclear platinum complex trans- $[\text{PtCl}(\text{NH}_3)_2]_2\mu\text{-dpzm}]^{2+}$ and its implications for anticancer drug delivery. *Journal of Inorganic Biochemistry* **2009**, *103*, 448-454.
182. Wang, G. S.; Zhang, H. Y.; Ding, F.; Liu, Y., Preparation and characterization of inclusion complexes of topotecan with sulfonatocalixarene. *Journal of Inclusion Phenomena and Macrocyclic Chemistry* **2011**, *69*, 85-89.
183. Liu, J.; Bu, W.; Pan, L.; Shi, J., NIR-triggered anticancer drug delivery by upconverting nanoparticles with integrated azobenzene-modified mesoporous silica. *Angewandte Chemie - International Edition* **2013**, *52*, 4375-4379.
184. Song, J.; Li, H.; Chao, J.; Dong, C.; Shuang, S., Spectroscopic studies on the inclusion interaction of p-sulfonatocalix[6] arene with vitamin B 6. *Journal of Inclusion Phenomena and Macrocyclic Chemistry* **2012**, *72*, 389-395.
185. Wang, X.; Luo, C.; Lv, Z.; Lu, F., Investigation of the inclusion behavior between p-sulfonocalix[8]arene and norfloxacin by fluorescence spectroscopy. *Journal of Luminescence* **2011**, *131*, 1986-1990.
186. Xue, Y.; Guan, Y.; Zheng, A.; Xiao, H., Amphoteric calix[8]arene-based complex for pH-triggered drug delivery. *Colloids and Surfaces B: Biointerfaces* **2013**, *101*, 55-60.
187. Ntountaniotis, D.; Mali, G.; Grdadolnik, S. G.; Maria, H.; Skaltsounis, A. L.; Potamitis, C.; Siapi, E.; Chatzigeorgiou, P.; Rappolt, M.; Mavromoustakos, T., Thermal, dynamic and structural properties of drug AT 1 antagonist olmesartan in lipid bilayers. *Biochim. Biophys. Acta* **2011**, *1808*, 2995-3006.
188. Ntountaniotis, D.; Kellici, T.; Tzakos, A.; Kolokotroni, P.; Tselios, T.; Becker-Baldus, J.; Glaubitz, C.; Lin, S.; Makriyannis, A.; Mavromoustakos, T., The application of solid-state NMR spectroscopy to study candesartan cilexetil (TCV-116) membrane

interactions. Comparative study with the AT1R antagonist drug olmesartan. *Biochim. Biophys. Acta* **2014**, 1838, 2439-2450.

189. Babu, K. S.; Tagore, A. R.; Reddy, G. S.; Venkateswarlu, G.; Reddy, P. P.; Anand, R. V., Synthesis of related substances of olmesartan medoxomil, anti-hypertensive drug. *Arkivoc II* **2010**, 292-302.

190. Murakami, T.; Konno, H.; Fukutsu, N.; Onodera, M.; Kawasaki, T.; Kusu, F., Identification of a degradation product in stressed tablets of olmesartan medoxomil by the complementary use of HPLC hyphenated techniques. *Journal of Pharmaceutical and Biomedical Analysis* **2008**, 47, 553-559.

191. Venkanna, G.; Madhusudhan, G.; Mukkanti, K.; Sankar, A.; Sampath Kumar, Y.; Venakata Narayana, G., Synthesis and characterization of process-related impurities of antihypertensive drug olmesartan medoxomil. *Journal of Chemistry* **2013**.

192. Jain, P. S.; Chaudhari, A. J.; Surana, S. J., Development and validation of stability-indicating RP-HPLC method for determination of olmesartan medoxomile in pharmaceutical dosage form and identification, characterization of alkaline degradation impurity of olmesartan medoxomile drug substance as well as drug product. *Chemical Industry and Chemical Engineering Quarterly* **2012**, 18, 595-604.

193. Zhang, H.; Unal, H.; Desnoyer, R.; Han, G. W.; Patel, N.; Katritch, V.; Karnik, S. S.; Cherezov, V.; Stevens, R. C., Structural Basis for Ligand Recognition and Functional Selectivity at Angiotensin Receptor. *The Journal of biological chemistry* **2015**, 290, 29127-39.

194. Ntountaniotis, D.; Agelis, G.; Resvani, A.; Halabalaki, M.; Liapakis, G.; Spyridaki, K.; Grdadolnik, S. G.; Merzel, F.; Kostidis, S.; Potamitis, C.; Tselios, T.; Matsoukas, J.; Skaltsounis, L. A.; Mavromoustakos, T., An efficient synthetic method and theoretical calculations of olmesartan methyl ether: study of biological function of AT1 antagonism. *Combinatorial chemistry & high throughput screening* **2014**, 17, 652-62.

195. Musafia, B.; Senderowitz, H., Biasing conformational ensembles towards bioactive-like conformers for ligand-based drug design. *Expert Opinion on Drug Discovery* **2010**, 5, 943-959.

196. Schönherr, H.; Cernak, T., Profound methyl effects in drug discovery and a call for new C-H methylation reactions. *Angewandte Chemie (International Edition)* **2013**, 52, 12256-12267.

197. Barreiro, E. J.; Kümmerle, A. E.; Fraga, C. A. M., The methylation effect in medicinal chemistry. *Chemical Reviews* **2011**, 111, 5215-5246.

198. Sturlese, M.; Bellanda, M.; Moro, S., NMR-Assisted Molecular Docking Methodologies. *Molecular Informatics* **2015**, 34, 513-525.

199. Avgy-David, H. H.; Senderowitz, H., Toward Focusing Conformational Ensembles on Bioactive Conformations: A Molecular Mechanics/Quantum Mechanics Study. *Journal of chemical information and modeling* **2015**, 55, 2154-2167.

200. Miura, S.; Kiya, Y.; Hanzawa, H.; Nakao, N.; Fujino, M.; Imaizumi, S.; Matsuo, Y.; Yanagisawa, H.; Koike, H.; Komuro, I.; Karnik, S. S.; Saku, K., Small molecules with similar structures exhibit agonist, neutral antagonist or inverse agonist activity toward angiotensin II type 1 receptor. *PLoS One* **2012**, 7, e37974.

201. Belostotskii, A. M., Calculated chemical shifts as a fine tool of conformational analysis: an unambiguous solution for haouamine alkaloids. *The Journal of organic chemistry* **2008**, 73, 5723-31.

202. Cotos-Yáñez, T. R.; García-Domínguez, P.; Iglesias, B.; Muñoz, L., Conformational analysis from statistical treatment of ¹³C NMR chemical shifts. *Chemometrics and Intelligent Laboratory Systems* **2015**, 149, Part A, 132-139.

203. Loguercio, C.; Festi, D., Silybin and the liver: From basic research to clinical practice. *World Journal of Gastroenterology* **2011**, *17*, 2288-2301.
204. Kren, V.; Walterová, D., Silybin and silymarin--new effects and applications. *Biomedical papers of the Medical Faculty of the University Palacký, Olomouc, Czechoslovakia*. **2005**, *149*, 29-41.
205. Morazzoni, P.; Bombardelli, E., Silybum marianum (Carduus marianus). *Fitoterapia* **1995**, *66*, 3-42.
206. Flora, K.; Hahn, M.; Rosen, H.; Benner, K., Milk thistle (Silybum marianum) for the therapy of liver disease. *American Journal of Gastroenterology* **1998**, *93*, 139-143.
207. Gažák, R.; Walterová, D.; Křen, V., Silybin and silymarin - New and emerging applications in medicine. *Current Medicinal Chemistry* **2007**, *14*, 315-338.
208. Dixit, N.; Baboota, S.; Kohli, K.; Ahmad, S.; Ali, J., Silymarin: A review of pharmacological aspects and bioavailability enhancement approaches. *Indian Journal of Pharmacology* **2007**, *39*, 172-179.
209. Theodosiou, E.; Purchartová, K.; Stamatis, H.; Kolisis, F.; Křen, V., Bioavailability of silymarin flavonolignans: Drug formulations and biotransformation. *Phytochemistry Reviews* **2014**, *13*, 1-18.
210. Crocenzi, F. A.; Roma, M. G., Silymarin as a new hepatoprotective agent in experimental cholestasis: New possibilities for an ancient medication. *Current Medicinal Chemistry* **2006**, *13*, 1055-1074.
211. Kroll, D. J.; Shaw, H. S.; Oberlies, N. H., Milk thistle nomenclature: Why it matters in cancer research and pharmacokinetic studies. *Integrative Cancer Therapies* **2007**, *6*, 110-119.
212. Abenavoli, L.; Capasso, R.; Milic, N.; Capasso, F., Milk thistle in liver diseases: Past, present, future. *Phytotherapy Research* **2010**, *24*, 1423-1432.
213. Napolitano, J. G.; Lankin, D. C.; Graf, T. N.; Brent Friesen, J.; Chen, S. N.; McAlpine, J. B.; Oberlies, N. H.; Pauli, G. F., HiFSA fingerprinting applied to isomers with near-identical NMR Spectra: The silybin/isosilybin case. *Journal of Organic Chemistry* **2013**, *78*, 2827-2839.
214. Ting, H.; Deep, G.; Agarwal, R., Molecular mechanisms of silibinin-mediated cancer chemoprevention with major emphasis on prostate cancer. *AAPS Journal* **2013**, *15*, 707-716.
215. Nambiar, D. K.; Rajamani, P.; Singh, R. P., Silibinin attenuates ionizing radiation-induced pro-angiogenic response and EMT in prostate cancer cells. *Biochemical and Biophysical Research Communications* **2015**, *456*, 262-268.
216. Rajamanickam, S.; Kaur, M.; Velmurugan, B.; Singh, R. P.; Agarwal, R., Silibinin suppresses spontaneous tumorigenesis in APC min/+ mouse model by modulating beta-catenin pathway. *Pharmaceutical Research* **2009**, *26*, 2558-2567.
217. Singh, R. P.; Gu, M.; Agarwal, R., Silibinin inhibits colorectal cancer growth by inhibiting tumor cell proliferation and angiogenesis. *Cancer research* **2008**, *68*, 2043-2050.
218. Raina, K.; Agarwal, C.; Agarwal, R., Effect of silibinin in human colorectal cancer cells: Targeting the activation of NF- κ B signaling. *Molecular Carcinogenesis* **2013**, *52*, 195-206.
219. Tyagi, A.; Singh, R. P.; Ramasamy, K.; Raina, K.; Redente, E. F.; Dwyer-Nield, L. D.; Radcliffe, R. A.; Malkinson, A. M.; Agarwal, R., Growth inhibition and regression of lung tumors by silibinin: Modulation of angiogenesis by macrophage-associated cytokines and nuclear factor- κ B and signal transducers and activators of transcription 3. *Cancer Prevention Research* **2009**, *2*, 74-83.
220. Zholobenko, A.; Modriansky, M., Silymarin and its constituents in cardiac preconditioning. *Fitoterapia* **2014**, *97*, 122-132.
221. Mira, L.; Silva, M.; Manso, C. F., Scavenging of reactive oxygen species by silibinin dihemisuccinate. *Biochemical Pharmacology* **1994**, *48*, 753-759.

222. Gažák, R.; Sedmera, P.; Vrbacký, M.; Vostálová, J.; Drahota, Z.; Marhol, P.; Walterová, D.; Křen, V., Molecular mechanisms of silybin and 2,3-dehydrosilybin antiradical activity-role of individual hydroxyl groups. *Free Radical Biology and Medicine* **2009**, *46*, 745-758.
223. Sonnenbichler, J.; Zetl, I., Biochemical effects of the flavonolignan silibinin on RNA, protein and DNA synthesis in rat livers. *Progress in clinical and biological research* **1986**, *213*, 319-331.
224. Weyhenmeyer, R.; Mascher, H.; Birkmayer, J., Study on dose-linearity of the pharmacokinetics of silibinin diastereomers using a new stereospecific assay. *International Journal of Clinical Pharmacology, Therapy, and Toxicology* **1992**, *30*, 134-138.
225. Zhu, H. J.; Brinda, B. J.; Chavin, K. D.; Bernstein, H. J.; Patrick, K. S.; Markowitz, J. S., An assessment of pharmacokinetics and antioxidant activity of free silymarin flavonolignans in healthy volunteers: A dose escalation study. *Drug Metabolism and Disposition* **2013**, *41*, 1679-1685.
226. Rickling, B.; Hans, B.; Kramarczyk, R.; Krumbiegel, G.; Weyhenmeyer, R., Two high-performance liquid chromatographic assays for the determination of free and total silibinin diastereomers in plasma using column switching with electrochemical detection and reversed-phase chromatography with ultraviolet detection. *Journal of Chromatography B: Biomedical Applications* **1995**, *670*, 267-277.
227. Jančová, P.; Šiller, M.; Anzenbacherová, E.; Křen, V.; Anzenbacher, P.; Šimánek, V., Evidence for differences in regioselective and stereoselective glucuronidation of silybin diastereomers from milk thistle (*Silybum marianum*) by human UDP-glucuronosyltransferases. *Xenobiotica* **2011**, *41*, 743-751.
228. Sfihi, H.; Legrand, A. P.; Doussot, J.; Guy, A., Solid-state ¹³C NMR study of β -cyclodextrin/substituted aromatic ketone complexes: Evidence for two kinds of complexation of the guest molecules. *Colloids and Surfaces A: Physicochemical and Engineering Aspects* **1996**, *115*, 115-126.
229. Nicolescu, C.; Aramă, C.; Monciu, C. M., Preparation and characterization of inclusion complexes between repaglinide and β -cyclodextrin, 2-hydroxypropyl- β -cyclodextrin and randomly methylated β -cyclodextrin. *Farmacia* **2010**, *58*, 78-88.
230. Nikolić, V.; Nikolić, L.; Stanković, M.; Kapor, A.; Popsavin, M.; Cvetković, D., A molecular inclusion complex of atenolol with 2-hydroxypropyl- β - cyclodextrin; the production and characterization thereof. *Journal of the Serbian Chemical Society* **2007**, *72*, 737-746.
231. Hirayama, F.; Uekama, K., Cyclodextrin-based controlled drug release system. *Advanced Drug Delivery Reviews* **1999**, *36*, 125-141.
232. Del Valle, E. M. M., Cyclodextrins and their uses: A review. *Process Biochemistry* **2004**, *39*, 1033-1046.
233. Laza-Knoerr, A. L.; Gref, R.; Couvreur, P., Cyclodextrins for drug delivery. *Journal of Drug Targeting* **2010**, *18*, 645-656.
234. Stella, V. J.; Rajewski, R. A., Cyclodextrins: Their future in drug formulation and delivery. *Pharm. Res.* **1997**, *14*, 556-567.
235. Uekama, K.; Hirayama, F.; Irie, T., Cyclodextrin drug carrier systems. *Chem. Rev.* **1998**, *98*, 2045-2076.
236. Davis, M. E.; Brewster, M. E., Cyclodextrin-based pharmaceuticals: Past, present and future. *Nat. Rev. Drug Discov.* **2004**, *3*, 1023-1035.
237. Fahr, A.; Liu, X., Drug delivery strategies for poorly water-soluble drugs. *Expert Opinion on Drug Delivery* **2007**, *4*, 403-416.
238. Challa, R.; Ahuja, A.; Ali, J.; Khar, R. K., Cyclodextrins in drug delivery: an updated review. *AAPS PharmSciTech [electronic resource]*. **2005**, *6*, E329-357.

239. Voinovich, D.; Perissutti, B.; Grassi, M.; Passerini, N.; Bigotto, A., Solid state mechanochemical activation of Silybum marianum dry extract with betacyclodextrins: Characterization and bioavailability of the coground systems. *Journal of Pharmaceutical Sciences* **2009**, 98, 4119-4129.
240. Primikyri, A.; Chatziathanasiadou, M. V.; Karali, E.; Kostaras, E.; Mantzaris, M. D.; Hatzimichael, E.; Shin, J. S.; Chi, S. W.; Briasoulis, E.; Kolettas, E.; Gerothanassis, I. P.; Tzakos, A. G., Direct binding of Bcl-2 family proteins by quercetin triggers its pro-apoptotic activity. *ACS chemical biology* **2014**, 9, 2737-41.
241. Weis, S. M.; Cheresch, D. A., Tumor angiogenesis: molecular pathways and therapeutic targets. *Nature medicine* **2011**, 17, 1359-70.
242. Maeda, H.; Wu, J.; Sawa, T.; Matsumura, Y.; Hori, K., Tumor vascular permeability and the EPR effect in macromolecular therapeutics: a review. *Journal of controlled release : official journal of the Controlled Release Society* **2000**, 65, 271-84.
243. Webb, B. A.; Chimenti, M.; Jacobson, M. P.; Barber, D. L., Dysregulated pH: a perfect storm for cancer progression. *Nature reviews. Cancer* **2011**, 11, 671-7.
244. Gutsche, C. D., *Calixarenes*. Royal society of chemistry: 1989.
245. Memon, S.; Yilmaz, M., A complimentary study of calixarene based bifunctional receptors for alkali or transition metal cations and Cr2O7²⁻-anions. *Journal of Molecular Structure* **2001**, 595, 101-109.
246. Bhatti, A.; Qureshi, I.; Memon, N.; Memon, S., Evaluation of perchlorate sorption behavior of calix[4]arene appended resin. *Journal of Inclusion Phenomena and Macrocyclic Chemistry* **2012**, 1-6.
247. Shinkai, S.; Arimura, T.; Araki, K.; Kawabata, H.; Satoh, H.; Tsubaki, T.; Manabe, O.; Sunamoto, J., Syntheses and Aggregation Properties of New Water-Soluble Calixarenes. *J Chem Soc Perk T 1* **1989**, 2039-2045.
248. Gutsche, C. D.; Alam, I., Calixarenes .23. The Complexation and Catalytic Properties of Water-Soluble Calixarenes. *Tetrahedron* **1988**, 44, 4689-4694.
249. Schrödinger Release 2015-2: LigPrep, version 3.4, Schrödinger, LLC, New York, NY, 2015.
250. Schrödinger Release 2015-2: MacroModel, version 10.8, Schrödinger, LLC, New York, NY, 2015.
251. Shivakumar, D.; Williams, J.; Wu, Y.; Damm, W.; Shelley, J.; Sherman, W., Prediction of Absolute Solvation Free Energies using Molecular Dynamics Free Energy Perturbation and the OPLS Force Field. *Journal of Chemical Theory and Computation* **2010**, 6, 1509-1519.
252. Harder, E.; Damm, W.; Maple, J.; Wu, C.; Reboul, M.; Xiang, J. Y.; Wang, L.; Lupyan, D.; Dahlgren, M. K.; Knight, J. L.; Kaus, J. W.; Cerutti, D. S.; Krilov, G.; Jorgensen, W. L.; Abel, R.; Friesner, R. A., OPLS3: A Force Field Providing Broad Coverage of Drug-like Small Molecules and Proteins. *Journal of Chemical Theory and Computation* **2016**, 12, 281-296.
253. Bochevarov, A. D.; Harder, E.; Hughes, T. F.; Greenwood, J. R.; Braden, D. A.; Philipp, D. M.; Rinaldo, D.; Halls, M. D.; Zhang, J.; Friesner, R. A., Jaguar: A high-performance quantum chemistry software program with strengths in life and materials sciences. *International Journal of Quantum Chemistry* **2013**, 113, 2110-2142.
254. Tannor, D. J.; Marten, B.; Murphy, R.; Friesner, R. A.; Sitkoff, D.; Nicholls, A.; Ringnalda, M.; Goddard Iii, W. A.; Honig, B., Accurate first principles calculation of molecular charge distributions and solvation energies from Ab initio quantum mechanics and continuum dielectric theory. *Journal of the American Chemical Society* **1994**, 116, 11875-11882.

255. Cao, Y.; Beachy, M. D.; Braden, D. A.; Morrill, L.; Ringnalda, M. N.; Friesner, R. A., Nuclear-magnetic-resonance shielding constants calculated by pseudospectral methods. *J Chem Phys* **2005**, *122*, 224116.
256. Matsoukas, M. T.; Cordomi, A.; Rios, S.; Pardo, L.; Tselios, T., Ligand binding determinants for angiotensin II type 1 receptor from computer simulations. *Journal of chemical information and modeling* **2013**, *53*, 2874-83.
257. Madhavi Sastry, G.; Adzhigirey, M.; Day, T.; Annabhimoju, R.; Sherman, W., Protein and ligand preparation: Parameters, protocols, and influence on virtual screening enrichments. *Journal of Computer-Aided Molecular Design* **2013**, *27*, 221-234.
258. Olsson, M. H. M.; Søndergaard, C. R.; Rostkowski, M.; Jensen, J. H., PROPKA3: Consistent treatment of internal and surface residues in empirical p K a predictions. *Journal of Chemical Theory and Computation* **2011**, *7*, 525-537.
259. Pringsheim, H.; Wolfsohn, K., *Ber. Dtsch. Chem. Ges.* **1922**, *57*, 887.
260. Friesner, R. A.; Banks, J. L.; Murphy, R. B.; Halgren, T. A.; Klicic, J. J.; Mainz, D. T.; Repasky, M. P.; Knoll, E. H.; Shelley, M.; Perry, J. K.; Shaw, D. E.; Francis, P.; Shenkin, P. S., Glide: A New Approach for Rapid, Accurate Docking and Scoring. 1. Method and Assessment of Docking Accuracy. *Journal of Medicinal Chemistry* **2004**, *47*, 1739-1749.
261. Cho, A. E.; Guallar, V.; Berne, B. J.; Friesner, R., Importance of accurate charges in molecular docking: Quantum Mechanical/Molecular Mechanical (QM/MM) approach. *Journal of Computational Chemistry* **2005**, *26*, 915-931.
262. Pringsheim, H.; Goldstein, K., *Ber. Dtsch. Chem. Ges.* **1923**, *56*, 1520.
263. Pringsheim, H.; Steingroever, F., *Ber. Dtsch. Chem. Ges.* **1924**, *57*, 1579.
264. Sherman, W.; Day, T.; Jacobson, M. P.; Friesner, R. A.; Farid, R., Novel procedure for modeling ligand/receptor induced fit effects. *Journal of Medicinal Chemistry* **2006**, *49*, 534-553.
265. Pringsheim, H., *Angew. Chem.* **1931**, *44*, 677.
266. Pringsheim, H.; Schapiro, E., *Ber. Dtsch. Chem. Ges.* **1926**, *59*, 996.
267. Tuckerman, M.; Berne, B. J.; Martyna, G. J., Reversible multiple time scale molecular dynamics. *Journal of Chemical Physics* **1992**, *97*, 1990-2001.
268. Martyna, G. J.; Klein, M. L.; Tuckerman, M., Nosé-Hoover chains: The canonical ensemble via continuous dynamics. *Journal of Chemical Physics* **1992**, *97*, 2635-2643.
269. Martyna, G. J.; Tobias, D. J.; Klein, M. L., Constant pressure molecular dynamics algorithms. *Journal of Chemical Physics* **1994**, *101*, 4177-4189.
270. Murphy, R. B.; Philipp, D. M.; Friesner, R. A., A mixed quantum mechanics/molecular mechanics (QM/MM) method for large-scale modeling of chemistry in protein environments. *Journal of Computational Chemistry* **2000**, *21*, 1442-1457.
271. Figueiras, A.; Carvalho, R. A.; Ribeiro, L.; Torres-Labandeira, J. J.; Veiga, F. J. B., Solid-state characterization and dissolution profiles of the inclusion complexes of omeprazole with native and chemically modified β -cyclodextrin. *European Journal of Pharmaceutics and Biopharmaceutics* **2007**, *67*, 531-539.
272. Günther, H., *NMR spectroscopy : basic principles, concepts, and applications in chemistry*. 2nd ed.; Wiley: Chichester ; New York, 1995; p xx, 581 p.
273. Chattah, A. K.; Mroue, K. H.; Pfund, L. Y.; Ramamoorthy, A.; Longhi, M. R.; Garner, C., Insights into novel supramolecular complexes of two solid forms of Norfloxacin and β -Cyclodextrin. *Journal of Pharmaceutical Sciences* **2013**, *102*, 3717-3724.
274. Fukami, T.; Ishii, T.; Io, T.; Suzuki, N.; Suzuki, T.; Yamamoto, K.; Xu, J.; Ramamoorthy, A.; Tomono, K., Nanoparticle processing in the solid state dramatically increases the cell membrane permeation of a cholesterol-lowering drug, probucol. *Molecular Pharmaceutics* **2009**, *6*, 1029-1035.

275. Io, T.; Fukami, T.; Yamamoto, K.; Suzuki, T.; Xu, J.; Tomono, K.; Ramamoorthy, A., Homogeneous nanoparticles to enhance the efficiency of a hydrophobic drug, antihyperlipidemic probucol, characterized by solid-state NMR. *Molecular Pharmaceutics* **2010**, *7*, 299-305.
276. Lamotte, Y.; Faucher, N.; Sançon, J.; Pineau, O.; Sautet, S.; Fouchet, M. H.; Beneton, V.; Tousaint, J. J.; Saintillan, Y.; Ancellin, N.; Nicodeme, E.; Grillot, D.; Martres, P., Discovery of novel indazole derivatives as dual angiotensin II antagonists and partial PPAR γ agonists. *Bioorganic and Medicinal Chemistry Letters* **2014**, *24*, 1098-1103.
277. Betzel, C.; Saenger, W.; Hingerty, B. E.; Brown, G. M., Topography of cyclodextrin inclusion complexes, part 20. Circular and flip-flop hydrogen bonding in β -cyclodextrin undecahydrate: a neutron diffraction study. *Journal of the American Chemical Society* **1984**, *106*, 7545-7557.
278. Jorgensen, W. L.; Maxwell, D. S.; Tirado-Rives, J., Development and testing of the OPLS all-atom force field on conformational energetics and properties of organic liquids. *Journal of the American Chemical Society* **1996**, *118*, 11225-11236.
279. Oh, I.; Lee, M. Y.; Lee, Y. B.; Shin, S. C.; Park, I., Spectroscopic characterization of ibuprofen/2-hydroxypropyl- β -cyclodextrin inclusion complex. *International Journal of Pharmaceutics* **1998**, *175*, 215-223.
280. Jadhav, G. S.; Vavia, P. R., Physicochemical, in silico and in vivo evaluation of a danazol- β -cyclodextrin complex. *International Journal of Pharmaceutics* **2008**, *352*, 5-16.
281. Barillaro, V.; Dive, G.; Bertholet, P.; Evrard, B.; Delattre, L.; Eric, Z.; Piel, G., Theoretical and experimental investigations on miconazole/cyclodextrin/acid complexes: Molecular modeling studies. *International Journal of Pharmaceutics* **2007**, *342*, 152-160.
282. Cirri, M.; Maestrelli, F.; Orlandini, S.; Furlanetto, S.; Pinzauti, S.; Mura, P., Determination of stability constant values of flurbiprofen-cyclodextrin complexes using different techniques. *Journal of Pharmaceutical and Biomedical Analysis* **2005**, *37*, 995-1002.
283. Case, D. A.; Cheatham III, T. E.; Darden, T.; Gohlke, H.; Luo, R.; Merz Jr, K. M.; Onufriev, A.; Simmerling, C.; Wang, B.; Woods, R. J., The Amber biomolecular simulation programs. *Journal of Computational Chemistry* **2005**, *26*, 1668-1688.
284. Case, D.; Darden, T. A.; Cheatham, T. E.; Simmerling, C.; Wang, J.; Duke, R.; Luo, R.; Crowley, M.; Walker, R.; Zhang, W.; Merz, K. M.; Wang, B.; Hayik, S.; Roitberg, A.; Seabra, G.; Kolossváry, I.; Wong, K. F.; Paesani, F.; Vanicek, J.; Wu, X.; Brozell, S.; Steinbrecher, T.; Gohlke, H.; Yang, L.; Tan, C.; Mongan, J.; Hornak, V.; Cui, G.; Mathews, D. H.; Seetin, M. G.; Sagui, C.; Babin, V.; Kollman, P., *AMBER 12*, University of California, San Francisco. 2012.
285. Frisch, M. J.; Trucks, G. W.; Schlegel, H. B.; Scuseria, G. E.; Robb, M. A.; Cheeseman, J. R.; Scalmani, G.; Barone, V.; Mennucci, B.; Petersson, G. A.; Nakatsuji, H.; Caricato, M.; Li, X.; Hratchian, H. P.; Izmaylov, A. F.; Bloino, J.; Zheng, G.; Sonnenberg, J. L.; Hada, M.; Ehara, M.; Toyota, K.; Fukuda, R.; Hasegawa, J.; Ishida, M.; Nakajima, T.; Honda, Y.; Kitao, O.; Nakai, H.; Vreven, T.; Montgomery Jr., J. A.; Peralta, J. E.; Ogliaro, F.; Bearpark, M. J.; Heyd, J.; Brothers, E. N.; Kudin, K. N.; Staroverov, V. N.; Kobayashi, R.; Normand, J.; Raghavachari, K.; Rendell, A. P.; Burant, J. C.; Iyengar, S. S.; Tomasi, J.; Cossi, M.; Rega, N.; Millam, N. J.; Klene, M.; Knox, J. E.; Cross, J. B.; Bakken, V.; Adamo, C.; Jaramillo, J.; Gomperts, R.; Stratmann, R. E.; Yazyev, O.; Austin, A. J.; Cammi, R.; Pomelli, C.; Ochterski, J. W.; Martin, R. L.; Morokuma, K.; Zakrzewski, V. G.; Voth, G. A.; Salvador, P.; Dannenberg, J. J.; Dapprich, S.; Daniels, A. D.; Farkas, Ö.; Foresman, J. B.; Ortiz, J. V.; Cioslowski, J.; Fox, D. J. *Gaussian 09*, Gaussian, Inc.: Wallingford, CT, USA, 2009.

286. Wang, J.; Wolf, R. M.; Caldwell, J. W.; Kollman, P. A.; Case, D. A., Development and testing of a general Amber force field. *Journal of Computational Chemistry* **2004**, *25*, 1157-1174.
287. Bayly, C. I.; Cieplak, P.; Cornell, W. D.; Kollman, P. A., A well-behaved electrostatic potential based method using charge restraints for deriving atomic charges: The RESP model. *Journal of Physical Chemistry* **1993**, *97*, 10269-10280.
288. Kirschner, K. N.; Yongye, A. B.; Tschampel, S. M.; González-Outeiriño, J.; Daniels, C. R.; Foley, B. L.; Woods, R. J., GLYCAM06: A generalizable biomolecular force field. carbohydrates. *Journal of Computational Chemistry* **2008**, *29*, 622-655.
289. Jorgensen, W. L.; Chandrasekhar, J.; Madura, J. D.; Impey, R. W.; Klein, M. L., Comparison of simple potential functions for simulating liquid water. *Journal of Chemical Physics* **1983**, *79*, 926-935.
290. Izaguirre, J. A.; Catarello, D. P.; Wozniak, J. M.; Skeel, R. D., Langevin stabilization of molecular dynamics. *Journal of Chemical Physics* **2001**, *114*, 2090-2098.
291. Ryckaert, J. P.; Ciccotti, G.; Berendsen, H. J. C., Numerical integration of the cartesian equations of motion of a system with constraints: molecular dynamics of n-alkanes. *Journal of Computational Physics* **1977**, *23*, 327-341.
292. Roe, D. R.; Cheatham, T. E., PTRAJ and CPPTRAJ: Software for processing and analysis of molecular dynamics trajectory data. *Journal of Chemical Theory and Computation* **2013**, *9*, 3084-3095.
293. Miller, B. R.; McGee, T. D.; Swails, J. M.; Homeyer, N.; Gohlke, H.; Roitberg, A. E., MMPBSA.py: An efficient program for end-state free energy calculations. *Journal of Chemical Theory and Computation* **2012**, *8*, 3314-3321.
294. Kollman, P. A.; Massova, I.; Reyes, C.; Kuhn, B.; Huo, S.; Chong, L.; Lee, M.; Lee, T.; Duan, Y.; Wang, W.; Donini, O.; Cieplak, P.; Srinivasan, J.; Case, D. A.; Cheatham III, T. E., Calculating structures and free energies of complex molecules: Combining molecular mechanics and continuum models. *Accounts of Chemical Research* **2000**, *33*, 889-897.
295. Gohlke, H.; Kiel, C.; Case, D. A., Insights into protein-protein binding by binding free energy calculation and free energy decomposition for the Ras-Raf and Ras-RalGDS complexes. *Journal of molecular biology* **2003**, *330*, 891-913.
296. Wang, W.; Kollman, P. A., Computational study of protein specificity: The molecular basis of HIV-1 protease drug resistance. *Proceedings of the National Academy of Sciences of the United States of America* **2001**, *98*, 14937-14942.
297. Benesi, H. A.; Hildebrand, J., A spectrophotometric investigation of the interaction of iodine with aromatic hydrocarbons. *J Am Chem Soc* **1949**, *71*, 2703-2707.
298. Perret, F.; Guéret, S.; Danylyuk, O.; Suwinska, K.; Coleman, A. W., A stepped bilayer packing motif for para-sulphonatocalix[4]arene: The solid-state structure of the para-sulphonatocalix[4]arene-triethylamine complex. *Journal of Molecular Structure* **2006**, *797*, 1-4.
299. Karrer, P.; Nägeli, C., *Helv. Chim. Acta* **1921**, *4*.
300. Caesar, G. V.; Cushing, M. L., The starch molecule. *Journal of Physical Chemistry* **1941**, *45*, 776-790.
301. Case, D.; Darden, T. A.; Cheatham, T. E.; Simmerling, C.; Wang, J.; Duke, R.; Luo, R.; Crowley, M.; Walker, R.; Zhang, W.; Merz, K. M.; Wang, B.; Hayik, S.; Roitberg, A.; Seabra, G.; Kolossváry, I.; Wong, K. F.; Paesani, F.; Vanicek, J.; Wu, X.; Brozell, S.; Steinbrecher, T.; Gohlke, H.; Yang, L.; Tan, C.; Mongan, J.; Hornak, V.; Cui, G.; Mathews, D. H.; Seetin, M. G.; Sagui, C.; Babin, V.; Kollman, P., *AMBER 14*, University of California, San Francisco. 2012.

302. Kräutler, V.; Van Gunsteren, W. F.; Hünenberger, P. H., A fast SHAKE algorithm to solve distance constraint equations for small molecules in molecular dynamics simulations. *Journal of Computational Chemistry* **2001**, *22*, 501-508.
303. Kellici, T. F.; Ntountaniotis, D.; Liapakis, G.; Tzakos, A. G.; Mavromoustakos, T., The dynamic properties of angiotensin II type 1 receptor inverse agonists in solution and in the receptor site. *Arabian Journal of Chemistry* <http://dx.doi.org/10.1016/j.arabjc.2016.11.014>.
304. Oliveira, T. R.; Lamy, M. T.; De Paula, U. M.; Guimaraes, L. L.; Toledo, M. S.; Takahashi, H. K.; Straus, A. H.; Lindsey, C. J.; Paiva, T. B., Structural properties of lipid reconstructs and lipid composition of normotensive and hypertensive rat vascular smooth muscle cell membranes. *Brazilian journal of medical and biological research = Revista brasileira de pesquisas medicas e biologicas / Sociedade Brasileira de Biofisica ... [et al.]* **2009**, *42*, 844-53.
305. Netticadan, T. J.; Ashavaid, T. F.; Nair, K. G., Characterisation of the canine cardiac sarcolemma in experimental myocardial ischemia. *Indian journal of clinical biochemistry : IJCB* **1997**, *12*, 49-54.
306. Miura, S.-i.; Kiya, Y.; Hanzawa, H.; Nakao, N.; Fujino, M.; Imaizumi, S.; Matsuo, Y.; Yanagisawa, H.; Koike, H.; Komuro, I.; Karnik, S. S.; Saku, K., Small Molecules with Similar Structures Exhibit Agonist, Neutral Antagonist or Inverse Agonist Activity toward Angiotensin II Type 1 Receptor. *PLoS ONE* **2012**, *7*, e37974.
307. Cunningham, B. C.; Wells, J. A., High-resolution epitope mapping of hGH-receptor interactions by alanine-scanning mutagenesis. *Science* **1989**, *244*, 1081-5.
308. Rasmussen, S. G.; DeVree, B. T.; Zou, Y.; Kruse, A. C.; Chung, K. Y.; Kobilka, T. S.; Thian, F. S.; Chae, P. S.; Pardon, E.; Calinski, D.; Mathiesen, J. M.; Shah, S. T.; Lyons, J. A.; Caffrey, M.; Gellman, S. H.; Steyaert, J.; Skiniotis, G.; Weis, W. I.; Sunahara, R. K.; Kobilka, B. K., Crystal structure of the beta2 adrenergic receptor-Gs protein complex. *Nature* **2011**, *477*, 549-55.
309. Dror, R. O.; Arlow, D. H.; Maragakis, P.; Mildorf, T. J.; Pan, A. C.; Xu, H.; Borhani, D. W.; Shaw, D. E., Activation mechanism of the beta2-adrenergic receptor. *Proceedings of the National Academy of Sciences of the United States of America* **2011**, *108*, 18684-9.
310. Chien, E. Y.; Liu, W.; Zhao, Q.; Katritch, V.; Han, G. W.; Hanson, M. A.; Shi, L.; Newman, A. H.; Javitch, J. A.; Cherezov, V.; Stevens, R. C., Structure of the human dopamine D3 receptor in complex with a D2/D3 selective antagonist. *Science* **2010**, *330*, 1091-5.
311. Beyermann, M.; Heinrich, N.; Fechner, K.; Furkert, J.; Zhang, W.; Kraetke, O.; Bienert, M.; Berger, H., Achieving signalling selectivity of ligands for the corticotropin-releasing factor type 1 receptor by modifying the agonist's signalling domain. *British Journal of Pharmacology* **2007**, *151*, 851-859.
312. Maggi, C. A.; Schwartz, T. W., The dual nature of the tachykinin NK1 receptor. *Trends in pharmacological sciences* **1997**, *18*, 351-5.
313. Sanni, S. J.; Hansen, J. T.; Bonde, M. M.; Speerschneider, T.; Christensen, G. L.; Munk, S.; Gammeltoft, S.; Hansen, J. L., β -Arrestin 1 and 2 stabilize the angiotensin II type I receptor in distinct high-affinity conformations. *British Journal of Pharmacology* **2010**, *161*, 150-161.
314. Perola, E.; Charifson, P. S., Conformational Analysis of Drug-Like Molecules Bound to Proteins: An Extensive Study of Ligand Reorganization upon Binding. *Journal of Medicinal Chemistry* **2004**, *47*, 2499-2510.
315. Stockwell, G. R.; Thornton, J. M., Conformational diversity of ligands bound to proteins. *J Mol Biol* **2006**, *356*, 928-44.

316. Unione, L.; Galante, S.; Diaz, D.; Canada, F. J.; Jimenez-Barbero, J., NMR and molecular recognition. The application of ligand-based NMR methods to monitor molecular interactions. *MedChemComm* **2014**, 5, 1280-1289.
317. Liang, B.; Tamm, L. K., NMR as a tool to investigate the structure, dynamics and function of membrane proteins. *Nat Struct Mol Biol* **2016**, 23, 468-474.
318. Rus, L.; Constantinescu, D.; Drăgan F.; Farcaș A.; Kacs I.; Borodi, G.; Bratu I.; M., B., Inclusion Complex of Enalapril Maleate/ β – Cyclodextrin. FTIR, XRay Diffraction, DSC and Molecular Modeling. *Farmacia* **2007**, 55, 185-192.
319. Kellici, T. F.; Ntountaniotis, D.; Leonis, G.; Chatziathanasiadou, M.; Chatzikonstantinou, A. V.; Becker-Baldus, J.; Glaubitz, C.; Tzakos, A. G.; Viras, K.; Chatzigeorgiou, P.; Tzimas, S.; Kefala, E.; Valsami, G.; Archontaki, H.; Papadopoulos, M. G.; Mavromoustakos, T., Investigation of the interactions of silibinin with 2-hydroxypropyl-beta-cyclodextrin through biophysical techniques and computational methods. *Mol Pharm* **2015**, 12, 954-65.
320. Lee, D. Y. W.; Liu, Y., Molecular structure and stereochemistry of silybin A, silybin B, isosilybin A, and isosilybin B, isolated from *Silybum marianum* (milk thistle). *Journal of Natural Products* **2003**, 66, 1171-1174.
321. Křen, V.; Ulrichová, J.; Kosina, P.; Stevenson, D.; Sedmera, P.; Přikrylová, V.; Halada, P.; Šimánek, V., Chemoenzymatic preparation of silybin β -glucuronides and their biological evaluation. *Drug Metabolism and Disposition* **2000**, 28, 1513-1517.
322. Sawatdee, S.; Phetmung, H.; Srichana, T., Sildenafil citrate monohydrate-cyclodextrin nanosuspension complexes for use in metered-dose inhalers. *International Journal of Pharmaceutics* **2013**, 455, 248-258.
323. Zhang, M.; Li, J.; Zhang, L.; Chao, J., Preparation and spectral investigation of inclusion complex of caffeic acid with hydroxypropyl- β -cyclodextrin. *Spectrochimica Acta, Part A: Molecular and Biomolecular Spectroscopy* **2009**, 71, 1891-1895.
324. Wang, F.; Yang, B.; Zhao, Y.; Liao, X.; Gao, C.; Jiang, R.; Han, B.; Yang, J.; Liu, M.; Zhou, R., Host-guest inclusion system of scutellarein with 2-hydroxypropyl-beta-cyclodextrin: Preparation, characterization, and anticancer activity. *Journal of Biomaterials Science, Polymer Edition* **2014**, 25, 594-607.
325. Kontogianni, V. G.; Charisiadis, P.; Primikyri, A.; Pappas, C. G.; Exarchou, V.; Tzakos, A. G.; Gerathanassis, I. P., Hydrogen bonding probes of phenol -OH groups. *Organic & biomolecular chemistry* **2013**, 11, 1013-25.
326. Primikyri, A.; Kyriakou, E.; Charisiadis, P.; Tsiafoulis, C.; Stamatis, H.; Tzakos, A. G.; Gerathanassis, I. P., Fine-tuning of the diffusion dimension of -OH groups for high resolution DOSY NMR applications in crude enzymatic transformations and mixtures of organic compounds. *Tetrahedron* **2012**, 68, 6887-6891.
327. Choi, Y.; Jung, S., Molecular dynamics (MD) simulations for the prediction of chiral discrimination of N-acetylphenylalanine enantiomers by cyclomaltoheptaose (β -cyclodextrin, β -CD) based on the MM-PBSA (molecular mechanics-Poisson-Boltzmann surface area) approach. *Carbohydrate Research* **2004**, 339, 1961-1966.
328. Beà, I.; Jaime, C.; Kollman, P., Molecular recognition by β -cyclodextrin derivatives: Molecular dynamics, free-energy perturbation and molecular mechanics/Poisson-Boltzmann surface area goals and problems. *Theoretical Chemistry Accounts* **2002**, 108, 286-292.
329. Fermeiglia, M.; Ferrone, M.; Lodi, A.; Pricl, S., Host-guest inclusion complexes between anticancer drugs and β -cyclodextrin: Computational studies. *Carbohydrate Polymers* **2003**, 53, 15-44.
330. Felton, L. A.; Popescu, C.; Wiley, C.; Esposito, E. X.; Lefevre, P.; Hopfinger, A. J., Experimental and Computational Studies of Physicochemical Properties Influence NSAID-Cyclodextrin Complexation. *AAPS PharmSciTech* **2014**.

331. Tiwari, P.; Kumar, A.; Balakrishnan, S.; Kushwaha, H. S.; Mishra, K. P., Silibinin-induced apoptosis in MCF7 and T47D human breast carcinoma cells involves caspase-8 activation and mitochondrial pathway. *Cancer investigation* **2011**, 29, 12-20.
332. Kim, T. H.; Woo, J. S.; Kim, Y. K.; Kim, K. H., Silibinin induces cell death through reactive oxygen species-dependent downregulation of notch-1/ERK/Akt signaling in human breast cancer cells. *The Journal of pharmacology and experimental therapeutics* **2014**, 349, 268-78.
333. Zhang, S.; Yang, X.; Morris, M. E., Flavonoids are inhibitors of breast cancer resistance protein (ABCG2)-mediated transport. *Molecular pharmacology* **2004**, 65, 1208-16.
334. Job, P., Job's method of continuous variation. *Ann Chim* **1928**, 9, 113-203.
335. Wawer, I.; Zielinska, A., ¹³C-CP-MAS-NMR studies of flavonoids. I. Solid-state conformation of quercetin, quercetin 5'-sulphonic acid and some simple polyphenols. *Solid state nuclear magnetic resonance* **1997**, 10, 33-8.
336. Morales, A.; Santana, A.; Althoff, G.; Melendez, E., Host-Guest Interactions between Calixarenes and Cp(2)NbCl(2). *Journal of organometallic chemistry* **2011**, 696, 2519-2527.
337. Kellici, T. F.; Ntountaniotis, D.; Leonis, G.; Chatziathanasiadou, M.; Chatzikonstantinou, A. V.; Becker-Baldus, J.; Glaubitz, C.; Tzakos, A. G.; Viras, K.; Chatzigeorgiou, P.; Tzimas, S.; Kefala, E.; Valsami, G.; Archontaki, H.; Papadopoulos, M. G.; Mavromoustakos, T., Investigation of the interactions of silibinin with 2-hydroxypropyl- β -cyclodextrin through biophysical techniques and computational methods. *Molecular Pharmaceutics* **2015**, 12, 954-965.
338. Galindo-Murillo, R.; Sandoval-Salinas, M. E.; Barroso-Flores, J., In Silico Design of Monomolecular Drug Carriers for the Tyrosine Kinase Inhibitor Drug Imatinib Based on Calix- and Thiocalix[n]arene Host Molecules: A DFT and Molecular Dynamics Study. *Journal of Chemical Theory and Computation* **2014**, 10, 825-834.
339. Slocik, J. M.; Stone, M. O.; Naik, R. R., Synthesis of gold nanoparticles using multifunctional peptides. *Small* **2005**, 1, 1048-52.
340. Chen, S.; Wang, Z. L.; Ballato, J.; Foulger, S. H.; Carroll, D. L., Monopod, bipod, tripod, and tetrapod gold nanocrystals. *J Am Chem Soc* **2003**, 125, 16186-7.
341. Christodoulou, E.; Kechagia, I. A.; Tzimas, S.; Balafas, E.; Kostomitsopoulos, N.; Archontaki, H.; Dokoumetzidis, A.; Valsami, G., Serum and tissue pharmacokinetics of silibinin after per os and i.v. administration to mice as a HP-beta-CD lyophilized product. *Int J Pharm* **2015**, 493, 366-73.